9 March 2007 | $10

Science

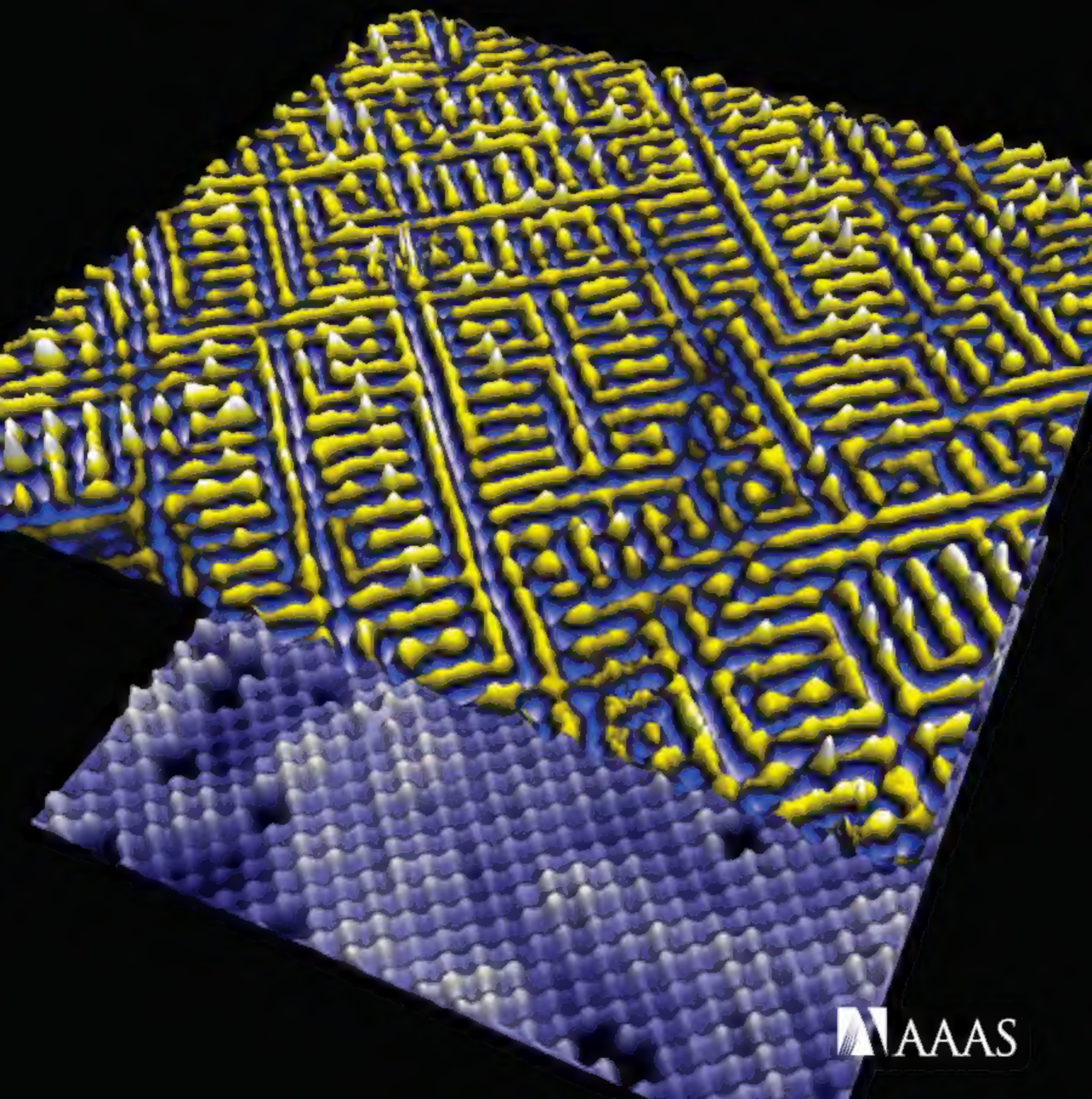

AAAS

One FailSafe™ PreMix is guaranteed to work.

Keep a dozen on hand for your PCR challenges

Using a unique blend of thermostable enzymes and a set of 12 standardized premixes, optimization of any PCR reaction is quick, easy and reproducible.

The FailSafe™ PCR System Amplifies—

- Up to 85% GC-rich templates
- Any templates up to 20 kb
- Multiplex PCR, consistently
- Low copy number templates

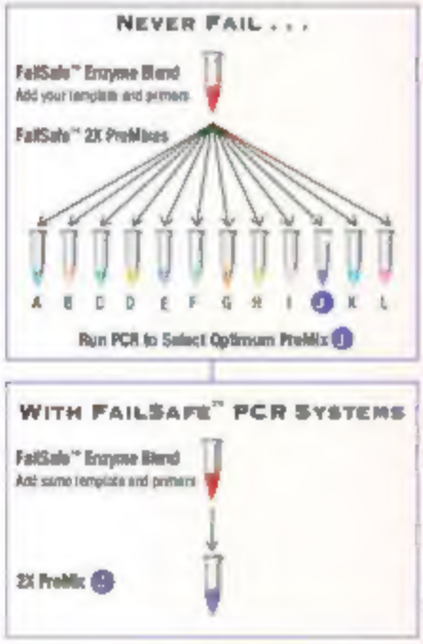

Amplification of an 80-85% GC-rich region of the human fragile X gene. PCR was performed using the FailSafe™ PCR System. Lanes A-L show the amplification products resulting from PCR using the 12 FailSafe PCR PreMixes. M, molecular weight marker. Optimal amplification was obtained with FailSafe PCR PreMix J.

Start using FailSafe and get your PCR to work *the first time and every time.*

EPICENTRE offers a money-back guarantee for successful PCR with one or more PreMix. If you're not happy, you don't pay.

To order yours, go to **www.EpiBio.com** and enter QuickInfo code: **FSA25**

EPICENTRE® Biotechnologies

TaKaRa

REAL TIME PCR

Real Time PCR Made *Real Easy*

SYBR® Green

SYBR® *Premix Ex Taq*™

SYBR® *Premix Ex Taq*™ (Perfect Real Time) delivers exceptional real time PCR results quickly and easily.

- **Easy-to-Use:** convenient premix formula.
- **Less Optimization:** great for first screens.
- **Versatile:** use on any real-time PCR instrument.
- **Low C_T Values:** high sensitivity with detection of as few as 10 copies.
- **Precise Quantification:** 2-fold difference can be accurately detected.
- **Fast:** works with high speed qPCR instruments.

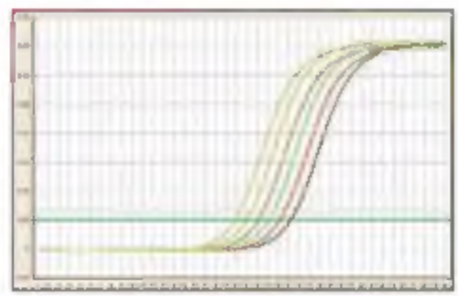

Accurate detection of 2-fold difference, using SYBR® *Premix Ex Taq*™ with an Applied Biosystems 7500 Real Time System.

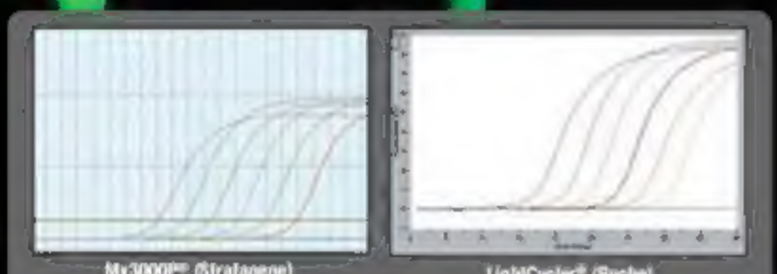

Mx3000P® (Stratagene) LightCycler® (Roche)

Excellent Amplification Curves Generated using SYBR® *Premix Ex Taq*™ with Several qPCR Instruments.

Also Available in a Premix for TaqMan® Probe Detection

TAKARA BIO INC.
The Biotechnology Company™

Otsu, Shiga, Japan
Phone: +81 77-543-7247
Fax: +81 77-543-9254

USA: Takara Mirus Bio Inc. Phone: 888-251-6618 • www.takaramirusbio.com
Europe: Takara Bio Europe S.A.S. Phone: +33 1 3904 6880 • www.takara-bio.eu
Korea: Takara Korea Biomedical Inc. Phone: +82 2 2081 2525 • www.takara.co.kr
China: Takara Biotechnology (Dalian) Co., Ltd. Phone: +86 411 8764 1681 • www.takara.com.cn

For more information and a list of Takara distributors worldwide, please visit our website today!

www.takara-bio.com

GE Healthcare

Bringing protein analysis to life with Ettan DIGE and Amersham ECL

When it comes to life sciences, GE Healthcare is setting the standard. Tens of thousands of scientists worldwide rely on our products and proven expertise in protein analysis and detection every day. But we're never content to stand still. We're constantly striving for innovations that boost accuracy and deliver quantitative data.

The result is new fluorescence platforms like the Ettan™ DIGE Imager and Amersham ECL Plex™ for quantitative protein analysis.

By continually developing technology that can turn your scientific ideas into reality, we're bringing science to life and helping to transform drug discovery and healthcare.

We call it Protein Analysis Re-Imagined.

Discover the full power of Ettan DIGE and the Amersham ECL™ family of Western blotting systems at

www.gehealthcare.com/protein_analysis

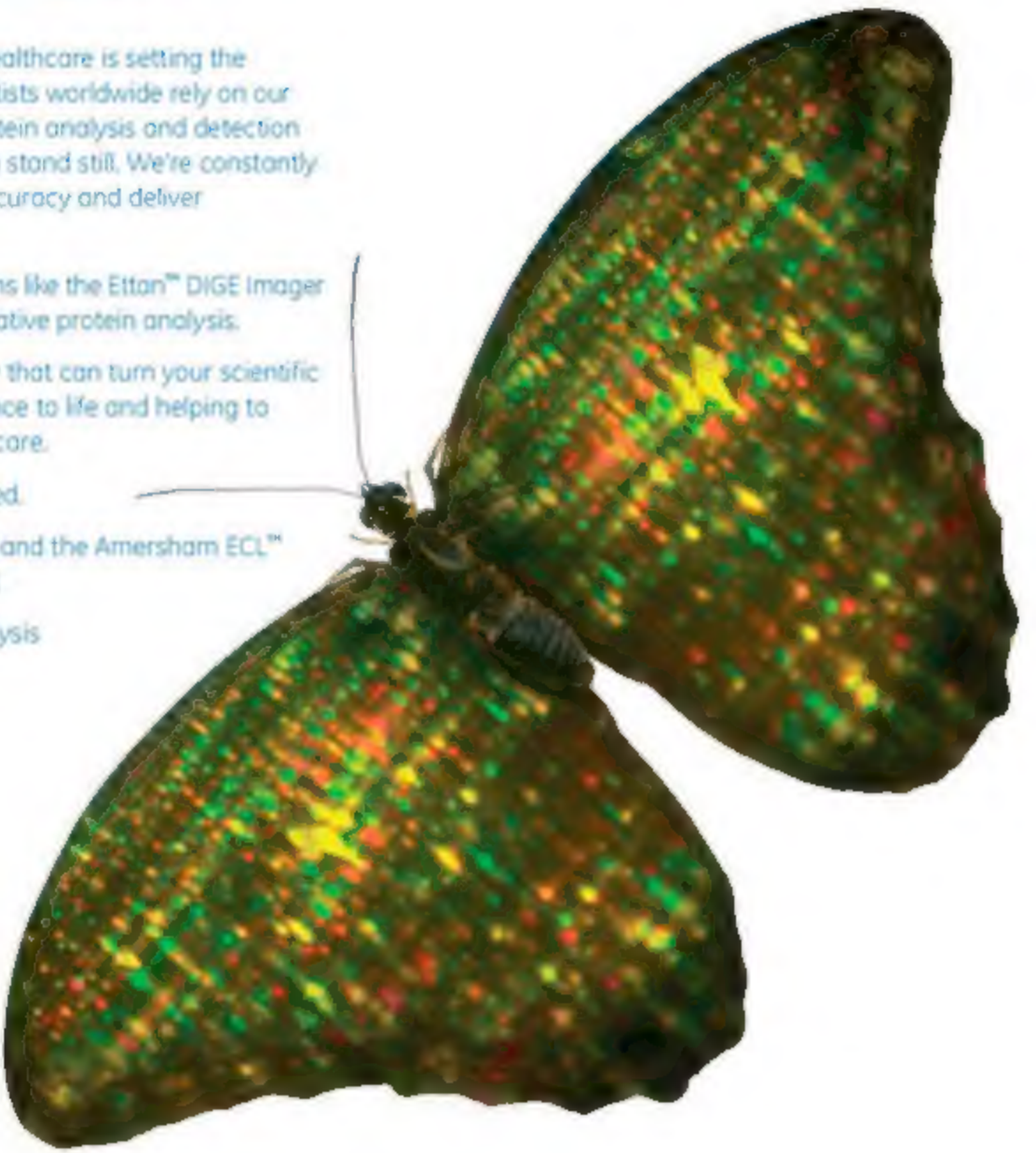

imagination at work

GE Healthcare Bio-Sciences AB, a General Electric Company
Björkgatan 30, 751 84 Uppsala, Sweden

GEDB-06

Volume 315, Issue 5817

COVER

A scanning tunneling microscopy image of a high-temperature superconductor (bottom) shows the regular atomic periodicity of the crystal. Simultaneously measured ratios of electron injection to extraction (top, yellow) reveal strong variations in electronic structure. See page 1380.

Image: Yuhki Kohsaka

DEPARTMENTS

EDITORIAL

NEWS OF THE WEEK

NEWS FOCUS

LETTERS

BOOKS *ET AL.*

POLICY FORUM

PERSPECTIVES

1373 & 1402

CONTENTS continued >>

Assay technologies by QIAGEN

Detect the essence of life

- Gene expression assays
- Pathogen detection*
- Genetic analysis
- HLA and haplotyping*

Contact QIAGEN today or visit www.qiagen.com/goto/AssayTech .

*artus PCR assays, GeneVision Cleanup Kits, and SBTexcellerator HLA Kits have not received clearance or approval for clinical use in US and Canada. SBTexcellerator HLA Kits are for research use only in Europe.

QIAGEN®

Sample & Assay Technologies

Science

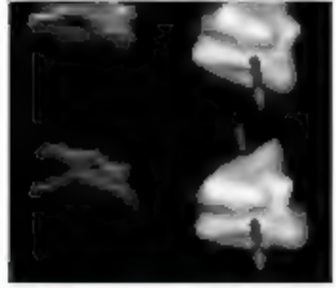

SCIENCE EXPRESS

www.sciencexpress.org

PLANT SCIENCE

A G Protein–Coupled Receptor Is a Plasma Membrane Receptor for the Plant Hormone Abscisic Acid
X. Liu, Y. Yue, B. Li, Y. Nie, W. Li, W.-H. Wu, L. Ma
A membrane-bound receptor for abscisic acid is identified.
10.1126/science.1135882

PERSPECTIVE: A Plant Receptor with a Big Family
E. Grill and A. Christmann
10.1126/science.1140761

PLANETARY SCIENCE

Spin Rate of Asteroid (54509) 2000 PH5 Increasing Due to the YORP Effect
P. A. Taylor et al.
Slowing of near-Earth asteroid (54509) 2000 PH5 is as expected for solar thermal torques as predicted by the YORP effect.
10.1126/science.1139038

PLANETARY SCIENCE

Direct Detection of the Asteroidal YORP Effect
S. C. Lowry et al.
Optical and radar observations of a near-Earth asteroid show that the radiation pressure from impacting sunlight is slowing its rotation, as predicted.
10.1126/science.1139040

BREVIA

RESEARCH ARTICLE

CREDIT (BOTTOM): A. BADERTSCHER/N. MEYSTRE

REPORTS

CONTENTS continued >>

The cAMP-Glo™ Assay, as close as it gets...

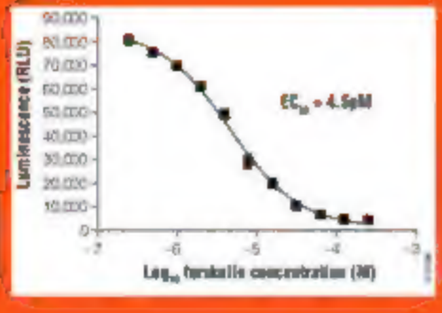

...to the real thing. The inherent complexity of GPCR signaling demands simple, robust technologies for quantifying receptor activation. The new cAMP-Glo Assay provides the simplest method available for measuring G_S or G_i coupled receptor activity. The wide dynamic range and high sensitivity of the bioluminescent cAMP-Glo Assay makes it ideally suited for 1536-well plate applications.

To receive more information and qualify for a FREE SAMPLE visit:
www.promega.com/campglo

PROMEGA CORPORATION • www.promega.com

Promega

REPORTS *CONTINUED...*

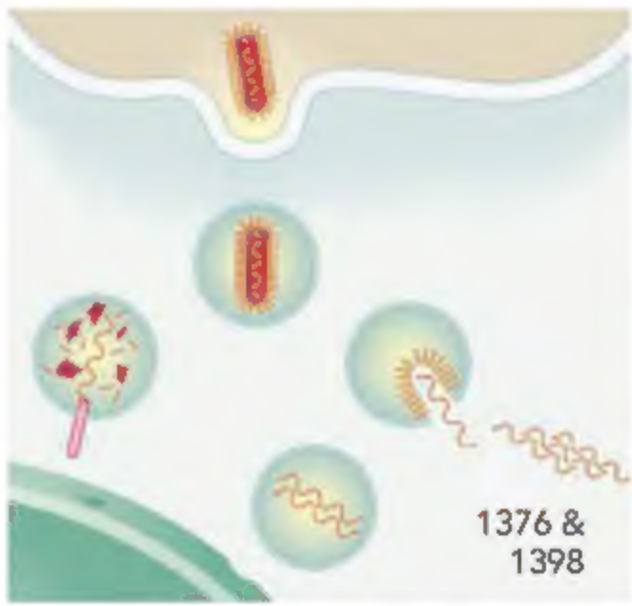

AAAS
ADVANCING SCIENCE, SERVING SOCIETY

SCIENCE (ISSN 0036-8075) is published weekly on Friday, except the last week in December, by the American Association for the Advancement of Science, 1200 New York Avenue, NW, Washington, DC 20005. Periodicals Mail postage (publication No. 484469) paid at Washington, DC, and additional mailing offices. Copyright © 2007 by the American Association for the Advancement of Science. The title SCIENCE is a registered trademark of the AAAS. Domestic individual membership and subscription (51 issues): $142 ($74 allocated to subscription). Domestic institutional subscription (51 issues): $710. Foreign postage extra: Mexico, Caribbean (surface mail) $55; other countries (air assist delivery) $85. First class, airmail, student, and canadian rates on request. Canadian rates with GST available upon request, GST #125488122. Publications Mail Agreement Number 1069624. **Printed in the U.S.A.**

Change of address: Allow 4 weeks, giving old and new addresses and 8-digit account number. **Postmaster:** Send change of address to AAAS, P.O. Box 96178, Washington, DC 20090-6178. **Single-copy sales:** $10.00 current issue, $15.00 back issue prepaid includes surface postage; bulk rates on request. **Authorization to photocopy** material for internal or personal use under circumstances not falling within the fair use provisions of the Copyright Act is granted by AAAS to libraries and other users registered with the Copyright Clearance Center (CCC) Transactional Reporting Service, provided that $30.00 per article is paid directly to CCC, 222 Rosewood Drive, Danvers, MA 01923. The identification code for *Science* is 0036-8075. *Science* is indexed in the Reader's *Guide to Periodical Literature* and in several specialized indexes.

CONTENTS continued >>

New — MicroRotofor lysis kits for easy, effective cell lysis and protein extraction

Fractionation just got simpler.

Reduce the complexity of your protein sample with the MicroRotofor™ system.

Fractionation is an essential step for increasing protein resolution in proteomic workflows. By fractionating, you reduce your sample complexity and enrich low-abundance proteins, both of which are central to biomarker discovery. Bio-Rad offers the MicroRotofor system for fractionation of proteins prior to most downstream proteomic applications, including 2-D gel electrophoresis and LC-MS/MS analysis.

- Handles small volumes (~2.5 ml) of precious samples
- Is compact and easy to use
- Separates proteins by liquid-phase isoelectric focusing
- Fractionates complex protein mixtures under native and denaturing conditions
- Offers customizable pH gradients to further enhance resolution of proteins of interest

MicroRotofor system

For more information, visit us on the Web at **www.bio-rad.com/microrotofor/**

Visit us on the Web at **discover.bio-rad.com**
Call toll free at 1-800-4BIORAD (1-800-424-6723); outside the US, contact your local sales office.

BIO-RAD

Lance-tailed manakins use the buddy system

SCIENCENOW

www.sciencenow.org

It Pays to Be the Wingman
In a South American bird, the alpha male always gets the girl, but his buddy benefits from tagging along

Dodging a Warming Bullet
Banning CFCs has removed a whole lot of greenhouse potential from the atmosphere

Submarine to Search for Early Americans
Expedition will look for traces of long-drowned salt mines in Gulf Coast

Boxed in by your narrow specialty?

SCIENCE CAREERS

www.sciencecareers.org

US: Opportunities—Breadth Versus Depth
P. Fiske
There are advantages to maintaining a broader point of view over your narrow field of interest

EUROPE: Italian Research Shake-Up Pending
S. Biagini
Italian researchers await new legislation promising new positions, funding, and procedures

US: Is Grants.gov in the FastLane?
A. Kotok
Will NSF continue its own FastLane system or join Grants.gov for electronic grant applications?

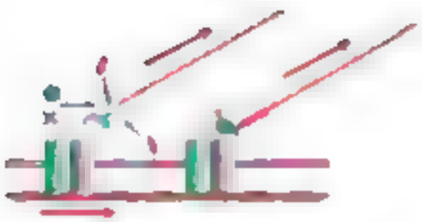

Are focal adhesions molecular clutches?

SCIENCE'S STKE

www.stke.org

PERSPECTIVE: Flux at Focal Adhesions—Slippage Clutch, Mechanical Gauge, or Signal Depot
Y. Wang
Why do various focal adhesion proteins undergo different degrees of correlated retrograde movement with actin filaments?

REVIEW: The Expanding Role for ITAM-Based Signaling Pathways in Immune Cells
C. L. Abram and C. A. Lowell
Activation of immune cells by many different receptors depends on ITAM-based signaling.

CREDIT: (SCIENCE NOW) EMILY DUVAL

Separate individual or institutional subscriptions to these products may be required for full-text access.

Phusion™ High-Fidelity DNA Polymerase from New England Biolabs

EXTREME PRECISION WITH UNPARALLELED SPEED AND ROBUSTNESS

With Phusion High-Fidelity DNA Polymerase, there is no need to compromise any aspect of your PCR performance. A superior choice for cloning, this recombinant polymerase has an error rate 50-fold lower than *Taq* DNA Polymerase, making it the most accurate thermostable polymerase available. Phusion DNA Polymerase is supplied in a variety of formats, or with a [redacted] for increased specificity.

Advantages:

- Extreme Fidelity – Highest of any thermostable polymerase
- High Speed – Extension times are dramatically reduced
- Robustness – Reduce reaction failures with minimal optimization
- High Yield – Increase product yields with minimal enzyme amounts
- Specificity – Hot start modification reduces non-specific amplification

• **Phusion High-Fidelity DNA Polymerase** (R)	**F-530S/L**
• **Phusion Hot Start High-Fidelity DNA Polymerase** (R)	**F-540S/L**
• **Phusion High-Fidelity PCR Master Mix** (R)	
with HF Buffer	**F-531S/L**
with GC Buffer	**F-532S/L**
• **Phusion High-Fidelity PCR Kit** (R)	**F-553S/L**

(R) = Recombinant

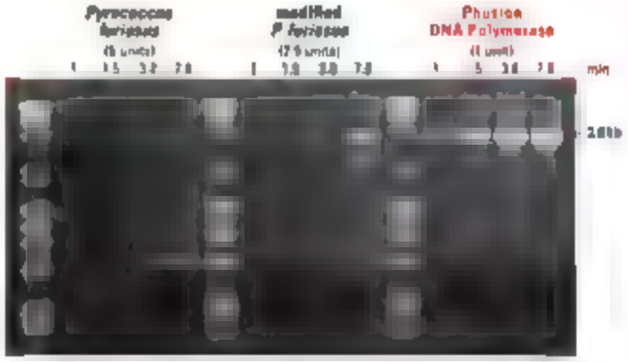

Experience extreme speed and yield with Phusion High-Fidelity DNA Polymerase. A 2.0 kb fragment from human beta globin gene was amplified according to suppliers' recommendations using varying extension times. Phusion DNA Polymerase was able to amplify the fragment with a combined annealing and extension step of only 1 minute. Also, a single unit of Phusion DNA Polymerase produced higher yields than 2.5 or 5 units of *Pyrococcus furiosus* DNA Polymerases.

Phusion™ is a trademark of Finnzymes Oy.

For more information please visit www.neb.com

- **New England Biolabs Inc.** 1-800-NEB-LABS Tel. (978) 927-5054 Fax (978) 921-1350 info@neb.com
- **Canada** Tel. (800) 387-1095 info@ca.neb.com
- **Germany** Tel. 0800/246 5227 info@de.neb.com
- **UK** Tel. (0800) 318486 info@uk.neb.com
- **China** Tel. 010-82378266 beijing@neb-china.com

Produced by

FINNZYMES

Distributed by

NEW ENGLAND BioLabs Inc.

the leader in enzyme technology

EDITED BY STELLA HURTLEY AND PHIL SZUROMI

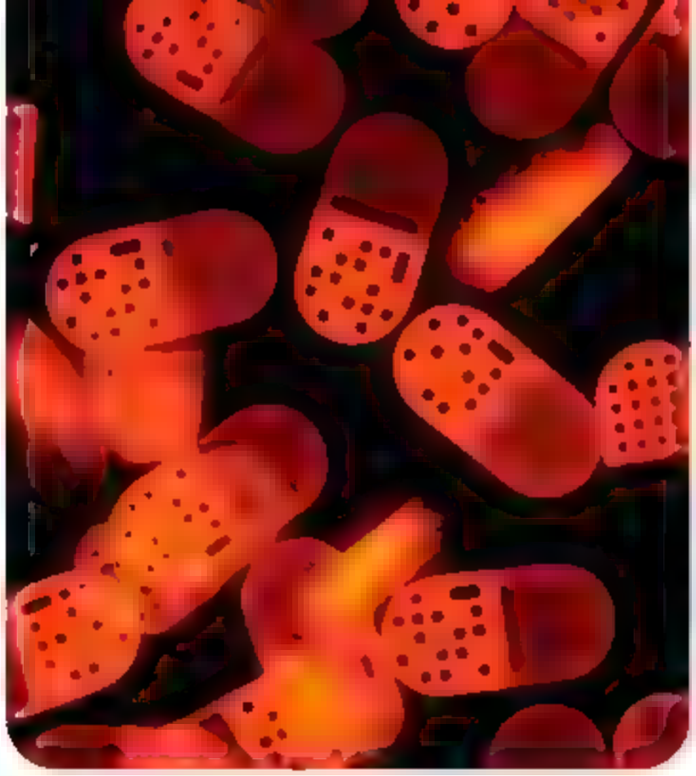

<< Flow the Codes

Ideally, molecular screening should allow for the simultaneous analysis of many molecular targets. **Pregibon *et al.*** (p. 1393) used microfluidics and lithographic masks to create flat particles with lateral dimensions of ~100 micrometers and thicknesses of about 30 micrometers. One half of each particle bears a distinct fluorescent barcode (out of more than 1 million possible codes); the other half bears a probe for target binding. After incubation with a sample, a flow-based analysis system then scans each particle via single-wavelength fluorescence for its code and evidence of bound target. Fluorescently labeled DNA targets could be detected at the 500-attomole level.

Electronic Superstructure and Superconductivity

The cuprates that exhibit high-temperature superconductivity (HTSC) are formed from parent antiferromagnetic insulators by chemical doping which removes electrons from the CuO_2 planes. Most HTSC theories have focused on the transition from antiferromagnetic to superconducting states and the effects of only lightly "hole doping" the materials have often been ignored. **Kohsaka *et al.*** (p. 1380, published online 8 February; see the cover and the Perspective by **Zaanen**) present scanning tunneling spectroscopy measurements for two families of underdoped cuprate superconductors with different lattice structures that reveal a common electronic superstructure in both materials. The authors argue that the electronic superstructure, which forms narrow stripes with a spatial period of four unit cells, is an intrinsic property of the cuprates and is the precursor parent phase to the onset of superconductivity. The results suggest that superconductivity in the cuprates emerges with increasing hole doping as electrons become delocalized from the intrinsic bond-centered electronic glass.

Quantum Hall Effect in Metal Oxides and Graphene

The quantum Hall effect (QHE), in which the resistance of a two-dimensional electron gas varies by precisely quantized steps in response to a magnetic field, has generally been confined to high-quality, high-mobility semiconductors at cryogenic temperatures. **Tsukazaki *et al.*** (p. 1388, published online 25 January) now report the observation of the QHE in an oxide heterostructure grown from layers of ZnO and $Mg_xZn_{1-x}O$. **Novoselov *et al.*** (p. 1379) report the observation of the QHE in graphene sheets at room temperature. These results present the possibility of combining quantum Hall physics with the versatile metal oxides and in the emerging graphene sheet system (see the Perspective by **Ramirez**).

Increasing Plasticity of Metallic Glasses

Bulk metallic glasses (BMGs) hold much promise because of their high strengths, but suffer from brittle fracture through the formation of shear bands. This mode of failure is not desirable in most applications because there is little warning of the impending material failure. **Liu *et al.*** (p. 1385) report observations of large compressive plasticity of >150% obtained in several zirconium-based BMGs at room temperature as a result of highly controlled tuning of the alloys' composition. The materials develop a two-phase microstructure that includes "strongly [illegible] regions" separated by narrow "weakly bonded regions." Although shear banding appears to be initiated in the weakly bonded regions, the strongly bonded regions act to prevent the further growth of the bands.

High and Dry

Particulate air pollution can provide many more nuclei for forming cloud droplets compared to unpolluted air. The increased number of cloud droplets that form decreases their size, which leads to less frequent coalescence into raindrops and less precipitation. This effect is thought to account for decreased orographic precipitation in which rainfall is caused by the upward deflection of an air mass by a ridge or a mountain, but this effect has not been tested against actual data on aerosol concentration and precipitation. **Rosenfeld *et al.*** (p. 1396) analyze a 50-year-long record of aerosols and precipitation from central China, one of the most polluted areas of the world. Strongly polluted air provided only half as much orographic precipitation as did clean air.

Eat Up to Meet Up

Different members of the Toll-like receptor (TLR) family have evolved to recognize the distinct signatures left by pathogens, including the single-stranded (ss) and double-stranded nucleic acid genomes of viruses. In the case of plasmacytoid dendritic cells (pDC), detection by TLRs coordinates [illegible] in a program of gene activation that helps these cells prime anti-viral, adaptive immune [illegible]. This response to some viruses, such as [illegible] is achieved without the need for replication of pDC, which makes the process of immune activation less dependent on direct infection of pDC. However, **Lee *et al.*** (p. 1398, published online 1 February; see the Perspective by **Reis e Sousa**) show that for RNA viruses that generate replication intermediates in the cytosol, a direct indicator of viral replication is needed. In such cases, autophagy—the sequestering of organelles and

Continued on page 1335

CREDITS (TOP TO BOTTOM): DANIEL PREGIBON, LIU ET AL.

www.roche-applied-science.com

LightCycler® 480
Real-Time PCR System

Looking for more versatility in real-time PCR?

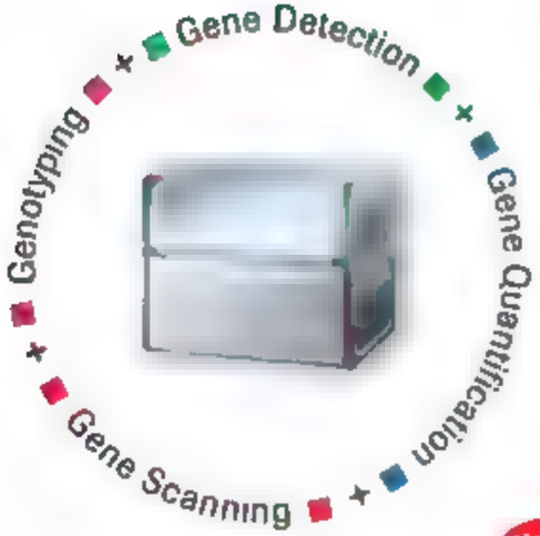

We have what you need to accomplish more — now and in the future.

Choose the LightCycler® 480 System (96- and 384-well formats) and get the power and flexibility to meet changing research needs.

- **Gene Detection:** Benefit from an advanced optical system and enhanced multiplexing capabilities to perform multitarget analysis.
- **Gene Quantification:** Utilize sophisticated software and unique algorithms to generate highly accurate gene quantification data.
- **Genotyping:** Achieve reliable genotyping results based on superior post PCR melting curve analysis.
- **Gene Scanning:** Employ the innovative high resolution melting (HRM) method to scan genes for unknown variations.

New

Be prepared for the evolving demands of real-time PCR.

Learn more about our cutting-edge technologies that provide versatility without compromise — visit ***www.lightcycler480.com*** today!

Roche

Roche Diagnostics GmbH
Roche Applied Science
68298 Mannheim
Germany

Continued from page 1333

long lived proteins for delivery to the lysosome for degradation. The pendulin ssRNA and its TLR sensing protein in the lysosome. It is not clear if this link between autophagy and innate recognition represents a broader means of facilitating immunity to pathogens.

Toward Antibacterial Development

The bacterial cell wall is built by glycosyltransferase (GT) and transpeptidase (TP) enzymes. Penicillin and related antibiotics act on TP enzymes, but bacterial resistance is developing against these antibiotics. GT enzymes are an attractive target for new drugs because they are essential and are membrane bound and thus accessible. **Lovering *et al.*** (p. 1402, see the Perspective by **Wright**) have determined the crystal structure of penicillin binding protein 2, a bifunctional enzyme from *Staphylococcus aureus* that contains both a GT and a TP domain. Structures with and without the inhibitor moenomycin bound in the GT domain provide insight into the mechanism of cell wall biosynthesis and provide a starting point for structure based design of antibacterials.

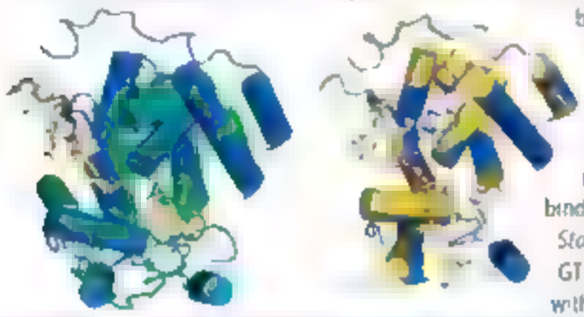

Checkpoint, What Checkpoint?

Cells use biochemical signaling mechanisms known as checkpoints to monitor the status of the cell so that cell division only occurs when conditions are right for successful mitosis. One such checkpoint allows cell division to occur only if DNA replication is complete and no active replication forks are present. However **Torres-Rosell *et al.*** (p. 1411, see the Perspective by **Weinert**) describe experiments in which incomplete replication of ribosomal DNA (rDNA) genes does not prevent cells from proceeding into anaphase. Thus, at least in the scenario studied in which yeast bear mutations in the genes encoding the Smc5 and Smc6 proteins (which function as a heterodimer in DNA repair), the delayed repair of rDNA do not trigger a checkpoint that blocks progression of the cells into mitosis.

Robotic Salamander

The locomotion of the salamander provides an opportunity to connect research on vertebrate swimming (such as in the lamprey) to research on tetrapod locomotion. **Ijspeert *et al.*** (p. 1416, see the news story by **Pennisi**) developed a biological model to show how a lamprey like swimmer can be extended to explain salamander locomotion. The model explains the transition from traveling to standing waves of body undulations, the automatic switch from one mode of locomotion to the other, the coordination between limbs and body during walking and the variation of speed and direction. To validate the model, the authors built a salamander like robot capable of producing and switching between swimming, serpentine crawling, and walking gaits.

Regulating Calcium in Plants

In *Arabidopsis*, the concentration of intracellular calcium fluctuates in a daily cycle above and beyond other responses to signaling inputs. **Tang *et al.*** (p. 1423) have now analyzed the interactions between intracellular and extracellular calcium concentrations and various signaling components in between, to arrive at a complex view of calcium physiology in the plant. Not simply a passive reflection of external calcium status, the calcium levels within a resting cell are actively monitored and managed.

Smell, Sleep, and Memory Consolidation

The evocative nature of smell is well known, but can smells actually enhance memory retention? **Rasch *et al.*** (p. 1426, see the news story by **Miller**) examined in humans whether memory consolidation is actively assisted by slow wave sleep. Subjects were first trained on an object place association task in the presence of a distinct odor. During subsequent slow wave sleep, this odor was reintroduced to facilitate reactivation of memories from the paired associate task. Odor application led to enhanced activity in the hippocampus. Subjects who experienced the odor during slow wave sleep performed better on an episodic memory retention test on the subsequent day.

CREDIT: LOVERING ET AL.

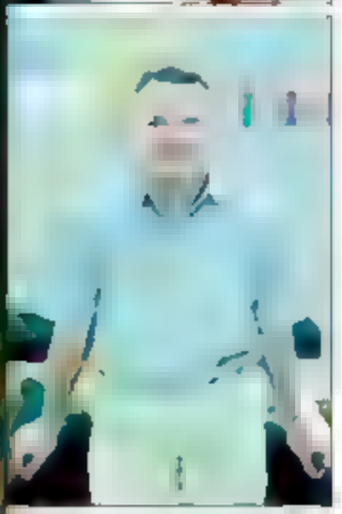

"Combining live imaging with high resolution electron microscopy is a real challenge."

"With the introduction of Green Fluorescent Protein (GFP) technology, cell biology and life sciences in general have entered a whole new exciting era of research. (...) In some instances however, the resolution of the light microscope is the limiting factor in answering our scientific questions. In these cases the higher resolution of the electron microscope is essential. Combining both light and electron microscopy is my field of interest. By performing so-called Correlative Light Electron Microscopy (CLEM) experiments one has the advantage of live cell imaging in the confocal microscope and afterwards have high resolution results from the transmission electron microscope of the same cell. The Leica EM RTS was specifically developed to be used in such experiments in conjunction with EM PACT2. It provides a high time resolution between the light and electron microscope allowing excellent preservation of the ultrastructure close to the natural state, an essential prerequisite for electron microscopy. It allows us to decide upon the exact moment of interest and study that particular event at high resolution."

Dr. Paul Verkade, Max Planck Institute for Molecular Cell Biology and Genetics, Dresden, Germany
Dr. Verkade works with the Leica EM PACT2 & RTS High Pressure Freezer

www.leica-microsystems.com

Leica
MICROSYSTEMS

R. J. Jackson is adjunct professor of Environmental Health at the University of California at Berkeley and former director of the Centers for Disease Control and Prevention National Center for Environmental Health.

Environment Meets Health, Again

THE SEEMINGLY INSURMOUNTABLE HEALTH CHALLENGE IN THE 19TH CENTURY WAS infectious disease. In the 21st century it will be a mix of global warming, poverty, and infectious and chronic diseases. Life expectancy in the United States is now twice that of the 19th century, and environmental health—healthier food, cleaner water, better places to live (the "built environment")—has been the greatest contributor. Can environmental health address 21st-century challenges?

Environmental health in the 19th century was practiced by physicians and scientists, but, importantly, also by business people, engineers, lawyers, architects, politicians, and many others outside health and science. The primary tools for health improvement were infrastructure and sanitation. For example, it was Frederick Law Olmsted, the man behind urban landscapes like New York City's Central Park, who headed the Sanitary Commission during the Civil War that saved thousands of lives.

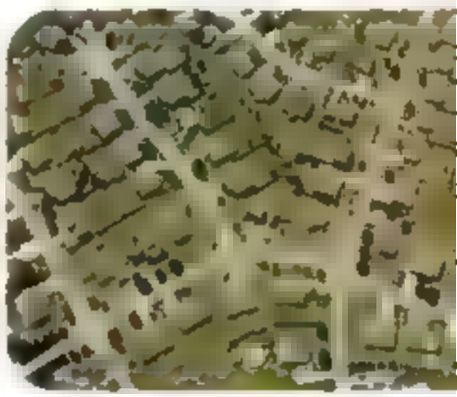

Over the past 50 years, environmental science and practice have become specialized but also fragmented. The U.S. Environmental Protection Agency, which was created largely out of federal health programs in 1970, focused on legal and engineering strategies related to air and water pollution, as well as species and land protection. Meanwhile, environmental health practitioners in local agencies hunkered down to enforceable and fee-supported activities like food service inspection. And environmental health scientists increasingly emphasized mechanisms of toxicity or illness within biological systems.

This separation led to decisions where a solution for one problem created unexpected collateral effects: the chemical MTBE that was added to gasoline to prevent air pollution caused groundwater contamination, flame retardants required in consumer products turned out to be human milk contaminants and carcinogens. Today, environmental health in the United States is vested in many agencies, not just those titled Environment or Health, but also Transportation, Education, Housing, Fisheries, Agriculture, and Defense. Each has its critical primary mandate, but each influences essential elements of the requirement to protect health and the environment. The complex challenges of the 21st century cannot be met by a set of stovepipes as disconnected as these.

Can we fix the present system? Two illustrations, one historical and the other emerging, hold hope. The first was the success of the focus on children's environmental health in the 1990s. The Food Quality Protection Act of 1996 required that children's health be the benchmark for decisions on allowable levels of pesticide residues in food, the tenet being that protecting the most exposed and sensitive in the population protects everyone. At the 10th anniversary of this Act, one-third of pesticide tolerances have been revoked. Recognizing the improvements that a children's health initiative could bring about, President Clinton ordered that all agencies develop strategies to improve the health of children, and mandated twice-yearly cabinet-level meetings to make it happen. After a cautious and questioning start, each agency recognized that it had large impacts on children's well-being, for example, Transportation in terms of safe routes to school or Housing in terms of indoor air quality. Several important efforts, including the proposal for the National Children's Study, grew out of this initiative.

The second example is more contemporary. Public health leaders are asserting—as had leaders 150 years earlier—that the built environment profoundly influences health. The focus this time is not urban tenements, but rather the fragmented and sprawling communities that foster car dependency, inactivity, obesity, loneliness, fossil fuel and resource consumption, and environmental pollution. Concern about the built environment's effects on health has caught fire, with conferences and strategy sessions, pending legislation, and an increasing number of new scientific studies. Disciplines long estranged from health issues—planners and architects, environmentalists, even builders and developers—are becoming engaged. It's a good time to spread ownership of health and environment challenges. The challenges of the 21st century will require leadership and collaboration. It worked in the 19th century; it can work today.

Richard J. Jackson

10.1126/science.1141968

CREDIT: HARRISON SHAL / GETTY

Fastest High Throughput & Large Scale Sample Prep System

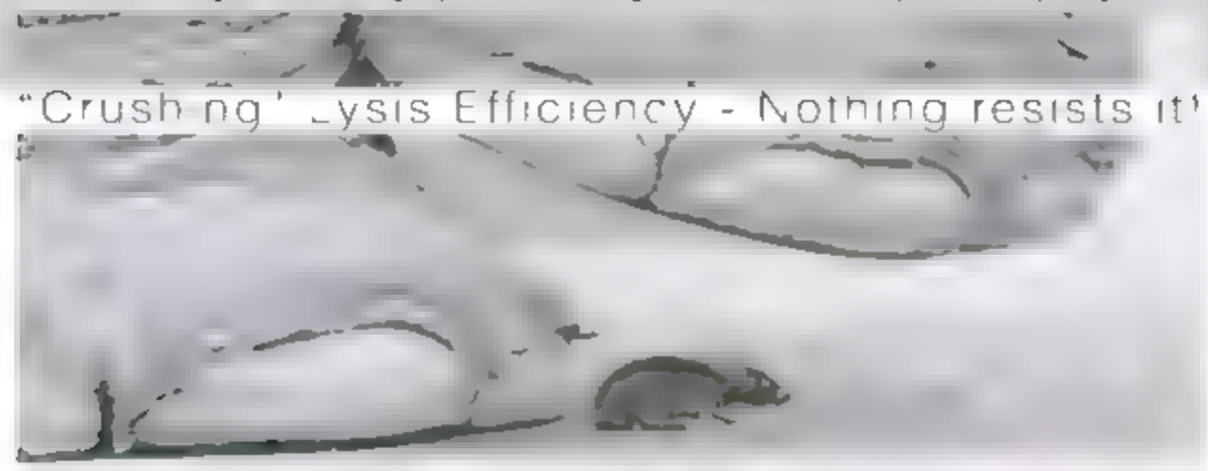

Lyse Any Tough Tissue or Cells in 40 Seconds or Less!

- *24 x 2 ml samples homogenized simultaneously*
- *2 x 50 ml large volume lysis**
- *Lyse efficiently tough tissues and cells with ease:*
  plants, seeds, gram+ bacteria, spores, bones, animal tissues, swabs, soil, feces, forensic samples, skin and tumors, etc.
- *Optimized lysing matrix and complete extraction and purification kits for all your needs*
- *Preserves integrity of DNA, RNA and proteins*
- *Removable sample holder*
- *Easy to clean/decontaminate*
- *Highly reproducible and easy to use*

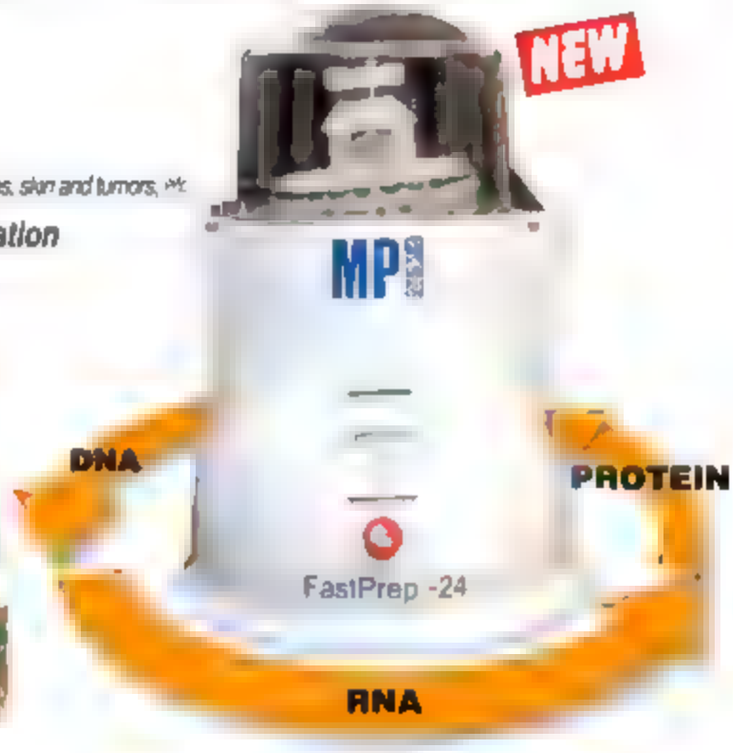

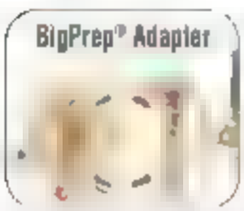

*Optional equipment, requires separate purchase Cat.No. 6002525

The newest generation of the proven Bio101® FastPrep® System, 5,000+ users worldwide

Order Today and SAVE!

Order the FastPrep®- 24 (Cat No 6002500) by April 30th and receive a FREE FastPrep® kit of your choice! Use promo code FPSCI2007

Free trial available for qualified customers! Use promo code FPSCI2007

www.mpbio.com

MP Biomedicals North America, Tel: 1.800 854.0530 • MP Biomedicals Europe, Tel: 00800 7777 9999

MP

BIO 101® Systems
Division of MP Biomedicals

EDITED BY STELLA HURTLEY AND JAKE YESTON

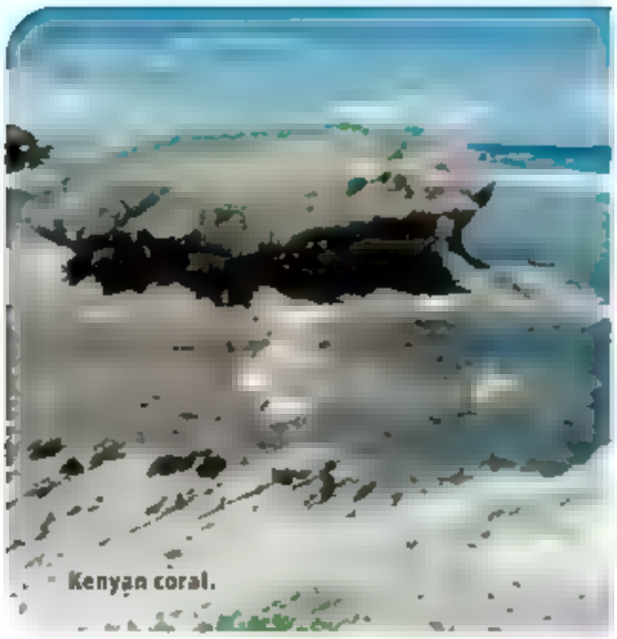

Kenyan coral.

GEOLOGY

Washing Soils Away

Soil erosion and land degradation are serious threats to developing countries. Not only do they diminish food security and threaten terrestrial ecosystems but they also cause substantial damage to near-shore marine environments. As the causes and extent of soil erosion are explored with an aim toward combating the problem, historical records are needed to place modern rates in perspective. Fleitmann *et al.* document how erosion has affected East Africa, a region particularly vulnerable to the loss of fertile soil, by analyzing a 300-year-long record of Ba/Ca ratios in corals found off the coast of Kenya. These ratios serve as a good proxy for soil erosion because most of the Ba flux to the seawater stems from river discharge at the location where the samples were acquired. Shortly after the year 1900, Ba/Ca ratios began to increase steadily beyond their comparatively low values in the preceding 200 years, the initial increase could be due to British settlement of the fertile highlands of Kenya around that time. If effective soil conservation policies are not instituted, the situation will probably worsen in the future because of the country's growing population, leading to more intensive land use, as well as the increased rains expected with global warming. — HJS

Geophys. Res. Lett. **34**, L04401 (2007)

ENVIRONMENTAL MICROBIOLOGY

Colorful Coexistence

The diversity of plankton in lakes is surprisingly high, and even an apparently uniform looking body of lake water can offer many ecological niches, depending on the scale of the ebb and flow of water masses, nutrients, temperature gradients, and so on. Hunsman *et al.* have now shown that changing degrees of light penetration also provide niches. In a study ranging from the open ocean to landlocked ponds, the authors found that red picoplankton (absorbing green light) dominate in clear blue waters and green types (absorbing red light) dominate in peaty brown turbid lakes. A model for competition between red- and green-light–absorbing picocyanobacteria in different light fields correctly mirrored nature. Along a gradient of increasing turbidity, red picoplankton are replaced by green, and where turbidity is intermediate, both types of picoplankton can coexist. Moreover, changes in the population density of the plankton itself will affect light absorbance and result in competitive exclusion of the reds by the greens. — CA

Ecol. Lett., in press

IMMUNOLOGY

Tumor-Tunneling T Cells

T cell responses begin inside the lymph nodes and spleen, and considerable headway has been made in monitoring how these immune cells behave at these sites through live intravital imaging techniques. A natural extension of this is to visualize how activated T cells conduct themselves once they've migrated to inflamed tissues or tumors.

Boissonnas *et al.* have combined immunofluorescence with intravital microscopy to follow cytotoxic T lymphocytes (CTLs) as they destroy tumors in vivo. Tumor cells were inoculated into mice at two separate sites, but with those at only one site engineered to express antigen to which T cells could respond. Although the solid tumors that formed at both sites became infiltrated with T cells, this pre-

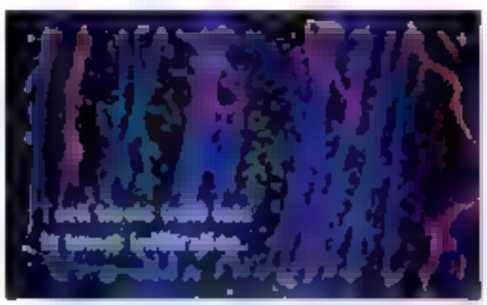

dominated in the antigen-expressing tumors. The behavior of the infiltrating T cells was also measurably different, with those in the antigen-bearing tumor displaying strong signs of activation and distinct migration patterns. In particular, the tumor-reactive CTLs initially displayed diminished motility, which they regained as tumor cells were killed off. These CTLs also burrowed more vigorously into the tumors that expressed antigen. It will now be interesting to determine if similar behavior occurs in other tumor settings (for example, where less potent antigens are expressed) or in nonmalignant tissues where CTLs also mediate cellular destruction (for example, in autoimmune diseases). — SJS

J. Exp. Med. **204**, 345 (2007)

ASTROCHEMISTRY

The Sun Reflected in Osbornite

Knowing the chemical composition of the solar nebula is critical for understanding how the Sun and planets condensed from a cloud of gas, and for making benchmark comparisons as solar system materials are reprocessed in the solar wind and planetary atmospheres. However, although the Sun contains 99.8% of the mass in the solar system, its composition remains unclear.

Meibom *et al.* argue that analysis of a rare mineral in a meteorite has allowed accurate inference of solar nebula nitrogen and carbon isotope ratios. A speck of osbornite (TiN) bearing some trapped TiC was spotted in a calcium-aluminum–rich inclusion within the carbonaceous chondrite meteorite Isheyevo, which has been little altered since its formation. The osbornite is produced at very high temperatures (~2000 K) so must have formed by gas-to-solid condensation in the solar nebula without changes in the

Continued on page 1341

CREDITS (TOP TO BOTTOM): CHINCH NEWCOMBE/SCIENCE; SOMMAS ET AL. J. EXP. MED. 204 (2007)

Solved!

INNOVATION ● WORK

Innovative Solutions for Ion Channel Research

Puzzled over who will meet your ion channel research needs? Look no further. We have the most extensive line of innovative products for ion channel research.

- Subunit selective antibodies
- Toxins
- Inhibitors and activators
- RNAi libraries
- PCR/Amplification Reagents, Quantitative PCR, Real-time PCR
- Cloning Systems, kTransfection Reagents, Competent Cells, Expression Vectors
- Cell Culture Media, Supplements, Growth Factors

Sigma is the Solution.

Visit sigma.com/ionchannelsolutions for more information.

Sigma also offers these convenient online tools for your research:

Antibody Explorer
sigma.com/antibody

Sigma-RBI Handbook of Receptor Classification and Signal Transduction
sigma.com/rbihandbook

Pathfinder Interactive Pathways
sigma.com/pathfinder

sigma.com

Accelerating Customers' Success through Leadership in Life Science, High Technology and Service

SIGMA-ALDRICH CORPORATION • BOX 14508 • ST. LOUIS • MISSOURI 63178 • USA

SIGMA

Continued from page 1339

isotopic composition. As supporting evidence, the measured $^{13}C/^{12}C$ ratio of 0.01125 ± 0.00008 (1σ) is consistent with the isotope ratio of carbon in the solar photosphere, and the $^{15}N/^{14}N$ ratio of (2.356 ± 0.018) × 10^{-3} matches the nitrogen composition in Jupiter's atmosphere and in the interstellar medium. — JB

Astrophys. J. **656**, L33 (2007)

ECOLOGY/EVOLUTION

Sowing Seed Far and Near

Although a great deal is known about the qualitative aspects of seed dispersal by animals (for example, which species feed on particular plants and disperse their seeds), the quantitative study of seed dispersal is still in its infancy. For example, the relative roles of different animal species in dispersing seeds over different distances are unclear. Genotyping techniques coupled with detailed field observations, are beginning to yield results. Jordano *et al.* assessed the relative contributions of large birds, small birds, and fruit-eating mammals to the dispersal of seeds of *Prunus mahaleb*, a common fleshy-fruited tree in southern Spain, by genotyping seeds in fecal pellets and match

***Prunus mahaleb* in fruit.**

ing them to genotypes of parent trees. Although dispersal distance correlated fairly well with increasing size of animal, only a small subset of larger species made significant contributions to longer-distance dispersal over several hundred meters. Loss of these critical species or fragmentation of habitat could thus have disproportionate effects on plant dispersal and gene flow. — AMS

Proc. Natl. Acad. Sci. U.S.A. **104**, 3278 (2007)

CHEMISTRY

A Universal Suitcase

In biochemical environments, amphiphilic molecules form bilayer vesicles that can stabilize polar molecules in their interiors while encapsulating nonpolar guests inside the hydrophobic walls. Radowski *et al.* sought to mimic this universal carrier ability in a synthetic molecular assembly by fabricating a spherical multishelled structure from three inexpensive commercially available building blocks. For the core, they used hyperbranched poly(ethylene imine) (PEI), which was appended to alkyl diacid segments that in turn were capped by monomethyl poly(ethylene glycol). The chain lengths of all three components were varied to optimize transport properties for guests of widely ranging polarity in water, ethanol, chloroform, and toluene. Uptake of the guest molecules (which included an array of drugs, vitamins, and dyes) was substantially enhanced by using a large PEI core and long (C_{18}) alkyl diacid. Dynamic light scattering measurements revealed that the macromolecules form aggregates that enhance their transport capabilities. The aggregates, which expanded with linear guests but contracted with globular ones, were highly robust, proving stable to filtration and chromatography and persisting in solution for more than a year. — MSL

Angew. Chem. Int. Ed. **46**, 1265 (2007)

MOLECULAR BIOLOGY

Dicing Triplets

Dicer, the endoribonuclease enzyme at the heart of RNA interference (RNAi), cleaves double-stranded RNA (dsRNA) and RNA hairpins to form small interfering RNAs (siRNAs) and microRNAs (miRNAs). The imperfect base-pairing of miRNA precursors requires that Dicer be fairly tolerant of mismatches in its substrates, and this in turn means that any RNA sequence that forms a passably presentable double helix can become a Dicer substrate.

Genes of the class of triplet repeat expansion diseases, including Huntington's disease, contain stretches of CNG (trinucleotide repeats that are dramatically expanded in afflicted individuals. Both the normal and expanded repeats are able to form hairpins in the messenger RNA (mRNA) in vitro. Are these repeats also substrates for Dicer? Krol *et al.* show that in vitro, Dicer can specifically cleave longer CNG hairpins both in isolation and in the local sequence context of mutant mRNAs. Furthermore, comparing mRNAs with normal and expanded repeats in cells from patients, Dicer selectively reduces the levels of mutant transcripts bearing the expanded numbers of repeats, generating siRNAs ("siCNGs") that can trigger further rounds of cleavage. The same effect can be achieved by the introduction of exogenous siCNGs, suggesting possible therapeutic interventions based on RNAi-driven selective knockdown of the mutant mRNAs. — GR

Mol. Cell **25**, 575 (2007)

CREDIT: DAN JORDANO/CSIC

www.sciencemag.org

Science

1200 New York Avenue, NW
Washington, DC 20005
Editorial: 202-326-6550, FAX 202-289-7562
News: 202-326-6500, FAX 202-371-9227

Bateman House, 82-88 Hills Road
Cambridge, UK CB2 1LQ
+44 (0) 1223 326500, FAX +44 (0) 1223 326501

Subscription Services For change of address, missing issues, new orders and renewals, and payment questions: 866-434-AAAS (2227) or 202-326-6417, FAX 202-842-1065. Mailing addresses: AAAS, P.O. Box 96178, Washington, DC 20090-6178 or AAAS Member Services, 1200 New York Avenue, NW, Washington, DC 20005

Institutional Site Licenses please call 202-326-6755 for any questions or information

Reprints: Author Inquiries 800-635-7181
Commercial Inquiries 803-359-4578
Corrections 202-326-6501

Permissions 202-326-7074, FAX 202-682-0816

Member Benefits Bookstore: AAAS/BarnesandNoble.com bookstore www.aaas.org/bn; Car purchase discount: Subaru VIP Program 202-326-6417; Credit Card: MBNA 800-847-7378; Car Rentals: Hertz 800-654-2200 CDP#343457, Dollar 800-800-4000 #AA1115; AAAS Travels: Betchart Expeditions 800-252-4910; Life Insurance: Seabury & Smith 800-424-9883; Other Benefits: AAAS Member Services 202-326-6417 or www.aaasmember.org.

science_editors@aaas.org (for general editorial queries)
science_letters@aaas.org (for queries about letters)
science_reviews@aaas.org (for returning manuscript reviews)
science_bookrevs@aaas.org (for book review queries)

Published by the American Association for the Advancement of Science (AAAS), *Science* serves its readers as a forum for the presentation and discussion of important issues related to the advancement of science, including the presentation of minority or conflicting points of view, rather than by publishing only material on which a consensus has been reached. Accordingly, all articles published in *Science*—including editorials, news and comment, and book reviews—are signed and reflect the individual views of the authors and not official points of view adopted by the AAAS or the institutions with which the authors are affiliated.

AAAS was founded in 1848 and incorporated in 1874. Its mission is to advance science and innovation throughout the world for the benefit of all people. The goals of the association are to: [illegible] communication among scientists, engineers, and the public; [illegible] international cooperation in science and its applications; [illegible] the responsible conduct and use of science and technology; foster education in science and technology for everyone; enhance the science and technology workforce and infrastructure; increase public understanding and appreciation of science and technology; and strengthen support for the science and technology enterprise.

Information for Authors

See pages 120 and 121 of the 5 January 2007 issue or access www.sciencemag.org/feature/contribinfo/home.shtml

[illegible] **Donald Kennedy**
[illegible] **Monica M. Bradford**
[illegible]
R. Brooks Hanson, Barbara R. Jasny, Katrina L. Kelner **Colin Norman**

Editorial [illegible] Phillip D. Szuromi [illegible] Valda [illegible]; [illegible] Pamela J. Hines, Paula A. Kiberstis [illegible] Stella M. Hurtley [illegible] Beverly A. Purnell [illegible] Bryan Ray, Guy Riddihough [illegible] David Voss; [illegible] Sherman J. Suter; [illegible] Etta Kavanagh; [illegible] Barbara P. Ordway [illegible] Trista Wagoner [illegible] Beverly Shields [illegible] Brian White [illegible] Sylvia S. Kihara [illegible]

News [illegible] Robert [illegible] Eliot Marshall, Jeffrey Mervis, Leslie Roberts; [illegible] Elizabeth Culotta, Polly Shulman; [illegible] Yudhijit Bhattacharjee, Adrian Cho [illegible] David Grimm [illegible] Erik Stokstad; John Simpson (intern); **contributing correspondents** Barry A. Cipra, Jon Cohen (San Diego, CA), Daniel Ferber, Ann Gibbons, Robert Irion, Mitch Leslie, Charles C. Mann, Evelyn Strauss, Gary Taubes, Ingrid Wickelgren; **copy editors** Linda B. Felaco, Rachel Curran, Sean Richardson; **administrative support** Scherraine Mack, Fannie Groom; **bureaus** Berkeley, CA: 510-652-0302, FAX 510-652-1867, New England: 207-549-7755, San Diego, CA: 760-942-3252, FAX 760-942-4979, Pacific Northwest: [illegible] 1940

Production director James Landry; **senior manager** Wendy K. Shank; **assistant manager** Rebecca Doshi; **senior specialists** Jay Covert, Chris Redwood; **specialist** Steve Forrester; **Preflight director** David M. Tompkins; **manager** Marcus Spiegler; **specialist** Jessie Mudjitaba

Art director Kelly Buckheit Krause; **associate art director** Aaron Morales; **illustrators** Chris Bickel, Katharine Sutliff; **senior art associates** Holly Bishop, Laura Creveling, Preston Huey; **associates** Nayomi Kevitiyagala, Jessica Newfeld; **photo editor** Leslie Blizard

Science International

Europe [illegible] **editorial** [illegible] Andrew M. Sugden [illegible] Julia Fahrenkamp-Uppenbrink; **senior editors** Caroline Ash (Geneva: +41 (0) 222 346 3106), Stella M. Hurtley, Ian S. Osborne, Stephen J. Simpson, Peter Stern; **associate editor** Joanne Baker; **editorial support** Alice Whaley; Deborah Dennison; **administrative support** Janet Clements, Jill White; **news:** [illegible] John Travis; [illegible] Daniel Clery; **correspondent** Gretchen Vogel (Berlin: +49 (0) 30 2809 3902, FAX +49 (0) 30 2809 8365); **contributing correspondents** Michael Balter (Paris), Martin Enserink (Amsterdam and Paris), John Bohannon [illegible]; **intern** Krista Zala

Asia Japan Office: Asca Corporation, Eiko Ishioka, Fusako Tamura, 1-8-13, Hirano-cho, Chuo-ku, Osaka-shi, Osaka, 541-0046 Japan; +81 (0) 6 6202 6272, FAX +81 (0) 6 6202 6271; asca@os.gulf.or.jp; **asia news editor** Richard Stone +66 2 662 5818 (rstone@aaas.org); **japan news bureau** Dennis Normile [illegible] +81 [illegible] 3 91 0410, FAX 81 (0) 3 5936 3531; dnormile@gol.com; **china rep-resentative** Hao Xin, + 86 (0) 10 6307 4439 or 6307 3676, FAX +86 (0) 10 6307 4358; cindyhao@gmail.com; **south asia** Pallava Bagla (contributing correspondent +91 (0) 11 2271 2896; pbagla@vsnl.com)

Africa Robert Koenig (contributing correspondent, rob.koenig@gmail.com)

EXECUTIVE PUBLISHER **Alan I. Leshner**
PUBLISHER **Beth Rosner**

Fulfillment & Membership Services (membership@aaas.org) **director** Marlene Zendell; **manager** Waylon Butler; **systems specialist** Andrew Vargo; **customer service supervisor** Pat Butler; **specialists** Laurie Baker, Tamara Alfson, Karena Smith, Vicki Linton, Latoya Casteel; **circulation associate** Christopher Refice; **data entry supervisor** Cynthia Johnson; **specialists** Tomeka Diggs, Tarrika Hill, Erin Layne

Business Operations and Administration director Deborah Rivera-Wienhold; **business manager** Randy Yi; **senior business analyst** Lisa Donovan; **business analyst** Jessica Tierney; **financial analysts** Michael LoBue, Farida Yeasmin; **rights and permissions: administrator** Emilie David; **associate** Elizabeth Sandler; **marketing: director** John Meyers; **marketing managers** Darryl Walter, Allison Pritchard; **marketing associates** Julianne Wielga, Mary Ellen Crowley, Catherine Featherston, [illegible] **international marketing manager** Wendy Sturley; **marketing/member services executive** Linda Rusk; **japan sales** Jason Hannaford; **site license sales director** Tom Ryan; **sales and customer service** Mehan Dossani, Kiki Forsythe, Catherine Holland, Wendy Wise; **electronic media: manager** Lizabeth Harman; **project manager** Trista Snyder; **assistant manager** Lisa Stanford; **production associates** Nichele Johnston, Kimberly Oster

Advertising director worldwide ad sales Bill Moran

Product (science_advertising@aaas.org); **midwest** Rick Bongiovanni: 330-405-7080, FAX 330-405-7081 • **west coast/w. canada** Teola Young: 650-964-2266 **east coast/e. canada** Christopher Breslin: 443-512-0330, FAX 443-512-0331 • **uk/europe/asia** Julie Skeet: +44 (0) 1223-326-524, FAX +44 (0) 1223-325-532 **japan** Mashy Yoshikawa: +81 (0) 33235 5961, FAX +81 (0) 33235 5852 **traffic manager** Carol Maddox; **sales coordinator** Dejandra Simms

Commercial Editor Sean Sanders: 202-326-6430

Classified (advertise@sciencecareers.org); **u.s.: recruitment sales manager** Ian King: 202-326-6528, FAX 202-289-6742; **u.s./industry:** Darrell Bryant: 202-326-6533; **midwest/canada:** Daryl Anderson: 202-326-6543; **northeast:** Allison Millar: 202-326-6572; **southeast:** Fernando Junco: 202-326-6740; **west:** Katie Putney: 202-326-6577; **sales coordinators** Erika Bryant, Rohan Edmonson, Shirley Young; **international: sales manager** Tracy Holmes: +44 (0) 1223 326525, FAX +44 (0) 1223 326532; **sales** Christina Harrison, Svitlana Barnes; **sales assistant** Louise Moore; **japan:** Jason Hannaford: +81 (0) 52 757 5360, FAX +81 (0) 52 757 5361; **advertising production operations manager** Deborah Tompkins; **associates** Christine Hall, Amy Hardcastle; **publications assistants** Robert Buck, Mary Lagnaoui

AAAS Board of Directors retiring president, chair John P. Holdren; **president** David Baltimore; **president-elect** James J. McCarthy; **treasurer** David E. Shaw; **chief executive officer** Alan I. Leshner; **board** John E. Dowling, Lynn W. Enquist, Susan M. Fitzpatrick, Alice Gast, Linda P. B. Katehi, Cherry A. Murray, Thomas D. Pollard, Kathryn D. Sullivan

AAAS
ADVANCING SCIENCE, SERVING SOCIETY

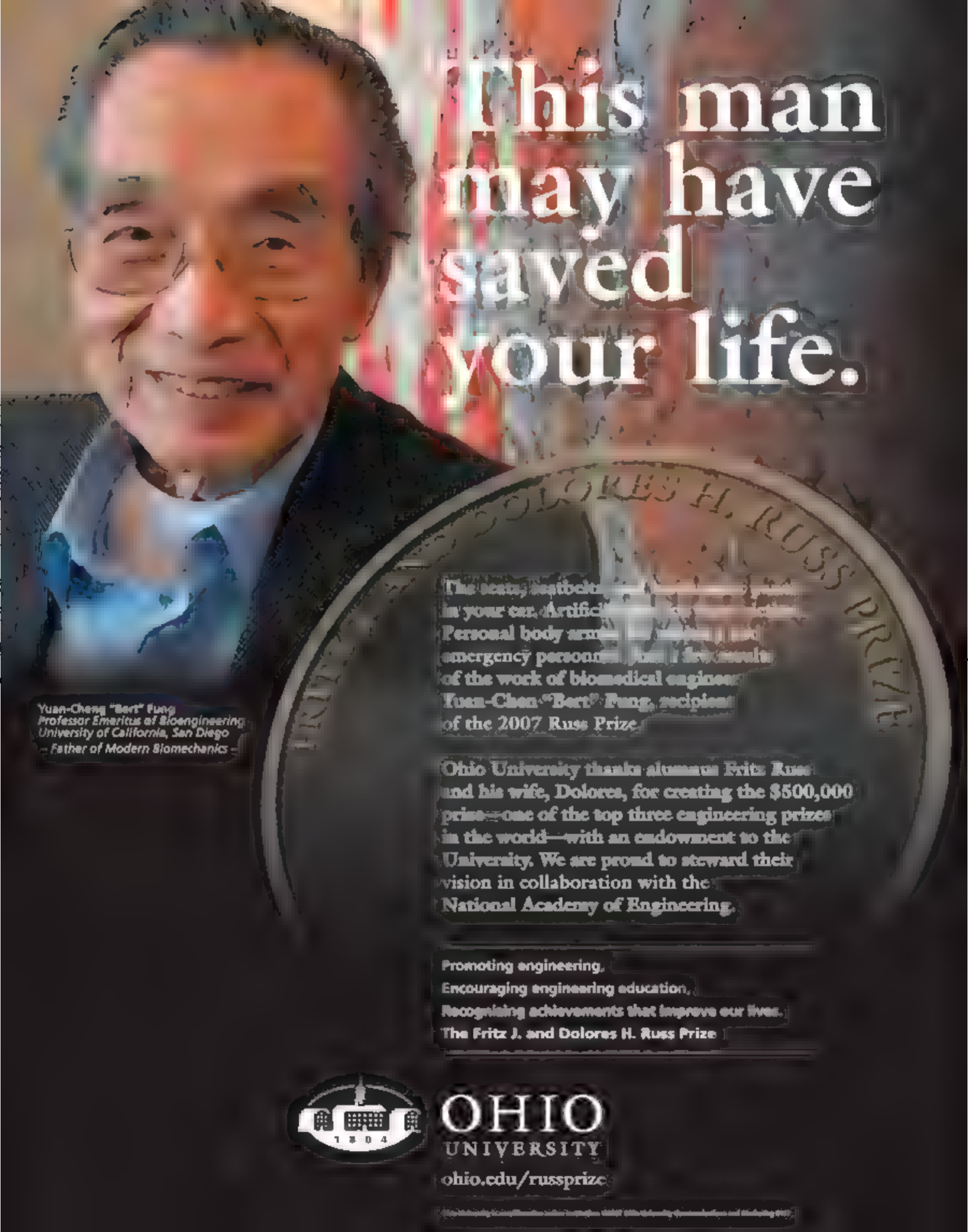
This man may have saved your life.
Yuan-Cheng "Bert" Fung
Professor Emeritus of Bioengineering
University of California, San Diego
– Father of Modern Biomechanics –
Ohio University thanks alumnus Fritz Russ and his wife, Dolores, for creating the $500,000 prize—one of the top three engineering prizes in the world—with an endowment to the University. We are proud to steward their vision in collaboration with the National Academy of Engineering.
Promoting engineering.
Encouraging engineering education.
Recognizing achievements that improve our lives.
The Fritz J. and Dolores H. Russ Prize
1804
OHIO
UNIVERSITY
ohio.edu/russprize

A 21st Century *Beagle*

To celebrate the 200th anniversary of Charles Darwin's birth, a pair of Brits have gotten together to build a working replica of HMS *Beagle*, the ship that bore Darwin around the world.

The HMS *Beagle* Project Wales, founded by David Lort Phillips, a Welsh farmer and British environmental writer Peter McGrath, intends the ship as a sailing classroom and laboratory. Identical to the original on the outside, the $6.4 million, privately funded ship will be furnished with 21st century navigation, safety, and communications equipment.

For its first voyage, the replica, crewed by 30 scientists and sailors, will sail around the world following the path of the original *Beagle* in the 1831–36 voyage that inspired Darwin's *On the Origin of Species*. After that, scientists will be able to use the new *Beagle* for research, primarily on climate change, says McGrath. One project he is considering is using the *Beagle*'s logs to compare the climate of the 1830s with that of today. Broadcasts of experiments as well as lectures will be available to labs and classrooms around the world via an as yet unbuilt Web site.

The project is intended to put some "awe back into science" and attract more young people to the field, says McGrath: "We need to use props like the *Beagle* to get their pulses to quicken." Construction is to begin early next year in Milford Haven, Wales.

Bird Flu Futures

Will North America have its first confirmed case of avian influenza before July? Health agencies can't answer such questions. But they may gain a much better sense of the bird flu menace thanks to a project at the University of Iowa that lets experts place bets on how the disease will spread.

With a $250,000 grant from the Robert Wood Johnson Foundation, the university will stake experts to Avian$1000 (U.S. $100) to play the futures game in a 2-year experiment starting this month. Players will buy "yes" or "no" shares in 11 different predictions, such as when and where the flu will spread and whether the World Health Organization will raise its pandemic warning level before 1 July. The price per share ranges up to Avian$1 depending on the market. Winning bettors collect Avian$1 for every share bought. The game is limited to experts who are members of ProMED, the disease-monitoring network of the International Society for Infectious Diseases.

"From our perspective, it's very innovative and exciting," says ProMED Editor Lawrence C. Madoff of Harvard Medical School in Boston, who hopes to enroll about 100 players (see flupredict.uiowa.edu). University of Iowa physician Philip Polgreen says the Iowa Electronic Markets, which began in 1988 by predicting the outcomes of presidential elections, started selling flu futures for the state of Iowa 2 years ago. Polgreen says despite the tiny profits—winners can gain only about $100—the project decided to deal in dollars because "there's a sense that people take less extreme positions" if real money is involved.

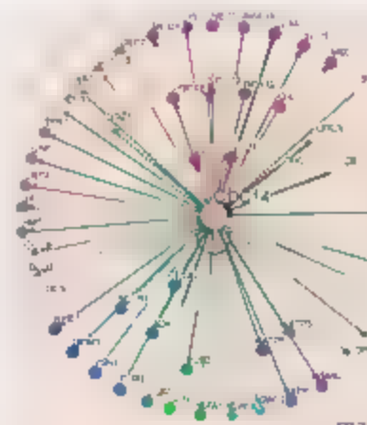

<< When Molecules Meet

NET WATCH

Webs of interconnected proteins and genes keep cells running. To explore these networks, visit BioGRID from molecular biologist Michael Tyers of the Samuel Lunenfeld Research Institute in Toronto, Canada, and colleagues.

Stowed here are all known genetic and protein interactions in budding yeast, along with partial lists for humans, nematodes, and fruit flies—more than 167,000 associations in all. Curators glean data from the literature and update the collection monthly. Each entry maps the liaisons of a particular protein or gene and summarizes the experimental evidence for each association. Above, the interaction network for the enzyme Cdc14, which controls the exit from mitosis. >> www.thebiogrid.org

MODELING VESUVIUS

Scientists keep a close eye on Vesuvius, one of the world's most dangerous volcanoes, which looms over the Bay of Naples. When it erupted in 79 C.E., it caused thousands of deaths. A similar eruption today would be far worse. More than a half-million people now live in the "Red Zone," a designated evacuation area around the volcano. Researchers headed by Augusto Neri at the National Institute of Geophysics and Volcanology in Pisa, Italy, have now completed what they say are the most detailed 3D simulations yet of just how things might unfold. Above is an image from a medium-scale eruption scenario involving "partial collapse" of the volcanic column. The two gray clouds represent pyroclastic density currents—avalanches of hot gases, ash, and rock—700 seconds after the onset of the collapse. The simulations are described in the 27 February *Geophysical Research Letters*.

You could be next

Yes, it *can* happen to you:
If you're a young scientist making inroads in neurobiology research, the next Eppendorf and *Science* Prize for Neurobiology could be yours!

This annual research prize recognizes accomplishments in neurobiology research based on methods of molecular and cell biology. The winner and finalists are selected by a committee of independent scientists, chaired by the Editor-in-Chief of *Science*. Past winners include post-doctoral scholars and assistant professors.

To be eligible, you must be 35 years of age or younger. If you're selected as this year's winner, you will receive $25,000, have your work published in the prestigious journal *Science* and be invited to visit Eppendorf in Hamburg, Germany.

Get recognized!
Deadline for entries:
June 15, 2007

www.eppendorf.com/prize
www.eppendorfscienceprize.org

$25,000 Prize

eppendorf
& Science
PRIZE FOR
NEUROBIOLOGY

Movers

PERU RISING. Ivan Ghezzi of Lima's Pontificia Universidad Catolica del Peru (PUCP) has become the archaeology director for the Instituto Nacional de Cultura—in effect, the nation's head archaeologist and overseer of one of the world's most important archaeological patrimonies. The Yale-trained researcher, who will keep his PUCP post, succeeds Yuri Castro.

Ghezzi belongs to a growing cadre of Latin American archaeologists who are gaining international prominence. Although Peruvians have made essential contributions to Andean studies since the days of Julio C. Tello (1880–1947), the field has typically been dominated by better-funded, better-equipped, and better-trained scientists from North America and Europe. Now, says archaeologist Luis Castillo of PUCP, "there's a new generation of researchers who can work as leaders or equal partners with people from France, Spain, and the U.S." The increase in local expertise, he says, is leading to "more and better work." One example: Ghezzi's study of a 3500-year-old observatory in northern coastal Peru that appeared in *Science* last week (2 March, p. 1206).

MONEY MATTERS

PUBLIC HEALTH INC. The founder of the world's largest pharmaceutical data services company and his wife have pledged $50 million to the institution at which he began his academic career. Biostatistician Dennis Gillings, who once served on the faculty of the School of Public Health at the University of North Carolina, Chapel Hill, and now heads Quintiles Transnational, wants the school to stimulate innovation on key local and global health challenges. In recognition of the gift, the school has been renamed the Dennis and Joan Gillings School of Global Public Health.

The school's dean, Barbara Rimer, says the funds will be used to start an endowment that will support "innovation laboratories" to work on issues such as access to drinking water and efficiency of clinical trials. "There must be a faster and maybe safer way [to conduct trials], particularly where our computing power can come in," Gillings says. The school hopes to foster the use of "business practices so that the discoveries [made by the labs] can be disseminated," Rimer adds. "There are too many good discoveries in public health that sit on shelves."

INSIDE GOVERNMENT

FUSION HEAD. Raymond Fonck is the new head of the Office of Fusion Energy Science at the U.S. Department of Energy (DOE). Fonck, who earlier this year became chief scientist of the U.S. project office for the International Thermonuclear Experimental Reactor, will be responsible for overseeing DOE's participation in the $12 billion effort. He comes to the post—vacant since former head Anne Davies retired in April 2006—from the physics faculty of the University of Wisconsin, Madison.

They Said It...

"I also want to show that people need not be limited by physical handicaps as long as they are not disabled in spirit."

—Physicist Stephen Hawking, who has Lou Gehrig's disease, on why he wants to take a zero-gravity flight this April. He says his primary reason is to encourage public interest in space flight.

SOURCE: *The New York Times*

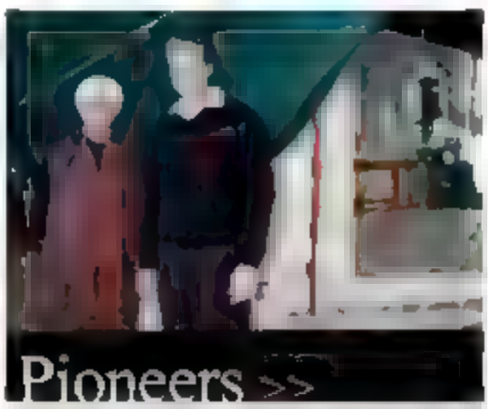

Pioneers >>

PACK 'N PLAY. While studying to diagnose disease in chimpanzees, Taranjit Kaur (above, left), a pathobiologist at Virginia Polytechnic Institute and State University in Blacksburg, wondered whether there was a way to reduce the environmental impact of her research. With the help of architect colleague Matt Lutz (above, right), she's come up with an answer: the world's first fully collapsible, mobile laboratory.

The two-story facility can hold laboratory equipment on the bottom floor, including computers, microscopes, and a refrigerator, and four researchers on the second floor. It's made of fiberglass rods and sliding aluminum panels that lock into place. The lab will be deployed this summer in Tanzania, where Kaur's group is establishing a health-monitoring program for chimpanzees.

Got a tip for this page? E-mail people@aaas.org

CREDITS: (TOP TO BOTTOM) I. GHEZZI; T. KAUR; TOM FULDNER

Hurricane Hunter? 1351

Salamander Kinetics 1352

NUCLEAR WEAPONS

Livermore Lab Dips Into the Past To Win Weapons Design Contest

What's the trick in winning a competition to design a nuclear bomb when you can't show it works by blowing it up? Imitate an already tested weapon just enough to prove your design will do the job.

That's the approach followed by weapons physicists at Lawrence Livermore National Laboratory in California in a Department of Energy (DOE) contest to design a new H-bomb. The challenge, which pitted Livermore against archrival Los Alamos National Laboratory in New Mexico, was to design a weapon that wouldn't require nuclear testing, a practice the U.S. effectively forswore in 1992. And DOE officials say the soundness of Livermore's design was superior to a more novel proposal from Los Alamos. "This was about starting off with the most conservative approach," says National Nuclear Security Agency (NNSA) interim head Thomas D'Agostino, who announced the outcome last week.

The Reliable Replacement Warhead (RRW) program was set up by Congress to modernize the aging U.S. stockpile. The two labs were competing to replace a warhead that currently sits atop missiles in U.S. submarines. Some of the bombs are more than 30 years old, and scientists can't detonate them to see how well they've held up. Although the focus is reliability, RRW is also intended to create safer, more secure, and greener weapons. But critics say the program, which could cost more than $725 million by 2012, is misdirected and counterproductive. "This could serve to encourage the very proliferation we are trying to prevent," says Senator Dianne Feinstein (D–CA).

To look to the future, both teams started with the past. Bolstered with engineering crews supplied by Sandia National Laboratories in Albuquerque, New Mexico, they began by scouring the archives of the roughly 1000 underground nuclear tests that the United States has performed. But they learned different lessons from the data. Livermore physicist and RRW leader Hank O'Brien says that a weapon design tested four times in the 1980s but deemed to be too "oversized and heavy" for use during the Cold War turned out to be a good basis for the new bomb. In contrast, Los Alamos official Glen Mara acknowledges that his team's design was not in the "unique sweet spots of previous [specific] designs that were in the stockpile," although many nuclear tests and models informed its design.

With basic design in hand, the California team went on to perform some 28,000 simulated explosions of the device on the lab's 100-teraflops supercomputer. Those runs suggested how certain manufacturing defects or design changes would affect its performance when subjected to radiation, shaking, and high temperatures. In early 2006, the teams exchanged what one official described as "phone-book-sized" dossiers of classified data on their weapon for mutual peer review, which also yielded some improvements. (Some of Los Alamos's RRW features might be integrated into the California design.) But for the Livermore team, says O'Brien, a key moment came last August, when a mockup of the weapon showed "an excellent agreement with our [computer] model" during a monitored detonation using conventional explosives at Livermore's Site 300 facility. That was both "very satisfying" to the team and extremely useful in proving the design's "credibility," says Livermore manager Bruce Goodwin.

Bank on it. Purple, the world's fourth most powerful supercomputer, helped Lawrence Livermore win a bomb-design competition.

Both winning and losing designs featured controls to thwart detonation by thieves and explosives that are safer to handle, two key facets NNSA had wanted. They also contained no beryllium, an element used in nukes that poses health problems. The New Mexico team added other bells and whistles, including a feature resistant to static electricity, which can cause accidental detonations. The New Mexico design had "many features that were more transformational [, and] some would argue are better" than their rival, says D'Agostino, a reversal of the lab's reputation as being the more conservative of the two labs. But he says Livermore's experimental "pedigree" of hundreds of tests gave it the edge.

That empirical evidence may not be enough to keep the program moving forward, however. Former Livermore director Bruce Tarter says he doesn't think DOE has yet come up with a specific method to measure whether the design meets the criterion of being certifiable "without requiring nuclear testing" as it advertises. Some lawmakers in Congress are wondering whether RRW is even needed, given recent findings that the plutonium inside the weapons can last longer than expected (*Science*, 8 December 2006, p. 1526). They also worry about its impact on efforts to curb nuclear proliferation. The program has a "make-it-up-as-you-go-along character," says Representative Pete Visclosky (D–IN), chair of a key House funding panel. He's threatened to cut funding for RRW unless he sees a more "coherent" explanation of its purpose.

A panel of nuclear weapons experts convened by the American Association for the Advancement of Science (which publishes *Science*) has called for "independent review teams" to monitor the next stages of the RRW program. Los Alamos has already been given that role as a consolation prize. Livermore's O'Brien says he's "honored" to have won and motivated to take the next steps, which include full-scale engineering studies allowing researchers to see how the design reacts to a "lifetime of shake, rattle, and roll." Says Goodwin, "We've taken the first steps, but it's a long road."

—ELI KINTISCH

CREDIT: IBM

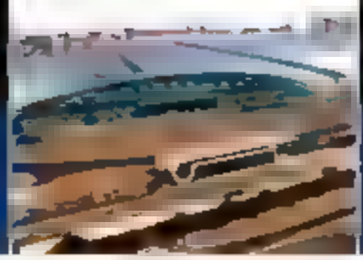

Big Science in China 1354

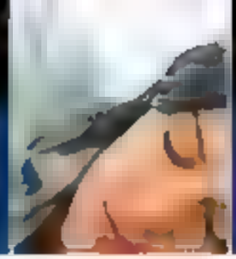

To sleep, perchance to remember 1360

WILDLIFE STUDIES

Researchers Explore Alternatives to Elephant Culling

PRETORIA, SOUTH AFRICA—Outsized tracking collars and dart guns will be in demand as scientists here embark on an ambitious new research program announced last week as part of the government's draft policy to manage South Africa's growing elephant population. The policy's most controversial provision would allow limited culling—which is not being done in any African country—if other approaches fail.

Presenting the policy at Addo Elephant National Park, Environmental Affairs Minister Marthinus van Schalkwyk said a multiyear research plan, suggested by a scientific advisory panel, "will hopefully reduce the scientific uncertainty" about the animals' numbers and movements while managers deal with "immediate challenges" such as minimizing the damage they cause in parks and reserves. In Kruger National Park, for example, the number of elephants has risen from 7800 to about 12,500 since culling was stopped in 1994. Numbers are also reported to be on the rise in Botswana and Zimbabwe.

This contrasts sharply with the trend in west and central Africa, where ivory poaching has decimated some elephant populations. Based on the amounts of ivory seized and DNA source tracking, a research group estimated in the *Proceedings of the National Academy of Sciences* (*PNAS*) last week that 23,000 African elephants were killed for their tusks last year—one

"Overall, the elephant populations might be increasing in perhaps five or six elephant range states" in southern Africa, says the lead author of the *PNAS* study, Samuel K. Wasser, director of the Center for Conservation Biology at the University of Washington, Seattle. But declining populations are a problem in "the other 30-plus range states."

Strict policing has limited ivory poaching at South Africa's game parks, but many ecologists blame poor management, including the drilling of more than 300 artificial watering holes over half a century in Kruger Park, for exacerbating the park's ecological problem by changing elephants' movements and feeding patterns. Zoologist Rudi van Aarde, chair of the University of Pretoria's Conservation Ecology Research Unit, argues that one remedy is to reduce the number of watering holes and remove fences to create transborder "megaparks."

Several such Transfrontier Conservation Areas have been mapped and are being negotiated in southern Africa through the efforts of the independent Peace Parks Foundation. In addition, as part of a long-term megaparks research project, van Aarde's group has outfitted 91 elephants in seven southern African countries with GPS tracking collars. He believes that the new South African research program should focus mostly on "adaptive management"—monitoring the ecological impact of specific actions, such as removing fences or watering holes. And tracking needs to continue for "several years," says Norman Owen-Smith, a large-mammal ecologist who directs the Centre for African Ecology at the University of the Witwatersrand in Johannesburg. "Most elephant movement studies so far have been superficial."

Both van Aarde and Owen-Smith are members of the Elephant Science Round Table, which the environment minister established last year to try to reach a scientific consensus. In December, the 21-member panel, which included Park Service elephant experts, submitted a 13-page plan that calls for the development of predictive models on elephant management, among other goals. The ministry has allocated about $700,000 to start the work and will seek additional funding later.

The environment minister suggests culling as a last resort if other options, including relocation, range manipulation, and contraception, don't work. But neither Owen-Smith nor van Aarde, both of whom generally support the minister's plan, thinks that culling is now warranted in Kruger Park, and both question its long-term effectiveness. "There is no point in culling at Kruger," says van Aarde. "We know now that the 27-year culling program there, which removed nearly 17,000 elephants, did not reduce their impact in the long run."

–ROBERT KOENIG

CREDIT: RUDI VAN AARDE

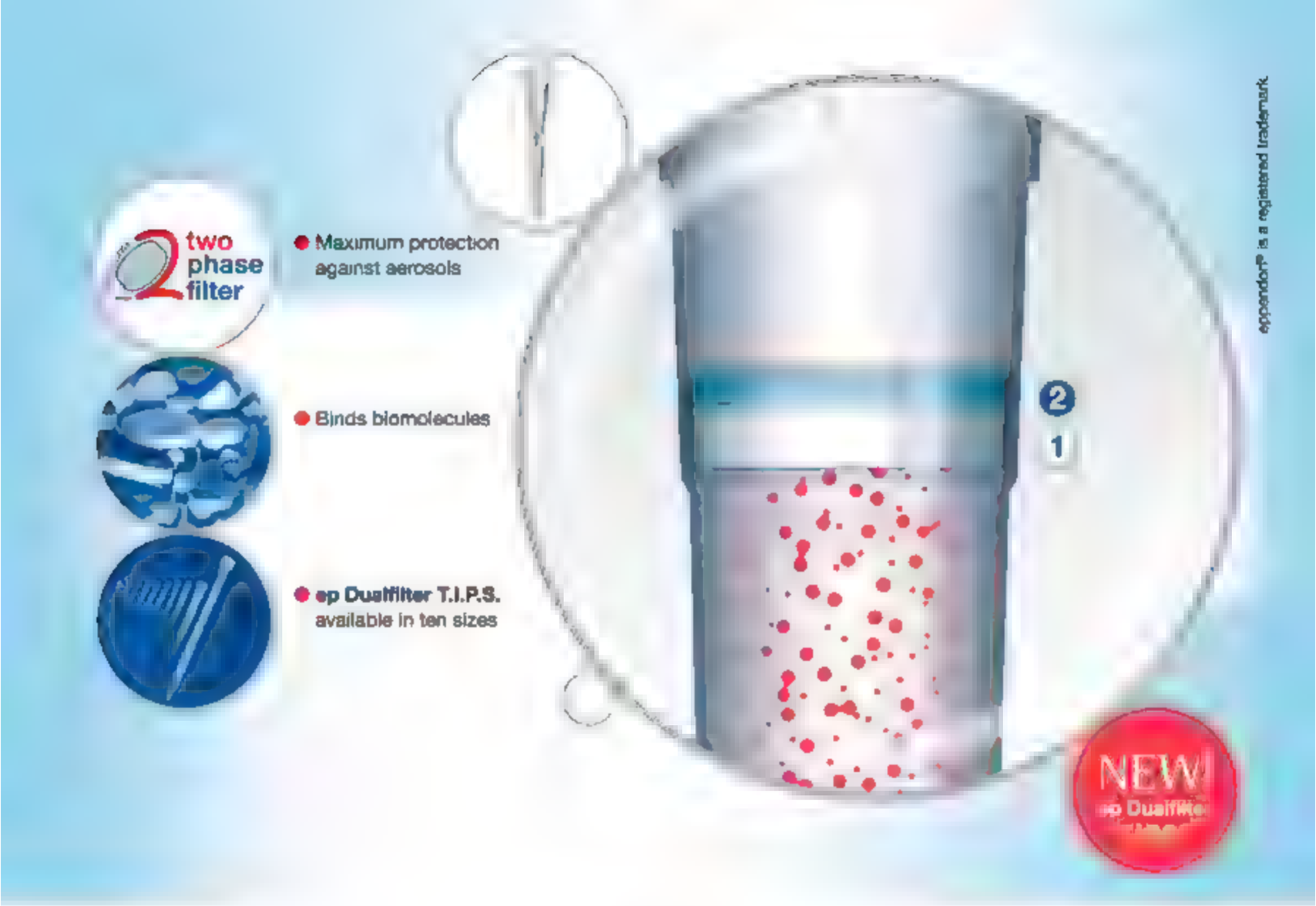

Stop aerosols!

Unique two phase filter protection with ep Dualfilter T.I.P.S.™

The new Eppendorf ep Dualfilter T.I.P.S., with their unique two-phase filter, provide the perfect shield against contamination.

The filter consists of two visible phases, each with a different pore size. This two-phase filter protection ensures ultimate absorption of aerosols ● and biomolecules ●, outmatching all conventional filters. Rely on it.

For more information go to
www.eppendorf.com/dualfilter

Features of the ep Dualfilter T.I.P.S.
Double protection provided by the two phase filter
- Provides maximum protection for both pipette and sample
- Ultimate absorption of aerosols and biomolecules
- Free from PCR inhibitor additives
- Patent pending two phase filter technology
- Supplied sterile, Eppendorf PCR clean and pyrogen-free
- IvD conformity
- Batch-related certificates available

eppendorf
In touch with life

Your local distributor: www.eppendorf.com/worldwide Application Support: +49 180-3 66 67 89
Eppendorf AG Germany +49 40 538 01-0 • Eppendorf North America, Inc. 800-645-3050

METEOROLOGY

A Dose of Dust That Quieted An Entire Hurricane Season?

The 2006 hurricane season was looking grim. Three hurricanes had ripped across Florida during the 2004 season. Four hurricanes, including Katrina, had ravaged the Gulf Coast in 2005. Now meteorological signs were unanimous in foretelling yet another hyperactive hurricane season, the eighth in 10 years. But the forecasts were far off the mark. The 2006 season was normal, and no hurricanes came anywhere near the United States or the Caribbean.

Now two climatologists are suggesting that dust blown across the Atlantic from the Sahara was pivotal in the busted forecasts. The dust seems to have suppressed storm activity over the southwestern North Atlantic and Caribbean by blocking some energizing sunlight, they say. "I think they're on to something," says hurricane researcher Kerry Emanuel of the Massachusetts Institute of Technology in Cambridge. Dust "might play a big role" in year-to-year fluctuations in hurricane activity.

As the 2006 season approached, conditions looked propitious for another blustery hurricane season. In particular, there was no sign of El Niño, whose Pacific warming can reach out to the Atlantic and alter atmospheric circulation to suppress hurricanes there. But, unremarked by forecasters, an unusually heavy surge of dust began blowing off North Africa and into the western Atlantic at the 1 June beginning of the official hurricane season. Two weeks later, the surface waters of the western Atlantic began to cool compared with temperatures in the previous season.

Climatologists William Lau of NASA's Goddard Space Flight Center in Greenbelt, Maryland, and Kyu-Myong Kim of the University of Maryland, Baltimore County, in Baltimore argue in the 27 February issue of *Eos* that the arrival of the thick dust and the subsequent cooling were no coincidence. The dust blocked some sunlight and cooled the surface, they say. That cooling went on to trigger a shift toward less favorable conditions for the formation and intensification of storms in the western Atlantic, they argue. As a result, no storm tracks crossed where none had passed the previous season.

Lau and Kim find that historically, El Niño's influence on Atlantic storms has in fact prevailed in the eastern tropical Atlantic, as it may have done last year when it put in a surprise appearance beginning in August. But in the west, near the Caribbean and the United States, dust has been the dominant external influence, they found. "We're not denying El Niño had an impact," says Lau, but "maybe we have neglected an equally important factor, if not a more important factor."

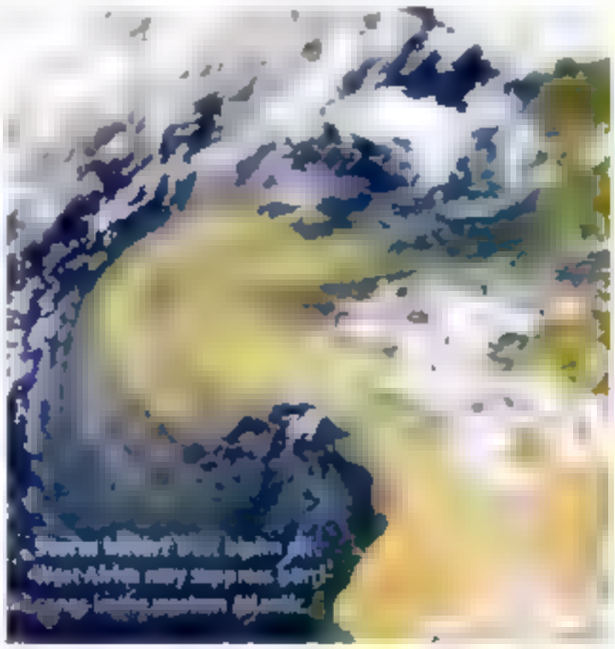

Many hurricane researchers are intrigued but cautious. "The authors have an intriguing hypothesis," says Christopher Landsea of the National Hurricane Center in Miami, Florida, but "there's not much evidence that there is a direct cause and effect going on here." And if dust were involved, it would have been more complicated than a simple cooling, says Jason Dunion of the National Oceanic and Atmospheric Administration's Atlantic Oceanographic and Meteorological Laboratory in Miami. The dust comes in a layer of air whose extreme dryness and high winds are thought to discourage storm development and intensification as well.

If dust is a major factor in the Atlantic, it will only complicate forecasting the severity of hurricane seasons. Anticipating the arrival of El Niño is proving tricky enough. Predicting far-traveled Saharan dust months ahead—both the necessary North African dryness and the dust-carrying winds—could be formidable.

–RICHARD A. KERR

CREDIT: SEAWIFS PROJECT/NASA/GSFC/NASA

SCIENCESCOPE

Broad Institute Given $100 Million

The already well-heeled Broad Institute in Cambridge, Massachusetts, this week announced a $100 million gift from a wealthy direct marketer to conduct research on severe mental illnesses such as bipolar disorder and schizophrenia. The funding from the Stanley Medical Research Institute will allow the Broad—a joint venture between the Massachusetts Institute of Technology and Harvard University—to create an interdisciplinary center that will draw on the universities' expertise in neuroscience and genomics. That center, located within the Broad Institute, will be led by Edward Scolnick, a former National Institutes of Health researcher and president of Merck Research Laboratories. The money from the Stanley Institute, founded by the family of Theodore and Vada Stanley, will help Broad researchers apply "the most advanced genomic tools" to the biology of mental illness, says Harvard Provost Steven Hyman.

–ANDREW LAWLER

Ganging Up on Jupiter

A NASA probe heading to Pluto and a European Space Agency (ESA) spacecraft on its way to a comet will team up in coming weeks in an unusual effort to observe Jupiter. ESA's Rosetta, launched in 2004 and currently in the neighborhood of Mars, will examine the ring of electrically charged particles around the gas giant planet that may stem from volcanic eruptions on its moon Io. Meanwhile, NASA's New Horizons mission (below) sped past Jupiter last week after leaving Earth in January 2006. As the probe uses the planet's gravity to slingshot its way to Pluto, the onboard instruments are monitoring the Jupiter system.

The roughly simultaneous observations from the two probes could provide a unique set of data on the planet. "We couldn't pass up this opportunity to study Jupiter's meteorology, rings, aurorae, satellites, and magnetosphere," says New Horizons principal investigator S. Alan Stern of Southwest Research Institute in Boulder, Colorado. The joint effort augurs well for future international cooperation in space science. Stern takes over as NASA's science chief next month.

–ANDREW LAWLER

Land ho. With just a change in signal strength this robot, modeled after a salamander, can swim to shore, crawl onto land, and walk away.

EVOLUTION

Robot Suggests How the First Land Animals Got Walking

Salamandra robotica is a triathlete. She walks. She crawls. She swims. One of very few robots capable of multiple modes of locomotion, this salamanderlike machine has demonstrated that it may have been relatively easy for early animals to take their first steps on land. From a neurological perspective, inducing a transition from swimming to walking is unexpectedly straightforward, explains Auke Ijspeert, a physicist at the Swiss Federal Institute of Technology in Lausanne. Thanks to *Salamandra*, he and his colleagues have shown that merely changing the strength of the brain signal driving locomotion can determine whether an animal walks or swims. Once the neural networks for moving legs were in place, little additional neural circuitry was required. Ijspeert and his colleagues report on page 1416.

"This is clearly an excellent fusion of biology and robotics to test neurological and evolutionary hypotheses," says Frank Fish, a biomechanist at West Chester University in Pennsylvania. "This paper will be a high-profile example of how robots can be used as surrogates for living and fossil systems."

Salamanders are a lot like the first land-based tetrapods. These amphibians swim in the same manner as primitive fish, such as lampreys, and they waddle, with legs splayed out, like alligators and their ancient relatives. The salamander "represents therefore a key animal to understand the evolutionary transition from swimming to walking," says Ijspeert, who combined forces with INSERM neurobiologist Jean-Marie Cabelguen of the University of Bordeaux, France, and two graduate students to determine how the brain controls this amphibian's movements compared to the lamprey's.

They focused on two networks of nerve cells, called central pattern generators, located along the spine. When a network is activated, its individual nerve cells alternate between firing and being quiet, causing rhythmic muscle contractions. Both the lamprey and the salamander have one network to drive the body musculature. For swimming, this network sends waves of muscular contractions down the body.

U.S. SCIENCE POLICY

Report Tells NSF to Think More Boldly

Has the U.S. National Science Foundation (NSF) gotten too conservative? A new draft report from its oversight body calls on the federal research agency to be more receptive to funding wild-eyed ideas that just maybe, could revolutionize science (nsf.gov/nsb).

The agency's director, Arden Bement, thinks the board's proposal for a separate "transformational research initiative" is itself a bit over the top. The $6 billion foundation is already doing everything it can to identify "potentially transformative" research, says Bement, adding that another program would tax an already overburdened staff.

NSF's peer-review system is widely seen as the gold standard for selecting high-quality research proposals. But board members say they are worried that some scientists don't even bother to apply for grants for ideas that cut across the scientific grain because of what the draft report calls "the external perception that NSF is not as welcoming as it should be to such research."

To erase that perception, the report suggests "a new, distinct, and separate foundation-wide program designed to solicit and support transformational and paradigm-challenging proposals." The mechanism would serve scientists with brilliant but not-ready-for-prime-time ideas, the kind that "might be at odds with the current thinking in the field," says board member Douglas Randall, a plant physiologist at the University of Missouri, Columbia. "And if it goes into that merit-review meat grinder, it'll just get spit out."

NSF is currently analyzing the results of

CREDITS: A. IJSPEERT/EPFL

repeatedly creating S-shaped waves that move tailward. Amphibians have a second one, which controls the limbs.

In 2003, Cabelguen and his colleagues discovered the region of the salamander's midbrain that fires off signals to these two central pattern generators. When the researchers gently stimulated this part of the brain electrically, they caused the limbs to move as if walking. As they gradually increased the applied current, neural activity in the limbs sped up until finally the nerve cells shut down. At this point, the amphibian's limbs stopped moving and the body started undulating much faster, as in swimming.

Ijspeert's group developed a mathematical model of this transition, from which they concluded that the limbs' central pattern generator interfered with the other neural network's ability to set up the S-waves. This interference produced the slower body bending necessary for walking. Only when the limb's central pattern generator was shut down was the salamander's other network of nerve cells free to fire as fast as needed to generate swimming or, on land, crawling.

Ijspeert then built *Salamandra robotica* to test the mathematical model's predictions. About 85 centimeters from snout to tail up and with four rotating legs and six movable joints along her body, she is powered by 10 motors instead of muscles. Using a remote control, Ijspeert and his graduate student Alessandro Crespi sent signals of varying strength to *Salamandra*.

As in Cabelguen's experiments, less intense signals caused the robot to walk. With stronger signals, the legs sped up. But with the strongest signals, the legs stopped moving and *Salamandra* began swimming. "This close correspondence suggests that the researchers may have accurately recreated some of the actual neural control mechanisms salamanders use," says John Long, a biomechanist at Vassar College in Poughkeepsie, New York. The results, Long and others say, suggest that early animals didn't need to invent completely new neural pathways to expand their locomotor repertoire.

> "This paper will be a high-profile example of how **robots can be used as surrogates** for living and fossil systems."
>
> —Frank Fish, West Chester University

Some researchers think this simple mechanism is not the whole story, however. Robert Full, an integrative biologist at the University of California, Berkeley, says Ijspeert and his colleagues "definitely need not only to include motion in their analyses but also the mechanics of the body and an understanding of the environment."

Nonetheless, says Long, the robot is "the best I've seen in terms of combining, coordinating, and alternating different vertebrate propulsive mechanisms." If nothing else, adds Miriam Ashley-Ross, a functional morphologist at Wake Forest University in Winston-Salem, North Carolina, "I think that more collaborations between biomechanists and neuroscientists and experts in computer modeling will start up and flourish, spurred on by this paper."

–ELIZABETH PENNISI

a community survey designed in part to determine whether that perception is true. Bement suspects that concerns have grown in step with the rising share of top-rated proposals that NSF is unable to fund, now one in three. He says he agrees with the board on the importance of funding as much potentially transformative research as possible but not with its conclusion that NSF should launch a separate initiative. "Every directorate has special programs for frontier research," he notes. "And every program officer is looking for exciting proposals to fund."

One constraint, he says, is a heavy workload. The number of proposals submitted has risen by 47% since 2000, with little growth in staff. Managing a new program, Bement says, would leave even less time to seek out the type of research proposals that the report is calling for.

Several board members say they would like the review process to place more emphasis on the investigator's ideas and track record and less on preliminary data showing that the project is feasible. "Business as usual is what people are comfortable with. We need something different," says board chair Steven Beering. The report asks NSF to come up with a management plan by August.

–JEFFREY MERVIS

The Continuation Saga (Cont.)

It's been more than a year since the U.S. Patent and Trademark Office (PTO) proposed limiting add-on patent applications, which allow additional information to be submitted on existing applications. PTO says so-called continuations are hurting patent quality and drowning examiners in paper (*Science*, 28 July 2006, p. 425). The proposal was met with a firestorm of attacks during a public comment period last year. Some biomedical scientists say continuations are necessary to keep patent applications up to date. "There must be some kind of nefarious political pressure on some numbnuts at the PTO, because almost every one of those public comments was resoundingly negative," wrote lawyer Mark Perdue of Storm LLP in Dallas, Texas, on the popular Patently-O blog last summer.

PTO Director Jon Dudas disagrees. "We're being very thoughtful about this," he told *Science*. "People don't want to change." He says he expected the backlash when he proposed the limits. He hasn't decided when to issue a final decision on the rules. Another Dudas initiative, a pilot project to allow the public to rate technical information to help examiners with software patents, is expected to go online soon.

–ELI KINTISCH

Different Ways to Compete

When it comes to improving U.S. innovation, some legislators are thinking big whereas others say that small is better. This week, Senate Majority Leader Harry Reid (D-NV) led a bipartisan coalition of senators endorsing the America COMPETES Act, a sprawling bill, drawn from the recommendations of a 2005 National Academies report on how to strengthen the U.S. scientific enterprise (*Science*, 21 October 2005, p. 423). The proposal would authorize a doubling of funding for the National Science Foundation (NSF) and the Department of Energy's (DOE's) Office of Science and support a raft of programs to train more scientists and improve science and math education at all grade levels. Reid said he plans a floor vote on the bill, whose provisions would cost $16 billion over 4 years, sometime next month.

Meanwhile, the House Science and Technology Committee last week approved a measure to expand early career and graduate training programs at NSF and DOE and monitor the need for research instrumentation across the government. The bill (H.R. 363) addresses a tiny slice of what the Senate legislation covers, but the panel's chair, Representative Bart Gordon (D-TN), believes that narrowly focused legislation stands a better chance of passage by Congress.

–JEFFREY MERVIS

China Supersizes Its Science

With little fanfare, China is about to spend hundreds of millions of dollars to build major science facilities for everything from crystallography to remote sensing

BEIJING— As the maglev train from Pudong airport races toward Zhangjiang High-Tech Park on the outskirts of Shanghai, passengers can glimpse what looks like a giant silver nautilus on the horizon. This 36,000-square-meter spiral structure is the Shanghai Synchrotron Radiation Facility (SSRF), scheduled to come on line in 2009.

At an investment of 1.2 billion yuan ($150 million), SSRF is the most expensive fundamental research project China has ever undertaken—for the time being, that is. The facility, which will generate powerful x-rays for studying the structures of molecules and advanced materials, will soon be joined by another heavyweight champ. Last month, the Chinese Academy of Sciences (CAS) signed an agreement with Guangdong Province in southern China to build the $250 million China Spallation Neutron Source (CSNS).

Thanks in part to a pledge to raise R&D spending from 1.3% of gross domestic product in 2005 to 2.5% by 2020 (*Science*, 17 March 2006, p. 1548), big science projects that have been on the drawing board for years and new concepts are fast becoming reality. The central government's National Development and Reform Commission (NDRC), the agency responsible for all major state investments, is bankrolling the construction of a dozen major facilities to the tune of $750 million—during the 11th 5-year plan, which runs through 2010. (SSRF was launched in the previous 5-year plan.) The spallation source alone will receive $163 million from the NDRC pot, with Guangdong authorities chipping in the rest. So far, NDRC has given an official go-ahead to five of 12 projects; the seven others are expected to receive approval later this year.

Proponents argue that China needs to invest in megaprojects to boost its rapid ascent as a research power. With large facilities, "we can proudly stand up in the international scientific community and no longer rely on foreign equipment to do many experiments," says Liang Rongji, an official at the "big-science" section of CAS.

However, some prominent researchers question the decision to shower such largess on machines. They say what China needs most is to build a critical mass of scientists in many disciplines to get the most out of the new facilities. "Many people are enthusiastic about building instruments, but there are not enough people to do the science," says Gan Zuzhan, a physicist at Beijing University.

NDRC officials declined to provide information on any of the projects, claiming that certain details are state secrets. And most scientists declined to discuss the matter on the record, expressing concern that their remarks could jeopardize funding for projects not yet finalized. But from published reports and interviews with two dozen scientists and officials, *Science* has pieced together a picture of China's ambitious Big Science agenda (see table, p. 1355).

Thinking big

Big science holds a hallowed place in China, where top politicians often wax nostalgic about *liang dan yi xing*, or "two bombs and one star": the development of the atomic and hydrogen bombs and the country's first satellite in the 1960s. "Leaders like to support megaprojects for their visibility," says Cong Cao, an expert on Chinese science policy at the State University of New York in New York City. Megaprojects also fit China's top-down approach to research, and successful projects justify political legitimacy. Just as the nuclear weapons program in the 1960s was touted as a triumph of Mao Zedong Thought, the Beijing Electron Positron Collider (BEPC) was held up as proof of Deng Xiaoping's foresight.

BEPC was the first big science project after the Cultural Revolution ended in 1976. It demonstrates how a large facility can take root in China, support at the highest level of government. Deng himself decreed that it be built, help from international advisers and collaborators, and most importantly, the work of indigenous physicists trained in nuclear weapons and particle physics who managed to turn Deng's dream of an expensive proton accelerator into a more modest but successful collider.

Among its achievements, BEPC boasts the most precise measurements of the tau lepton's mass, data that have helped verify the Standard Model of particle physics. To enhance collaborations with foreign scientists, BEPC's host, the Institute of High Energy Physics (IHEP), forged China's first high-speed Internet link to the outside world—a connection between IHEP and the Stanford Linear Accelerator Center in 1994. And BEPC has

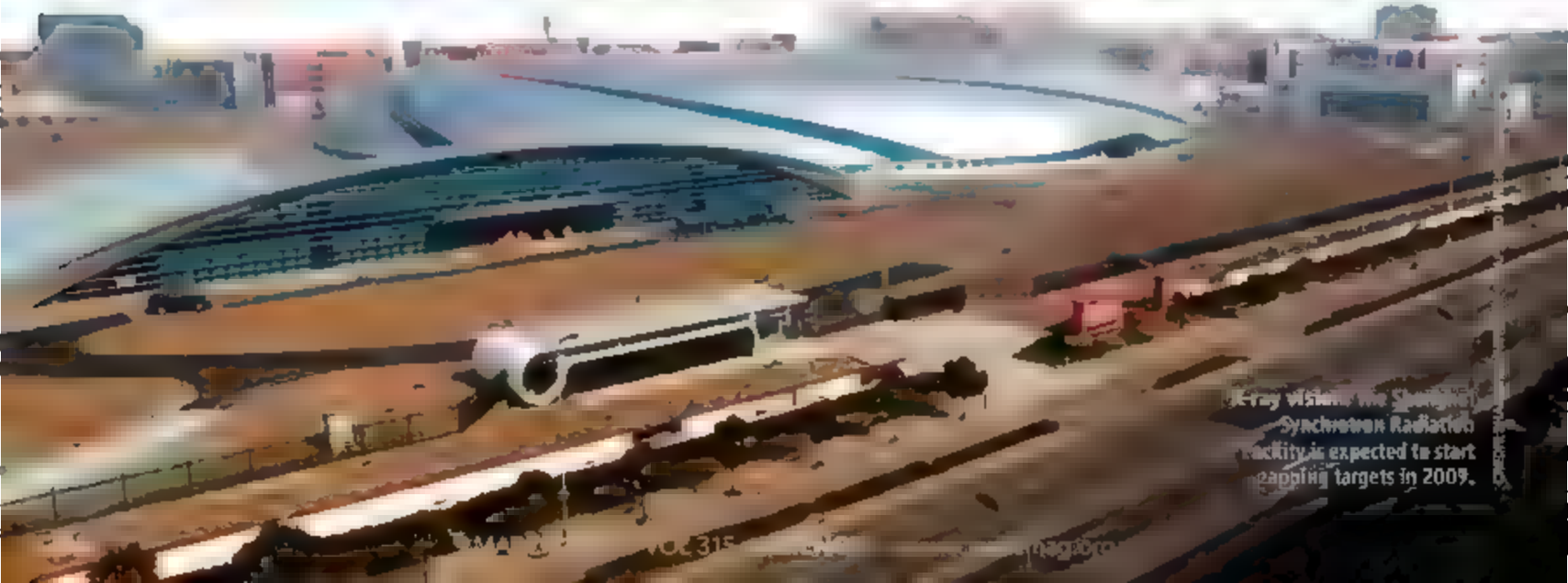

Artist's view of the Shanghai Synchrotron Radiation Facility, is expected to start zapping targets in 2009.

helped China develop technical capacity. "Construction of a large facility needs many novel parts and technologies," says IHEP Director Chen Hesheng. "Mastering the process greatly improves indigenous skills." After learning how to make accelerator parts, IHEP now exports some components to Japan, South Korea, and the United States.

Buoyed by its success, BEPC has attracted friends in high places. Its VIP visitor log is a Who's Who of China's political elite. That has kept the funds flowing. In 2000, the central government approved $80 million to renovate the facility. The upgrade—called BEPC II—was scheduled for completion next year. Its power should increase 100-fold, enabling ever-finer measurements of tau lepton mass. Down the road, IHEP plans to build the $2 billion Beijing Tau-Charm Factory to extend the accelerator energy up to 3 GeV for experiments on both the tau lepton and charm quark. And the institute is participating in the International Linear Collider project.

Thinking bigger

China's current scientific leaders hope to steal a page from BEPC's playbook. CAS President Lu Yongxiang, who has made innovation a central theme at the academy, has often urged researchers to transition from "following what others do" to "coming up with what to do." Nevertheless, several big science projects appear to be "me-too" facilities, including CSNS, which Lu initiated after a tour in 2000 of ISIS, a pulsed neutron source at Rutherford Appleton Laboratory near Oxford, United Kingdom.

According to J. K. Zhao, a senior scientist at Oak Ridge National Laboratory in Tennessee and a consultant to CSNS, Lu was impressed by the multidisciplinary research at ISIS and asked CAS's Institute of Physics for a feasibility study of a similar facility in China. A group of neutron scientists enlisted Zhao and other overseas experts to help draft ISIS-inspired plans.

CAS approved the conceptual design in 2005 and funded a preparatory team, led by Wei Jie of Brookhaven National Laboratory in Upton, New York, and IHEP, to start on an engineering design in 2006. To ensure reliability, the team will adopt mature technology whenever possible, says Fu Shinian, Wei's deputy at IHEP. The phase I design calls for a linear accelerator and rapid-cycling synchrotron to speed up protons to 1.6 GeV and deliver an initial beam power of 120 kilowatts, which can be doubled and quadrupled in future upgrades. The high-energy protons bombard a heavy-metal target, such as tungsten, to knock off a spray of neutrons. "It's like shooting the cue ball into a pile of billiard balls," says Zhao. Each proton can shear 20 to 30 neutrons off the target, generating an intense pulse for probing microstructures of superconductors, for instance, or proteins. Phase I construction is expected to take 6 years.

Remarkably, CSNS will be built far from the traditional science strongholds of Beijing and Shanghai. Dongguan, a city in the prosperous Pearl River Delta in southern China, offered free land and $63 million toward infrastructure costs. "It's a reasonable deal for Dongguan, where strong economic growth and weak research capacity result in highly unbalanced development," says CAS's Liang. "Many scientific talents may be attracted to the city."

Although Zhao wonders how many senior scientists with families will relocate to Dongguan, he is confident that universities in Guangdong and Hong Kong will pack the facility with young researchers. Fu says senior scientists from Beijing will train the neophytes but acknowledges that "experts sent by IHEP alone certainly are not enough." So CSNS will open its doors to foreign researchers. For starters, Dongguan in April will host the 18th Meeting of the International Collaboration on Advanced Neutron Sources, the first time the event will be held in China.

Chinese astronomers, meanwhile, should soon hear a decision on the amount NDRC will spend on the world's largest single radio telescope, the Five-hundred-meter Aperture Spherical Telescope (FAST). The instrument, first proposed by China's National Astronomical Observatories (NAO) in 1994, would allow astronomers to peer farther than ever before, deep into the early universe, says project director Peng Bo.

NAO chose a limestone karst depression in southwest Guizhou Province as the site to suspend a receiving dish made of 4600 triangular panels, taking advantage of the natural topography to reduce construction costs. FAST had been in the running to host the Square Kilometer Array, an international radio astronomy project that would enable astronomers to observe the formation of the early universe and test Einstein's theory of general relativity (*Science*, 18 August 2006, p. 910). However, last September, the international consortium narrowed the sites down to candidates in Australia and South Africa. That "won't affect the investment and construction of FAST," says Peng. He estimates

	Project	Lead Organization	NDRC Funding ($ millions)	Expected Completion
APPROVED	Aviation Remote Sensing System	Institute of Electronics, CAS	100	2010
	Important Engineering Material Service Safety Research Facility	Beijing University of Science and Technology	63	N/A
	High Magnetic Field Facility	Hefei High Magnetic Field Lab, CAS; Huazhong University of Science and Technology, Wuhan	48	5 years
	Meridian Space Weather Monitoring Project, Phase I	Center for Space Science and Applied Research, CAS	25	2008
	Agricultural Biosafety Research Facility	Chinese Academy of Agricultural Sciences	18	2008
PENDING APPROVAL (FUNDING ESTIMATED)	China Spallation Neutron Source (CSNS), Phase I	IHEP, CAS, Dongguan	163	2012
	Protein Science Research Facility	CAS	125	N/A
	Five-hundred-meter Aperture Spherical Telescope (FAST)	National Astronomical Observatories, Guizhou	86	2013
	Continental Structure and Environment Monitoring Network	China Earthquake Administration	N/A	5 years
	Ultralow-Frequency Geoelectromagnetic Exploration Network for Underground Resources and Earthquake Prediction	China Earthquake Administration	N/A	5 years
	4000-Ton Oceanographic Research Vessel	State Oceanic Administration	N/A	N/A
	Icing Wind Tunnel	China Aerodynamics Research & Development Center, Mianyang, Sichuan	N/A	N/A

The mega dozen. China has set its sights on launching 12 major science facilities by 2010.

SOURCE: COMPILED FROM VARIOUS SOURCES

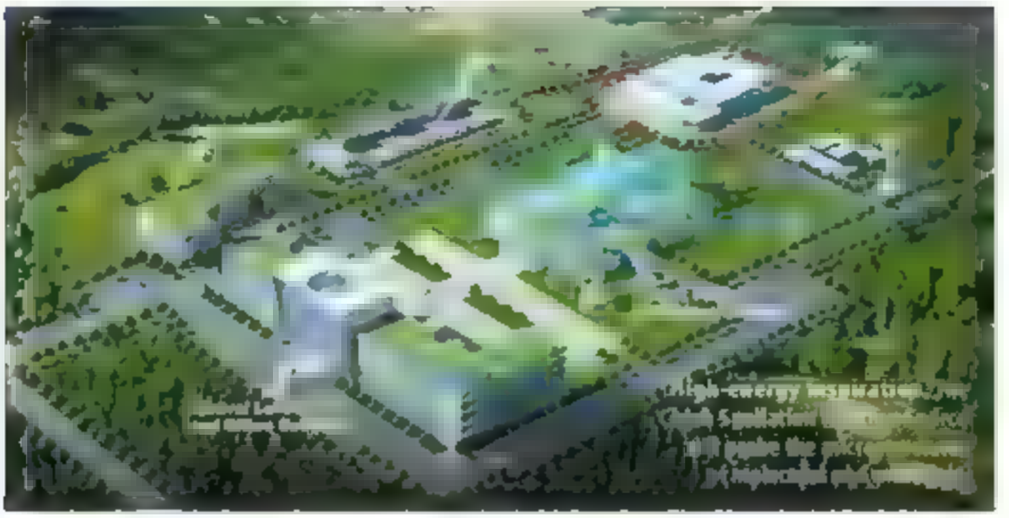

that FAST will cost at least $86 million and take 6 years or more to build.

In comparison, the gestation time of the High Magnetic Field Facility has been much shorter. Scientists first proposed the big science project in autumn 2004 and received NDRC approval earlier this year. The facility will be hosted in two cities to "take advantage of the existing technical capability of each city," says Kuang Guangli, director of CAS's Hefei High Magnetic Field Lab in Anhui Province.

Hefei will be home to 35- to 40-tesla water-cooled and superconducting steady-field magnets, primarily for materials science research, such as probing the quantum Hall effect, and for magnetic resonance imaging. Wuhan, in Hubei Province, will get 50- to 80-tesla pulsed field magnets to complement an existing low-temperature lab and pulsed-power generator. Researchers there will plumb the effects of ultralow temperatures and ultrahigh magnetic fields. NDRC has allotted $48 million for the 5-year construction effort.

Thinking wider

With megaprojects sprouting like bamboo shoots after a spring rain, big science is no longer the sole province of CAS's physical sciences division. Other new entries span fields such as agriculture, biology, geology, and remote sensing.

One of the first projects NDRC finalized in 2005, is the Meridian Space Weather Monitoring Project. It has a wide reach from fundamental astrophysics—such as probing how solar flares and coronal mass ejections influence Earth's upper atmosphere—to monitoring near-Earth space to ensure safe satellite operation.

Run by CAS's Center for Space Science and Applied Research, the project will equip 15 ground-based observation stations with laser radars and other instruments to record temperature, air density, and electromagnetic data from above an altitude of 20 kilometers to several hundred kilometers. Its first phase will cost $25 million and is expected to take 3 years to complete. Project scientists have also proposed an International Space Weather Meridian Circle Program to link national arrays of ground-based monitors to enhance space environment observation worldwide.

Other big science initiatives are less well defined. Take the estimated $125 million "protein science research facility." At the height of the SARS outbreak in 2003, after Rao Zihe's group at Qinghua University in Beijing cracked the crystal structure of the main protease of the SARS virus using IHEP's synchrotron source, NDRC wanted to reward Rao with a major protein crystallography facility at CAS's Institute of Biophysics, where Rao had become director in 2004. But the project derailed when Rao left Beijing last year to become president of Nankai University in Tianjin. CAS Vice President Chen Zhu then proposed building the facility at Shanghai's Zhangjiang High-Tech Park, near SSRF, to take advantage of the new synchrotron source. But many biologists have said that protein science is more than crystallography and that the new center should not be so far from existing biological institutes.

The political tussle is heating up. Sources say that one faction is lobbying for the facility to be built downtown, near CAS's Shanghai Institutes of Biological Sciences. "Zhangjiang is too far to go for experiments if you study proteins in living cells," says one researcher. Others are trying to carve off funds for existing labs in Beijing. They argue that if too much money is spent in equipping a single facility, waste is inevitable.

Indeed, researchers acknowledge that China's funding system for megaprojects has a serious flaw. It favors one-shot projects, revolution, not evolution. "In Japan or South Korea, they build synchrotron sources one beamline at a time as needed," says Fudan University physicist Zhang Xinyi, who directed the National Synchrotron Radiation Lab (NSRL) in Hefei before moving to Shanghai. "But in China, we have to build the facility as one big project because all the funding comes in a single chunk."

In addition, an unwritten rule sets a facility's operating budget at one-tenth the construction cost. "On many occasions, the operating budget is determined before construction begins," says CAS's Liang. This hamstrings researchers when unforeseen problems arise. For example, when NSRL in the 1990s encountered trouble with beam stability, which thwarted experiments, its operating budget was insufficient to carry out a fix. NSRL's synchrotron source was stabilized in 2004, only after NDRC approved $15 million for an upgrade.

Zhang wants to apply lessons learned from managing the Hefei synchrotron to the construction of the Shanghai source. He has suggested to NDRC that some money be set aside so users can bid to design their beamlines and experimental stations. However, he says NDRC preferred to stick with its usual approach to allocating money. Zhang still hopes that SSRF's management will be more flexible. It has already agreed to let him design his own beamline for research on condensed matter physics and synchrotron radiation imaging, with funding from Fudan University.

But most would-be users do not have the couple of million dollars for this kind of instrument work. IHEP's Xian Dingchang, one of China's foremost synchrotron experts, says that letting major users participate in construction and management is popular in foreign synchrotron labs, but "our system does not allow it. Organizations want to control all the resources they've got."

Xian hopes that China's spallation neutron source can do better. According to Fu, CSNS has involved users from the beginning and modified designs after input from large user meetings. "We also learned lessons about the operating budget from previous projects," says Fu, who intends to argue for more operation and maintenance funds from the central government. Guangdong Province already has promised some help.

Some Chinese scientists criticize the government's funding system for prizing machines over people. Ultimately, however, it is what scientists achieve with CSNS and its big brethren that will prove the wisdom of China's big investment in Big Science.

–HAO XIN AND JIA HEPENG

Jia Hepeng is a writer in Beijing. With reporting by Gong Yidong of *China Features* in Beijing.

CREDIT: COURTESY OF CSNS

RETROVIRUS MEETING

Hope on New AIDS Drugs, but Breast-Feeding Strategy Backfires

Two novel drugs show promise in hard-to-treat patients, but breast-feeding studies underscore the difficulty of applying advances in the real world

LOS ANGELES, CALIFORNIA—In the arcade game Whac-a-Mole, mallet-wielding players pound moles into the ground only to have the buck-toothed pests pop out of another hole. HIV has a lot in common with those moles. Although research has shown that breast-feeding carries a significant risk of transmitting HIV from an infected mother to her baby, new studies presented here last week at the largest annual U.S. AIDS meeting* highlight the dangers that alternative strategies such as infant formula present in poor countries. Similarly, talks at the meeting underscored that despite much success in increasing access to anti-HIV drugs, great disparities still exist between the developed and the developing world. But there was one bright spot. Data on two new medications indicate that they can knock down HIVs that have become resistant to current drugs and are popping back up.

The most dramatic talk on alternatives to breast-feeding focused on Botswana, where the government advises all HIV-infected women to use infant formula to avoid transmitting the virus. (The World Health Organization, by contrast, recommends that HIV-infected women use formula only when it is "acceptable, feasible, affordable, sustainable, and safe.") Nearly two-thirds of infected mothers in Botswana now use formula, which is provided free by the government. But that policy appears to have had a tragic downside. Researchers studying an especially deadly outbreak of diarrhea, diseases last year reported that infant formula, as compared to breast-feeding, increased a child's risk of death from diarrheal disease 50 times, likely because a severe flood contaminated the water used to make the formula.

From January to March 2006, 532 children under 5 in the country died from diarrhea, up from 21 the year before. Medical epidemiologist Tracy Creek of the U.S. Centers for Disease Control and Prevention in Atlanta, Georgia, and colleagues studied a cohort of 153 Botswanan children hospitalized for diarrhea. Of these, 33 died, and all but one were formula-fed. The HIV-infected status of the mother and the infant was not associated with any of the deaths. Stool samples showed widespread infection with cryptosporidium, *Escherichia coli*, and salmonella. "It's a stunning story," says pediatrician Hoosen Coovadia of the University of KwaZulu-Natal in South Africa.

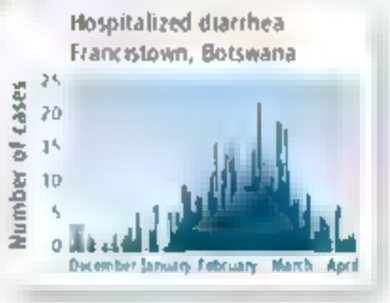

Creek's team has advised Botswana to reevaluate its universal formula policy, stressing that the risk of viral transmission from breast-feeding must be balanced against the risks of formula use in such settings. But James McIntyre, an obstetrician-gynecologist at Baragwanath Hospital in Soweto, South Africa, cautioned that researchers and policymakers should not lose sight of the real goal: to make both feeding approaches safer. Several studies under way are evaluating a myriad of strategies to do just that, including distributing chlorination solutions and using anti-HIV drugs in mothers and uninfected babies more aggressively. But a Zambian study presented at the meeting found that one seemingly logical way to make breast-feeding safer, early weaning, offered no benefit. The study, which compared abrupt weaning at 4 months to breast-feeding for an average of 16 months, found an equal number of HIV infections and deaths by 2 years of age.

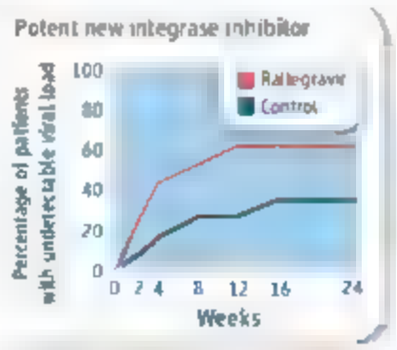

The most promising news at the meeting came from reports of large efficacy trials of two AIDS drugs, slated for approval as early as this year, that have novel targets. One of the drugs, raltegravir, made by Merck & Co. in Rahway, New Jersey, cripples HIV's integrase enzyme. In studies of nearly 800 patients who had viruses that were highly resistant to existing drugs, about 60% had undetectable levels of HIV in their blood after 24 weeks of treatment with raltegravir and an "optimized" cocktail of other drugs. In the control group, which received just the optimized regimens, viral loads became undetectable in roughly 30%.

The second drug, maraviroc, targets human immune cells rather than the virus. HIV enters cells by attaching to the CD4 receptor and one of two chemokine receptors, CCR5 or CXCR4. Maraviroc, made by Pfizer in New York City, gums up CCR5 to prevent HIV from binding to it. In studies of more than 500 people infected with HIVs that prefer CCR5 receptors, maraviroc drove viral levels down to undetectable in 48.5% of the treated group versus 24.6% in a control group that received optimized regimens alone.

David Cooper of the University of New South Wales in Sydney, Australia, who has tested both drugs, says if their potency and safety hold up, clinicians should reevaluate when to start treatment. Current recommendations encourage delaying treatment until serious immune damage occurs, in part to reduce toxic effects. But the tradeoff is that people suffer from the prolonged immune stimulation that HIV triggers, which Cooper says is likely responsible for the increased number of deaths from heart, liver, and kidney disease. "If you start people earlier, you might have a significant impact on all of these," he says.

For the vast majority of HIV-infected people who live in poor countries, however, it may be many years before maraviroc and raltegravir offer any relief. Matthias Egger of the University of Berne in Switzerland and colleagues reported that 59 different drug regimens are available to most AIDS patients in North America, but only three are typically available in Asia and Africa. Solve one problem, another surfaces.

–JON COHEN

* 14th Conference on Retroviruses and Opportunistic Infections, 25–28 February, Los Angeles, California

IMAGES (TOP TO BOTTOM): T. CREEK/CDC; D. COOPER/UNIVERSITY OF NEW SOUTH WALES

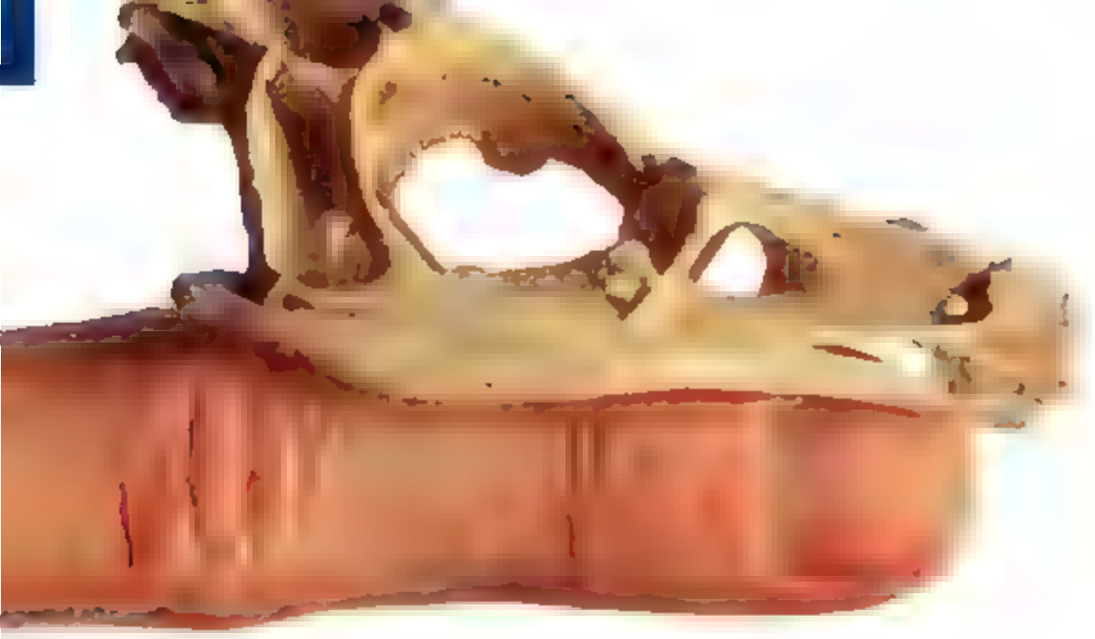

EVOLUTION

Jurassic Genome

Dinosaur fossils are helping scientists tease apart why the sizes of genomes vary so dramatically among species

Tyrannosaurus rex, it turns out, had a pretty small genome. A team of American and British scientists estimates that it contained a relatively puny 1.9 billion base pairs of DNA, a little over half the size of our own genome.

The scientists who came up with this estimate—along with estimates for the genomes of 30 other dinosaur species—had no ancient DNA to study. *T. rex*, after all, became extinct 65 million years ago, and its genome is long gone. Instead, they discovered a revealing correlation. Big genomes tend to be found in animals with big bone cells. By comparing the size of cells in dinosaur fossils to those of living animals, the scientists got statistically sound estimates for the sizes of the dinosaur genomes.

The findings, published by *Nature* this week, are more than just a curiosity. Chris Organ, a Harvard University paleontologist and the lead author of the new paper, says the estimates shed new light on a big puzzle. Why do the genomes of living species come in such a staggering range of sizes, varying more than 3000-fold in animals? A fruit fly's genome is 350 times smaller than ours, whereas the marbled lungfish genome is 37 times bigger. Recently, some large-scale comparisons of genome sizes have suggested that natural selection may favor big genomes in some species and small genomes in others. But some skeptics argue that genome size may not be adaptive at all. Now, with the advent of what Organ likes to call "dinogenomics," scientists can begin to tease out some answers by adding extinct species to the emerging picture of genome evolution.

The new study will have its most direct impact on tracing the evolution of bird genomes. "Birds are dinosaurs, they're the last vestige," says Organ. Scientists have long noted that birds have small genomes compared to reptiles, their closest living relatives, but it was unclear how and when that change occurred. Organ's study suggests that the dinosaur ancestors of birds had evolved small genomes long before birds took to the sky. "I think it's very exciting," says T. Ryan Gregory, an expert on genome size at the University of Guelph in Canada. "It's the kind of paper we've needed for a long time."

Giant genomes in lowly creatures

The wide array of genome sizes startled scientists when it came to light in the early 1950s. Until then, the prevailing wisdom had been that complex animals needed bigger genomes than simple ones needed. And yet, as one paper explained, a salamander's genome "contains 70 times as much DNA as is found in a cell of the domestic fowl, a far more highly developed animal." As researchers sized up more genomes, the paradox grew deeper. Some single-celled protozoans turned out to have bigger genomes than humans. The genome of *Gonyaulax polyhedra*, for example, is 28 times the size of ours.

A solution of sorts emerged in the 1970s: so-called junk DNA. In addition to protein-coding genes, genomes contain stretches of DNA that encode RNA molecules or are just vestiges of old genes. Many genomes, including our own, are dominated by virus-like sequences of DNA called mobile elements that can make new copies of themselves that get inserted in new spots in the same genome. The human genome is 98.5% noncoding DNA.

Comparing the genomes of living species, scientists have found that genomes can expand and shrink quickly, with mobile elements spreading like a genomic plague. The cotton genome, for example, tripled in size over the past 5 million to 10 million years. On the other hand, copying errors can cause cells to snip out large chunks of noncoding DNA by accident, shrinking their genomes in the process.

To test whether natural selection plays a strong role in determining the size of a species' genome, scientists have compared a wide range of species, searching for correlations between genome size and other traits that might be adaptive. Finding these correlations has been difficult, however, because relatively few genomes had been measured until recently, and many of those measurements turned out to be wrong. Genome sizes are easy to misjudge, even with modern genome sequencing methods. When scientists sequence a genome, they generally break it up into fragments and then try to piece them together like a puzzle. Noncoding DNA is loaded with repeating sequences which are difficult to assemble properly.

Things are improving, says Gregory. New techniques are enabling more-precise measurements—for instance, scientists are adding DNA-staining compounds to cells and then using image-processing software to analyze the amount of stain. And the results of these studies are now being stored in online databases, making possible large-scale comparisons. Gregory maintains a database of animal genome sizes at the University of Guelph (genomesize.com), Kew Gardens biologists manage one for plants

Genomes Big and Small

Nematode (*Caenorhabditis elegans*): 100 million bp

Thale cress (*Arabidopsis thaliana*): 160 million bp

Fruit fly (*Drosophila melanogaster*): 180 million bp

Pufferfish (*Takifugu rubripes*): 400 million bp

Rice (*Oryza sativa*): 490 million bp

Human (*Homo sapiens*): 3.5 billion bp

Leopard frog (*Rana pipiens*): 6.5 billion bp

Onion (*Allium cepa*): 16.4 billion bp

Mountain grasshopper (*Podisma pedestris*): 16.5 billion bp

Tiger salamander (*Ambystoma tigrinum*): 31 billion bp

Easter lily (*Lilium longiflorum*): 34 billion bp

Marbled lungfish (*Protopterus aethiopicus*): 130 billion bp

CREDIT: LOUIE PSIHOYOS/CORBIS

and algae (www.kew.org/genomesize/homepage.html), and biologists at the Estonian University of Life Sciences run a database for fungi (www.zbi.ee/fungal-genomesize). Together, the databases contain information on more than 10,000 species.

One of the first correlations scientists noticed was between the size of genomes and the size of cells. It cropped up in a study on red blood cells in vertebrates. Later studies also found a link between cell size and genome size in other groups of species, such as plants and protozoans, and in other types of cells in vertebrates, although not all.

Some scientists have argued that natural selection favors big or small genomes because they produce big or small cells. Take the case of *Trichomonas vaginalis*, a sexually transmitted protozoan that lives in the human vagina. When a multi-institute group led by Jane Carlton, who is now at New York University, published the organism's genome in the 12 January issue of *Science* (p. 207), they observed that *T. vaginalis* is padded with far more mobile elements than are found in related protozoans that live elsewhere in the body. The scientists suggest that when *T. vaginalis* moved into its current ecological niche, its genome expanded rapidly. The protozoan itself became bigger as a result, which made it more effective at chasing and engulfing its bacterial prey.

Changing cell size may benefit other kinds of species in other ways. In some groups of animals, species with high metabolic rates tend to have small genomes, for example, whereas species with slow metabolisms have big ones. One possible explanation is that small genomes give rise to small blood cells, which have a high surface-to-volume ratio and can transport oxygen faster across their membranes. If a warm-blooded animal needs to use a lot of oxygen to fuel its metabolism, a small genome might give it an evolutionary edge.

The fossil record

Consistent with this hypothesis, birds have much smaller genomes than those of their reptilian relatives. But if birds evolved smaller genomes for their high metabolism, the question naturally arises, when did that shrinkage take place? Organ realized that dinosaur fossils might hold the answer.

Some dinosaur fossils are so well preserved that they still have the cavities that once held their bone cells (known as osteocytes). But no one had ever established a link between genome size and osteocyte size. "That was our first step," says Organ. They examined bones from 26 species of birds, reptiles, mammals, and amphibians. With colleagues at Harvard and the University of Reading, U.K., he mapped his measurements onto an evolutionary tree. The correlation was good enough that they could use the size of a species' osteocytes to accurately predict its genome size. The scientists then added to the tree branches for 31 species of dinosaurs and used the size of their osteocytes to estimate the size of their genomes. From that information, they inferred how the size of dinosaur genomes had evolved over time.

Their analysis suggests that the common ancestor of dinosaurs, a small four-footed reptile that lived about 230 million years ago, had a relatively big genome about the same size as an alligator's. That common ancestor gave rise to several major branches of dinosaurs. One of those branches, the ornithischians, included big herbivores such as stegosaurs and *Triceratops*. Their genomes did not change much. "These guys have a typical reptilian-sized genome," says Organ.

But another branch of dinosaurs—bipedal predators known as theropods—evolved significantly smaller genomes. Theropods would ultimately give rise to birds. "This blows out of the water the idea that small genomes coevolved with flight," says Organ.

Organ suggests that theropods evolved to have higher metabolic rates than other dinosaurs had, and as a result, natural selection favored smaller genomes and smaller cells. Other paleontologists have also found evidence for bird biology in bipedal dinosaurs, including feathers, rapid growth, and nesting behavior. "You don't decide you're going to fly and be warm-blooded like a bird and then make all these changes," says Organ. "They're all small cumulative things that go way, way back, and they come together to produce this end form."

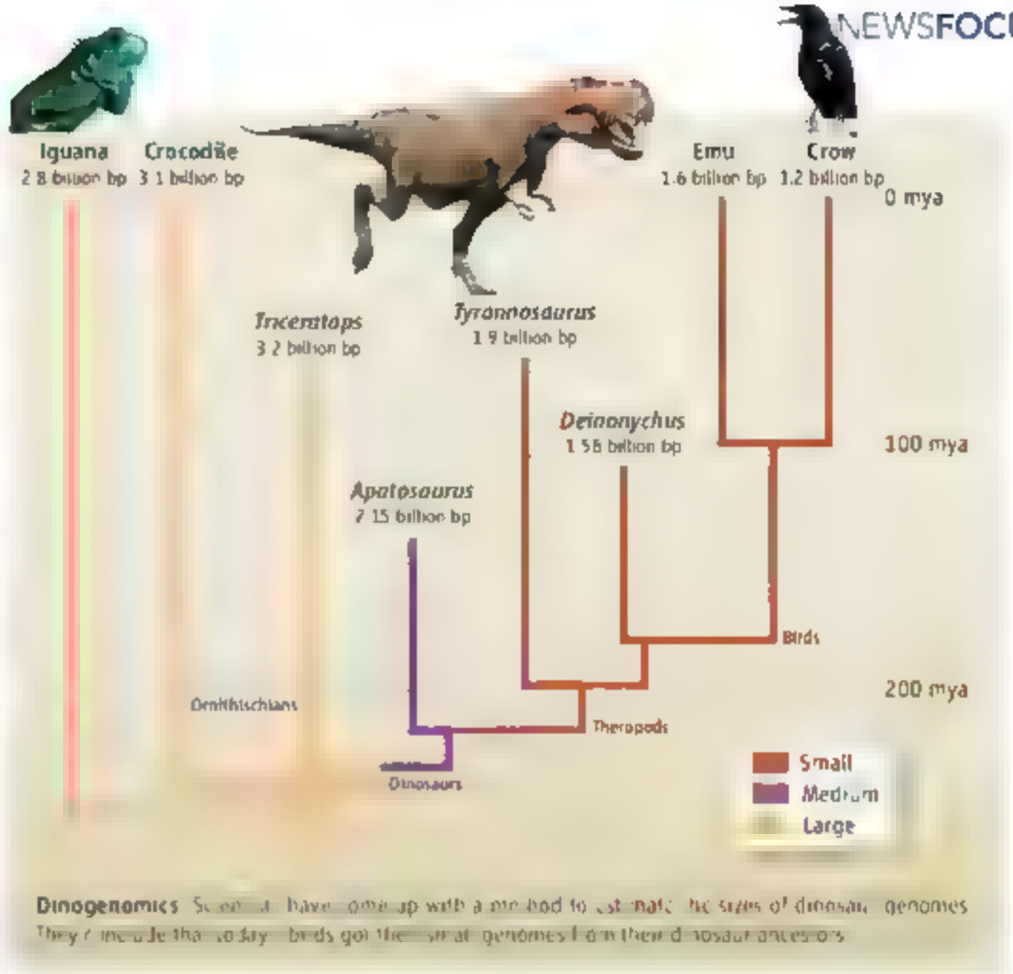

Dinogenomics Scientists have come up with a method to estimate the sizes of dinosaur genomes. They conclude that today's birds got their small genomes from their dinosaur ancestors.

Although Gregory and others praise Organ's paper, some scientists are not as impressed. "It's a cute paper, but I'm not terribly confident in the outcome," says Michael Lynch of Indiana University, Bloomington, who questions whether natural selection is responsible for driving genomes to different sizes to fine-tune metabolism. "There's a correlation of the two, but I don't know of any direct demonstration of causality."

Gregory concedes that even if metabolism can account for the small genomes of animals such as dinosaurs and birds, it won't explain all the patterns scientists find. Plants, for example, have a similar correlation between cell size and genome size, for example, but they don't have an animal-like metabolism. It's possible that plants have different genome sizes because genome size changes the way their cells capture sunlight or transport fluids. "Any one feature isn't really going to cover it," Gregory says. "You have to look from the bottom up and the top down in every case."

—CARL ZIMMER

Carl Zimmer's latest book, on *E. coli* and the meaning of life, will be published next spring.

NEUROSCIENCE

Hunting for Meaning After Midnight

The brain is anything but quiet during sleep. Is it making memories, searching for insight, or up to something else entirely?

Even sound sleepers have restless brains. Your body may be largely motionless once your head hits the pillow, but inside your skull, millions of neurons are busily firing away, often in synchronized bursts that send waves of electricity sweeping across the surface of your brain.

What all this neural activity accomplishes, if anything, is a mystery, and part of the even larger puzzle of why we sleep. One idea that has gained favor in recent years is that during certain stages of sleep, the brain replays experiences from the day to strengthen the memory of what happened. Support for this notion comes from a variety of experiments with rodents and people, including a new study in this issue suggesting that boosting such memory-related activity in the sleeping brain can improve memory performance in humans.

Some researchers suspect that replaying the recent past during sleep is more than a memory aid. This review may also give the brain a chance to catch important information it missed the first time around. "There's more and more evidence accruing that what we're seeing during sleep is not just a strengthening of memories," says Robert Stickgold, a neuroscientist at Harvard Medical School in Boston. "What the brain is really trying to do is extract meaning."

Such ideas aren't universally accepted, however. One new and controversial hypothesis suggests that memory and other cognitive benefits are merely side effects of the true function of sleep: dialing down synapses that have gotten overexcited by daytime activity. And some skeptics aren't convinced that sleep has anything to do with memory at all. Given all the uncertainties, researchers say the quest to understand the sleeping brain is just beginning. But they're already finding fascinating clues about what happens when we're off in the Land of Nod.

Let me see that again

The first experimental evidence that the brain replays recent experiences during sleep came from experiments with rats begun in the 1990s by neuroscientist Bruce McNaughton of the University of Arizona, Tucson, and his graduate student Matthew Wilson. McNaughton and Wilson recorded the electrical activity of neurons called place cells in the rat hippocampus. These neurons have an affinity for particular locations, so that as a rat runs around its enclosure, a given place cell fires each time the rodent passes through that cell's favorite spot. Because individual place cells respond only to a specific location, each time a rat takes a different route, a different sequence of place cells fires. Subsequent studies found that sequences of place cell firing that occur as a rat explores a new environment are replayed the next time the rat dozes, as if the animal retraces its steps during sleep.

Humans may do something similar. In 2004, a research team led by Pierre Maquet of the University of Liege, Belgium, used positron emission tomography (PET) to monitor brain activity in men playing a virtual-reality game in which they learned to navigate through a virtual town (actually a scene from the shoot-'em-up video game Duke Nukem). The same regions of the hippocampus that revved up when the subjects explored the virtual environment also became active when the men slipped into slow-wave sleep that night. This sleep stage is often considered the deepest. Slow-wave sleepers are hard to rouse. During this sleep stage, electroencephalogram (EEG) traces show waves of electrical activity throughout the brain that peak about once a second. PET scans revealed that the more intense hippocampal activity a volunteer had during slow-wave sleep, the better he performed the next day.

CREDIT: BJÖRN RASCH

when he sprinted through the virtual town to find certain objects as quickly as possible. Maquet and colleagues reported in the 28 October 2004 issue of *Neuron*.

Maquet's findings showed a nice correlation between neural activity during sleep and subsequent memory performance, says Jan Born, a neuroscientist at the University of Lübeck in Germany. The natural next step, Born says, was to see whether artificially boosting memory-related neural activity during sleep could improve memory performance. On page 1426, Born's team describes an attempt to do just that.

The researchers had volunteers play a video version of the card game Memory (also known as Concentration), in which they had to learn and remember the locations of pairs of cards bearing the same image in a group of 30 cards. Each matched pair flashed on the screen for a few seconds, one at a time, with all the other cards facing down. After the volunteers had seen the locations of all the pairs, the researchers tested the subjects' recall by turning one of the 30 cards face up and asking them to find its match. The researchers then used EEG electrodes to monitor the volunteers' brain activity while they slept.

Once the volunteers entered slow-wave sleep, the researchers released into each person's room a puff of rose-scented odor. They'd previously given some of the subjects a whiff of rose during their initial training session with the cards, reasoning that the odor would reactivate memories of the training session in these subjects without waking them. Indeed, functional magnetic resonance imaging (fMRI) scans in sleeping subjects revealed that the odor activated the hippocampus in those who had experienced it previously, even though the EEG showed no disruptions in the subjects' slumber. Although they didn't remember smelling roses in their sleep, the subjects who got the fragrant prompt remembered the matched pairs better the next day, getting 97% correct compared to 86% for subjects who'd received no odor while sleeping. Subjects who got the rose odor either while awake or while in REM sleep, on the other hand, showed no memory boost, nor did presenting the odor during slow-wave sleep help subjects who hadn't been exposed to rose during the training session. "It's the first study to really demonstrate that one can influence memory with stimuli that explicitly activate the hippocampus during sleep," says Wilson, now an associate professor at the Massachusetts Institute of Technology in Cambridge.

Born's findings fit with a popular view of how the brain files memories away for long-term storage, a process neuroscientists call memory consolidation. According to this hypothesis, memories are first encoded by the hippocampus and later—perhaps in a matter of hours or days—transferred for long-term storage to the cerebral cortex, or neocortex. Several lines of evidence support this scenario, among them the observation that many people who suffer amnesia following damage to the hippocampus can still recall events and facts learned prior to their injury even though they're unable to form new memories. In such patients, old memories must reside somewhere other than the hippocampus. How the brain might transfer memories from the hippocampus to the neocortex isn't known, but it's assumed to require some kind of back-and-forth communication between the two structures.

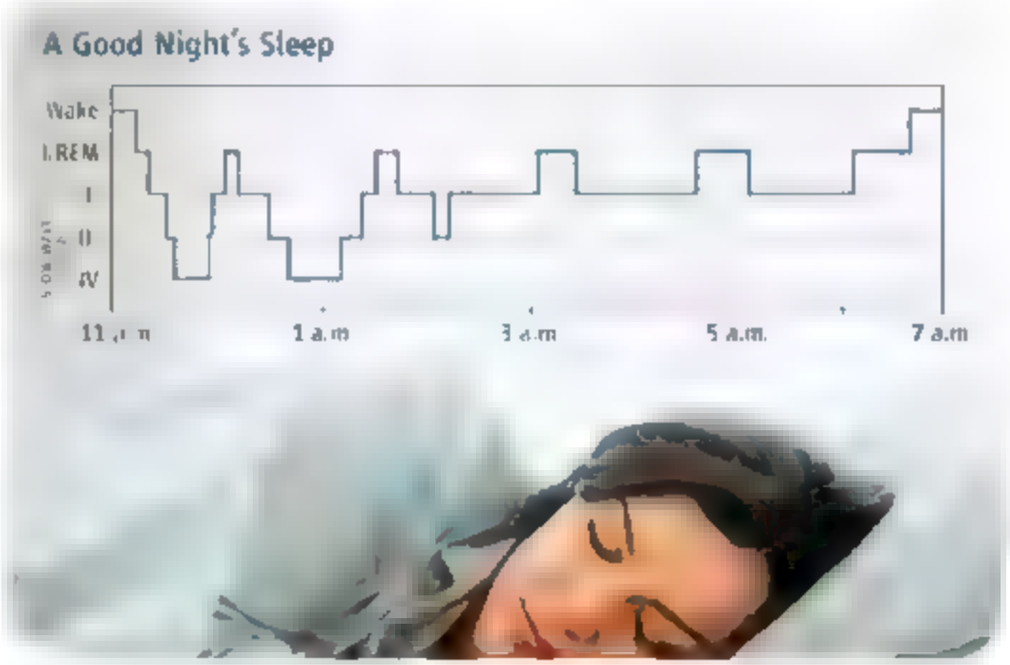

CREDIT: JOSE LUIS PELAEZ INC./GETTY IMAGES

A study by Wilson and postdoctoral fellow Daoyun Ji published in the January issue of *Nature Neuroscience* supports this idea. Wilson and Ji found that, much like hippocampal place cells, neurons in the visual cortex of rats replay firing sequences during slow-wave sleep that match their activity during the rats' daytime maze running. Moreover, the scientists found that the replay in the visual cortex happens in lockstep with replay in the hippocampus. "It's the first time we see sequences both in the hippocampus and the neocortex and their coordination in time," says Maquet.

More than memory

Beyond simply fortifying memories, the brain may be sifting through recent experiences during sleep to identify rules about cause and effect or other useful patterns, some researchers suspect. One of the first hints of this phenomenon came from a 2004 *Nature* paper by Born's group. They reported that people playing a game that required manipulating strings of numbers were more than twice as likely to have a flash of insight that enabled them to solve the problem more quickly after a night of sleep than after a similar time of wakefulness.

More recently, at a sleep research meeting last month at the Salk Institute for Biological Studies, Stickgold presented findings suggesting that people find missing connections while they sleep. His group had volunteers play a card game in which they attempted to predict whether it would "rain" based on cards the researchers had shown them. The game was rigged so that the card with the diamonds, for instance, was followed by sunny weather 80% of the time. Each card had its own rule, but the volunteers did not know the rules even existed. As expected, they did no better than chance at first. But after 200 predictions, their success rates improved. When the subjects came back 12 hours later to try again, they had improved even more—but those who'd slept improved about 10% more than those who hadn't. Although it's a modest improvement, "there's a growing sense that there's active learning during sleep," says Wilson.

There's also increasing evidence that different stages of sleep are involved in consolidating different kinds of memory, says Matthew Walker, a neuroscientist at Harvard Medical School. Spatial memories, like those formed by playing Memory or by navigating through a maze or virtual town, seem to be consolidated during slow-wave sleep. The same appears to be true for declarative memories, which involve remembering facts—but not necessarily other kinds of memory. Some studies have found that the brain processes memories with a

strong emotional component during rapid-eye-movement (REM) sleep and processes memory for motor skills, such as tapping out a difficult sequence on a keyboard, during stage 2 and REM sleep (see diagram, p. 1361). Why this division of labor exists is a puzzle, but Walker and others speculate that the different physiological and neurochemical milieus associated with different sleep stages may favor certain kinds of neural plasticity.

Some researchers point out, however, that the literature on which sleep stages relate to which types of memory is peppered with contradictions. "There is inconsistency here, and someone has to be wrong," says Jerome Siegel, a neuroscientist at the University of California, Los Angeles. Stickgold and other proponents of a sleep-memory link acknowledge that they face many unresolved issues about the role of sleep in memory consolidation. "There are massive questions remaining about how extensive it is, how important it is, exactly which stages of sleep affect which types of memory," Stickgold says.

Another wide-open issue is whether there's a link between dreaming and memory-related neural activity during sleep. The kind of direct replay of recent experience suggested by Wilson's work, for example, doesn't seem to be the stuff of dreams. Stickgold's group has found that only 1% to 2% of episodes from dreams reflect events from the previous day. If dreams don't directly reflect the memory-consolidation process, what do they reflect? "We're in no man's land," says Walker.

Another hypothesis

Not everyone is onboard with the idea that brain activity during sleep is primarily about replaying recent experiences. Giulio Tononi, a neuroscientist at the University of Wisconsin, Madison, has recently advanced a very different hypothesis. He proposes that the purpose of sleep, at least as far as the brain is concerned, is to weaken neural connections throughout the brain.

In Tononi's view, the synaptic connections between neurons get progressively stronger during the day as a result of long-term potentiation (LTP), a physiological process by which neurons that fire at the same time strengthen their connections with each other. Most neuroscientists consider LTP a major mechanism of neural plasticity—and therefore of learning and memory (*Science*, 22 December 2006, p. 1854). Yet a day's worth of LTP can be too much of a good thing, Tononi contends. Stronger synapses increase the brain's energy needs—a serious concern for an energy-hogging organ that already accounts for 20% of a person's metabolism. Stronger synapses are also bigger, taking up precious space. And finally, too much LTP may saturate synapses, leaving them unable to get any stronger when the brain needs to learn something new.

Sleep restores homeostasis by ratcheting down synaptic strengths, Tononi argues. It's a far more important service than providing a modest boost in memory performance, he says. "Sleep is too high a price to pay for the 15% improvement we see in some things," Tononi says. "I think it does something much more fundamental to the neuron. It's the price we pay for plasticity." How might sleep reset synaptic strengths? One clue, Tononi says, comes from a study by Swiss researchers published in the 15 January *Journal of Physiology*. They reported that stimulating slices of rat brain to cause once-per-second bursts of neural firing induces a type of synaptic weakening called long-term depression (LTD). Tononi thinks it's no coincidence that the coordinated neural firing during slow-wave sleep happens at this same frequency. The slow waves, one per second, could induce LTD to dial down synapses that got too strong during the day.

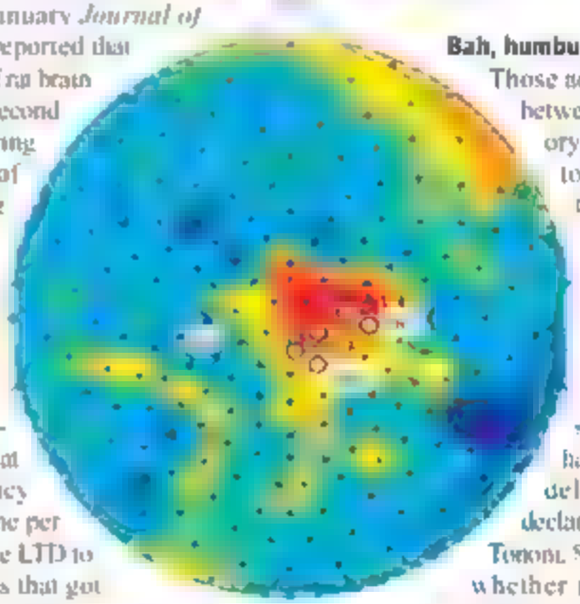

Hot spot. EEG recordings during sleep indicate peak slow-wave activity (red) in brain regions involved in daytime learning.

CREDIT: HUBER ET AL., NATURE 430, 79 (2004)

Other evidence comes from human studies, including one from Tononi's group that found that slow waves measured by EEG in sleeping subjects were most intense in brain regions involved in learning an arm-movement task the previous day. That's consistent with the idea that the slow waves happen where they're needed most to restore synaptic homeostasis. Conversely, immobilizing a person's arm in a sling decreases slow-wave intensity in arm-related areas of neocortex the following night. Tononi and colleagues reported in the September 2006 issue of *Nature Neuroscience*.

Tononi also points to a paper Walker's group published in *Nature Neuroscience* in January. Those researchers found that undergraduate volunteers deprived of a night's sleep were less able than well-rested peers to learn new word pairs the next day. (fMRI scans suggested that the deficit was specifically related to memory—brain regions that modify attention and alertness functioned normally in the sleep-deprived undergrads.) With no slow-wave sleep to dampen their synapses, the subjects were unable to learn as well the next day, Tononi says.

Tononi's view of the role of sleep is "an interesting and intuitive idea," Walker says. He also thinks it's not necessarily incompatible with the notion that sleep enhances memory by strengthening the underlying synapses, as proponents of the memory-replay scenario have generally assumed. "I think they could act not just independently but synergistically."

But not everyone is ready to embrace Tononi's proposal. Says Stickgold, "It's an elegant hypothesis that doesn't have a lot of data behind it."

Bah, humbug

Those advancing the links between sleep and memory have other hurdles to overcome. One of the most disconcerting inconsistencies in the sleep-memory literature, Siegel explains, is that studies of total sleep deprivation have failed to find a deleterious effect on declarative memory. Like Tononi, Siegel also questions whether relatively modest memory benefits offer enough of an adaptive advantage to compensate for being unresponsive for hours a day. "I'm just not convinced that there is any connection at all" between sleep and memory, Siegel says. He favors the idea that sleep evolved to help animals conserve energy for their entire bodies and to prevent them from being active at times when they're less likely to find food and more likely to be eaten.

To be sure, memory is not the only function of sleep, counters Stickgold, but the evidence that it is one function of sleep, at least in mammals, is too great to ignore. Once sleep evolved, he says, evolution figured out how to make that downtime as productive as possible. Stickgold also argues that the modest improvements typically seen in sleep-memory studies are nothing to yawn at. He is fond of pointing out that a 15% gap in performance is the difference between winning the Boston Marathon and coming in 3000th. In competitive circumstances, small advantages can make a big difference. But whatever you do, try not to lose any sleep over it.

–GREG MILLER

LETTERS

edited by Etta Kavanagh

Did the Olmec Know How to Write?

IN THEIR RESEARCH ARTICLE "EARLIEST WRITING IN AMERICA" (15 Sept. 2006, p. 1610), Ma. del Carmen Rodríguez Martínez *et al.* suggest that the inscribed "Cascajal block" is the first discovery of Olmec writing. Although we agree with the authors that it is possible that the Olmec did write, we have strong reservations concerning this artifact and its incised motifs.

1) Being found by persons unknown in a pile of bulldozer debris does not constitute reliable provenance.

2) The block does not fit any known category of Mesoamerican inscribed artifact; it is not a stela, celt, sculpture, or jewel. The heartland Olmec did not build in stone; therefore, it cannot be an architectural inscription. Indeed, there are many hundreds of similar serpentine blocks known at La Venta that were used as basal ornament on earthen platforms and in the buried pavements, but not a single one of these has engraving or relief carving. The authors' musings about the block being used for practice and repeatedly erased (resulting in a concave surface) are farfetched.

3) Known Mesoamerican writing systems are written either vertically or linearly (or a combination of the two, as in Maya glyph blocks), they do not randomly "bunch" glyphs as on the Cascajal block [e.f. (*1*)].

4) Many of the so-called glyphs replicate decorative motifs found on a wide range of largely unprovenanced (i.e., their authenticity is not proven, nor can it be proved) small-scale artifacts. None of these motifs in their original context has been identified as a form of writing. For example, "glyph" # 2 24 38 52 is found as part of the headdress assemblage on a number of the celts (nos. 116, 117, 118, 119) reproduced in *Olmec Art of Ancient Mexico* (2); "glyph" # 28 58 is found on another celt (no. 114), and "glyph" # 4 is inscribed on a stone figure (no. 47) again in the same catalog.

5) What we can only describe as the "coome" glyph (# 1 23 50) fits no known category of Mesoamerican glyph and, together with the context of the discovery, strongly suggests a practical joke.

KAREN O. BRUHNS[1] AND NANCY L. KELKER[2]

[1]San Francisco State University, San Francisco, CA 94132, USA. E-mail: kbruhns@sfsu.edu [2]Middle Tennessee State University, Murfreesboro, TN 37132, USA. E-mail: nkelker@mtsu.edu

References

1. J. Marcus, *Mesoamerican Writing Systems: Propaganda, Myth, and History in Four Ancient American Civilizations* (Princeton Univ. Press, Princeton, NJ, 1992).
2. E. P. Benson, E. M. de la Fuente, *Olmec Art of Ancient Mexico* (National Gallery of Art, Washington, DC, 1996).

The Cascajal block.

CREDIT: RODRÍGUEZ MARTÍNEZ ET AL.

Response

WE THANK BRUHNS AND KELKER for articulating several issues that others have raised concerning the Cascajal block and for providing us the opportunity to lay them to rest.

1) The provenance of the block is what it is, reported by monarchaeologists but still fixed to an area of a few square meters within a known archaeological site in Veracruz, Mexico. Many other bona fide examples of ancient writing have even less secure find spots, including every known example of Mesoamerica's Isthmian Script and Egypt's Rosetta Stone. Such objects will continue to appear in the future, and each will require careful study for evidence of reliability. We have done this to the extent of our ability with the Cascajal block and stand by our considered and, to most scholars, valid assessment that it is a key addition to the corpus of inscriptions in Mesoamerica.

2) The authors claim that "[t]he heartland Olmec did not build in stone; therefore, it cannot be an architectural inscription." Then, in their next sentence, they cite precisely such architectural ornaments at the Olmec site of La Venta. We now suspect that the block may have served such a function. Such texts, especially from coastal Veracruz and the Maya region, characteristically are executed in shallow lines. Indeed, the celebrated La Mojarra Stela 1, found in circumstances much like those of the Cascajal block, was housed in the Museo de Antropología, Xalapa, for more than a year before anyone noticed the more than 500 glyphs on its face. It took some further time to see that an additional text appeared on its side, this on a sculpture under exceptionally thorough scrutiny (*1*). Therefore, we would not be surprised to learn that other previously discovered examples went unnoticed.

3) The signs form purposeful sequences; they do not "randomly 'bunch,'" as Bruhns and Kelker assert. The patterns in the Cascajal text are spelled out carefully in our paper.

4) The block contains signs found on objects with provenance and others that lack it. Some of the latter have been known since the 19th century (i.e., the "Humboldt Celt") (*2*). One previously unknown sign (glyph 19) appeared years after the discovery of the block in a secure archaeological context at Canton Corralito, Chiapas, Mexico (*3*). All known hieroglyphic systems in the world relate to pre-existing iconography or codified symbolism; new signs appear when warranted by scribal needs. Any hieroglyphic

system that deviated from local iconography would be not only unique but, indeed, an inexplicable phenomenon.

5. If the "insect glyph" was a practical joke, the jokester was an Olmec. The motif is shown three-dimensionally in the diminutive Monument 43 at San Lorenzo, discovered and excavated by one of us (Coe) in 1966 and published by Coe and Diehl in 1980 (*4*).

We reject the author's specific criticisms and their implicit claim that the block is a modern forgery. However, we appreciate the fact that such challenges are the essence of scientific enquiry and that they eventually lead to truth. We still affirm that the Cascajal block is the oldest example of writing in the New World and among the most important finds ever made in Mesoamerica.

MA. DEL CARMEN RODRIGUEZ MARTINEZ,[1] PONCIANO ORTÍZ CEBALLOS,[2] MICHAEL D. COE,[3] RICHARD A. DIEHL,[4] STEPHEN D. HOUSTON,[5] KARL A. TAUBE,[6] ALFREDO DELGADO CALDERÓN[1]

[1]Centro del Instituto Nacional de Antropología e Historia, Benito Juárez Numero 425 431, Veracruz, Mexico. [2]Instituto de Antropología de La Universidad Veracruzana, Juárez Numero 70, Xalapa, Veracruz, Mexico. [3]376 Ronan Street, New Haven, CT 06511, USA. [4]Department of Anthropology, University of Alabama, Tuscaloosa, AL 35487, USA. [5]Department of Anthropology, Brown University, Providence, RI 02912, USA. [6]Department of Anthropology, University of California Riverside, Riverside, CA 92521, USA.

References

1. J. S. Justeson, T. Kaufmann, *Science* **277**, 207 (1997).
2. A. Peñafiel, *Monumentos de Arte Mexicano Antiguo*, Vol. 1 (Asher, Berlin, 1890).
3. D. Cheetham, J. E. Clark, *XIX Simposio de Investigaciones Arqueológicas en Guatemala, 2005*, J. P. Laporte, B. Arroyo, H. E. Mejía, Eds. (Ministerio de Cultura y Deportes, Guatemala City, Guatemala, 2006).
4. M. D. Coe, R. A. Diehl, *In the Land of the Olmec*, Vol. 1 (Univ. of Texas Press, Austin, TX, 1980).

Hurricanes Not the Key to a Sustainable Coast

IN THEIR DISCUSSION OF THE SIGNIFICANCE of wetland sedimentation during Hurricanes Rita and Katrina, R. E. Turner and co-authors concluded that "riverine sources bring relatively trivial amounts of inorganic sediments into the marsh" ("Wetland sedimentation from Hurricanes Katrina and Rita," Reports, 20 Oct. 2006, p. 449). Although this new study adds to the body of knowledge concerning the role of tropical storms in sediment redistribution, the authors' conclusion about the unimportance of the Mississippi River in delivering sediment to the coast defies all that we know about deltas and their sustainability. The authors also do not mention that although some marshes received sediments, a net total of 562 km² of coastal marshes, natural levee ridges, and barrier islands was converted to open water during the two hurricanes (*1*, *2*).

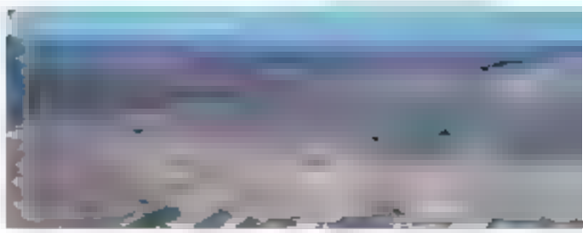

Sand overwash on the former location of the coastal community of Holly Beach, LA (photo taken 18 November 2005 by R. E. Turner).

CREDIT: TURNER ET AL.

Turner *et al.* vaguely refer to the sediment deposited by the two hurricanes as having arrived "from offshore." Resuspension and transport of sediments from offshore and delta-plain sources by storms are among the mechanisms by which sediments originally supplied by rivers are distributed across the Mississippi and other deltas

(3–6). Their samples, mostly taken many kilometers inland, were not analyzed in a manner that would enable them to determine the source (i.e., offshore or inshore water bottoms, barrier islands, or pre-existing marshes).

The comparison of the sediment benefits of hurricanes with the benefits of the Caernarvon Freshwater Diversion structure by Turner *et al.* was out of context, since this structure was designed in the mid-1980s to convey fresh water (not sediments), to manage salinities, and to benefit oysters. Without major sediment contributions by the river, sediments redistributed by storms are the dominant sediment source for wetlands. Contrary to the conclusions of Turner *et al.*, two recent scientific panels have suggested that more aggressive diversion of the Mississippi River water and sediments is needed to build and maintain land in coastal Louisiana (*7*, *8*).

VIRGINIA BURKETT,[1] C. G. GROAT,[2] DENISE REED[3]

[1]U.S. Geological Survey, 700 Cajundome Boulevard, Lafayette, LA 71449, USA. [2]Jackson School of Geosciences, University of Texas, 1 University Station C1100, Austin, TX 78712–0254, USA. [3]Department of Earth and Environmental Science, University of New Orleans, New Orleans, LA 70148, USA.

References and Notes

1. Preliminary estimates of net wetland losses after Hurricanes Katrina and Rita were released by the U.S. Geological Survey on 1 Nov. 2005 (http://www.nwrc.usgs.gov/releases/pr05_007.htm)
2. J. A. Barras, *U.S. Geol. Surv. Open-File Rep. 06-1274*, 2006 (2006).
3. E. Uchupi, in *The Ocean Basins and Margins, Vol. 3, Physiography of the Gulf of Mexico and Caribbean Sea*, A. E. M. Nairn, F. G. Stehli, Eds. (Plenum Press, New York, 1975).
4. D. J. Reed, *Estuaries* **12**, 222 (1989).
5. L. D. Wright, C. A. Nittrouer, *Estuaries* **18**, 494 (1995).
6. J. M. Coleman, H. H. Roberts, G. W. Stone, *J. Coastal Res.* **14**, 698 (1998).
7. EFGC, Report of the Technical Group, Envisioning the Future of the Gulf Coast (futureofthegulfcoast.org/files/finalreport.pdf) (2006).
8. National Research Council, *Drowning Louisiana's New Map, Addressing Land Loss in Coastal Louisiana* (National Academies Press, Washington, DC, 2006), pp. 115–138.

Response

BURKETT *ET AL.* ACKNOWLEDGE THAT OFFshore sediments provide coastal marshes with inorganic sediments and that our quantification of these sediments "adds to the body of knowledge concerning the role of tropical storms in sediment redistribution." They clearly realize that we made comparisons of the quantity of hurricane-derived inorganic sediments with the amount of inorganic sediments flowing over the natural levees of an unconfined channel and through crevasses in the constructed levees, but not at the river mouth. They take us to task for minimizing the contributions of river divers on to maintaining wetland coasts, which is an approach they favor, and for ignoring wetland loss caused by hurricanes. They also mention that two recent panels endorse river diversions.

We made our comparisons about sediment delivery because it is part of building a sediment budget for this coast. There are published estimates available and various management documents that highlight sediment introductions via diversions as a positive attribute (*1*). We did not examine the significant hurricane-induced marsh to open water conversions, which may not be permanent (*2*), because that was not our research objective.

We offered a hypothesis, not a conclusion, that these new sediments came from the shallow water zone immediately offshore of the deposition site. The Chenier Plain in the western half of the state received about 50% of posthurri-

cane sediment deposition, it has no large rivers or large estuarine bays to act as a between-hurricane sediment storage site and the newly deposited sediments at the oceanic shoreline were mostly sands. Burkett *et al.* offer no alternative hypothesis for the newly deposited Chenier Plain sediment sources. Surely the other 50% deposited on the deltaic plain is partially from offshore sources.

We did not, and do not, make a recommendation about building river diversions. There are many factors influencing such management choices, including scientific analyses and sociopolitical aspects. We trust that reputable science panels and insightful administrators might wish to receive, not exclude, new information. For example, we agree with Burkett *et al.* that salinity control at the Caernarvon diversion is a design objective meant to enhance oyster yields. Would a science panel not consider new information indicating that oyster yields in the Gulf of Mexico will be diminished with additional freshwater introductions (*1*)?

Building a more robust sediment budget for these coastal wetlands can be part of the process of making more informed decisions. We provided a field-based quantification of the new sediments deposited during these two hurricanes. Use these data and constructively critique the methods, but please don't fear the consequences about conclusions not made.

R. EUGENE TURNER,[1] JOSEPH J. BAUSTIAN,[1] ERICK M. SWENSON,[1] JENNIFER S. SPICER[2]

[1]School of the Coast and Environment, Louisiana State University, Baton Rouge, LA 70803, USA. [2]North Inlet-Winyah Bay National Estuarine Research Reserve, Post Office Box 1630, Georgetown, SC 29442, USA.

References

1. U.S. COE Caernarvon Fact Sheet (1998) (http://www.mvn.usace.army.mil/pao/caernarvon/caernarvon.htm).
2. J. A. Barras, *U.S. Geol. Surv. Open-File Rep.* **2006**, 1274 (2006).
3. R. E. Turner, *Estuaries Coasts* **29**, 345 (2006).

Letters to the Editor

Letters (~300 words) discussing material published in *Science* in the previous 3 months or issues of general interest may be submitted through the Web (www.submit2science.org) or by regular mail (1200 New York Ave., NW, Washington, DC 20005, USA). Letters are not acknowledged upon receipt, nor are authors generally consulted before publication. Whether published in full or in part, letters are subject to editing for clarity and space.

COMPUTERS

From *Whole Earth* to the Whole Web

Henry Lieberman

We're pretty damn lucky we got the Internet we did: a worldwide network in which almost anybody can read, publish, and program pretty much anything. It didn't have to turn out that way. It could have been dominated by a few corporations, spoon-feeding junk-food media to the masses, just like television. Or balkanized communications providers could have saddled users with deceptive charging schemes and stifled technical innovation, just like cell phones at one slice through this marvelous story. Unlike many other histories that focus on the technical innovators—the Vint Cerfs, the Tim Berners-Lees, the Alan Kays, the Marvin Minskys—this account focuses on a key player whose role was making the counterculture-cyberculture connection: Stewart Brand. Brand's contribution was reporting on this phenomenon, theorizing about it, popularizing it, cheerleading for it, and organizing, networking, and providing resources for it. Brand articulated the unspoken consensus values of the communities. It's hard to say exactly what he did, but everybody knew him, and that sure helped.

Though the book has lots of personal details of Brand's life, it is not a biography. Rather, it focuses on events that swirl around him. It traces his involvement with 1960s communes and conceptual art communities. The *Whole Earth Catalog* and magazines served as a kind of primitive "hard-copy Web" of resources that reflected the common values of both communities and led to *Wired*. The WELL, an early message board system, was an influential example, attracting both cyberculture and counterculture participants.

That we happened to get such an open network was a miracle. But it wasn't an accident. The technical community that built today's digital infrastructure did so around a certain set of cultural values, among them openness, sharing, personal expression, and innovation. These were core values of the early digital pioneers (the hackers), embodied in what we proudly call the "hacker ethic." Today we take the digital revolution for granted and seldom appreciate to what extent these values were sparked by the 1960s counterculture, which preceded the digital revolution. countercultures begat cyberculture.

Because of the happy coincidence that the corporate and bureaucratic establishments of the time understood digital technology so poorly, the hackers were able to pull off the revolution before the bureaucracy knew what hit them. Like the fall of communism, it happened so fast that we haven't yet really taken the time to fully celebrate the victory and examine how it happened.

Fred Turner's fascinating *From Counterculture to Cyberculture* gives us a detailed look

The reviewer is at the MIT Media Laboratory, Cambridge, MA 02139, USA. E-mail: lieber@media.mit.edu

Brand's Global Business Network, a consulting company, tried to make countercultural and cybercultural ideas accessible to high-level corporate planners.

The great thing about this book is that Turner (a former journalist now in the Department of Communication, Stanford University) really took the time to sweat the details. There are a myriad of fascinating little historical details that he dug up that will surprise and enlighten even the key players in the drama who pick up this book. He doesn't always get things right, though. I won't quibble with various inaccuracies from my personal knowledge, but only say that it shouldn't be the only book you read on this subject. Sometimes Turner's account has that not-wrong-but-not-quite-the-whole-story feel of a tourist sharing cultural perceptions after reading a guidebook and a week's trip.

First of all, go back to at least some of the original sources. I fear younger readers might never have seen a *Whole Earth Catalog*. They may not get what the fuss is about just from reading Turner's descriptions and the book's fuzzy reproductions of two pages. Ted Nelson's *Computer Lib/Dream Machines* (*1*), dismissed by Turner in a single sentence, drew the counterculture-cyberculture connection even more explicitly than *Whole Earth*. Steven Levy's *Hackers* (*2*) is also a must. Brand's own short and inspiring "Spacewar: Fanatic Life and Symbolic Death Among the Computer Bums" (*3*) simply says it all.

Whereas Brand is all about enthusiasm, Turner's writing is in the dry and detached style of a sociology thesis. Brand is a terrific writer, but Turner is no Brand. So, bring your own enthusiasm to the book, from your own experience in the cyberculture, the counterculture, or both. But when you're ready to understand how that enthusiasm got us to where we are today, read Turner.

To get you started, I'll leave you with Brand's introduction to the "Fanatic Life" piece (*3*):

> Ready or not, computers are coming to the people.
>
> That's good news, maybe the best since psychedelics. It's way off the track of the "Computers—Threat or Menace?" school of liberal criticism but surprisingly in line with the romantic fantasies of the forefathers of the science such as Norbert Wiener, Warren McCulloch, J. C. R. Licklider, John von Neumann, and Vannevar Bush.
>
> The trend owes its health to an odd array of influences. The youthful fervor and firm disestablishmentarianism of the freaks who design computer science, an astonishingly enlightened research program from the very top of the Defense Department, an unexpected market-flanking movement by the manufacturers of small calculating machines, and an irrepressible midnight phenomenon known as Spacewar.

References

1. T. H. Nelson, *Computer Lib: You Can and Must Understand Computers Now!/Dream Machines: New Freedoms Through Computer Screens—A Minority Report* (T. H. Nelson, Chicago, 1974).
2. S. Levy, *Hackers: Heroes of the Computer Revolution* (Doubleday, Garden City, NY, 1984).
3. S. Brand, *Rolling Stone* 7 December 1972, pp. 50–58.

10.1126/science.1138361

ENDOCRINOLOGY

Many Players in the Concerto of Sex

Sandra Eder

In 1889, the elderly and eminent French physiologist Charles-Edouard Brown-Séquard announced that he had "rejuvenated" himself with injections of testicular extracts of dogs and guinea pigs. This episode marks the slightly embarrassing commencement of modern endocrinology, a beginning that clinical endocrinologist Hans Lisser in 1957 still regarded as "calamitous." (Embarrassing because Brown-Séquard died in 1894, only a few years after his famous self-experiment. His rejuvenation had not been as successful as claimed. Calamitous, because the contempt and ridicule he aroused nearly killed the budding science.) Not surprisingly, this aspect of endocrinological science was never put on the front pages of medical annals.

It does, however, open Chandak Sengoopta's masterly new history of sexual endocrinology, *The Most Secret Quintessence of Life*. Examining a century's scientific and popular fascination with endocrine glands and their effects on the body, Sengoopta (a historian of medicine and science at Birkbeck College, University of London) concludes that in the end, it was all about sex. Sex was seen at the center of life, vitality and energy, and for a time, glands seemed to hold the keys to it. This focus on sex allows Sengoopta to follow multiple historical relationships, particularly those between clinicians and basic scientists and between biomedicine and the wider popular culture.

These relationships were dynamic. In the 1920s, the golden age of the sex glands, most laboratory work was done by clinicians—and driven by clinical agendas. In the 1930s, the clinician's hegemony waned as the star of basic biochemistry research rose. Sengoopta shows, however, that the clinician gained new power as the authenticator of the newly purified hormonal extracts. Throughout, the engineering aspect of scientific medicine shaped research on the sex glands and its clinical applications.

Often, cultural influences were more important than scientific advances in changing clinical practice or values. Take sex antagonism for example. In the 1910s, the renowned Viennese physiologist Eugen Steinach's experiments led him to believe that male and female sex glands were in direct opposition to one another, thus establishing the concept of sexual antagonism. The idea that male and female are binary opposites certainly resonated with cultural gender norms. Sengoopta traces the scientific discourse that undermined Steinach's model of functionally opposed sex glands, such as Dorothy Price and Carl Moore's 1932 announcement of a feedback loop between the pituitary and the gonads and Bernhard Zondek's 1934 discovery of estrogen in the urine of a stallion.

By the 1940s, endocrinologists saw the model as oversimplified: androgens and estrogens were found in both women and men. As Sengoopta aptly puts it, most authorities had, by the end of the thirties, come to regard the gonads as the solo instruments in the concerto of sex, essential but not sufficient in themselves to endow the body with virility or femininity. Other instruments had to work in harmony with them under the baton of a conductor: the enigmatic pituitary gland."

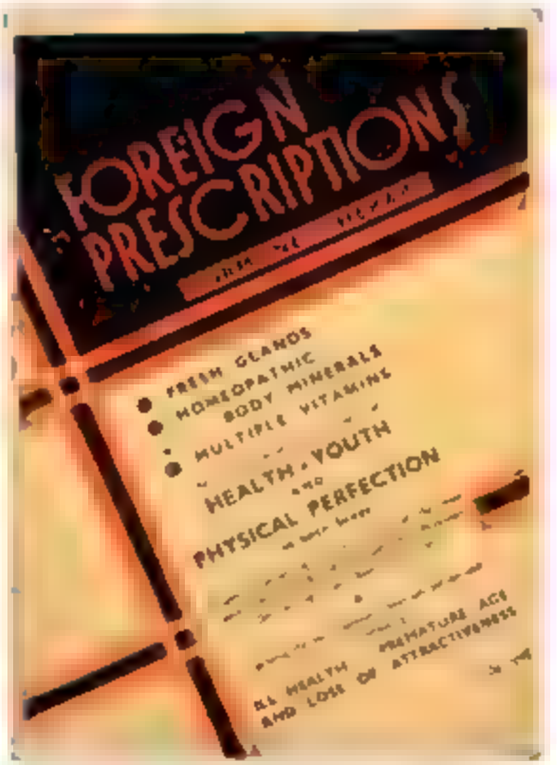

Nevertheless, the old concept of sexual antagonism persisted in the daily practice of the clinic. In the 1940s and 1950s, endocrinologists studied the relation between hormones and cancer. Breast cancer, for example, was thought to be caused by estrogens. If hormones could cause it, could they also cure it? Steered by empirical therapeutic research (guided by clinical results rather than biochemical or physiological findings), clinicians recommended androgenic and antiestrogenic treatments. Sengoopta shows how the reasoning behind these admittedly successful endocrine treatments of breast cancer was driven by an outmoded conception that assumed that the opposite hormone acted antagonistically on the body.

Sengoopta's exploration of the relations among the intersecting forces of science, clinic, and culture deepens our understanding of the development of modern endocrinology. Research on sex glands was shaped by the clinicians' therapeutic optimism and an interest in the physiological engineering of the human body. Even as scientific ideas were disproved and corrected, certain themes and agendas remained central to endocrinological research. The 1940s concern with the relationship between cancer and hormones sounds strikingly modern, considering recent highly televised debates about the connection between hormone replacement therapy for menopausal women and breast cancer. The use of hormones to combat the aging process did not die with Brown-Séquard. It was popularized by Steinach 30 years later, and today anti-aging hormones again capture the public's attention.

Sengoopta takes the science of the past seriously and on its own terms, refusing to evaluate its findings or judge its values by 21st-century standards. At first glance, this might disappoint anyone but historians. After all, why should we read about scientific theories that have been proven wrong? Quite simply, modern science is influenced not only by those theories that are proven correct. It is also profoundly affected by its reputedly wrong, strange, or obscure past. Sometimes "false" scientific theories produce the right treatments. Sometimes they inspire a research tradition that shapes entire disciplines. In *The Most Secret Quintessence of Life*, endocrinology emerges as part of a process, of a dynamic relationship among cultural, clinical, and scientific forces rather than as facts waiting to be discovered.

The reviewer is at the Institute of the History of Medicine, Johns Hopkins University School of Medicine, Baltimore, MD 21205–2169, USA. E-mail: seder1@jhmi.edu

10.1126/science.1139058

CLIMATE CHANGE

CO_2 Arithmetic

Wallace S. Broecker

Strict emission limits will be necessary if the rise in atmospheric carbon dioxide is to be stemmed.

If we are ever to succeed in stopping the buildup of the atmosphere's CO_2 content, we must make a first-order change in the way we view the problem. Most policies that have been discussed, including cap-and-trade systems and the Kyoto treaty, have treated the problem exclusively in terms of incremental reductions in CO_2 emissions. These, however, will not stabilize atmospheric CO_2 levels; they only slow the rate of increase. Instead, to actually stop the increase, we must develop the concept of what might be called a "carbon pie." Currently, for each 4 gigatons (Gt) of fossil carbon burned, the atmosphere's CO_2 content rises about 1 ppm, including deforestation, we now emit about 8 Gt of carbon per year. Further, this four-to-one ratio will only change slowly in the coming decades. Hence if we set a desirable upper limit on the extent to which we allow the CO_2 content of the atmosphere to increase, then this fixes the size of the carbon pie. If, for example, this limit were to be double the preindustrial CO_2 amount (i.e., 560 ppm), then the size of the pie would be 720 Gt of carbon (i.e., $4 \times (560 - 380)$). Were the limit to be set at 450 ppm, the size of the pie would be only 280 Gt.

Once the size of pie has been established, each of the world's nations would be allocated a slice. In an ideal world, the size of these slices would be based on population. In this case, the world's rich countries would get only about 20% of the pie. If the limit agreed upon were 560 ppm, then the rich nations' share would be about 150 Gt. As these countries together currently consume about 6 Gt of fossil carbon per year, if they continued at this pace, their allotment would be consumed in just 25 years. Faced with this limit, each of these rich nations would be forced to rapidly reduce its emissions (see figure, above). Poor nations would be able to sell portions of their pie slice to the rich countries and still have enough left to permit them to industrialize.

If this scenario were to be implemented, I find it highly unlikely that any combination of increased efficiency in energy use, implementation of non–fossil fuel energy sources, and capture of CO_2 produced in coal gasification plants would be capable of meeting the required reduction schedule. An additional element would be necessary. The gap (see figure, right) between actual and allowed emissions would have to be made up either by purchase of CO_2 allocated to poorer nations or by burial of CO_2 captured from the atmosphere. Stemming the rise in CO_2 would require participation of rapidly industrializing nations such as China and India. Under the pie concept, there would be an incentive for them to join for they would have a considerably longer period of time to adjust their CO_2 emissions than rich nations. The sooner such an agreement was put into force, the better the situation would be for these nations. Until this is done, the size of the carbon pie will continue to shrink at a rate of 70 to 80 Gt per decade.

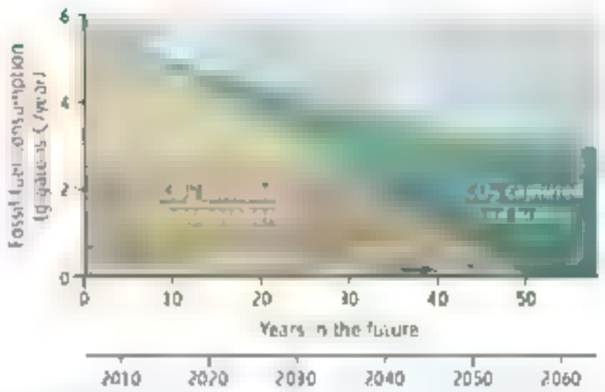

Hypothetical scenario for use by rich nations of their 150-Gt wedge of the carbon pie. As time passes, the excess of fossil-fuel burning over the diminishing permissible emission limit will have to grow, requiring an increase in the amount of CO_2 to be captured and buried.

Because CO_2 sales would serve only as a temporary stopgap, capture of CO_2 from the atmosphere would be necessary. CO_2 capture from the atmosphere is feasible but has yet to be implemented, and faces several technological challenges. If the CO_2 carried by the air streams used to drive wind turbines were to be captured, then on an energy-equivalent basis, the physical dimensions of the CO_2 capture devices would be only 1% of the sweep of the turbines (1). In other words, in a sense air streams carry 100 times more CO_2 than kinetic energy.

In addition to allowing the gap between actual and permissible emissions to be filled, air extraction has other attractive features. (i) It could be done at sites far from population centers and close to the sites of CO_2 storage. (ii) Once the rise in CO_2 had been stemmed, the CO_2 content of the atmosphere could be drawn back down to a level at which the earth's ice caps were stabilized. (iii) It would provide a mechanism by which the thorny issue of compensation for past CO_2 emissions by richer nations could be negotiated.

While there is no question that CO_2 capture from the atmosphere is doable, the cost is still unknown. Capture would be affordable if it caused the price of fossil fuel energy to increase by 10 to 30%. However, a large fraction of the operating cost would be for the purchase of the energy required to accomplish the capture and burial. If the cost of sufficient fossil fuel to generate this energy is too high, then this strategy would be impractical.

The largest of the costs associated with air-capture will be those associated with the release of the CO_2 from the capture material and with the recycling of any chemicals used. As sodium hydroxide, an obvious choice, holds onto CO_2 too tenaciously, a better option would be a material that would be able to pick up CO_2 but would release it more readily. Regardless of what material is to be used, it is absolutely essential that research on capture and sequestration be carried out to determine whether the energy costs can be brought down to an acceptable level. Capture from coal gasification plants should also be implemented.

In the present political climate, any attempt to achieve an agreement on either the size of a carbon pie or its allocation among the world's nations would be difficult. However unless we advance beyond thinking only in terms of conservation and alternate sources and began to think in terms of a carbon pie, we will have no chance to stop the rise in atmospheric CO_2.

The author is at the Lamont-Doherty Earth Observatory of Columbia University, Palisades, NY 10964–8000, USA. E-mail: broecker@ldeo.columbia.edu

References and Notes

1. K. S. Lackner, H.-J. Ziock, P. Grimes, in *Proceedings of the 24th International Conference on Coal Utilization & Fuel Systems*, B. Saikkeelad, Ed. (Coal Technology Association, Clearwater, FL, 1999), pp. 885–896.

2. I thank R. Conrad, G. Heal, and K. S. Lackner for discussions.

10.1126/science.1139585

PHYSICS

Watching Rush Hour in the World of Electrons

An improved imaging technique reveals that electrons in a material can suffer gridlock like cars in a city. This may help researchers understand the mechanism by which currents flow without resistance in superconductors

Jan Zaanen

During the last decade, a revolution has been unfolding in our understanding of the behavior of electrons in solids. Quantum mechanics rules in this microscopic world, and researchers assumed that the smearing and averaging effects of the quantum motions would render this behavior exceedingly simple. In studying high transition temperature (T_c) superconductivity in copper oxides, however, physicists found instead that the electron systems in these materials were exceptionally complex. On page 1380 of this issue, Kohsaka *et al.* (*1*) present an experimental breakthrough, studying the electron system on the surface of copper oxide superconductors by means of scanning tunneling spectroscopy. By cleverly exploiting the effects of the electron interactions, they manage to probe the electron traffic directly. They discover a world of amazing richness, shaped by the quantum motions of the electrons forming complex spatial patterns.

A main effect of strong interactions in the classical world is well known to anybody living in a metropolitan area. When the density of cars becomes too high during rush hour, the traffic comes to a standstill. The same phenomenon should occur with electrons in solids, but the weirdness of quantum physics interferes. Electrons should execute continual quantum motions, and these are so violent in conventional metals and superconductors that the effects of the interactions are washed away. In this regard, the electron systems found in high-T_c superconductors are exceptional. Due to the strong potentials exerted on the electrons by the crystal lattice of copper oxide planes, the quantum motions are hindered to a degree that the electron traffic might even get completely jammed. Copper oxides in their pristine state are thus insulators and, in order to turn them into superconductors, one has to remove electrons by chemical doping (that is, the addition of impurity elements).

The electron motions in these doped cuprates can be viewed as quantized stop-and-go traffic. Stop-and-go traffic in our world tends to develop complex collective patterns, and something similar happens with the electrons. In calculations, physicists found that electrons moving around in the copper oxide planes tend to arrange themselves in one-dimensional "highways" where they move rather easily, surrounded by insulating domains (*2*) and in recent years experimental support was found for the existence of such stripe patterns (*3*). There are indications that they occur in good superconductors as fluctuating patterns (*3*, *4*), while in some cuprates they actually come to a standstill, likely due to imperfections in the crystal lattice having an effect similar to roadwork on our highways. These static stripes are clearly observed in both neutron-scattering (*3*) and resonant x-ray–scattering experiments (*5*), but these experiments only pick up average properties of the stripes. Researchers would like to view them in real space (as opposed to the reciprocal space of diffraction), and this is exactly what Kohsaka *et al.* claim to have accomplished.

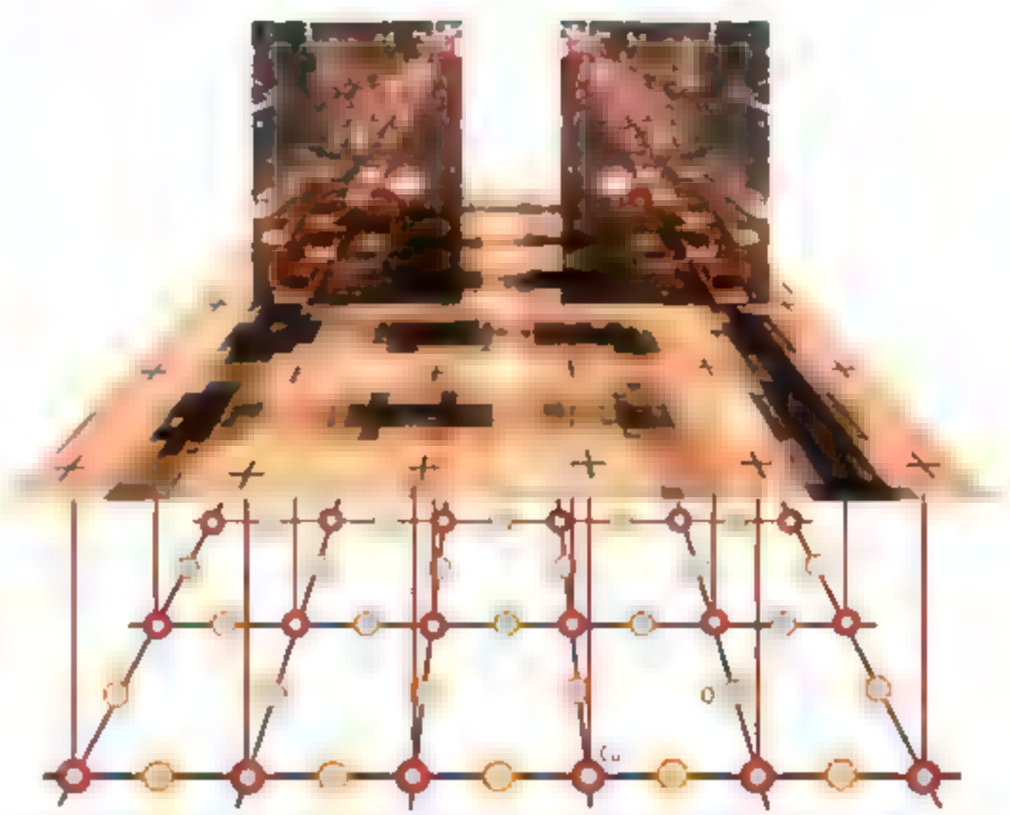

Traffic patterns. Scanning tunneling spectroscopy can directly probe the spatial distributions of the electron motions in the copper oxide layers of a high-T_c superconductor. The patterns can be viewed as a quantum analog of stop-and-go traffic self-organizing into one-dimensional highways where the electron traffic flows relatively freely, separated by severely jammed areas. Locations of copper and oxygen atoms are shown below the image of electron flow.

How do Kohsaka *et al.* manage to probe these electron structures? They use scanning tunneling spectroscopy, a technique that measures the quantum mechanical probability of adding or removing an electron at a specific location and at a given energy. In strongly interacting electron systems like those of the high-T_c superconductors, this probability is very hard to interpret. Kohsaka *et al.* have found a way around this difficulty, based on a clever but simple idea of Anderson and Ong (*6*) that exploits the effects of the strong electron-electron interactions. To understand the essence of the idea, one just needs freeway experience. To merge from the ramp on a freeway with stop-and-go traffic requires patience, whereas it is a relief to spot an exit sign. The same effect occurs in the stop-and-go electron system. It is much easier to remove electrons than to add them. To obtain the overall probability of either

The author is in the Department of Physics, University of Leiden, Leiden 2333, the Netherlands. E-mail: jan@lorentz.leidenuniv.nl

CREDIT: FRANK KRUEGER/UNIVERSITY OF LEIDEN

removing or adding an electron, one has to simply integrate the tunneling current for a positively charged tip (pulling electrons out) and for a negatively charged tip (injecting electrons) over a sizable voltage range at a given location, and by taking the ratio of these quantities one obtains a map of the electron traffic.

As shown in the figure, the bright areas are where the electrons move around relatively freely, and the dark regions are where the electron traffic is jammed. The image has atomic-scale resolution, and it is clear that the mobile electrons have a preference for oxygen over copper. Zooming out to the nanometer scale, one clearly discerns the stripes, the "rivers of charge" separated by insulating regions, while on an even larger field of view these turn into a glassy pattern (*1*), illustrating the sensitivity of the stripes to disorder in the crystal lattice (*3*). There is actually much more going on in these images than is apparent at a first glance, and the million dollar question is whether these subtleties reveal anything about the origin of superconductivity at high T_c. This is still as much a mystery as it was 21 years ago when it was discovered (*7*, *8*). It is believed that, as in normal superconductors, the electrons bind in pairs that subsequently undergo Bose condensation that causes the superconductivity. It might well be that the images obtained by Kohsaka *et al.* are about electron pairs coming to a partial standstill, instead of the electrons themselves. When I stare with my trained eyes at the images I see these pairs everywhere. This might well be an illusion, but by combining the present technique with the energy-resolved spectroscopic information, it should be possible to generate hard evidence for the reality of these pairs.

References

1. Y. Kohsaka *et al.*, *Science* **315**, 1380 (2007); published online 8 February 2007 (10.1126/science.1139584).
2. J. Zaanen, O. Gunnarsson, *Phys. Rev. B* **40**, 7391 (1989).
3. S. A. Kivelson *et al.*, *Rev. Mod. Phys.* **75**, 1201 (2003).
4. J. Zaanen, *Nature* **440**, 1118 (2006).
5. P. Abbamonte *et al.*, *Nature Phys.* **1**, 155 (2005).
6. P. W. Anderson, N. P. Ong, *J. Phys. Chem. Solids* **67**, 1 (2006).
7. Special feature on high T_c superconductivity, *Nature Phys.* **2**, 133 (March 2006).
8. Special Report: High-Temperature Superconductivity Turns 20, *Science* **314**, 1072–1079 (2006).

10.1126/science.1139805

BIOCHEMISTRY

A New Target for Antibiotic Development

The crystal structure of a bacterial membrane protein may guide the development of new antibiotics that interrupt a previously neglected molecular target.

Gerard D. Wright

The discovery and clinical development of penicillin ushered in the modern antibiotic era and stimulated the discovery of the antibiotics in current clinical use. Some 80 years after their discovery, penicillins and related antibiotics (collectively called β-lactams) remain clinically useful. Nevertheless, the remarkable ability of bacteria to develop resistance to β-lactam and other antibiotics means that there is a continued need for new antibiotic targets and new antimicrobial agents. On page 1402 of this issue, Lovering *et al.* (*1*) report the crystal structure of a bifunctional bacterial membrane protein that provides target sites not only for β-lactams but also for new antibiotics.

Penicillin and other β-lactam antibiotics target several bacterial enzymes, collectively termed penicillin-binding proteins (PBPs). PBPs are necessary for the growth and maintenance of the peptidoglycan layer, which forms part of the bacterial cell wall and protects the cell from osmotic stress. Inhibition of peptidoglycan biosynthesis and of its controlled breakdown (for example, to enable partition of the cell wall during cell division) therefore inhibits cell growth. Because the peptidoglycan polymer is ubiquitous and essential to bacterial cells, its assembly and maintenance are targets for many antibiotics (*2*).

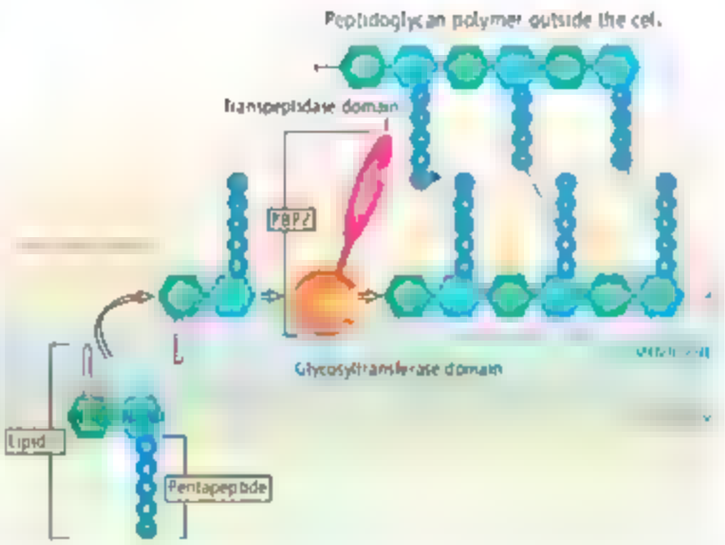

Beyond penicillins. Bacteria use a peptidoglycan layer to protect themselves from osmotic stress. Synthesis of this layer proceeds in several steps. First, lipid II is synthesized in the cell. It is then translocated to the outside where it is added to the peptidoglycan polymer by membrane-associated transglycosylase enzymes. Finally, the polymer is cross-linked via interstrand peptide bonds catalyzed by transpeptidase enzymes. Lovering *et al.* now report the three-dimensional structure of a bifunctional transglycosylase-transpeptidase. The structure should aid development of new antibiotics targeting the transglycosylation domain.

The peptidoglycan consists of a backbone chain of repeating two-sugar units (called NAG and NAM) and a pentapeptide chain bound to each NAM (see the figure). The NAG-NAM-pentapeptide core (called lipid II) is synthesized in the cell and tethered to the cell membrane by a lipid linker. Lipid II is then transferred from the inside of the cell to the outside, where membrane-associated glycosyltransferases assist in grafting it onto the polymer. Transpeptidases catalyze the formation of peptide bonds between polymer strands, thereby making the wall more rigid. These tasks are performed by bifunctional enzymes that contain glycosyltransferase and transpeptidase domains, the latter are sensitive to β-lactams.

Previous studies of the final steps of peptidoglycan biosynthesis have tended to focus on the transpeptidase stage of assembly. However, the inhibition of transpeptidase activity by penicillins is only half the story, and the glycosyltransferase activity of the bifunctional enzymes is an excellent target for the development of new antibiotics (*3*, *4*).

The author is in the Antimicrobial Research Centre, Department of Biochemistry and Biomedical Sciences, DeGroote School of Medicine, McMaster University, Hamilton, Ontario, Canada, L8N 3Z5. E-mail: wrightge@mcmaster.ca

The bifunctional enzymes include PBP1b from *Escherichia coli* and PBP2 from *Staphylococcus aureus*. Despite their importance to bacterial physiology and drug discovery, they have resisted detailed study mainly because these large membrane proteins are difficult to purify, assay, and crystallize (*3*). Lovering *et al.* have now overcome these obstacles and report the first three-dimensional structure of PBP2. As the authors point out, this structure is regarded as the holy grail for antibiotic drug discoverers and bacterial physiologists.

As predicted, the structure is divided into two separate lobes connected by a linker. The C-terminal transpeptidase domain is positioned on the outside of the cell, where it can find its substrate (the pentapeptide chains). This is also where the hydrophilic β-lactam antibiotics can interact with the enzyme and block its function. In contrast, the N-terminal transglycosylase domain interacts with the membrane where its lipid II substrate is located. The structure of this domain does not resemble other known glycosyltransferases. Rather, it is related to bacteriophage λ lysozyme, which cleaves the peptidoglycan glycosyl bond—the reverse reaction of synthesis (*5*).

Lovering *et al.* have also determined the structure of PBP2 in complex with moenomycin, an antibacterial glycosyltransferase inhibitor that is mostly used in animal health (*4*). Moenomycin is one of a very few antibiotics discovered thus far that target the glycosyltransferase reaction in peptidoglycan biosynthesis. The new observations provide a starting point to engineer this antibiotic for use in treating human infection. The glycosyltransferase reaction is a promising antibiotic target, with moenomycin 1000 times as potent as vancomycin, a glycopeptide antibiotic that also targets peptidoglycan synthesis.

The structure of the complex reveals that the glycosyltransferase jaw closes down on the sugar "warhead" of the antibiotic, forming extensive interactions with a number of amino acids and accounting for its tight affinity for the enzymes. The lipid tail of the antibiotic likely directs the warhead of the antibiotic to the membrane for interaction with the target glycosyltransferase. The orientation of the inhibitor in the enzyme active site also answers the important question of whether lipid II is the donor or the acceptor in glycosyl bond formation. The structure is only consistent with the latter.

The three-dimensional structure of PBP2 therefore provides answers to long-standing questions of bacterial biochemistry, physiology, and antibiotic activity. What's next?

We are clearly in need of new antibiotics to overcome the problem of antibiotic resistance and the emergence of new infectious diseases (*6*). A major challenge in the development of new antibiotic agents is the ability to identify new targets and to creatively continue to exploit the collection of proven ones. The structure of PBP2 provides an opportunity to revisit an "old" target with new tools. This is a breakthrough in a field that has been bereft of the means to fully explore peptidoglycan biosynthesis with modern strategies in drug discovery.

References

1. A. L. Lovering, L. De Castro, D. Lim, N. V. Strynadka, *Science* **315**, 1402 (2007).
2. C. T. Walsh, *Antibiotics, Actions, Origins, Resistance* (ASM Press, Washington, DC, 2003).
3. J. Halliday, D. McKeveney, C. Muldoon, P. Rajaratnam, W. Meutermans, *Biochem. Pharmacol.* **71**, 957 (2006).
4. B. Ostash, S. Walker, *Curr. Opin. Chem. Biol.* **9**, 459 (2005).
5. C. Eward, J. Fastrez, J. P. Declercq, *J. Mol. Biol.* **276**, 151 (1998).
6. G. H. Talbot *et al.*, *Clin. Infect. Dis.* **42**, 657 (2006).

10.1126/science.1140374

CELL BIOLOGY

What a Cell Should Know (But May Not)

Normal yeast cells may not know whether DNA replication is complete before starting mitosis. How does the cell cycle progress in an orderly manner?

Ted Weinert

During the normal cell cycle, DNA replication is completed before the cell divides (mitosis). How the cell ensures that mitosis always follows DNA replication is the subject of a study by Torres-Rosell and colleagues on page 1411 of this issue (*1*). Investigators have long known that cellular controls called checkpoints act as surveillance mechanisms to guarantee that each event during the cell cycle is completed before the next one begins (*2*–*4*). But the findings of Torres-Rosell *et al.* suggest that this is not always the case, and pose the heretical possibility that the cell may be blind to whether it is really done with replication before mitosis begins.

A key point is that checkpoints coordinate cell cycle events by detecting errors in chromosome structure. For example, the spindle checkpoint, which is required for proper chromosome segregation, detects chromosome detachment from a cellular structure called the mitotic spindle. DNA damage checkpoints detect broken chromosomes. When activated, either checkpoint blocks mitosis, allowing time for errors to be corrected. Thus, these checkpoints ensure that mitosis takes place only when chromosomes are intact and properly assembled on the spindle.

A similar but distinct problem is how a cell coordinates the completion of DNA replication with the onset of mitosis. The well-known DNA replication checkpoint triggers a delay in mitosis upon detecting damaged or stalled replication forks (DNA regions where replication is taking place) (*5*) (see the figure). However, it may be quite a different task for the cell to determine if normal replication forks have completed their tasks before mitosis. One would predict that such a control must exist because of the likelihood that an occasional replication fork, of the many that are formed (~400 in a budding yeast cell) (*6*), might mistakenly persist late into the cell cycle, up to the time of mitosis. DNA replication occurs during S phase, but late replication might occur at the end of the G_2 phase that follows (see the figure). Such a "DNA replication-completion checkpoint" is considered unique because it would detect a normal structure present at the wrong time. Indeed, Torres-Rosell *et al.* discovered a mutant yeast cell that they argue contains normal replication forks at the wrong time. Despite the presence of the forks, cells proceed into mitosis, with consequential chromosome missegregation. The authors reasonably conclude that normal yeast cells do not contain a DNA replication-completion checkpoint.

Torres-Rosell *et al.* tested the idea of a DNA replication-completion checkpoint by studying the ribosomal DNA (rDNA) locus, which in a budding yeast cell consists of ~150 repeats of rDNA genes in one region of chro-

The author is in the Department of Molecular and Cellular Biology, University of Arizona, Tucson, AZ 85721, USA. E-mail: tweinert@email.arizona.edu

mosome XII. Their test was made possible by virtue of special features of DNA replication at this locus. Each of the 35S genes in the rDNA locus contains a replication fork barrier site, to which binds a protein called Fob1 (7). This site of interaction is located downstream of the highly transcribed 35S rDNA gene and enforces polarity to replication fork movement, that is, replication forks replicate only in the direction of 35S transcription but not in the opposite direction.

By tagging chromosome XII with a green fluorescent protein, the authors observed that the rDNA locus missegregates in cells that express mutant forms of proteins that normally concentrate at the rDNA locus (8). Those proteins—Smc5 and Smc6—belong to a class of molecules called cohesins and condensins that organize chromosome structure (9). The key observation by Torres-Rosell *et al.* is that in yeast cells lacking functional Smc6, DNA replication forks in the rDNA locus persist as cells enter mitosis. And, it is late replication, not the *smc6* mutation per se, that causes the observed chromosome missegregation. When the authors disabled the "stalling" activities of the replication machinery such that replication forks were unimpeded in the rDNA region, chromosome segregation was nearly normal in the *smc6* mutants. Overall then, because a *smc6* mutant cell contains DNA-replication structures that do not block mitosis, it was concluded that a DNA replication–completion checkpoint may not exist.

Is this the last word on the existence of a DNA replication-completion checkpoint? Probably not. Two details about the elegant system used by Torres-Rosell *et al.* may cause concern about the generality of their conclusions. First, it is unclear what fraction of the DNA-replication forks that persist into mitosis resemble "normal" replication structures. This concern stems from the use of the replication fork barrier site–containing locus endemic to the rDNA region. Because of the barrier site, the number and structure of normal forks in the rDNA region in *smc6* mutants at the time of mitosis is also unclear. Second, the use of *smc6* mutants to generate late replication is also of concern. Why this region replicates late in *smc6* mutants is unknown, and there is the nagging possibility that a DNA replication-completion checkpoint requires Smc5 and Smc6 proteins. Recent evidence in the fission yeast *Schizosaccharomyces pombe* suggests that Smc6 and an interacting protein, Rad60, have roles in replication forks and replication-associated checkpoint signaling (*10, 11*). Torres-Rosell *et al.* do show that *smc6* mutants are proficient for DNA damage and replication checkpoints. But the generality of their conclusions must be tempered with their analysis of the locus and mutants that were needed to ask the question.

There is also a report suggesting that a DNA replication-completion checkpoint does exist (*12*). Van Brabant *et al.* constructed a large artificial yeast chromosome that took longer to replicate than the duration of S phase. Cell cycle kinetics indicated that this delayed entry into mitosis. Both Torres-Rosell *et al.* and van Brabant *et al.* crafted special situations to generate late-replication scenarios, raising questions about the generality of their conclusions.

The debate over a DNA replication-completion checkpoint will continue, and until resolved, one can speculate on the consequences of not having such a control. There is the case of mammalian fragile sites, specific regions in chromosomes that replicate late and are prone to break in mitosis (*13*). Perhaps fragile sites break because they contain normal forks late in G_2. Cells enter mitosis anyway because there is no DNA replication-completion checkpoint.

If there is no DNA replication-completion checkpoint, how might a cell make fairly sure, without being certain, that mitosis follows the completion of DNA replication? One idea is that the cell relies on innate timing of mitosis and replication. In this model, as a cell exits G_1 (the growth phase of the cell cycle), it commits to a specific time for replication in S phase and for the beginning of mitosis. Evidence in budding and fission yeasts indicates the existence of a timing mechanism that is independent of DNA replication. Mutant yeast cells that cannot initiate DNA replication exit G_1, but do not subsequently replicate DNA, and yet still enter mitosis as if it were a normal cell cycle (*14, 15*). The cell thus relies on the timing of DNA replication and mitosis to get the job done. If this is the case, what the cell doesn't know may not hurt enough for it to have evolved a mechanism that, as the present work argues, in fact does not exist.

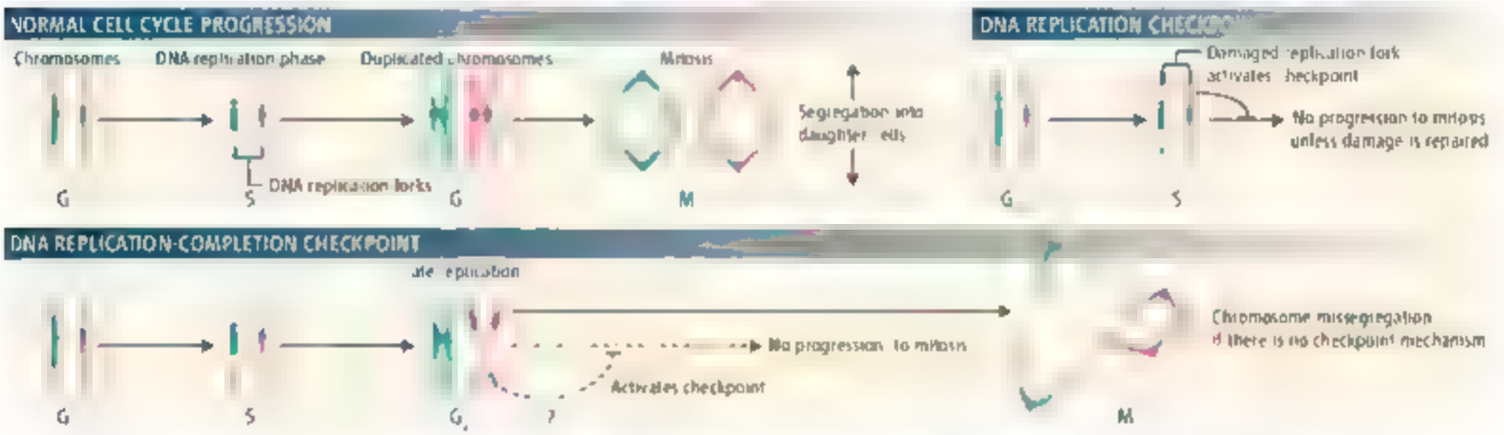

Order, order, order. (Top, left) The cell divides on cycle allows replication of DNA before its segregation into daughter cells. **(Top, right)** The sequence of events is ensured by checkpoints that sense DNA integrity and stalled or damaged replication structures. **(Bottom)** The order may also be ensured by a DNA replication completion checkpoint (dashed line).

References

1. J. Torres-Rosell *et al.*, *Science* **315**, 1411 (2007).
2. L. H. Hartwell, T. A. Weinert, *Science* **246**, 629 (1989).
3. M. B. Kastan, J. Bartek, *Nature* **432**, 316 (2004).
4. D. J. Lew, D. J. Burke, *Annu. Rev. Genet.* **37**, 251 (2003).
5. O. Branzei, M. Foiani, *Curr. Opin. Cell Biol.* **17**, 568 (2005).
6. M. K. Raghuraman *et al.*, *Science* **294**, 115 (2001).
7. S. Lambert, A. M. Carr, *Biochimie* **87**, 591 (2005).
8. J. Torres-Rosell *et al.*, *Nat. Cell Biol.* **7**, 412 (2005).
9. A. Losada, T. Hirano, *Genes Dev.* **19**, 1269 (2005).
10. Y. Miyabe, T. Morishita, T. Hishida, S. Yonei, H. Shinagawa, *Mol. Cell. Biol.* **26**, 343 (2006).
11. E. Ampatzidou, A. Irmisch, M. J. O'Connell, M. Murray, *Mol. Cell. Biol.* **26**, 9387 (2006).
12. A. J. van Brabant, C. D. Buchanan, E. Charboneau, W. L. Fangman, B. J. Brewer, *Mol. Cell* **7**, 705 (2001).
13. M. E. Arlt, A. M. Casper, T. W. Glover, *Cytogenet. Genome Res.* **100**, 92 (2003).
14. J. M. Toyn, A. L. Johnson, L. H. Johnston, *Mol. Cell. Biol.* **15**, 5312 (1995).
15. T. J. Kelly *et al.*, *Cell* **74**, 371 (1993).

10.1126/science.1140759

IMMUNOLOGY

Eating In to Avoid Infection

Caetano Reis e Sousa

Detection of replicating virus involves a cellular process that normally maintains balance between production and turnover of cellular structures.

Viral invasion elicits a quick and powerful immune response by the host organism, designed to limit pathogen spread. The molecular mechanisms that sense viral presence and couple it to the production of cytokines—factors that coordinate immunity—are being rapidly unraveled. On page 1398 of this issue, Lee *et al.* uncover an intriguing new dimension to viral sensing that involves autophagy, the process by which cells normally dispose of effete organelles and proteins to maintain homeostasis (*1*). Through autophagy, the operation of two classes of viral-sensing receptors overlap and are not distinct as previously thought.

Organisms sense unwanted virus through two basic strategies that rely on detecting foreign nucleic acids. One strategy, shared by all nucleated cells, involves host receptors in the cytoplasm that recognize RNA (and probably DNA) from viruses (*2*). When activated, these receptors promote the expression of many genes, including type I interferons (IFN-α β), cytokines that are critical for viral resistance. The other strategy is restricted to fewer cell types, most notably of the immune system. It relies on a subset of receptors of the Toll-like receptor (TLR) family, including TLR3, TLR7, TLR8, and TLR9. These receptors can access the endosomal compartment and sense nucleic acids of viruses that have been engulfed by the host cell through the process of endocytosis (*2*).

The endosomal system can effectively be considered a topological continuation of the extracellular space. In this sense, TLRs present in endosomes are thought to recognize viruses present in the cell's extracellular milieu. This means that, unlike the recognition system that relies on cytoplasmic receptors, the endosomal TLR system can detect virus independently of actual cellular infection—an "exogenous" recognition pathway (see the figure). Indeed, activation of endosomal TLRs by noninfectious inactivated viruses has been observed (*2*). What Lee *et al.* demonstrate is that this exogenous pathway is not the only mechanism by which cells can use TLRs to detect viral presence. The authors noted that for some viruses, such as vesicular stomatitis virus or Sendai virus, infection of murine plasmacytoid dendritic cells, specialized cells of the immune system, elicits more IFN-α production than treatment of the same cells with inactivated, nonreplicating viruses. Yet, the response depends on TLR7, in line with previous observations that plasmacytoid dendritic cells rely heavily on this particular receptor to respond to RNA viruses. As such, TLR7 likely recognizes viral RNA replicating in the cytoplasm, rather than the viral genome acquired through endocytosis. But how can an endosomal receptor gain access to cytoplasmic viral RNAs?

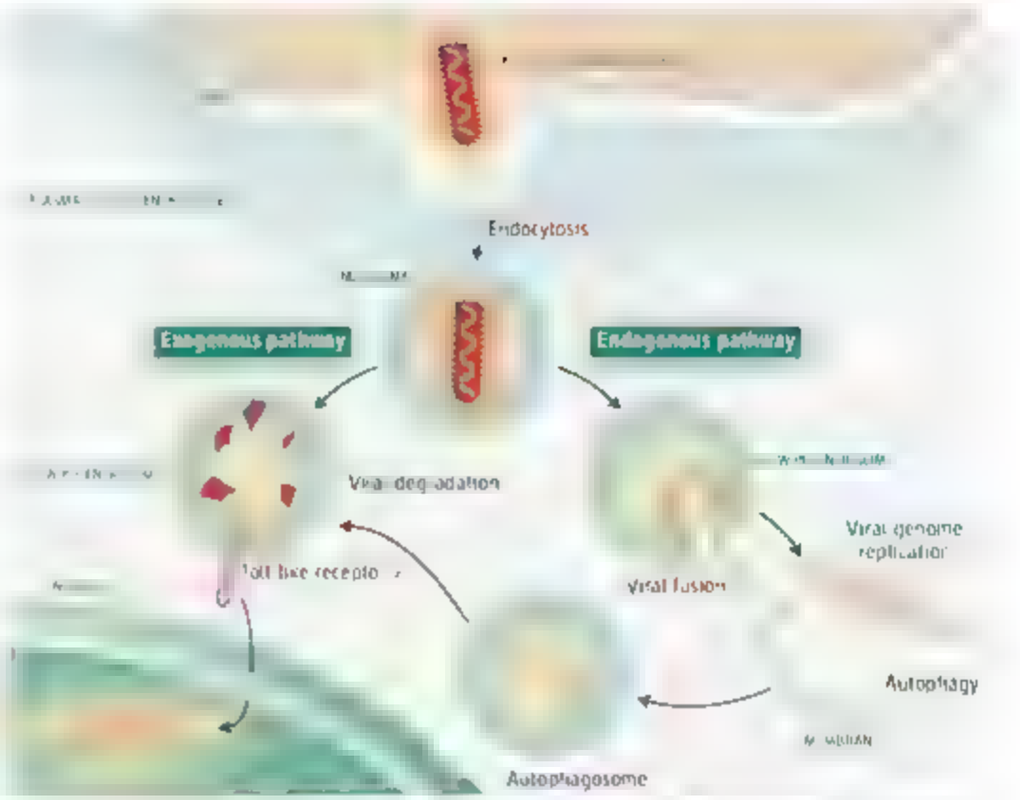

Detecting viral infection Through an exogenous pathway, RNA within internalized virions is detected by a Toll-like receptor 7 in endosomes after digestion of the viral envelope and capsid proteins by host cell enzymes. In the endogenous pathway, autophagy performs an analogous function to endocytosis, transferring viral RNA from the cytoplasm to intracellular compartments containing Toll-like receptor 7.

Autophagy allows a cell to engulf parts of its own cytoplasm to recycle catabolic products and supply anabolic needs. This engulfment generates vesicles (autophagosomes) that mature into degradative compartments (autolysosomes) (*3*). The process is emerging as an important player in multiple facets of cell physiology, including programmed cell death, development, and senescence. Autophagy also regulates immunity by providing cytoplasmic proteins that can be processed for presentation in association with major histocompatibility complex (MHC) class II molecules (*3*). Additionally, autophagy can act as an innate effector pathway for pathogen elimination by permitting degradation of bacteria that would otherwise persist within phagosomes or the cytoplasm of infected cells (*3*). However, the involvement of autophagy in the initial sensing of pathogens had not been reported previously, and that is what Lee *et al.* set out to determine.

The authors analyzed autophagy in plasmacytoid dendritic cells taken from a transgenic mouse in which the autophagosome-associated protein LC3 was fused to green fluorescent protein. Ten to 15% of the dendritic cells displayed a punctate fluorescent pattern indicative of large-scale autophagosome formation. Exposure to virus did not alter the overall frequency of fluorescent cells (although it is possible that changes in the frequency of autophagy would be seen among the small number of cells that actually get infected). To address the functional importance of this observation, the authors analyzed the effect of inhibiting class III phosphatidylinositol 3-kinases, enzymes that are critical for executing autophagy. They

Immunobiology Laboratory, Cancer Research UK, London Research Institute, Lincoln's Inn Fields Laboratories, 44 Lincoln's Inn Fields, London WC2A 3PX, UK. E-mail: caetano@cancer.org.uk

also checked the functional capacity of plasmacytoid dendritic cells that lack Atg5, a necessary component of the autophagic machinery. In both cases, eliminating autophagy abrogated cytokine responses to infection with vesicular stomatitis virus. Along the same line, mice with an Atg5-deficient immune system failed to mount a rapid interferon response (dependent on plasmacytoid dendritic cells) when infected with virus. Thus, autophagy by this immune cell type is essential for delivering cytoplasmic viral RNA to the endosomal pathway, thereby allowing recognition of some RNA viruses by TLR7 (*1*).

One unexpected observation in the study could affect this conclusion. TLR7 and TLR9 signaling in most cell types elicits production of cytokines such as interleukin-12 p40 (IL-12 p40), but not IFN-α. The distinctiveness of plasmacytoid dendritic cells lies partly in being able to retain nucleic acids in an endocytic compartment where TLR7 and TLR9 signaling is coupled to IFN-α expression (*4*). Surprisingly, the authors find that plasmacytoid dendritic cells lacking Atg5 produce IL-12 p40, but not IFN-α, in response to exogenous TLR9 agonists. Atg5 may somehow be involved in sorting TLRs to the appropriate compartments, where signaling for IFN-α production can take place. Thus, the role of autophagy in TLR signaling may extend beyond ligand delivery and include intracellular receptor trafficking.

In most cell types, autophagy increases in response to cellular stresses such as starvation or infection. Induction of autophagy upon infection, either as a host response or as a pathogen-driven process (*5*), may thus allow cells other than plasmacytoid dendritic cells to make use of TLRs for detecting pathogens in the cytoplasm. However, it also raises a problem. TLR7 responds to stretches of polyuridylic acid found in both host (self) and viral RNA (*6*). Discrimination between the two is presumably based on the fact that viral RNA is protected within a proteinaceous capsid, whereas self RNA is unprotected and susceptible to degradation by extracellular RNAses before it can access endosomes. If autophagy delivers cytoplasmic RNA directly to TLR-bearing compartments, RNA discrimination must be accomplished by additional means.

Until now, the TLR system and cytosolic receptors were thought to perform analogous functions but in distinct regions of the cell. For immunologists brought up on a diet of adaptive immunity—that is, immune responses by lymphocytes—this has interesting parallels with the dichotomy between MHC class I and class II molecules, which similarly survey those same two regions where pathogens are encountered. However, just as the division of labor between MHC class I and class II is not absolute, the cytoplasmic and endosomal innate immune receptors may be seeing overlapping worlds. Autophagy can provide endogenous antigens for MHC class II presentation (*3*) and, as Lee *et al.* show, viral RNAs for recognition by a TLR. Conversely, cross-presentation pathways allow MHC class I molecules to present exogenous antigens, much like cytoplasmic receptors can sometimes mediate responses to stimuli applied to the outside of a cell (*7*, *8*). Perhaps the mechanisms underlying pathogen sensing by the innate and adaptive immune systems are not so different after all.

References

1. H. K. Lee, J. M. Lund, B. Ramanathan, N. Mizushima, A. Iwasaki, *Science* **315**, 1398 (2007).
2. T. Kawai, S. Akira, *Nat. Immunol.* **7**, 131 (2006).
3. V. Deretic, *Curr. Opin. Immunol.* **18**, 375 (2006).
4. K. Honda *et al.*, *Nature* **434**, 1035 (2005).
5. I. Wileman, *Science* **312**, 875 (2006).
6. S. S. Diebold *et al.*, *Eur. J. Immunol.* **36**, 3256 (2006).
7. H. Kato *et al.*, *Nature* **441**, 101 (2006).
8. S. Gilm *et al.*, *Proc. Natl. Acad. Sci. U.S.A.* **103**, 8459 (2006).

10.1126/science.1140002

APPLIED PHYSICS

Oxide Electronics Emerge

Arthur P. Ramirez

Microelectronics are built from materials whose electrons interact strongly and can exhibit properties as a group that are not seen in any one particle

Most condensed-matter physics researchers either pursue basic questions of complex phenomena in large numbers (10^{22}) of particles, or seek out new materials for technological applications. When these paths intersect in a single experiment, one feels that the future comes a little better into focus. Emergent phenomena, in which new properties arise from the interactions of many particles in a complex system, generate special interest. In the experiments of Tsukazaki *et al.* reported on page 1388 of this issue (*1*), the authors show how novel devices can be made from a class of materials—the transition-metal oxides—that often show signs of emergent phenomena when in bulk form. The devices made by Tsukazaki *et al.* exhibit high charge carrier mobility, needed for high-performance switching, as well as an exotic emergent state called the quantum Hall effect. The appearance of these two features in an oxide is a milestone in our ability to control materials. Moreover, this level of control shows a clearer path to using such materials in applications as varied as advanced computing and clean energy production.

Emergent phenomena (*2*, *3*) in condensed matter cannot be understood in terms of simple interactions between pairs of particles. Examples of such phenomena are magnetic excitations in low-dimensional materials, superconductivity in "heavy electron" magnets, and fractionally charged particles in a two-dimensional electron gas. A traditional route to understanding these kinds of emergent states is to create them in new materials. In this way, one can study states with different

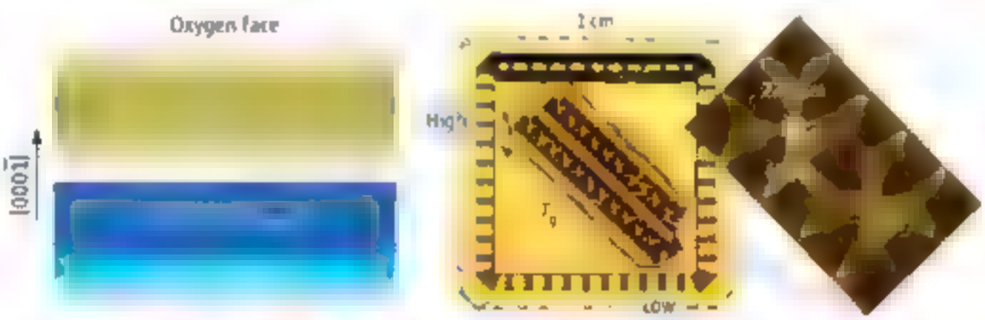

Old material with new properties. (**Left**) Schematic diagram of oxide layer structure that Tsukazaki *et al.* used to observe the quantum Hall effect. (**Right**) Micrograph of the actual devices used, where T_g is the growth temperature. A single device with dimensions 220 μm × 60 μm is highlighted. (Adapted from (*1*))

The author is with Bell Labs, Alcatel-Lucent, 600 Mountain Avenue, Murray Hill, NJ 07974, USA. E-mail: apr@bell-labs.com

characteristics and either test theoretical descriptions of such states or realize entirely new states of matter. Searches for emergent phenomena are often performed in bulk or thin-film materials, either crystalline or nanometer-scale in size.

The commercial development of a new material exhibiting emergent behavior for a particular device application presents a different set of challenges. Although this research is aimed at ensuring reliability and compatibility with existing materials, and at driving down the cost of manufacturing, such investigations can also lead to qualitatively new materials. For instance, as part of the program to synthesize ever-purer semiconductor structures in the 1970s, Cho and Arthur (*4*) developed the technique of molecular beam epitaxy, in which highly ordered atomic layers are grown and lattice-matched to the underlying substrate. Molecular beam epitaxy was further refined to create the two-dimensional structures leading to the fractional quantum Hall effect, a completely unexpected emergent state of electrons discovered by Tsui *et al.* (*5*).

The semiconducting behavior underlying modern microelectronics is found in compounds of silicon or combinations of materials from columns III and V of the periodic table, such as gallium and arsenic. Emergent phenomena, however, occur in a wide variety of other materials such as carbon-based organics, intermetallics, and transition-metal oxides. It is the oxides, however, that present the richest variety of emergent states, including metals with electron masses several hundred times the bare mass, spin magnetism with zero-point entropy, and superconductivity at record high temperatures. Materials physicists have dreamed of creating new classes of devices that harness such emergent states of matter (*6*). Indeed, with the end of Moore's law in sight as transistors in microprocessors approach low-nanometer-scale dimensions, even the silicon industry is looking to alternative materials and architectures for computing beyond 2020 (*7*).

Tsukazaki *et al.* describe a semiconductor heterostructure formed at the interface of layers of zinc oxide (ZnO) and a related compound, $Mg_xZn_{1-x}O$ (see the figure). These two materials have different values of the semiconducting gap, the energy needed to excite an electron into its conduction band. The different gap values form a potential energy (quantum) well that confines electrons to a two-dimensional region.

ZnO already finds many applications including piezoelectric actuators (*8*), phosphors in displays (*9*), and transparent conducting films (*10*). As an example of the versatility of ZnO, some of the authors of the report by Tsukazaki *et al.* had recently shown that ZnO films can be altered to transport holes as well as electrons, both essential attributes for a light-emitting diode (*11*).

To create high-performance devices, however, it is necessary to eliminate the defects that can trap electrons and thus reduce the switching speed. In addition, the presence of such defects can also prevent the formation of delicate emergent states. The absence of charge trapping is measured by the material's mobility. Useful mobility values occur over an extremely wide range, from 1 $cm^2 V^{-1} s^{-1}$ (in computer displays) to 1000 $cm^2 V^{-1} s^{-1}$ (in silicon used in microprocessors) to more than 10^7 $cm^2 V^{-1} s^{-1}$ (in the highest-quality gallium arsenide heterostructures cooled down to 100 mK). Recent advances in the growth of single-crystal and ordered films of ZnO demonstrated mobilities in excess of 2000 at 50 K (*12*), thus opening the door to high-quality oxide devices.

For a high-performance quantum well, it is essential that the defect density in the interface region be low. Sharp interfaces had already been achieved in a different pair of oxide materials, strontium titanate lanthanum titanate (*13*), and oscillations in electrical resistance as a function of magnetic field (*14*), normally attributed to low-defect metals, were observed. Tsukazaki *et al.* were able to achieve similarly low defect levels in this work to form ZnO $Mg_xZn_{1-x}O$ quantum wells with low-temperature mobilities greater than 5000 $cm^2 V^{-1} s^{-1}$.

The materials used to make the heterostructures should also facilitate the transfer of electrons from the bulk into the interface. Tsukazaki *et al.* noted that whereas the ZnO layers have sizable tensile strain, which induces charge segregation through the piezoelectric effect, the underlying $Mg_xZn_{1-x}O$ layers have negligible strain. Thus, a net charge density is induced electrostatically from the ZnO region into the interface. The authors further developed a synthesis technique that allowed them to vary the thickness of the layers, hence they could study samples with different charge densities in the two-dimensional interface region.

These efforts represent a high degree of materials control, and as a result, Tsukazaki *et al.* were able to observe quantized values of the Hall resistance (related to the voltage developed transversely across a sample in response to longitudinal current flow) at temperatures near absolute zero. This so-called quantum Hall effect is the main result of the paper and typically only occurs in the highest-purity two-dimensional metals. Thus, a hallmark experiment, first performed in 1980 by von Klitzing *et al.* in high-mobility silicon heterostructures (*15*), has now been repeated in an entirely new materials class. We know that the Hall resistance in the quantum Hall effect is precisely related to ratios of fundamental constants, the electronic charge e and Planck's constant h. The extreme precision (to 1 part in 100 million) of the experimental resistance plateaus was explained theoretically by Laughlin (*16*) and since 1990 has been the international standard of resistance.

The quantum Hall effect has been observed only in a few materials and never before in a device made from oxide materials. In a related development, Novoselov *et al.* report on page 1379 of this issue (*17*) the observation of the quantum Hall effect at room temperature in one of the simplest possible devices—a single-atom-thick sheet of elemental carbon, called graphene. Here the observation of an effect that had been confined to the domain of low-temperature physics is attributed to graphene's unusual atomic structure that suppresses scattering of electrons by thermal lattice vibrations. The importance of the room-temperature quantum Hall effect in graphene stems from the material's uniqueness. In contrast, the importance of the results of Tsukazaki *et al.* stems from the ubiquity and versatility of the oxide family of materials. The work consummates the marriage of two disparate fields of condensed-matter physics—the physics of devices, and the physics of multifunctional (opto-, electro-, magneto-, and elasto-) sensing and control—and the implications transcend the obvious scientific attraction of uncovering an exotic state of matter in a new material. The present experiment suggests that we have entered the era of oxide electronics, and research in this field promises exciting discoveries for many years.

References

1. A. Tsukazaki *et al.*, *Science* **315**, 1388 (2007); published online 25 January 2007 (10.1126/science.1137430).
2. R. B. Laughlin, D. Pines, *Proc. Natl. Acad. Sci. U.S.A.* **97**, 28 (2000).
3. P. W. Anderson, *Science* **177**, 393 (1972).
4. A. Cho, J. Arthur, *Prog. Solid State Chem.* **10**, 157 (1975).
5. D. C. Tsui, H. L. Störmer, A. C. Gossard, *Phys. Rev. Lett.* **48**, 1559 (1982).
6. C. Zhou, D. M. Newns, J. A. Misewich, P. C. Pattnaik, *Appl. Phys. Lett.* **70**, 598 (1997).
7. W. Arden, *Mater. Sci. Eng. B* **134**, 104 (2006).
8. S. C. Minne, S. R. Manalis, C. F. Quate, *Appl. Phys. Lett.* **67**, 3918 (1995).
9. K. Vanheusden *et al.*, *J. Appl. Phys.* **79**, 7983 (1996).
10. D. C. Look, *Mater. Sci. Eng. B* **80**, 383 (2001).
11. A. Tsukazaki *et al.*, *Nat. Mater.* **4**, 42 (2005).
12. D. C. Look, J. W. Hemsky, J. R. Sizelove, *Phys. Rev. Lett.* **82**, 2552 (1999).
13. A. Ohtomo, D. A. Muller, J. L. Grazul, H. Y. Hwang, *Nature* **419**, 378 (2002).
14. A. Ohtomo, H. Y. Hwang, *Nature* **427**, 423 (2004).
15. K. von Klitzing, G. Dorda, M. Pepper, *Phys. Rev. Lett.* **45**, 494 (1980).
16. R. B. Laughlin, *Phys. Rev. B* **23**, 5632 (1981).
17. K. S. Novoselov *et al.*, *Science* **315**, 1379 (2007); published online 15 February 2007 (10.1126/science.1137201).

10.1126/science.1138578

Room-Temperature Quantum Hall Effect in Graphene

K. S. Novoselov,[1] Z. Jiang,[2,3] Y. Zhang,[2] S. V. Morozov,[1] H. L. Stormer,[2] U. Zeitler,[4] J. C. Maan,[4] G. S. Boebinger,[3] P. Kim,[2]* A. K. Geim[1]*

The quantum Hall effect (QHE), one example of a quantum phenomenon that occurs on a truly macroscopic scale, has been attracting intense interest since its discovery in 1980 (*1*). The QHE, exclusive to two-dimensional (2D) metals, has elucidated many important aspects of quantum physics and has deepened our understanding of interacting systems. It has also led to the establishment of a new metrological standard, the resistance quantum, h/e^2, that contains only fundamental constants of the electron charge e and Planck's constant, h (*2*). As with many other quantum phenomena, the observation of the QHE usually requires low temperatures, typically below the boiling point of liquid helium (*1*). Efforts to extend the QHE temperature range by, for example, using semiconductors with small effective masses of charge carriers have so far failed to reach temperatures above 30 K (*3*, *4*). These efforts are driven by both an innate desire to observe apparently fragile quantum phenomena under ambient conditions and the pragmatic need to perform metrology at room, or at least liquid-nitrogen, temperatures. More robust quantum states, implied by their persistence to higher temperatures, would also provide added freedom to investigate finer features of the QHE and, possibly, allow higher quantization accuracy (*2*). We show that in graphene, a single layer of carbon atoms tightly packed in a honeycomb crystal lattice, the QHE can be observed even at room temperature. This is due to the highly unusual nature of charge carriers in graphene, which behave as massless relativistic particles (Dirac fermions) and move with little scattering under ambient conditions (*5*, *6*).

Figure 1A shows one of our devices used in the QHE measurements. At room temperature, its Hall conductivity, σ_{xy}, reveals plateaus at $2e^2/h$ for both electrons and holes, while the longitudinal conductivity, ρ_{xx}, approaches zero (< 10 ohms) exhibiting an activation energy $\Delta E \approx 600$ K (Fig. 1B). The quantization at σ_{xy} is exact within an experimental accuracy ~0.2% (Fig. 1C). The survival of the QHE to such high temperatures can be attributed to the large cyclotron gaps, $\hbar\omega_c$, characteristic to Dirac fermions in graphene. Their energy quantization in a magnetic field, B, is described by $E_N = v_F\sqrt{2e\hbar BN}$, where $v_F \approx 10^6$ m s^{-1} is the Fermi velocity and N an integer Landau level (LL) number (*5*, *6*). The expression yields an energy gap $\Delta E \approx 2800$ K at $B = 45$ T if the Fermi energy, E_F, lies between the lowest LL, $N = 0$, and the first excited one, $N = \pm 1$ (Fig. 1B, inset). This implies that, in our experiments at room temperature, $\hbar\omega_c$ exceeded the thermal energy, k_BT, by a factor of 10. In addition to the large $\hbar\omega_c$, there are a number of other factors that help the QHE in graphene to survive to such high temperatures. First, graphene devices allow for very high carrier concentrations (up to 10^{13} cm^{-2}) with only a single 2D subband occupied, which is essential to fully populate the lowest LL even in ultra-high B. This is in contrast to traditional 2D systems (for example, GaAs heterostructures), which are either depopulated already at moderate B or exhibit multiple subband occupation, leading to the reduction of the effective energy gap to values well below $\hbar\omega_c$. Second, the mobility, μ, of Dirac fermions in our samples does not change appreciably from liquid-helium to room temperature. It remains at ~10000 cm^2 V^{-1} s^{-1}, which yields a scattering time of $\tau \sim 10^{-13}$ s so that the high field limit $\omega_c\tau = \mu \cdot B >> 1$ is reached in fields of several T.

These characteristics of graphene foster hopes for the room-temperature QHE observable in fields substantially smaller than 30 T. In fact, we observed the Hall plateaus developing already in $B < 20$ T at 300 K. The need for high B is attributed to broadened LLs caused by disorder, which reduces the activation energy. We expect that improving sample homogeneity and achieving higher μ (currently limited by static defects) should allow the observation of the room-temperature QHE by using conventional magnets. This should open up new vistas for developing graphene-based resistance standards (certainly operational above liquid-nitrogen temperatures) and for novel quantum devices working at elevated temperatures.

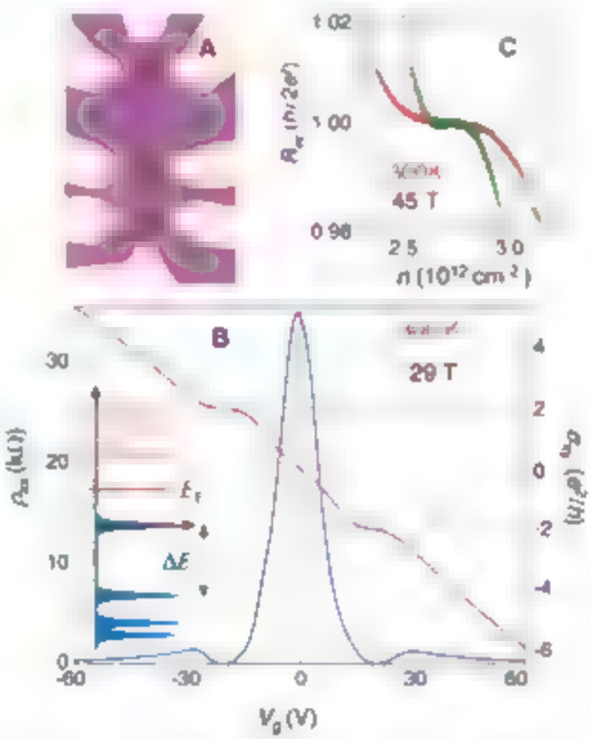

Fig. 1. Room-temperature QHE in graphene. (**A**) Optical micrograph of one of the devices used in the measurements. The scale is given by the Hall bar's width of 2 μm. Device fabrication procedures were described in (*5*). (■) σ_{xy} (red) and ρ_{xx} (blue) as a function of gate voltages (V_g) in a magnetic field of 29 T. Positive values of V_g induce electrons, and negative values of V_g induce holes, in concentrations $n = (7.2 \times 10^{10}\ \text{cm}^{-2}\text{V}^{-1})V_g$ (*5*, *6*). (Inset) The LL quantization for Dirac fermions. (**C**) Hall resistance, R_{xy}, for electrons (red) and holes (green) shows the accuracy of the observed quantization at 45 T.

References and Notes

1. S. Das Sarma, A. Pinczuk, *Perspectives in Quantum Hall Effects* (Wiley, New York, 1997).
2. B. Jeckelmann, B. Jeanneret, *Rep. Prog. Phys.* **64**, 1603 (2001).
3. S. Q. Murphy *et al.*, *Physica E (Amsterdam)* **6**, 293 (2000).
4. G. Landwehr *et al.*, *Physica E (Amsterdam)* **6**, 713 (2000).
5. K. S. Novoselov *et al.*, *Nature* **438**, 197 (2005).
6. Y. Zhang, Y. W. Tan, H. L. Stormer, P. Kim, *Nature* **438**, 201 (2005).

7. This work was supported by Engineering and Physical Sciences Research Council (UK), NSF (DMR-03 52738), EuroMagNet (EU, RII3-CT-2004-506239), U.S. Department of Energy (DOE) (DE-AIO2-04ER46133 and DE-FG02-05ER4615), the Royal Society, Leverhulme Trust, Microsoft Corporation, and W. M. Keck Foundation. The experiments were partially performed at the National High Magnetic Field Laboratory (supported by NSF cooperative agreement no. DMR-0084173, by the state of Florida, and by the DOE) and the Netherlands High Field Magnet Laboratory (supported by the Foundation for Fundamental Research on Matter and the EU).

6 November 2006; accepted 31 January 2007
Published online 15 February 2007;
10.1126/science.1137201
Include this information when citing this paper.

[1]Department of Physics, University of Manchester, Manchester M13 9PL, UK. [2]Department of Physics, Columbia University, New York, NY 10027, USA. [3]National High Magnetic Field Laboratory, Tallahassee, FL 32310, USA. [4]High Field Magnet Laboratory, Radboud University Nijmegen, 6525 ED Nijmegen, Netherlands.

*To whom correspondence should be addressed. E-mail: pkim@phys.columbia.edu (P.K.); geim@man.ac.uk (A.K.G.)

An Intrinsic Bond-Centered Electronic Glass with Unidirectional Domains in Underdoped Cuprates

Y. Kohsaka,[1] C. Taylor,[1] K. Fujita,[1,2] A. Schmidt,[1] C. Lupien,[3] T. Hanaguri,[4] M. Azuma,[5] M. Takano,[5] H. Eisaki,[6] H. Takagi,[2,4] S. Uchida,[2,7] J. C. Davis[1,8]*

Removing electrons from the CuO_2 plane of cuprates alters the electronic correlations sufficiently to produce high temperature superconductivity. Associated with these changes are spectral-weight transfers from the high-energy states of the insulator to low energies. In theory, these should be detectable as an imbalance between the tunneling rate for electron injection and extraction—a tunneling asymmetry. We introduce atomic-resolution tunneling-asymmetry imaging, finding virtually identical phenomena in two lightly hole-doped cuprates: $Ca_{1.88}Na_{0.12}CuO_2Cl_2$ and $Bi_2Sr_2Dy_{0.2}Ca_{0.8}Cu_2O_{8+\delta}$. Intense spatial variations in tunneling asymmetry occur primarily at the planar oxygen sites; their spatial arrangement forms a Cu-O-Cu bond-centered electronic pattern without long-range order but with $4a_0$ wide unidirectional electronic domains dispersed throughout (a_0, the Cu-O-Cu distance). The emerging picture is then of a partial hole localization within an intrinsic electronic glass evolving, at higher hole densities, into complete delocalization and highest-temperature superconductivity.

Metallicity of the cuprate CuO_2 planes arises from doped holes residing in oxygen 2p and copper 3d orbitals (Fig. 1A). Coulomb interactions lift the degeneracy of the relevant d-orbital, producing lower and upper d-states separated by the Mott-Hubbard energy U (Fig. 1B). The lower d-states and oxygen p-state become hybridized, yielding a correlated insulator with charge-transfer gap Δ (Fig. 1B). The "hole-doping" process, which generates highest-temperature superconductivity, then removes electrons from the CuO_2 plane, creating new hole-like electronic states with predominantly oxygen 2p character (2). This is a radically different process than hole-doping a conventional semiconductor because, when an electron is removed from a correlated insulator, the states with which it was correlated are also altered fundamentally. Numerical modeling of this process (3) indicates that when n holes per unit cell are introduced, the correlation changes generate spectral-weight transfers from both filled and empty high-energy bands resulting in the creation of ~$2n$ new empty states just above the chemical potential μ (Fig. 1B). But precisely how these spectral-weight transfers result in cuprate high-temperature superconductivity remains controversial.

Recently, it has been proposed that these doping-induced correlation changes might be observable directly as an asymmetry of electron tunneling currents with bias voltage (4, 5): electron extraction at negative sample bias being strongly favored over electron injection at positive sample bias. Such effects should be detectable with a scanning tunneling microscope (STM). The STM tip-sample tunneling current is given by

$$I(\vec{r}, z, V) = f(\vec{r}, z)\int_0^{eV} N(\vec{r}, E)\,dE \qquad (1)$$

where z is the tip's surface-normal coordinate, V is the relative sample-tip bias, and $N(\vec{r}, E)$ is the sample's local-density-of-states (LDOS) at lateral location $\vec{r}$ and energy E. Unmeasurable effects due to the tunneling matrix elements, the tunnel-barrier height, and z variations from electronic heterogeneity are contained in $f(\vec{r}, z)$ (see supporting online text 1). For a simple metallic system where $f(\vec{r}, z)$ is a featureless constant, Eq. 1 shows that spatial mapping of the differential tunneling conductance $dI/dV(\vec{r}, V)$ yields $N(\vec{r}, E = eV)$. However, for the strongly correlated electronic states in a lightly hole-doped cuprate, the situation is much more complex. In theory (4), the correlations cause the ratio $Z(V)$ of the average density-of-states for empty states $\overline{N}(E = +eV)$ to that of filled states $\overline{N}(E = -eV)$ to become asymmetric by an amount

$$Z(V) = \frac{\overline{N}(E = +eV)}{\overline{N}(E = -eV)} \approx \frac{2n}{1-n} \qquad (2)$$

Spectral-weight sum rules (5) also indicate that the ratio $R(\vec{r})$ of the energy-integrated $N(\vec{r}, E)$ for empty states ($E > 0$) to that of filled states ($E < 0$) is related to n by

$$R(\vec{r}) = \frac{\int_0^{\Omega_0} N(\vec{r}, E)\,dE}{\int_{-\Omega_0}^{0} N(\vec{r}, E)\,dE} \approx \frac{2n(\vec{r})}{1-n(\vec{r})} + O\left(\frac{nt}{U}\right) \qquad (3)$$

Here t is in-plane hopping rate and Ω_0 satisfies "all low-energy scales" $< \Omega_0 < U$.

As a test of such ideas, we show in Fig. 1C the predicted evolution of the tunneling asymmetry (TA) with n from (4), and in Fig. 1D we show the measured evolution of spatially averaged TA in a sequence of lightly hole-doped $Ca_{2-x}Na_xCuO_2Cl_2$ samples with different x. We see that the average TA is indeed large at low x

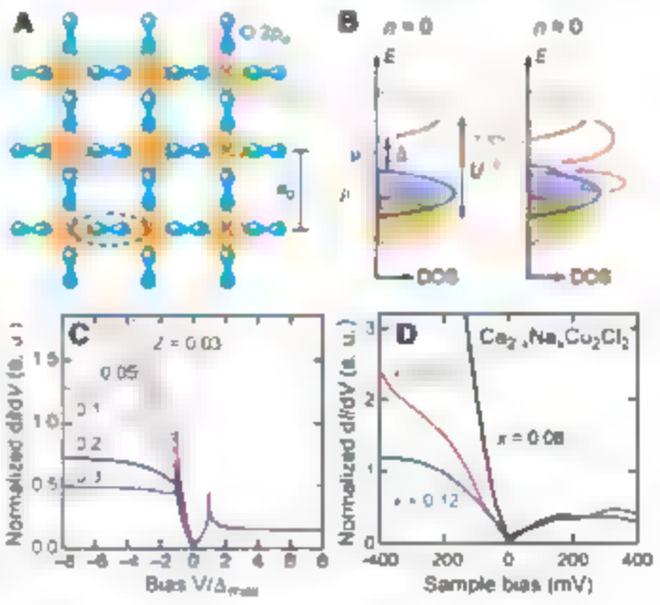

Fig. 1. (**A**) Relevant electronic orbitals of the CuO_2 plane: Cu 3d orbitals are shown in orange and oxygen 2p orbitals are shown in blue. A single plaquette of four Cu atoms is shown within the dashed square box, and a single Cu-O-Cu unit is within the dashed oval. (**B**) Schematic energy levels in the CuO_2 plane and the effects of hole doping upon it. (**C**) The expected tunneling asymmetry between electron extraction (negative bias) and injection (positive bias) from (4) where low values of Z occur at low hole densities n. (**D**) Measured doping dependence of average tunneling asymmetry in $Ca_{2-x}Na_xCuO_2Cl_2$. a.u., arbitrary units.

[1]Laboratory of Atomic and Solid State Physics, Department of Physics, Cornell University, Ithaca, NY 14853, USA. [2]Department of Advanced Materials Science, University of Tokyo, Kashiwa, Chiba 277-8651, Japan. [3]Département de Physique, Université de Sherbrooke, Sherbrooke, QC J1K 2R1, Canada. [4]Magnetic Materials Laboratory, RIKEN, Wako, Saitama 351-0198, Japan. [5]Institute for Chemical Research, Kyoto University, Uji, Kyoto 611-0011, Japan. [6]National Institute of Advanced Industrial Science and Technology, Tsukuba, Ibaraki 305-8568, Japan. [7]Department of Physics, University of Tokyo, Bunkyo-ku, Tokyo 113-0033, Japan. [8]Condensed Matter Physics and Materials Science Department, Brookhaven National Laboratory, Upton, NY 11973, USA.

*To whom correspondence should be addressed. E-mail: jcdavis@ccmr.cornell.edu

and diminishes rapidly with increasing x, as predicted (*3*, *5*). But because such effects are detectable by spatially resolved techniques (*6*, *7*), the TA proposals (*4*, *5*) also identify the first atomic-scale probe of the doping-induced correlation changes.

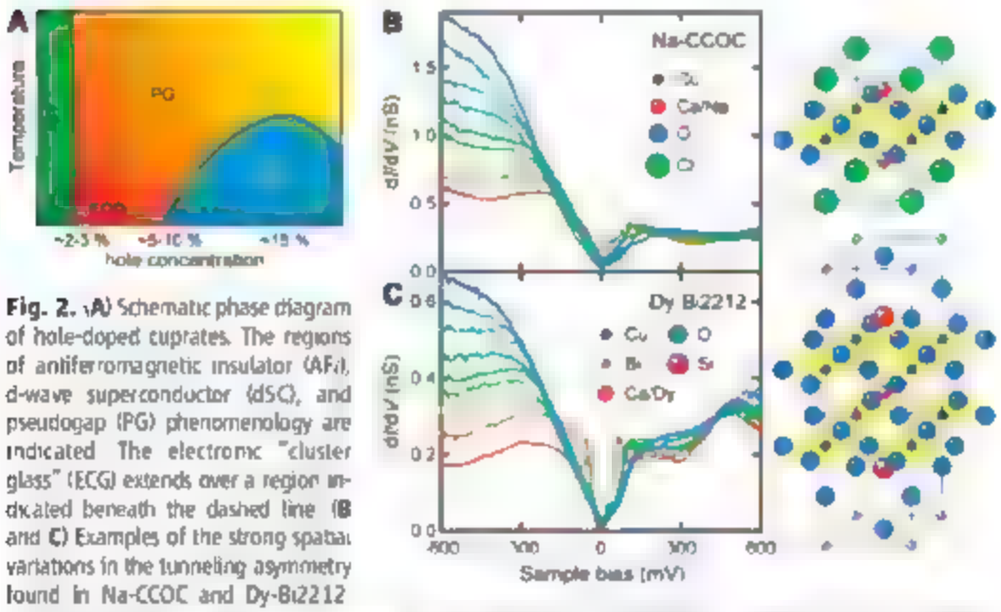

Fig. 2. (**A**) Schematic phase diagram of hole-doped cuprates. The regions of antiferromagnetic insulator (AFI), d-wave superconductor (dSC), and pseudogap (PG) phenomenology are indicated. The electronic "cluster glass" (ECG) extends over a region indicated beneath the dashed line. (**B** and **C**) Examples of the strong spatial variations in the tunneling asymmetry found in Na-CCOC and Dy-Bi2212. Because experimental normalization keeps integrated d*I*/d*V* at positive biases constant, the large variations are seen at negative bias and directly reflect spatial variation of the TA tunnel junction set at 200 pA, 600 mV. As can be seen, electron extraction is strongly favored over injection and varies spatially. These phenomena are quite similar in the two materials.

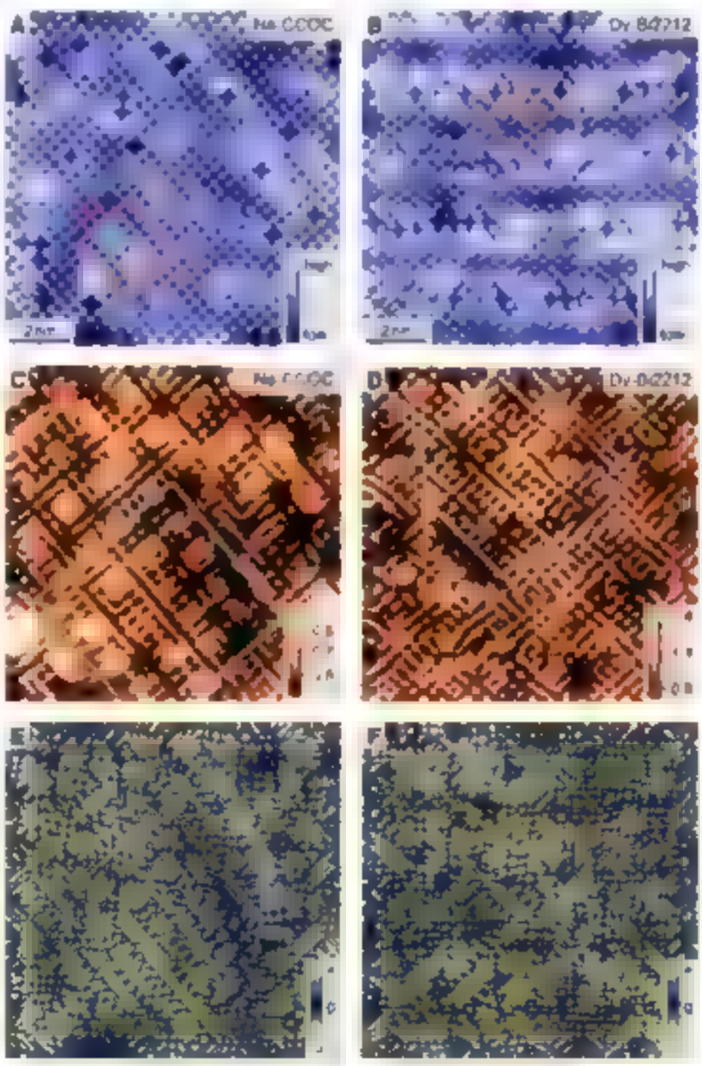

Fig. 3. (**A** and **B**) Constant-current topographic images of Na-CCOC and Dy-Bi2212 in 12-nm^2 fields of view. Imaging conditions are (A) 50 pA at 600 mV and (B) 50 pA at 150 mV. The orange boxes in (A) and (B) indicate areas described in Fig. 4, B and C, and Fig. 4, E and F, respectively, and the Cu-O bond directions are shown as pairs of orthogonal black arrows. (**C** and **D**) R maps taken at 150 mV [i.e., $R(\vec{r}, 150\ \text{mV}) = I(\vec{r}, +150\ \text{mV})/I(\vec{r}, -150\ \text{mV})$] in the same field of view shown in Fig. 3, A and B, respectively. Large R (bright in this color scale) means that the corresponding tunneling spectrum is more symmetric, whereas low R (dark) means that it is more asymmetric. The blue boxes in (C) and (D) indicate the boxed areas of Fig. 4, A and D, respectively. (**E** and **F**) Images of $\nabla^2 R$ (Laplacian) computed from Fig. 3, C and D, respectively, for better visualization of the atomic-scale arrangements of the spatial patterns.

Electronic "cluster glass" state of lightly hole-doped cuprates. Figure 2A shows schematically that cuprate antiferromagnetism disappears at a doped-hole density per CuO_2 $n \sim 2$ to 3%. The superconductivity usually does not appear until $n \sim 5$ to 10%. Therefore, another low-temperature state intervenes; it is usually thought of as an electronic "cluster glass" (ECG) state (*8*, *21*). At higher dopings, the ECG signatures coexist with diminishing intensity with the stripe-enhancing superconductivity, until they disappear somewhere near $n \sim 15\%$. Although the ECG state exhibits no known long-range spin or charge order, some electronic order of nanometer spatial form is always detected at nm scale by local probes of the spin (*9*–*15*) and charge (*14*, *20*); hence the "cluster" designation. And, because it is from this ECG state that high-temperature superconductivity emerges with hole doping (*22*), it is critical to determine what it is, how it is generated by hole doping, and how it evolves into and coexists with the superconducting state.

Much is known about the cuprate ECG state. Direct evidence for hole localization comes from (i) in-plane dc resistivity, which exhibits logarithmically increasing temperature dependence $\rho_{ab} \sim \ln T$ (*23*, *24*) and (ii) Hall-number measurements showing that the delocalized hole density approaches the chemically doped values only when $n \geq 10\%$ (*25*). Muon-spin rotation measurements (*8*, *13*) find glassy dynamics of spins but exhibiting some unknown form of spatial order at the nm scale; the spin component of the ECG "cluster." Similarly, torque magnetometer studies show (*26*) substantial free-spin paramagnetism. Nuclear magnetic quadrupole resonance measurements (*14*, *20*) reveal static charge heterogeneity at the nm scale; the hole-density component of the ECG "cluster." Powder neutron diffraction reveals related local lattice distortions (*27*), and optical spectroscopy, the anomalous anisotropic conductivity and electron-phonon couplings (*27*). Finally, neutron-scattering measurements indicate that the holes are clustered in nm-sized regions with some form of magnetic short-range order (*28*). In summary, the cuprate ECG state is pervasive, exhibiting partial hole localization in a state without long-range order but that, nonetheless, supports some unknown form of electronic domains. A long-standing problem has been whether these effects are an intrinsic element of hole-doped CuO_2 electronic structure or are extrinsic, perhaps triggered by random dopant and/or impurity disorder.

Theoretical hypotheses for the cause and structure of the cuprate ECG state include, for example, loss of electronic translational invariance because of (i) an electronic glass caused by random exchange couplings (*29*), (ii) a dopant-disorder-induced random electronic glass (*30*), (iii) a spontaneous (*31*) or dopant-induced (*30*, *32*) glass of self-organized electronic nanodomains, and (iv) a nematic electronic liquid crystal of such nanodomains (*33*). But a

direct test of such ideas has not been possible because neither the real-space electronic structure of the ECC state, nor that of an individual cluster," could be determined directly as no suitable imaging techniques existed.

Design of TA studies in $Ca_{1.88}Na_{0.12}CuO_2Cl_2$ and $Bi_2Sr_2Dy_{0.2}Ca_{0.8}Cu_2O_{8+\delta}$. STM-based imaging might appear inappropriate to address such issues. But dI/dV imaging is fraught with problems in lightly doped cuprates. For example, a standard dI/dV image, although well defined, is not a direct image of the LDOS (see supporting online text 1). Moreover, there are theoretical concerns that, in $Ca_{2-x}Na_xCuO_2Cl_2$, the topmost CuO_2 plane may be in an "extraordinary" state (*34*) or that interference between two tunneling trajectories through the $3p_z$-Cl orbitals adjacent to a dopant Na ion may cause rotational symmetry breaking in the tunneling patterns (*35*).

The new proposals (*4*, *5*) for tunneling asymmetry measurements provide a notable solution to problems with standard dI/dV imaging because Eqs. 2 and 3 have a crucial practical advantage. If we define the ratios $Z(\vec{r}, V)$ and $R(\vec{r}, V)$ in terms of the tunneling current I

$$Z(\vec{r}, V) = \frac{\frac{dI}{dV}(\vec{r}, -V)}{\frac{dI}{dV}(\vec{r}, V)} \qquad (4a)$$

$$R(\vec{r}, V) = \frac{I(\vec{r}, -V)}{I(\vec{r}, V)} \qquad (4b)$$

we see immediately from Eq. 1 that the unknown effects in $f(\vec{r}, z)$ are all canceled out by the division process. Thus, $Z(\vec{r}, V)$ and $R(\vec{r}, V)$ not only contain important physical information (*4*, *5*) but, unlike $N(\vec{r}, E_F, \Delta_0)$, can be expressible in terms of measurable quantities only. We have confirmed that the unknown factors $f(\vec{r}, z)$ are indeed canceled out in Eq. 4 (see supporting online text and fig. S2).

To address the material-specific theoretical concerns (*34*, *35*), we have designed a sequence of identical TA imaging experiments in two radically different cuprates: strongly underdoped $Ca_{1.88}Na_{0.12}CuO_2Cl_2$ (Na-CCOC, critical temperature T_c = 21 K) and $Bi_2Sr_2Dy_{0.2}Ca_{0.8}Cu_2O_{8+\delta}$ (Dy-Bi2212, T_c = 45 K). As indicated schematically in Fig. 2, B and C, they have completely different crystallographic structure, chemical constituents, and dopant species and sites in the termination layers lying between the CuO_2 plane and the STM tip. Na-CCOC has a single CuO_2 layer

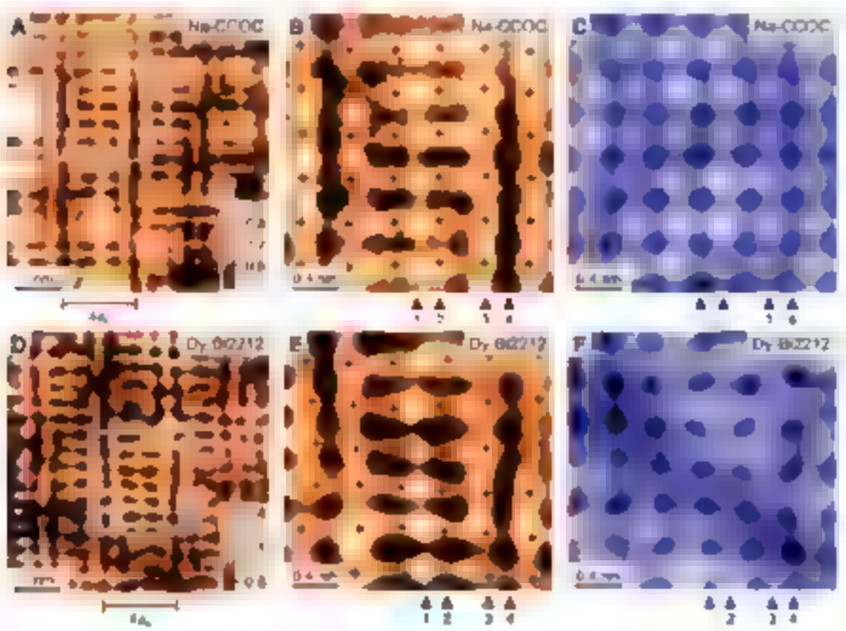

Fig. 4. (**A** and **D**) *R* maps of Na-CCOC and Dy-Bi2212, respectively (taken at 150 mV) from areas in the blue boxes of Fig. 3, C and D. The fields of view are (A) 5.0 nm by 5.3 nm and (D) 5.0 nm by 5.0 nm. The blue boxes in (A) and (D) indicate areas of Fig. 4, B and C, and Fig. 4, E and F, respectively. (**B** and **E**) Higher resolution *R* map within equivalent domains from Na-CCOC and Dy-Bi2212, respectively (blue boxes of Fig. 4, A and D). The locations of the Cu atoms are shown as black crosses. (**C** and **F**) Constant current topographic images simultaneously taken with Fig. 4, B and E, respectively. Imaging conditions are (C) 50 pA at 600 mV and (F) 50 pA at 150 mV. The markers show atomic locations, used also in Fig. 4, B and E. The fields of view of these images are shown in Fig. 3, A and B, as orange boxes.

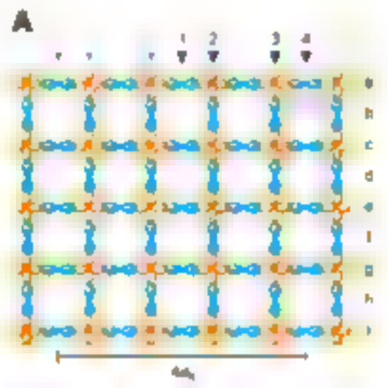

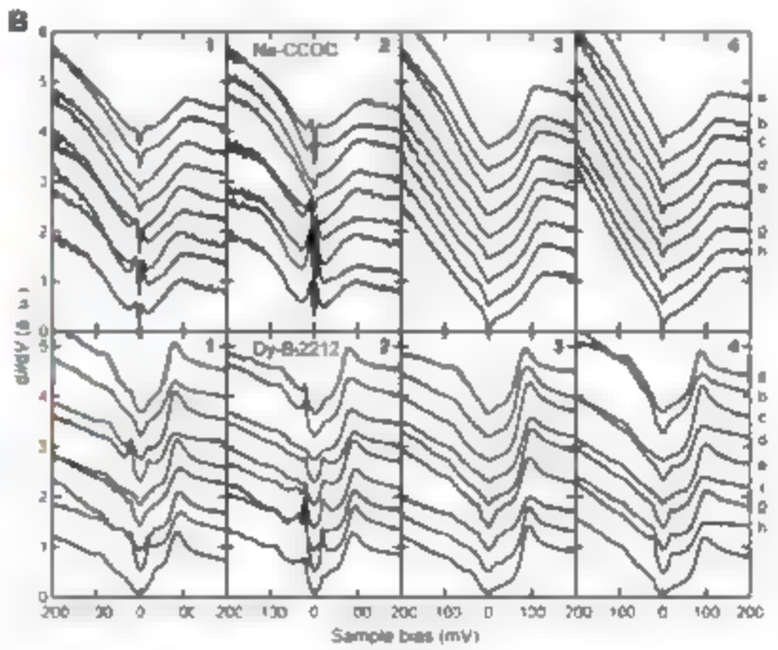

Fig. 5. (**A**) Locations relative to the O and Cu orbitals in the CuO_2 plane where each dI/dV spectrum at the surfaces of Fig. 4, C and F, and shown in Fig. 5B, is measured. Spectra are measured along equivalent lines labeled 1, 2, 3, and 4 in both domains of Fig. 4, B and E, and Fig. 5A. (**B**) Differential tunneling conductance spectra taken along parallel lines through equivalent domains in Na-CCOC and Dy-Bi2212. All spectra were taken under identical junction conditions (200 pA, 200 mV). Numbers (1 to 4) correspond to trajectories where these sequences of spectra were taken. Locations of the trajectories, relative to the domains, are shown between Fig. 4B (C) and 4E (F) by arrows.

capped by a perfectly square CaCl layer and with Na dopant atoms substituted at the Ca site. Dy-Bi2212 has a CuO_2 bilayer, above which are both BiO and SrO layers whose unit cells undergo the incommensurate crystal supermodulation, nonstoichiometric oxygen dopant atoms are located interstitially near the BiO layer. Therefore, we assert that TA-imaging phenomena that are identical in these two materials should be ascribed to their only common characteristic—the intrinsic electronic structure of the CuO_2 plane.

Atomic-resolution TA imaging. In Fig. 2, B and C, we show standard dI/dV spectra measured under identical junction conditions at random locations on the surfaces of the Na-CCOC and Dy-Bi2212 samples (all data were acquired at 4.2 K). Within $E < 100$ meV, they both exhibit the expected V-shaped dI/dV centered on $E = 0$ (*6*, *7*). Unexpectedly, at higher energies, the same intense spatial variations in the tunneling asymmetry of spectra were observed in both materials. These can be seen vividly at the left-hand perimeter of Fig. 2, B and C (because our procedures normalize the integrated dI/dV on the positive side). The corresponding variations in TA indicate the existence of intense atomic-scale variations in electronic structure.

To explore the spatial arrangements of these phenomena, we used an atomic resolution "*R* map" spatially imaging $R(\vec{r}, V)$ of Eq. 4b. Figure 3, A and B, show typical topographic images of the CaCl and BiO layers obtained by cleavage, in cryogenic ultrahigh vacuum, of Na-CCOC and Dy-Bi2212, respectively. The brightest regions in Fig. 3A indicate the locations of Cl atoms that are directly above the Cu atoms in Na-CCOC, whereas those in Fig. 3B indicate the Bi atoms that are above the Cu atoms in Dy-Bi2212. The dark, cross-shaped regions in Fig. 3A are the missing Cl atoms and, in Fig. 3B, are displaced Bi atoms along maxima of the crystalline supermodulation. Figure 3, C and D, are images of $R(\vec{r}, V = 150\ \text{mV})$ measured in the identical fields of view of Fig. 3, A and B, respectively. These *R* maps are markedly similar in texture and exhibit far finer spatial details than their related surface topographs; the reason is that much of their contrast stems from features occurring within each Cu plaquette (Fig. 1A). The *R* maps exhibit no long-range spatial order of any kind. Nevertheless, autocorrelation analysis shows that they do have short-range ~ $4a_0 \times 4a_0$ periodic correlations, where a_0 is the Cu-O-Cu distance. The most obvious and arguably most important observation in Fig. 3, C and D, is a loss of both translational and 90° rotational (C_4) invariance in the spatial arrangements of electronic structure at the $4a_0$ scale—these effects being virtually indistinguishable in Na-CCOC and Dy-Bi2212. It is also evident from Fig. 3, C and D, that the internal structure of these "domains," as well as the overall matrix in which they are embedded, retains further degrees of electronic complexity at the atomic scale.

Cu-O-Cu bond-centered electronic glass with disperse $4a_0$-wide domains. To visualize these spatial elements more clearly, we take the Laplacian $\nabla^2 R$ of Fig. 3, C and D (Fig. 3, E and F). At atomic scale, we then see an electronic structure consisting of a_0-length elements distributed in a disordered fashion along both Cu-O directions. Within this matrix are embedded $4a_0$-wide unidirectional regions or "domains." These domains, because they are periodic along the long axis, appear to be ordered. Repeating $4a_0$-wide domains of this type are always unidirectional, extending along one or other Cu-O direction. Thus, at the nm scale, the electronic structure of these lightly hole-doped cuprates breaks both C_4 symmetry and translational symmetry of the ideal square crystal lattice.

In Fig. 4, A and D, we show higher-resolution studies of equivalent domains from Na-CCOC and Dy-Bi2212, respectively (at the fine blue boxes of Fig. 3, C and D). Here the *R* maps are rotated to put a CuO axis, and thus the domain axis, vertical. The pairs of dark lines (representing high TA) in *R* maps indicated by the arrows are precisely $4a_0$ apart and represent the perimeter of a single domain. In Fig. 4, A and D, unidirectional, $4a_0$-wide domains run from the bottom to the top of each image, exhibiting virtual vertical mirror symmetry in both materials.

We next examine, in Fig. 4, B and E, the internal structure of the domains (at the boxes of Fig. 3, A and B, and Fig. 4, A and D) with identification of atomic sites from the simultaneous topographs (Fig. 4, C and F, respectively). We see immediately that the primary spatial variations in the *R* maps are concentrated, not on the Cu sites, but rather on the O site within each Cu-O-Cu bond. Here the domain's symmetry axis is along a vertical line starting at the arrows labeled 1. Along this axis are a line of oxygen sites, each within a horizontal Cu-O-Cu bond and all exhibiting high *R*. The vertical line labeled 2 is the line of vertical Cu-O-Cu bonds; these oxygen sites exhibit low *R*. Thus, *R* is very different for the horizontal Cu-O-Cu bonds transverse to line 1 and the vertical Cu-O-Cu bonds along line 2, even though these bonds share a Cu atom on the corner of the same plaquette. The next vertical line of Cu atoms away from the axis is labeled 3, and line 4 represents the line of oxygen sites that is $2a_0$ to the right of axis 1. The sequence of horizontal Cu-O-Cu bonds along line 4 exhibits a uniformly low *R*. These patterns exhibit mirror symmetry about the vertical axis 1—meaning that the whole domain is precisely $4a_0$ wide. We find these uniaxial domains in all *R* maps—randomly dispersed with equal probability of orientation along the two Cu-O axes (Fig. 3, E and F) and with virtually identical structure in both materials.

A noteworthy observation here is that the O sites within Cu-O-Cu bonds, even though crystallographically equivalent, are in electronically inequivalent states (Figs. 3 and 4). In general, the spatial arrangements of these Cu-O-Cu bond states exhibit no long-range order. Nonetheless, there are clear short-range relations between them: Sequential vertical or horizontal Cu-O-Cu bonds along a vertical axis can all be in the same state, whereas the Cu-O-Cu bonds at 90° to each other and sharing a corner Cu atom are electronically inequivalent. Most notably, these TA images indicate that the cuprate electronic "cluster glass" (*8*–*21*) stems from spatial variations in the electronic state of each Cu-O-Cu bond.

Atomic-scale electronic structure within the $4a_0$-wide domains. Next, we consider the energy dependence of electronic structure of the domains in Fig. 4. Although dI/dV images are not simply related to spatial arrangements of LDOS, individual dI/dV spectra still retain much physical importance—especially in the

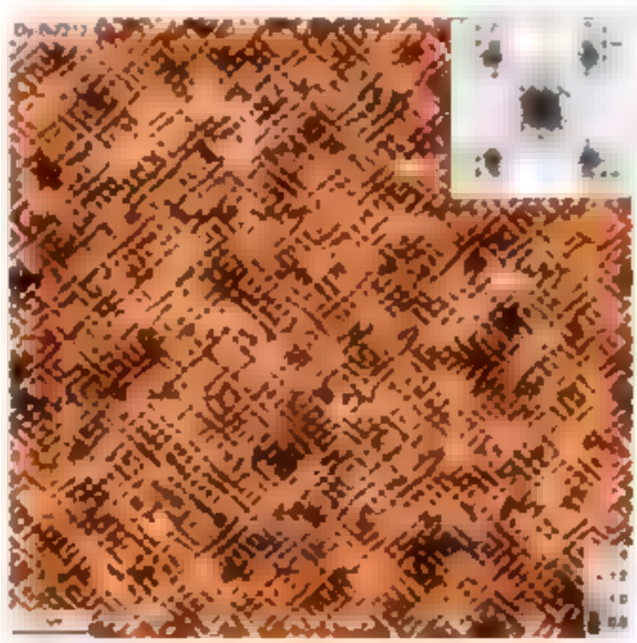

Fig. 6. A 25-nm^2 *R* map; no long-range order is apparent. Instead, we see randomly distributed electronic variations of the Cu-O-Cu bond state with equal probability of orientation along the two Cu-O axes. The Cu-O bond directions are shown as pairs of orthogonal black arrows. The inset shows its Fourier transform. The predominant peaks occur at wave vectors $\vec{q}$ = (3/4,0) and (0,3/4) in units $2\pi/a_0$ (orange arrows), and the peaks at $\vec{q}$ = (1/4,0) and (0,1/4) (blue arrows) are weaker. Atomic peaks $\vec{q}$ = (1,0) and (0,1) are shown by black arrows.

energy value at which their key features occur. To clarify the locations, relative to the O and Cu orbitals in the CuO_2 plane, of each dI/dV spectrum measured on the surfaces of Fig. 4, C and F, we show a schematic in Fig. 5A. The dI/dV spectra are measured along equivalent lines labeled 1, 2, 3, and 4 in both domains of Fig. 4, B and E, and Fig. 5A. The nine spectra (a to i) along lines labeled 1 and 4 are taken at a sequence of five planar oxygen sites with four empty sites in between, whereas those along lines 2 and 3 are taken at a sequence of five planar copper sites with four oxygen sites in between. In both materials, they reveal similar spatial evolutions. Line 1 shows spectra with minimal TA and clear low-energy features (at −10 meV in Na-CCOC and ~20 meV in Dy-Bi2212); line 2 exhibits rapid TA fluctuations but low-energy features similar to those of line 1; line 3 shows higher TA; and line 4 shows the highest TA with weak low-energy features. These patterns of dI/dV spectra exhibit mirror symmetry about the domain's vertical axis. All spectra show a pronounced feature at $E \sim +100$ meV with a related feature near $E \sim -100$ meV but masked by the rapid rise due to tunneling asymmetry. The low-energy features, whether of peaks (lines 1 and 2) or shoulders (lines 3 and 4), appear at ~ −10 meV for Na-CCOC and ~ −20 meV for Dy-Bi2212 with a clear reduction of dI/dV toward $E = 0$. These types of spectral shapes, and the different energy ranges in samples with different T_c, may indicate their relation to the superconductivity.

Long-range electronic structure. Returning to the largest scales, the R map shown in Fig. 6 spans a 25-nm^2 field of view. No long-range order can be detected (even out to 50 nm; fig. S3). But the Fourier transform of such R maps (inset to Fig. 6) reveals further surprises. The predominant peaks occur at wave vectors $\vec{q} \sim (3,4,0)$ and $(0,3,4)$ (in units of $2\pi/a_0$), whereas the peaks at $\vec{q} \sim (1,4,0)$ and $(0,1,4)$ that would be expected trivially from a $4a_0 \times 4a_0$ modulation are weaker. We find that these characteristic TA modulations at $\vec{q} \sim (3,4,0)$ and $(0,3,4)$ occur not because of mixing between $(3,4,0)$ and $(1,0)$, but primarily because three maxima in R typically exist within each $4a_0$-wide domain.

Discussion and conclusions. Because we find virtually identical phenomena in Na-CCOC and Dy-Bi2212 samples of radically different physical, chemical, and dopant structure, material-specific explanations (*34*, *35*) for the TA effect can be ruled out. Instead, we consider these phenomena to be intrinsic electronic characteristics of the CuO_2 plane. Furthermore, the effects reported here cannot be governed by individual dopant atoms because there is only a single dopant atom for every ~20 Cu-O-Cu bonds and, in any case, they occur at quite different locations in the unit cells of Na-CCOC and Dy-Bi2212. Similarly, the creation by random dopant distributions of virtually identical unidirectional $4a_0$-wide electronic domains in both materials (Fig. 4) appears extremely unlikely. Indeed, the spatial arrangements of electronic structure revealed by TA imaging (Figs. 3, 4, and 6), rather than exhibiting a random patchy configuration as expected if dopant disorder predominates, occur because of variations in the electronic state at each Cu-O-Cu bond. Such a bond-centered electronic glass, if intrinsic and universal to cuprates, would provide a plausible and consistent explanation for why long-range spin charge-ordered states are not detected at low doping.

Tunneling asymmetry measurements are designed to yield key information on how correlations affect electronic structure of the hole-doped cuprates (*4*, *5*). But the primary spatial contrast in TA images, although undoubtedly electronic, has not yet been independently calibrated for the degree of charge-density variations it represents and may also contain quantum interference effects (*35*). In addition, the relation between the higher-energy R maps and the low-energy dI/dV maps is incompletely understood. For example, Fourier transforms of dI/dV images at $E < 50$ meV reveal "checkerboard" dI/dV modulations with peaks at $\vec{q} \sim (0,3,4)$ and $(3,4,0)$ (*6*). This implies two, at present indistinguishable, possibilities about the relations between R maps and dI/dV maps: (i) The physical entity of the bond-centered domains may appear differently in the two experimental quantities (see supporting online text 1); and or (ii) the localized electronic domains affect delocalized low-energy states, possibly via scattering interference (*36*). But independent of which explanation for "checkerboard" dI/dV modulations holds, these new TA-imaging techniques are well defined, avoid the systematic errors from $f(\vec{r},z)$ in dI/dV imaging, access higher-energy scales than previously, and may reveal insightful new physical information (*37*–*39*).

Because the TA images always contain $4a_0$-wide unidirectional patterns, an obvious question is whether they are segments of the charge/spin-ordered "stripes" (*37*–*41*). It is argued from neutron scattering that $4a_0$-wide unidirectional long-range charge order forms the basis of static stripes (*42*, *43*). Consistent with this picture, resonant X-ray scattering in $La_{1.875}Ba_{0.125}CuO_4$ reveals $4a_0$-periodic modulations of hole density at oxygen sites (*44*). But the complete atomic-scale electronic structure of a cuprate "stripe" is unknown because direct spectroscopic imaging has been unachievable. Our TA data on $4a_0$-wide unidirectional domains (Figs. 3, 4, and 5) seem consistent with the experimental understanding (*42*–*44*) of the "stripes" in La-based cuprates, except that here there is no long-range order [consistent with results from (*45*)]. A possible explanation is that a Cu-O-Cu bond-centered electronic glass, although ubiquitous in cuprates at low hole doping, may be converted to long-range static "stripe" order due to unique crystal symmetry and commensuration in $La_{2-x}Ba_xCuO_4$ and $La_{1.6-x}Nd_{0.4}Sr_xCuO_4$ at $x = 1/8$. In any case, direct detection of $4a_0$-wide unidirectional electronic domains by STM represents an exciting opportunity to determine the internal electronic structure of a cuprate "stripe" (Fig. 4). Furthermore, because our data appear consistent with the "cluster" phenomenology (*8*, *21*, *23*–*25*), the $4a_0$-wide electronic domains also represent excellent candidates to be the ubiquitous "clusters" of the ECG state.

Finally, our samples also exhibit the tenuous d-wave superconductivity of lightly hole-doped cuprates. This coexists spatially with the bond-centered tunneling asymmetry patterns described here. A priori, the TA contrast represents variations in the ratio of probability of electron extraction to injection, implying atomically varying probability of electronic occupancy. By contrast, the superconductivity consists of delocalized d-wave electron pairs. How such disparate effects can coexist at low doping, and how the full delocalization (*25*) associated with highest-temperature superconductivity emerges from this state with increased doping, remain to be determined.

References and Notes

1. J. Zaanen, G. A. Sawatzky, J. W. Allen, *Phys. Rev. Lett.* **55**, 418 (1985).
2. C. T. Chen *et al.*, *Phys. Rev. Lett.* **66**, 104 (1991).
3. M. B. J. Meinders, H. Eskes, G. A. Sawatzky, *Phys. Rev. B* **48**, 3916 (1993).
4. P. W. Anderson, N. P. Ong, *J. Phys. Chem. Solids* **67**, 1 (2006).
5. M. Randeria, R. Sensarma, N. Trivedi, F.-C. Zhang, *Phys. Rev. Lett.* **95**, 137001 (2005).
6. T. Hanaguri *et al.*, *Nature* **430**, 1001 (2004).
7. K. McElroy *et al.*, *Phys. Rev. Lett.* **94**, 197005 (2005).
8. Y. J. Uemura *et al.*, *J. Phys. (Paris) Colloq.* **49**, 2087 (1988).
9. D. R. Harshman *et al.*, *Phys. Rev. B* **38**, 852 (1988).
10. Ch. Niedermayer *et al.*, *Phys. Rev. Lett.* **80**, 3843 (1998).
11. C. Panagopoulos *et al.*, *Phys. Rev. B* **66**, 064501 (2002).
12. A. T. Savici *et al.*, *Phys. Rev. B* **66**, 014524 (2002).
13. S. Sanna, G. Allodi, G. Concas, A. D. Hillier, R. De Renzi, *Phys. Rev. Lett.* **93**, 207001 (2004).
14. J. Haase, C. P. Slichter, C. T. Milling, *J. Supercond.* **15**, 339 (2002).
15. H.-J. Grafe, M. J. Curro, M. Hücker, B. Büchner, *Phys. Rev. Lett.* **96**, 017002 (2006).
16. J. H. Cho, F. Borsa, D. C. Johnston, D. R. Torgeson, *Phys. Rev. B* **46**, 3179 (1992).
17. F. C. Chou *et al.*, *Phys. Rev. Lett.* **71**, 2323 (1993).
18. M.-H. Julien *et al.*, *Phys. Rev. Lett.* **83**, 604 (1999).
19. P. M. Singer, A. W. Hunt, T. Imai, *Phys. Rev. Lett.* **88**, 047602 (2002).
20. R. Ofer, S. Levy, A. Kanigel, A. Keren, *Phys. Rev. B* **73**, 012503 (2006).
21. E. S. Bozin, G. H. Kwei, H. Takagi, S. J. L. Billinge, *Phys. Rev. Lett.* **84**, 5856 (2000).
22. V. J. Emery, S. A. Kivelson, *Physica C* **209**, 597 (1993).
23. H. Takagi *et al.*, *Phys. Rev. Lett.* **69**, 2975 (1992).
24. Y. Ando, G. S. Boebinger, A. Passner, T. Kimura, K. Kishio, *Phys. Rev. Lett.* **75**, 4662 (1995).
25. F. F. Balakirev *et al.*, *Nature* **424**, 912 (2003).
26. L. Li *et al.*, *J. Magn. Magn. Mater.* 10.1016/j.jmmm.2006.10.535 (2006).
27. W. J. Padilla, M. Dumm, S. Komiya, Y. Ando, D. N. Basov, *Phys. Rev. B* **72**, 205101 (2005).
28. J. M. Tranquada, N. Ichikawa, S. Uchida, *Phys. Rev. B* **59**, 14712 (1999).
29. O. Parcollet, A. Georges, *Phys. Rev. B* **59**, 5341 (1999).
30. G. Alvarez, M. Mayr, A. Moreo, E. Dagotto, *Phys. Rev. B* **71**, 014514 (2005).
31. J. Schmalian, P. G. Wolynes, *Phys. Rev. Lett.* **85**, 836 (2000).
32. M. Hasselmann, A. H. C. Neto, C. M. Smith, Y. Dimashko, *Phys. Rev. Lett.* **82**, 2135 (1999).

33. S. A. Kivelson, E. Fradkin, V. J. Emery, *Nature* **393**, 550 (1998).
34. S. E. Brown, E. Fradkin, S. A. Kivelson, *Phys. Rev. B* **71**, 224512 (2005).
35. Y. Chen, T. M. Rice, F. C. Zhang, *Phys. Rev. Lett.* **97**, 237004 (2006).
36. L. Capriotti, D. J. Scalapino, R. D. Sedgewick, *Phys. Rev. B* **68**, 014508 (2003).
37. N. Read, S. Sachdev, *Phys. Rev. Lett.* **62**, 1694 (1989).
38. J. Zaanen, O. Gunnarsson, *Phys. Rev. B* **40**, 7391 (1989).
39. S. R. White, D. J. Scalapino, *Phys. Rev. Lett.* **80**, 1272 (1998).
40. V. J. Emery, S. A. Kivelson, J. M. Tranquada, *Proc. Natl. Acad. Sci. U.S.A.* **96**, 8814 (1999).
41. S. Sachdev, *Rev. Mod. Phys.* **75**, 913 (2003).
42. J. M. Tranquada, B. J. Sternlieb, J. D. Axe, Y. Nakamura, S. Uchida, *Nature* **375**, 561 (1995).
43. J. M. Tranquada *et al.*, *Nature* **429**, 534 (2004).
44. P. Abbamonte *et al.*, *Nat. Phys.* **1**, 155 (2005).
45. S. Smadici *et al.*, *Phys. Rev. B* **75**, 075104 (2007).

46. We acknowledge and thank P. Abbamonte, P. W. Anderson, E. Dagotto, S. A. Kivelson, D.-H. Lee, A. P. Mackenzie, N. P. Ong, M. Randeria, T. M. Rice, S. Sachdev, A. Sandvik, G. A. Sawatzky, D. J. Scalapino, J. M. Tranquada, N. Trivedi, S. R. White, Y. J. Uemura, J. Zaanen, and F. C. Zhang for helpful conversations and communications. This work was supported by the U.S. Department of Energy, Office of Naval Research, Natural Sciences and Engineering Research Council of Canada, Grant-in-Aid for Scientific Research from the Ministry of Science and Education (Japan), and the 21st-Century Centers of Excellence Program for the Japan Society for the Promotion of Science. Fellowship support is acknowledged by K.F. from I²CAM and by A.S. from the Army Research Office.

Supporting Online Material

www.sciencemag.org/cgi/content/full/1138584/DC1
SOM Text
Figs. S1 to S3
References

8 December 2006; accepted 26 January 2007
Published online 8 February 2007;
10.1126/science.1138584
Include this information when citing this paper.

REPORTS

Super Plastic Bulk Metallic Glasses at Room Temperature

Yan Hui Liu, Gang Wang, Ru Ju Wang, De Qian Zhao, Ming Xiang Pan, Wei Hua Wang*

In contrast to the poor plasticity that is usually observed in bulk metallic glasses, super plasticity is achieved at room temperature in ZrCuNiAl synthesized through the appropriate choice of its composition by controlling elastic moduli. Microstructures analysis indicates that the super plastic bulk metallic glasses are composed of hard regions surrounded by soft regions, which enable the glasses to undergo true strain of more than 160%. This finding is suggestive of a solution to the problem of brittleness in, and has implications for understanding the deformation mechanism of, metallic glasses.

High strength has been a long-standing objective pursued in metals and alloys and was often achieved through the reduction of grain size (*1*). However, with increasing strength, plasticity is normally reduced. This trend has persisted in nanocrystalline metals and alloys, which display highly improved strength but very little plastic deformation (*2*), and in bulk metallic glasses (BMGs) with completely disordered atomic structures. BMGs have strengths approaching the theoretical limit (~Young's modulus E/10) (*3*), but their plasticity at room temperature is very low. In uniaxial tension, the plastic strain is near zero (*4*). Even under compression, the plastic strain still remains very limited (<2%), resulting from shear localization and work softening. Lack of plasticity makes BMGs prone to catastrophic failure in load-bearing conditions and restricts their widespread application. This also hinders precise study on some fundamental issues in glasses such as the deformation mechanism and the dynamics of plastic deformation, in which large plasticity is needed for detailed analysis (*5*).

Plastic deformation of metallic glasses at room temperature occurs through the formation and evolution of shear bands and is localized in a few shear bands. Therefore, brittleness is regarded as an intrinsic defect of metallic glasses. Efforts have been made to enhance the plasticity of BMGs, but most focus on the fabrication of BMG composites (*6*–*9*). It is expected that the formation of multiple shear bands throughout a sample is needed for improving its plasticity because each band contributes to the plasticity and none carry enough deformation to cause catastrophic failure (*10*). By careful selection of their compositions, several BMGs have been found to exhibit substantially increased plasticity (*4*, *6*, *9*). However, the hypotheses have not been fully verified, and methods for controlling the formation and evolution of shear bands in BMGs to improve their plasticity is a remaining challenge.

It was recently found that the toughness of BMGs correlates with Poisson's ratio ν (*11*). A large ν is regarded as an indicator of the plastic character of a BMG and could therefore be used as a means of identifying plastic BMGs (*9*). This idea was verified in a ductile Pt-based BMG (*9*) and in brittle Mg-based BMGs (*12*), as well as in Fe-based BMGs that display crossover from brittle to ductile behavior via the control of ν (*13*). Furthermore, it was also found that elastic

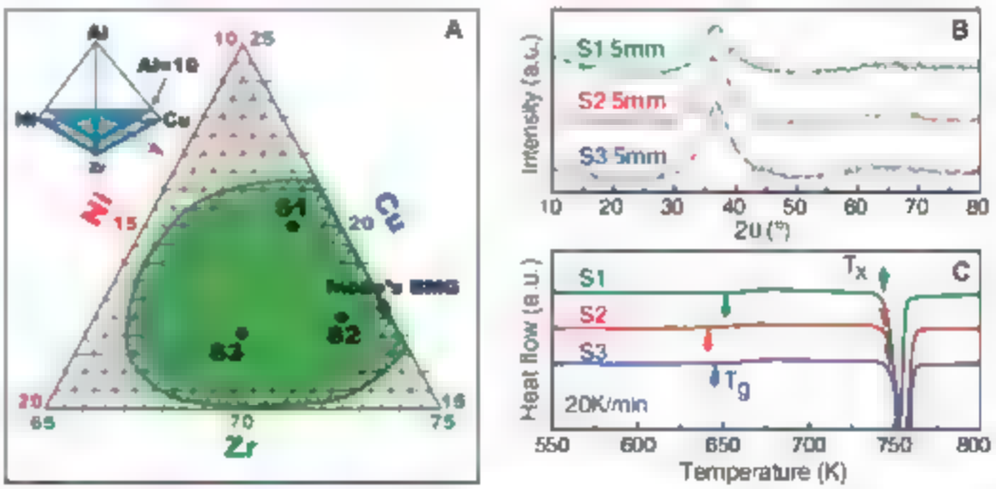

Fig. 1. (**A**) A family of quaternary ZrCuNiAl BMGs is obtained in the composition range (green area). In three compositions (circles labeled S1 to S3), ν is larger relative to that of other compositions (the values for ν of the ZrCuNiAl BMGs with poor plasticity are normally around 0.365). The representative Inoue's BMG is included for comparison. (**B**) XRD patterns of the BMGs in the form of 5-mm rods show no crystals. (*I*, XRD scattering angle; a.u., arbitrary units. (**C**) DSC curves exhibit distinct glass transition and crystallization, confirming the glassy nature of the as-cast super plastic BMGs (the heating rate is 20 K/min).

Institute of Physics, Chinese Academy of Sciences, Beijing 100080, China.

*To whom correspondence should be addressed. E-mail: whw@aphy.iphy.ac.cn

constants of metallic glasses scale with the weighted averages of those of their components (*14*). Therefore, the elastic moduli provide useful guidelines for the development of plastic BMGs with large ν by the appropriate choice of their composition.

In this study, a family of BMGs consisting of conventional metallic components Zr, Cu, Ni, and Al was obtained. Through compositional changes, we created BMGs that have relative large ν values and display an ability to undergo superplasticity-like deformation behavior at room temperature. The exceptional deformability is ascribed to the homogeneous and concurrent nucleation and evolution of high-density shear bands throughout the samples, which are composed of hard regions surrounded by soft regions.

The BMGs were prepared by arc melting the pure elements under a purified Ar atmosphere and in situ suction casting in a Cu mold. The amorphous nature of the as-cast alloys was ascertained by x-ray diffraction (XRD), differential scanning calorimetry (DSC) with a heating rate of 20 K/min, transmission electron microscopy (TEM), and high-resolution TEM (HRTEM). Elastic moduli of the BMGs were monitored by means of an ultrasonic method (*14*). The samples with a gauge aspect ratio of 2:1 were cut out of the as-cast 2-mm rods for uniaxial compression tests.

A family of quaternary Zr-Cu-Ni-Al BMGs was obtained with the compositions shown in the green area of Fig. 1A. Acoustic measurements show that some compositions, such as $Zr_{61.88}Cu_{18}Ni_{10.32}Al_{10}$, $Zr_{64.13}Cu_{15.75}Ni_{10.12}Al_{10}$, and $Zr_{62}Cu_{15.5}Ni_{12.5}Al_{10}$ (labeled as S1, S2, and S3, respectively), exhibit larger values of ν relative to that of other BMGs in this composition range (Table 1). However, their densities are very similar (Table 1). Figure 1B shows that these BMGs can be cast into entirely glassy rods with diameters up to 5 mm without the observation of any apparent crystalline Bragg peaks. Clear glass transitions and sharp crystallization events are observed in the DSC traces (Fig. 1C), confirming the glassy nature of the BMGs. The thermal parameters are also summarized in Table 1.

Multiple compression tests were performed at room temperature on compositions S1 to S3. Figure 2A shows the true stress–true strain curve of S2 and those of S1 and S3 are shown in the inset. Similar to other typical BMGs, S1, S2, and S3 exhibit elastic strain limits of ~2%, before yielding at 1733, 1690, and 1851 MPa, respectively. However, after yielding, the materials display stress overshoot, as is often observed in superplastic deformation in the supercooled liquid state (*15*, *16*). True strains as large as ~160% were achieved. As a result of such intense deformation, the BMG rods were compressed into flakes (Fig. 2B) without fracturing. The diameter of the flakes is more than 5 mm and could be expanded to larger sizes, implying high flowability of the BMGs. Moreover, the BMGs could be bent into desired shapes (Fig. 2C) similar to flexible metals such as Al and Cu. The maximum bending angle approaches 90° in both rods and plates. Such unusual degrees of plasticity and flexibility were previously obtained for BMGs in a supercooled liquid state at high temperatures (*17*).

As shown in Fig. 2A, the flow stress of S2 increases with increasing strain after stress overshoot. However, the rapid increase of flow stress (when strain is ~80%) is not due to the strain-hardening. We conducted compression tests on S2 and unloaded at different plastic strains. As shown in Fig. 2D, the samples' barrel-like shape implies that friction occurs at the contact surfaces between the sample and the tungsten carbide platens (*18*). The friction would increase flow stress, especially in the late stage of deformation because of the large increase of transversal area of the specimen and thus the decreased aspect ratio (*19*). The hardness of the heavily deformed flake is only slightly greater than that of the as-cast sample, suggesting that only negligible strain-hardening occurs. Consistent with previous work (*20*, *21*), the deformation of the BMGs also exhibits strain-rate softening and serrated flow behaviors.

Unlike in crystalline metals, dislocation-mediated deformation is not available in BMGs. The formation and evolution of shear bands are the main processes that account for the plasticity of BMGs, especially at low temperatures. Scanning electron microscope (SEM) observations on the specimen surface are given in Fig. 3. Figure 3A shows two important features of shear bands at true plastic strain of 2.7%. First, the uniform shear bands, including premature shear bands, are formed in different directions even at the initial stage of the plastic deformation. This results from the interaction of the shear bands that alter surrounding stress fields and bring an increased local stress level (*22*) to compensate the shear band–induced softening (*8*). The premature bands would carry further plastic strain, avoiding the occurrence of catastrophic failure. Second, the shear bands appear wavy. The periodicity of the wave is about 1 to 3 μm, which is consistent with the size of the hard regions in the glasses. In addition, wing-like shear bands were formed along the primary shear bands (black arrows in Fig. 3A) and even along the premature wavy shear bands (white arrows in Fig. 3A, inset). The wing-like bands can be extended and joined together to sustain ever-increasing deformation. After true plastic strain of ~160%, a high density of shear bands is formed (Fig. 3B). The BMGs have evolved into polycrystal-like patterns with shear bands serving as "grain boundaries." Nanoscale cracks were also found, but none of them earned enough deformation to cause specimen fracture. The BMGs seem to deform in a

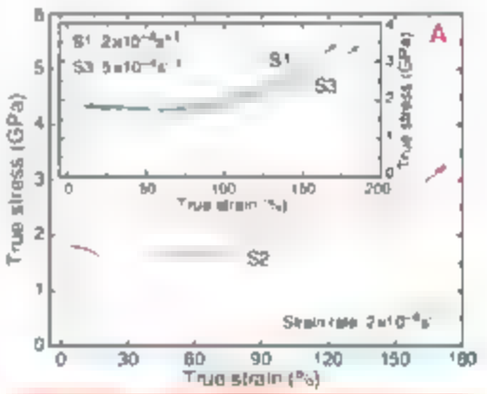

Fig. 2. (**A**) True stress–true strain curve of S2 tested at room temperature. The inset shows those of S1 and S3. The strain rate imposed is 2×10^{-4} s^{-1} for S1 and S2 and 5×10^{-4} s^{-1} for S3, respectively. (**B**) Compressed flakes of S1, S2, and S3. (**C**) S2 bent into different shapes, showing exceptional deformability. (**D**) S2 deformed to various nominal strains. A barrel shape can be seen, which implies that friction between the sample and the platens occurred.

Table 1. Glass transition temperature T_g, crystallization temperature T_x, obtained by DSC at a heating rate of 20 K/min, and elastic constants (*E*, the shear modulus *G*, the bulk modulus *K*, and ν) measured by an ultrasonic method for the superplastic BMGs and a representative BMG (Inoue's Zr-Cu-Ni-Al BMG) in the green BMG-forming composition range indicated in Fig. 1A are shown. The range of values for ν of the Zr-Cu-Ni-Al BMGs with poor or limited plasticity in the composition range is from 0.350 to 0.375. ρ, density.

BMG	T_g (K)	T_x (K)	ρ (g/cm^3)	*E* (GPa)	*G* (GPa)	*K* (GPa)	ν
$Zr_{61.88}Cu_{18}Ni_{10.32}Al_{10}$ (S1)	653	744	6.649	80.12	29.10	108.33	0.377
$Zr_{64.13}Cu_{15.75}Ni_{10.12}Al_{10}$ (S2)	643	745	6.604	78.41	28.46	106.63	0.377
$Zr_{62}Cu_{15.5}Ni_{12.5}Al_{10}$ (S3)	652	748	6.615	79.65	28.89	109.03	0.378
Inoue's $Zr_{65}Cu_{15}Ni_{10}Al_{10}$			6.642	82.96	30.27	106.65	0.355

microscopically near-homogeneous manner through profuse and concurrent shear-band formation (9), even though the plastic strain is localized. The case resembles that of crystals, where plastic strain is localized in slip bands.

In order to correlate the extraordinary plasticity of the glasses with their structure, TEM investigations were performed to reveal their microstructural features. Figure 4A shows the bright-field image of the as-cast S2. The most notable characteristic is that the BMGs are composed of isolated dark zones, ranging from 2 to 5 μm in size, that are surrounded by continuous bright zones, which are about 0.5 to 1 μm in width. The volume fraction of the bright zones is estimated to be ~10%. The strong contrast indicates that the bright zones are thinner than the dark ones, implying a higher thinning rate in the bright zones under the ion beam, which comes from the difference in mass-to-thickness contrast produced by the lower density of the bright zones, where holes even occur (Fig. 4A). Similar microstructures are observed for S1 and S3 (Fig. 4C and fig. S1) but cannot be found in a conventional BMG (Fig. 4D), indicating that this is not an artifact from TEM sample preparation. The selected-area electron diffraction (SAED) patterns in both bright and dark zones are halo rings, confirming the glassy nature in both zones. No traces of phase separation, which occurs usually on the nanoscale (3), were observed. The energy-dispersive x-ray analysis did not show any substantial composition variation in both bright and dark zones, excluding the possibility of the occurrence of phase separation (3) (fig. S2). The detailed structure of the bright and dark zones was also examined by means of HRTEM (Fig. 4B). The similar mazelike patterns without any crystalline fringe, which are typical features of glass, can be widely observed. Instrumented nanoindentation tests on the as-cast superplastic BMGs show that a large fluctuation of load is exposed to a specific identical depth (500 nm, corresponding to an indentation size of ~4 μm) (fig. S3), which indicates strength variations in the glasses. The structural studies confirm the chemical and compositional homogeneity and single-glassy nature of the BMGs. However, the preferential thinning in the bright zones indicates that the bright zones are softer than the dark zones or that there are much more thermally unstable atomic-scale open volumes existing in the bright zones (24, 25). A similar structural feature has also been found in Pd-based BMGs (26). We suggest a microstructure composed of hard regions surrounded by soft regions (with larger values of v), in the superplastic BMGs. The slight increase in the fraction of the soft regions would augment v steeply without substantial changes in overall density (26). The relatively large v value of these BMGs, which was determined by an ultrasonic method, is an indicator of the high concentration of such open volumes in the glasses. The question of what gives rise to this distinctive structural feature is a challenging subject for the future.

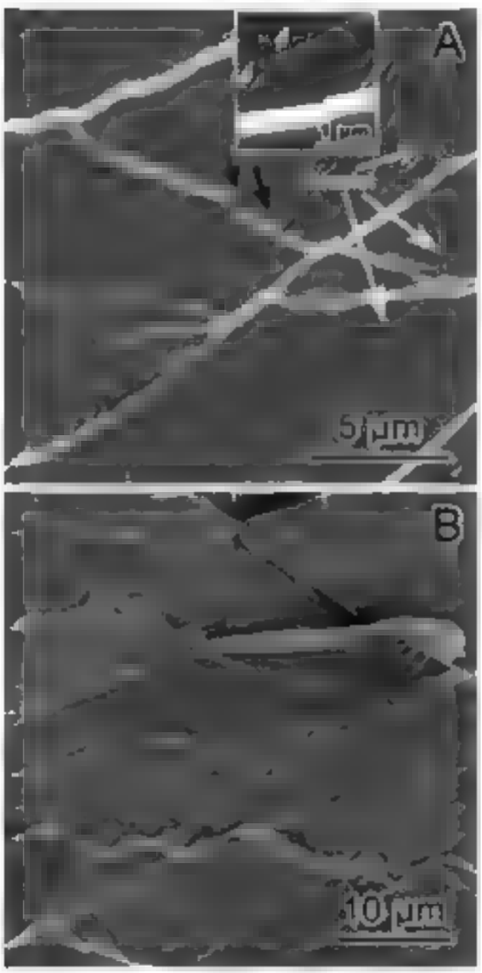

Fig. 3. The SEM images of the surface of the S2 specimen deformed to true plastic strain of ~2.7% (**A**) and ~159% (**B**), respectively. The shear bands in (A) appear wavy, and the length of the wave is comparable to that of the dark regions in Fig. 4, (A) and (B). Black arrows indicate winglike shear bands. Nuclei, shear-band nuclei. The inset shows winglike shear bands along the premature wavy ones (arrows).

A possible explanation for the origin of the concurrent and homogeneous formation of copious shear bands, and hence the extreme deformability, is based on the distinctive structure of the BMGs. The shear transformation zones (27), which begin as small regions where the local atomic structure is capable of rearrangement under an applied shear stress, serve as the nucleation sites for the shear bands. The ability of a region to undergo a shear transformation depends on the local microstructure (28). The shear transformation zones occur preferentially in soft regions in BMGs and evolve into shear bands upon loading. Consequently, numerous shear-band nuclei are formed concurrently in the soft regions. However, the shear-band propagation would be impeded by the hard regions. This impedance alters the propagating directions and assists shear-band multiplication, resulting in the wavelike appearance of the shear bands and the formation of wing bands. The interactions between the shear bands and hard regions would compensate the softening induced by their formation (8). The consistency between the wavy periodicity of shear bands in Fig. 3A and that of hard regions in Fig. 4 supports the assumption. Because the soft regions cannot carry more plastic strain, further plastic deformation has to proceed in hard sections so that more plasticity is still attainable. These factors imbue the BMGs with superplasticity. HRTEM observations do not reveal nanocrystals even in heavily deformed flakes. This indicates that the superplasticity is not a result from the stress-induced nanocrystallization as found in other BMGs (29); instead, it is an intrinsic property. Annealing of the BMGs below the glass transition temperature dramatically decreases the plasticity, because the annealing can remove thermally unstable atomic-scale open volumes that exist in the soft regions, decreasing the fraction of the soft regions and increasing v (30, 31). On the other hand, the introduction of a high population of preexisting

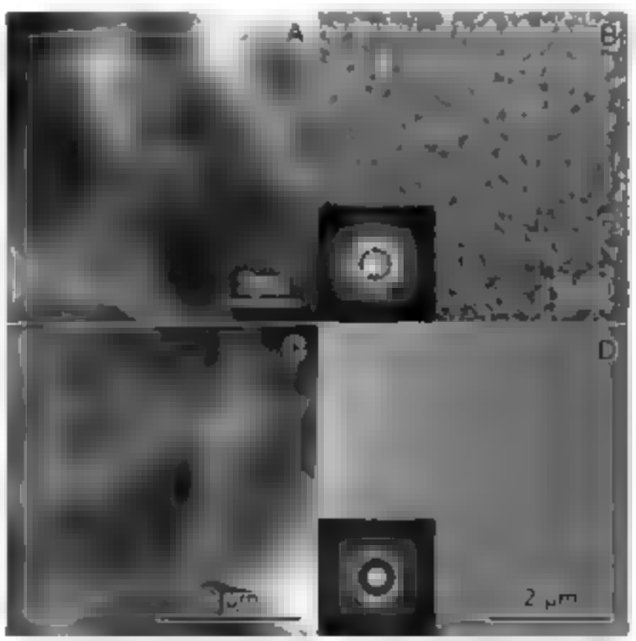

Fig. 4. (**A**) TEM image of S2 showing dark regions surrounded by bright regions (corresponding to hard and soft regions, respectively), in which some soft regions were thinned into holes. (**B**) HRTEM images show mazelike patterns that confirm the glassy nature of the BMGs. The insets in (B) and (D) show SAED patterns. In both dark and bright regions, HRTEM and SAED patterns are identical, implying that no phase separation occurs. Similar structures are also found in S1 (**C**). However, the structures are not observed in conventionally brittle BMGs, such as $Zr_{59.63}Cu_{15.75}Ni_{14.62}Al_{10}$ (**D**).

shear bands can dramatically increase plasticity of BMGs (*32*). These results confirm that a structural feature is the cause of the super plasticity of the BMGs, and the homogeneous and concurrent formation of multiple shear bands throughout the samples is crucial for the improvement of plasticity in BMGs.

This unusual plasticity can shed light on some fundamental issues on the deformation and fracture of BMGs, such as the dynamics of plastic deformation (*5*). We measured the evolution of shear-band spacing d with increasing nominal strain ε. It was found that d correlates with ε via a power-law relation ($d = A\varepsilon^{-B}$) where A is a constant and $B = 1.45$, which is different from the value obtained by decreasing the sample's aspect ratio (height/diameter) to less than 1.0 (*8*).

Similar to the glass-forming ability of BMG-forming alloys (*33*), the super plasticity of the BMGs is very sensitive to their composition. Minor deviations in content (~1 atomic %) can substantially change the plasticity of the BMGs. The results indicate that, even in the reported BMG systems, extraordinarily plastic BMGs may be obtained by the appropriate choice of their composition with the use of the Poisson's ratio strategy. The present investigation has focused on Zr-based BMGs. We expect that the strategy would provide useful guidelines for the development of super plastic BMGs as high-performance structural materials in other known or unknown BMG-forming alloys and open an area of research of both fundamental and applied importance.

References and Notes

1. J. Schiøtz, K. W. Jacobsen, *Science* **301**, 1357 (2003).
2. K. S. Kumar, H. V. Swygenhoven, S. Suresh, *Acta Mater.* **51**, 5743 (2003).
3. A. L. Greer, *Science* **267**, 1947 (1995).
4. L. D. Jiang, Y. Li, R. B. Ramesh, J. Li, T. C. Hufnagel, *Phys. Rev. B* **64**, 180201 (2001).
5. D. M. Dimiduk, C. Woodward, R. deSar, M. D. Uchic, *Science* **312**, 1188 (2006).
6. J. Das *et al.*, *Phys. Rev. Lett.* **94**, 205501 (2005).
7. Z. F. Zhang, H. Zhang, X. F. Pan, J. Das, J. Eckert, *Philos. Mag. Lett.* **85**, 513 (2005).
8. H. Bei, S. Xie, E. P. George, *Phys. Rev. Lett.* **96**, 105503 (2006).
9. J. Schroers, W. L. Johnson, *Phys. Rev. Lett.* **93**, 255506 (2004).
10. F. Ma, *Mat. Manuf.* **2**, 7 (2003).
11. J. J. Lewandowski, W. H. Wang, A. L. Greer, *Philos. Mag. Lett.* **85**, 77 (2005).
12. Q. Zheng, H. Ma, E. Ma, J. Xu, *Scripta Mater.* **55**, 541 (2006).
13. X. J. Gu, A. G. McDermott, S. J. Poon, G. J. Shiflet, *Appl. Phys. Lett.* **88**, 211905 (2006).
14. W. H. Wang, *J. Appl. Phys.* **99**, 093506 (2006).
15. J. Lu, G. G. Ravichandran, W. L. Johnson, *Acta Mater.* **51**, 3429 (2003).
16. Y. Kawamura, A. Inoue, T. Masumoto, *Appl. Phys. Lett.* **71**, 779 (1997).
17. F. Spaepen, *Acta Mater.* **25**, 407 (1977).
18. F. El-Agoury, J. S. Plante, A. H. Slocum, J. K. Vogan, *Rev. Sci. Instrum.* **76**, 075108 (2005).
19. M. M. Charalambides, S. M. Goh, L. Wanigasooriya, J. G. Williams, W. Xiao, *J. Mater. Sci.* **40**, 3375 (2005).
20. T. Mukai, T. G. Nieh, Y. Yoshihiko, A. Inoue, K. Higashi, *Intermetallics* **10**, 1071 (2002).
21. T. C. Hufnagel, T. Jiao, Y. Li, K. T. Ramesh, *J. Mater. Res.* **17**, 1443 (2002).
22. W. J. Wright, R. Saha, W. D. Nix, *Mater. Trans.* **42**, 642 (2001).
23. J. Eckert *et al.*, *Intermetallics* **14**, 876 (2006).
24. C. Nagel, K. Rätzke, E. Schmidtke, F. Faupel, W. Ulfert, *Phys. Rev. B* **60**, 9212 (1999).
25. D. Suh, R. H. Dauskardt, P. A. Kumar, P. A. Sterne, R. H. Howell, *J. Mater. Res.* **18**, 2021 (2003).
26. T. Ichitsubo *et al.*, *Phys. Rev. Lett.* **95**, 245501 (2005).
27. A. S. Argon, *Acta Mater.* **27**, 47 (1979).
28. B. P. Kanungo, S. C. Glade, P. A. Kumar, K. M. Flores, *Intermetallics* **12**, 1073 (2004).
29. M. W. Chen, A. Inoue, W. Zhang, T. Sakurai, *Phys. Rev. Lett.* **96**, 245502 (2006).
30. L. M. Wang, W. H. Wang, R. J. Wang, *Appl. Phys. Lett.* **77**, 1147 (2000).
31. P. Murali, U. Ramamurty, *Acta Mater.* **53**, 1467 (2005).
32. Y. Zhang, W. H. Wang, A. L. Greer, *Nat. Mater.* **5**, 857 (2006).
33. D. Wang, H. Tan, Y. Li, *Acta Mater.* **53**, 2969 (2005).

34. Financial support is from the NSF of China (grant number 50671061) and the Chinese Academy of Sciences.

Supporting Online Material

www.sciencemag.org/cgi/content/full/315/5817/1385/DC1
Materials and Methods
Figs. S1 to S3
References

25 October 2006; accepted 4 January 2007
10.1126/science.1136776

Quantum Hall Effect in Polar Oxide Heterostructures

A. Tsukazaki,[1] A. Ohtomo,[1,2]* T. Kita,[3,4] Y. Ohno,[4] H. Ohno,[3,4] M. Kawasaki[1,5]*

We observed Shubnikov–de Haas oscillation and the quantum Hall effect in a high-mobility two-dimensional electron gas in polar ZnO/$Mg_xZn_{1-x}O$ heterostructures grown by laser molecular beam epitaxy. The electron density could be controlled in a range of 0.7×10^{12} to 3.7×10^{12} per square centimeter by tuning the magnesium content in the barriers and the growth polarity. From the temperature dependence of the oscillation amplitude, the effective mass of the two-dimensional electrons was derived as 0.32 ± 0.03 times the free electron mass. Demonstration of the quantum Hall effect in an oxide heterostructure presents the possibility of combining quantum Hall physics with the versatile functionality of metal oxides in complex heterostructures.

Zinc oxide (ZnO), a wide band gap semiconductor, is of growing importance in advanced electronics, and its potential applications include transparent conducting oxide layers for flat-panel displays and transparent field-effect transistors (*1*). Research focused on the epitaxial growth of ZnO, particularly in terms of its novel excitonic properties, has led to the recent realization of homostructural light-emitting diodes (*2*). Studies of the intrinsic properties of ZnO have yielded a recipe for the preparation of high-quality epilayers having high mobility and excitonic luminescence with high quantum efficiency (*3*, *4*).

Certain aspects of two-dimensional electron gas (2DEG) behavior in semiconductor heterostructures have been studied by observing the quantum Hall effect (QHE)—a quantized magnetotransport accompanied by Shubnikov–de Haas (SdH) oscillations in the longitudinal resistivity ρ_{xx} and Landau plateaus in the Hall resistivity ρ_{xy} (*5*). Early results were obtained in the material systems of Si/SiO_2 or GaAs/AlGaAs (*6*, *7*). However, after discovery of the fractional QHE (*8*, *9*), the focus has been extended to a variety of other material systems, such as III-nitrides (*10*) and graphene (*11*). The observation of SdH oscillation requires conditions such as $\omega_c\tau > 1$ and $\hbar\omega_c > k_BT$, where ω_c is the cyclotron frequency equal to eB/m^* (where e is the charge on the electron, B is magnetic field, and m^* is the electron effective mass), τ is the carrier relaxation time, $\hbar$ is Planck's constant divided by 2π, k_B is Boltzmann's constant, and T is absolute temperature. Although several epitaxial oxide heterostructures have satisfied these conditions (*12*), the QHE has not been observed in those materials. However, a QHE-like state was seen in a quasi-2D crystal of bulk η-Mo_4O_{11} (*13*).

In our study, (0001)-oriented ZnO/$Mg_xZn_{1-x}O$ heterostructures were grown by laser molecular beam epitaxy with the use of a semiconductor-laser heating system (*3*). The $Mg_xZn_{1-x}O$ layer acts as a potential barrier for the 2DEG in the adjacent ZnO layer (*14*). We used a temperature gradient method that allowed us to grow the films over a wide range of temperatures on a single substrate (*3*). The three samples (samples A, B, and C) discussed here were of such high quality that we were able to look at the effects of growth temperature (T_g) of the ZnO layers and Mg content x in the barrier layers (Table 1) [see (*15*) for sample preparation and characterizations]. Sample A was selected from the highest-T_g region

[1]Institute for Materials Research, Tohoku University, Sendai 980-8577, Japan. [2]PRESTO, Japan Science and Technology Agency, Kawaguchi 332-0012, Japan. [3]ERATO Semiconductor Spintronics Project, Japan Science and Technology Agency, Sendai 980-0023, Japan. [4]Laboratory for Nanoelectronics and Spintronics, Research Institute of Electrical Communication, Tohoku University, Sendai 980-8577, Japan. [5]CREST, Japan Science and Technology Agency, Kawaguchi 332-0012, Japan.

*To whom correspondence should be addressed. E-mail: aohtomo@imr.tohoku.ac.jp (A.O.); kawasaki@imr.tohoku.ac.jp (M.K.)

of a film with an $x = 0.15$ barrier, whereas samples B and C were selected from lower- and intermediate-T_g regions, respectively, of another film with an $x = 0.2$ barrier. From the low-field Hall coefficient R_H, carrier densities $n = 1/(R_H e)$ and mobilities $\mu = R_H/\rho_{xx}$ at 1 K were evaluated to be 0.66×10^{12} to 3.7×10^{12} cm^{-2} and 2700 to 5500 cm^2 V^{-1} s^{-1}, respectively. These values were nearly independent of temperature below 1 K, but with increasing temperature n increased while μ decreased, eventually reaching the room-temperature values also listed in Table 1 (see fig. S4).

We found that n systematically depended on x and T_g for the ZnO layers. Our previous study showed that T_g was a good parameter to control the free carrier density: the intrinsic donor concentration increases with increasing T_g (*3*). To investigate the dependence on x, it is necessary to consider spontaneous and piezoelectric polarization effects along the polar (0001) orientation of wurtzite ZnO (*16*, *17*). These polarizations induce surface charges in individual layers, resulting in accumulation or depletion of free electrons at the heterointerfaces (*18*). Because the growth direction of our samples was identified to be the O face (*2*), the direction of spontaneous polarization was upward toward the surface (Fig. 1A). From high-resolution x-ray diffraction analysis (fig. S3), the piezoelectric effect vanishes in unstrained $Mg_xZn_{1-x}O$ layers, whereas upward piezoelectric polarization should arise in ZnO layers from tensile strain (*14*). Thus, the total polarization is defined by

$$\sigma = \begin{cases} P_{sp}(0) - P_{pe}(x) & P_{sp}(x) \\ P_{sp}(x) - P_{pe}(x) & P_{sp}(x) \end{cases} \quad (1)$$

where $P_{sp}(x)$ is spontaneous polarization in the $Mg_xZn_{1-x}O$ layer, and $P_{pe}(x)$ is piezoelectric polarization in the strained ZnO layer on unstrained $Mg_xZn_{1-x}O$. Note that positive σ means that free electrons are accumulated at the heterointerface, and negative σ means that free electrons are accumulated at the ZnO surface.

We calculated σ as a function of x (Fig. 1B). When x is higher than ~0.1, polarization-induced positive charges $\sigma = e$ (blue shading) are formed at the heterointerfaces, and their density increases as x increases. There is good agreement between experimental n (solid circles) and estimated σ/e, despite the ambiguity in $P_{pe}(x)$, a range of the theoretical values representing all of the shaded regions, and the lack of consideration of charge compensation with free electrons. Using the aforementioned polarization charges and band offset (*19*), we can construct the potential diagram near the heterointerfaces (Fig. 1C). The subband energies are estimated using a triangular-potential approximation (*20*) and are listed in the upper panel. The energy separations between the two lowest subband levels are greater than the Fermi energy, which suggests that in the temperature range of the experiments described below, carrier occupation in the second subband is negligible.

We measured the magnetotransport properties (Fig. 2, A and B) using a standard lock-in technique with ac excitation (10 nA, 19 Hz). At low field, all the samples exhibited negative magnetoresistance, presumably because of weakly localized carriers. Above ~2 T, clear ρ_{xx} oscillations that were periodic in $1/B$ appeared, and their amplitudes increased with increasing B. Although the zero-resistance state was absent because of the large scattering rate, each minimum of ρ_{xx} coincided with the quantized ρ_{xy} plateaus equal to $h/(\nu e^2)$, where ν is the Landau filling index. These observations confirmed the existence of the QHE in our samples and allowed direct determination of the 2DEG density (n_{2DEG}). Note that in sample A, the odd states, such as $\nu = 3$ and 5, had much wider Hall plateaus and larger amplitudes of ρ_{xx} minima relative to those of the even states (Fig. 2A). Consequently, the even states, such as $\nu = 4$, were barely observable in $d\rho_{xy}/dB$ (see circle superimposed on red broken line). These features were

Table 1. Growth and electronic parameters of ZnO/$Mg_xZn_{1-x}O$ heterostructures. Electron densities were obtained independently from the low-field Hall coefficient R_H and the low- and high-field slopes S_L and S_H, respectively (see Fig. 2C).

Sample	Thickness of ZnO (μm)	Growth temp. (°C)	Mg content x	Electron density (10^{12} cm^{-2}) n_{2DEG} eS_L/h	eS_H/h	$n = 1/R_H e$		Mobility μ (cm^2 V^{-1} s^{-1}) R_H/ρ_{xx}	
				45 mK (A), 1 K (B, C)		1 K	300 K	1 K	300 K
A	1.1	1020	0.15	0.2	0.6	0.66	39	5500	150
B	0.4	900	0.20	0.4	1.2	1.8	5.0	4900	160
C	0.4	1000	0.20	0.9	1.8	3.7	11	2700	160

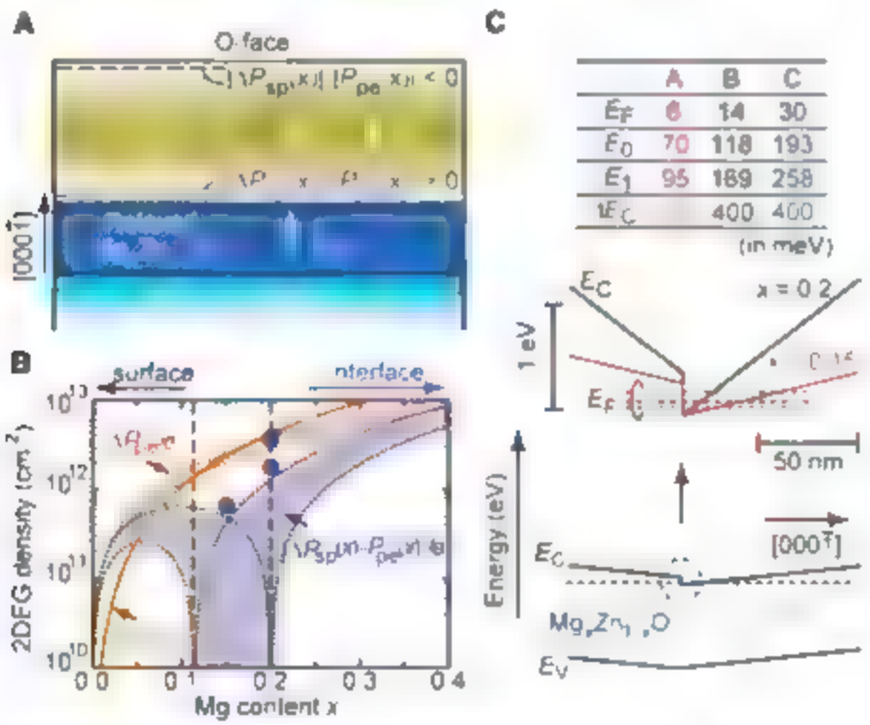

Fig. 1. (**A**) Schematic of the ZnO/$Mg_xZn_{1-x}O$ heterostructures grown on $ScAlMgO_4$ substrates. Depending on the sign of $|\Delta P_{sp}(x)| - |P_{pe}(x)|$, an accumulation layer represented by broken lines is formed either at the surface or in the interface. (**B**) Calculated (gray and blue shaded regions) and measured (solid circles) n as a function of Mg content x in the barrier. Red shaded region, $|P_{pe}(x)/e|$, and solid orange curve, $|\Delta P_{sp}(x)/e|$, were calculated by using theoretical values listed in tables S1 and S2. (**C**) Potential diagram near the hetero-interfaces. Calculated energy parameters are listed in the upper panel, where E_F is the Fermi energy, E_0 and E_1 are the first and second subband energies with respect to the bottom of the conduction band in the wells, respectively, and ΔE_C is the conduction band offset. The colors of the potential profile (solid line) and position of E_F (broken lines) in the middle panel correspond to those of the upper panels, representing samples A, B, and C, respectively.

well preserved at elevated temperatures (see Fig. 2A and upper panel of Fig. 2D).

Standard analyses were performed using fan diagrams (Fig. 2C), where indices of extrema in ρ_{xx} and/or $d\rho_{xy}/dB$ are plotted as a function of $1/B$. Taking low- and high-field slopes (S_L and S_H), we independently evaluated n_{2D} as eS_L/h and eS_H/h, respectively, and compared these values with n (Table 1), where eS_H/h generally corresponds to the 2DEG density contributing to the QHE. The obtained eS_H/h values were systematically smaller than n by 9% to 51%, apparently indicating that 2D confinement becomes weaker with increasing n. To investigate carrier dimensionality, we further studied the B orientation dependence of the SdH effect under the configuration shown in the inset of Fig. 2D. Sample A exhibited weak oscillation, even with B parallel to the interface ($\theta = 90°$), and similar behavior was obtained for sample B (fig. S6). In contrast, sample C, which was expected to have more unconfined free carriers, showed vanishing oscillations with θ approaching 90°. The fact that the oscillation periods depended on the perpendicular B component ($B \cos\theta$)$^{-1}$, as evidenced by the data at $\theta = 30°$ (open circles in Fig. 2C), is consistent with a 2D character of the electron gas. In this regard, however, we found inconsistent results between n_{2D} extracted from fan diagrams and carrier dimensionality evidenced by angular dependencies of the SdH oscillations (see below).

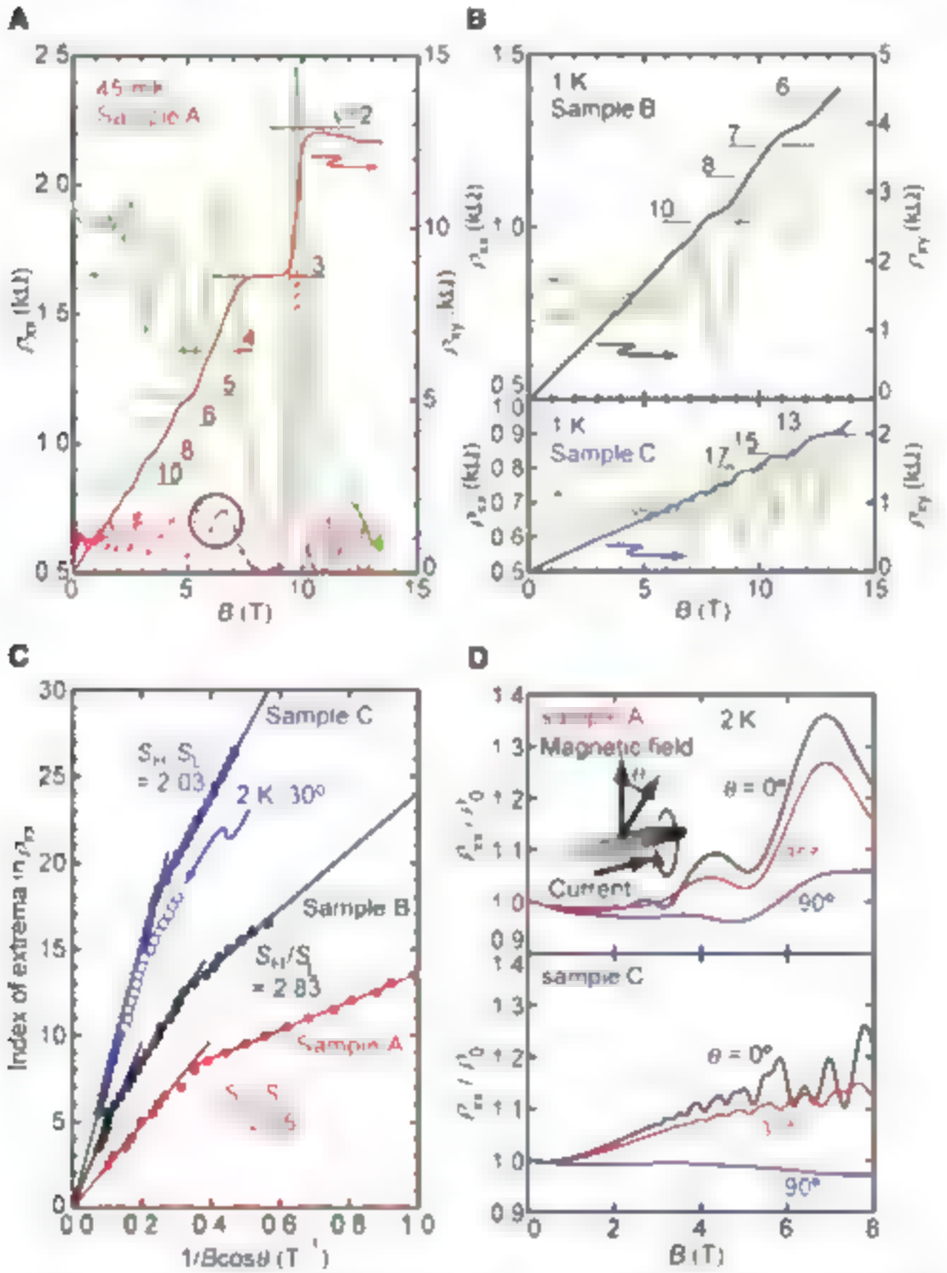

Fig. 2. (**A**) Longitudinal resistivity ρ_{xx}, Hall resistivity ρ_{xy}, and differential Hall resistivity $d\rho_{xy}/dB$ versus B measured at 45 mK for sample A. Integers on the horizontal tick marks are the Landau level filling factors defined as $\nu = h/(\rho_{xy}e^2)$. (**B**) ρ_{xx} and ρ_{xy} versus B measured at 1 K for samples B (top) and C (bottom). (**C**) Standard fan diagrams extracted from the data shown in (A) and (B). The symbols S_L and S_H refer to the low- and high-field slopes, respectively. Colors are consistent with those used for $\rho_{xy}(B)$ in (A) and (B). Open symbols were evaluated from data of sample C at 2 K and $\theta = 30°$ shown in (D). Note that each increment of index of extrema is set to 0.5. (**D**) Angular dependence of normalized magnetoresistance measured at 2 K for sample A (top) and sample C (bottom). Inset depicts the measurement configuration.

Having established the presence of SdH oscillations, we extracted the value of m^* from the temperature dependence of the SdH oscillation amplitude. The resulting Dingle plot for sample C is shown in the inset of Fig. 3. We subtracted the ordinary magnetoresistance from the raw $\rho_{xx}(B)$ data and normalized it through $[\rho_{xx}(B) - \rho_{xx}(0)]/\rho_{xx}(0)$ (*21*). The slope of a linear fit to the plot at B = 3.9 T gave $m^* = 0.32 \pm 0.03\ m_0$ (where m_0 is the free electron mass), and similar values were obtained for B ranging from 0.2 to 4.5 T. This m^* value is somewhat heavier than the bulk polaron mass (0.28 m_0) estimated by cyclotron resonance (*22*), giving rise to the possibility of mass enhancement with 2D polaronic correction (*23*, *24*).

We next discuss anomalous periodicities of the SdH oscillations. The S_H/S_L ratios were found to be ~3 for samples A and B, and ~2 for sample C. These results suggest that an internal electric field arising from the asymmetric triangular well substantially removed spin degeneracy even in zero magnetic field. In this case, the ratio of the slopes directly gives the carrier populations in two spin-split subbands, n_+ and n_-, as $S_H/S_L = (n_+ + n_-)/(n_+ - n_-)$. When applied to sample A, this analysis gives a carrier density in one band twice as large as that in the other band at low fields and total carrier density $n_{2D} = n_+ + n_- = 6 \times 10^{11}$ cm^{-2} (*25*, *26*). As for sample C, we obtained clear evidence of the 2D nature and, hence we expected that n_{2D} would be equal to n, but in fact we found that n_{2D} was about half of n. Together with the approximately linear slopes, this finding implies that the missed ρ_{xx} extrema occurred in a systematic fashion. In this situation, the values of n_{2D} and S_H/S_L are no longer reliable. Because of the stronger polarization fields in samples B and C, rather large spin splitting would be expected, making it difficult to resolve all Landau states (*23*). Relatively lower μ and higher ν may further reduce the ability to discriminate the Landau levels. In fact, even states with $\nu < 10$ tended to disappear in sample A, which has the highest μ. In the above discussion, we ignored the possibility of valley splitting because there was no evidence that either ZnO or $Mg_xZn_{1-x}O$ has an indirect band structure. Whether or not the spin-splitting scenario is likely in our samples, it is an interesting problem to be studied in future experiments.

Despite this open question, the observation of the $\nu = 2$ state is remarkable, particularly when compared with isostructural $Al_xGa_{1-x}N/GaN$ heterostructures. It is difficult to obtain an n_{2D} value lower than 10^{12} cm^{-2} in nitrides having

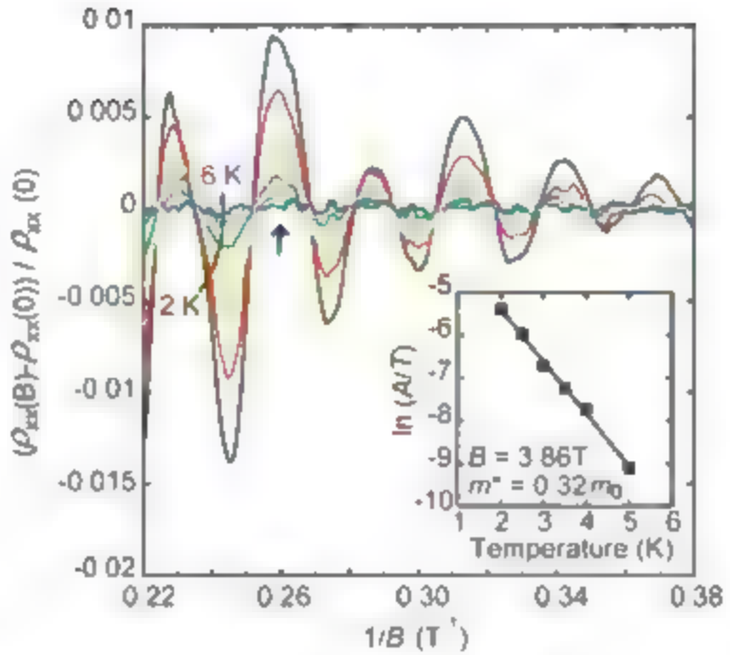

Fig. 3. Normalized magnetoresistivity versus $1/B$ recorded at various temperatures for sample C. Inset depicts temperature dependence of the logarithmic amplitude of ρ_{xx} peak at 3.86 T (indicated by arrow).

$Al_xGa_{1-x}N$ lattice constants smaller than GaN (*18*). A P_{sp} direction opposite to that in ZnO results in piling up of charges induced by both polarizations. Thus, our results imply the exciting possibility of realizing the fractional QHE in the present polar heterostructure if the carrier mobility can be improved. In addition, given chemical compatibility with certain other classes of oxides, the quantized Hall state may be combined with a broad range of physical properties in a complex oxide heterostructure.

References and Notes

1. K. Nomura *et al.*, *Science* **300**, 1269 (2003).
2. A. Tsukazaki *et al.*, *Nat. Mater.* **4**, 42 (2005).
3. A. Tsukazaki, A. Ohtomo, M. Kawasaki, *Appl. Phys. Lett.* **88**, 152106 (2006).
4. S. F. Chichibu *et al.*, *J. Appl. Phys.* **99**, 093505 (2006).
5. K. von Klitzing, G. Dorda, M. Pepper, *Phys. Rev. Lett.* **45**, 494 (1980).
6. J. Wakabayashi, S. Kawaji, *J. Phys. Soc. Jpn.* **44**, 1839 (1978).
7. D. C. Tsui, A. C. Gossard, *Appl. Phys. Lett.* **38**, 550 (1981).
8. D. C. Tsui, H. L. Stormer, A. C. Gossard, *Phys. Rev. Lett.* **48**, 1559 (1982).
9. R. Willett *et al.*, *Phys. Rev. Lett.* **59**, 1776 (1987).
10. M. A. Khan, J. N. Kuznia, J. M. Van Hove, N. Pan, J. Carter, *Appl. Phys. Lett.* **60**, 3027 (1992).
11. K. S. Novoselov *et al.*, *Science* **306**, 666 (2004).
12. A. Ohtomo, H. Y. Hwang, *Nature* **427**, 423 (2004).
13. M. Sasaki *et al.*, *Solid State Commun.* **109**, 357 (1999).
14. A. Ohtomo *et al.*, *Appl. Phys. Lett.* **72**, 2466 (1998).
15. See supporting material on *Science* Online.
16. I. B. Kobiakov, *Solid State Commun.* **35**, 305 (1980).
17. J. Jerphagnon, H. W. Newkirk, *Appl. Phys. Lett.* **18**, 245 (1971).
18. O. Ambacher *et al.*, *J. Appl. Phys.* **87**, 334 (2000).
19. A. Ohtomo *et al.*, *Appl. Phys. Lett.* **75**, 980 (1999).
20. F. Stern, *Phys. Rev. B* **5**, 4891 (1972).
21. H. L. Stadler, *Phys. Rev.* **110**, 817 (1958).
22. K. J. Button *et al.*, *Phys. Rev. Lett.* **28**, 1637 (1972).
23. T. Ando, A. B. Fowler, F. Stern, *Rev. Mod. Phys.* **54**, 437 (1982).
24. S. D. Sarma, *Phys. Rev. B* **27**, 2590 (1983).
25. H. L. Stormer *et al.*, *Phys. Rev. Lett.* **51**, 126 (1983).
26. J. P. Eisenstein, H. L. Stormer, V. Narayanamurti, A. C. Gossard, W. Wiegmann, *Phys. Rev. Lett.* **53**, 2579 (1984).

27. We thank S. F. Chichibu, K. Ueno, and T. Fukumura for valuable discussions. Supported by a Japan Society for the Promotion of Science research fellowship (A.T.); Creative Scientific Research grant 14GS0204 from the Ministry of Education, Culture, Sports, Science, and Technology of Japan; and the Inter-university cooperative program of the Institute for Materials Research, Japan.

Supporting Online Material

www.sciencemag.org/cgi/content/full/1137430/DC1
Materials and Methods
Figs. S1 to S6
Tables S1 and S2
References

10 November 2006; accepted 20 December 2006
Published online 25 January 2007
10.1126/science.1137430
Include this information when citing this paper.

A Molecule Carrier

K. L. Wong,[1] G. Pawin,[1] K.-Y. Kwon,[1] X. Lin,[1] T. Jiao,[1] U. Solanki,[1] R. H. J. Fawcett,[1] L. Bartels,[1]* S. Stolbov,[2] T. S. Rahman[2]

We found that anthraquinone diffuses along a straight line across a flat, highly symmetric Cu(111) surface. It can also reversibly attach one or two CO_2 molecules as "cargo" and act as a "molecule carrier," thereby transforming the diffusive behavior of the CO_2 molecules from isotropic to linear. Density functional theory calculations indicated a substrate-mediated attraction of 0.12 electron volt (eV). Scanning tunneling microscopy revealed individual steps of the molecular complex on its diffusion pathway with increases of 0.03 and 0.02 eV in the diffusion barrier upon attachment of the first and second CO_2 molecule, respectively.

The development of molecules that, when adsorbed onto a surface, exhibit dynamics or electronic properties resembling those of macroscopic objects or machines has attracted considerable attention (*1*–*3*). Examples include rotors (*4*), nanocars and nanowalkers (*5*–*7*), various kinds of electrical switches and leads (*8*, *9*), and ratchets (*10*, *11*). For any realization of molecular-scale machinery, controlled transport of "cargo" molecules is a key functionality, much as transportation of macroscopic objects is the key purpose of many machines (e.g., conveyor belts, trucks). Control of surface transport by means of adsorbed molecules may additionally offer novel avenues for the optimization of surface processes such as growth epitaxy, reactivity, catalysis, and friction lubrication.

At metal surfaces, diffusion is generally the surface process with the lowest energetic barrier, hence it is the lowest-temperature surface process. Diffusion is random in nature and isotropic on flat surfaces unless the surface itself is anisotropic (*12*, *13*); step edges (*14*), anisotropic surfaces (*15*), and surface templates (*7*, *16*, *17*) can restrict diffusion to specific pathways or areas. The use of such surface features is, however, a very inflexible approach for guiding surface transport. Previous studies have shown that the isotropic diffusion of adsorbates on flat surfaces can be turned into linear and guided motion by means of incorporation of either two sequentially moving thiol substrate linkers (*6*) or follicent wheels (*5*, *13*) into the adsorbate.

Although these approaches were successful for one specific molecule each, neither of them has yet been generalized to a class of molecules. Moreover, within the mentioned approaches, no transport of any "cargo" molecules has yet been realized, although concerted motion of adsorbates has been observed in unrelated systems (*18*, *19*). Here we show that anthraquinone (AQ) molecules (Fig. 1A) can transport one or two CO_2 molecules in a linear and guided fashion across an isotropic Cu(111) surface.

This study used a custom-built variable-temperature scanning tunneling microscope (STM) system housed in a vacuum chamber

[1]Pierce Hall, University of California, Riverside, CA 92521, USA. [2]Department of Physics, University of Central Florida, Orlando, FL 32816, USA.

*To whom correspondence should be addressed. E-mail: udwg.bartels@ucr.edu

(base pressure <10^{-10} torr). Preparation of the Cu(111) sample involved cycles of sputtering (Ar^+, 3 kV) and annealing (~800 K). After confirmation of sample cleanliness by STM imaging at 90 K, AQ was deposited in a line-of-sight fashion from a glass capillary attached to the ultrahigh-vacuum system. During deposition, the chamber pressure increased by <2 × 10^{-10} torr. Although the CO_2 content of the background pressure during deposition is sufficient that individual species can be found on the surface, for quantitative measurements we deposited CO_2 onto the sample through a needle valve. More than 10 samples were prepared to confirm the effects reported here.

AQ on Cu(111) is imaged by STM as an elongated protrusion that is aligned with the substrate high-symmetry direction. Time-lapse imaging reveals rapid and strictly linear diffusion at temperatures as low as 20 K. CO_2 molecules appear as depressions in STM images. Both species are mobile in the same temperature range and they diffuse in an isotropic fashion (Fig. 1). On surfaces with ultralow coverages of AQ and CO_2, we find attachment of CO_2 molecules to each side of AQ by random diffusion of either species or lateral manipulation by the STM tip. In the resultant complex, AQ maintains its characteristic linear diffusion and its elongated shape; however, its center ring is imaged as less protruding. A sequence of detachment and reattachment of one of two CO_2 molecules from AQ is shown in Fig. 2, A to C (*20*). Unhooking can occur by means of the STM tip or spontaneously at temperatures of ~50 K. Manipulation of CO_2 molecules requires a factor of ~3 increase in the tunneling current relative to imaging (i.e., a few nA) at biases of ~100 mV.

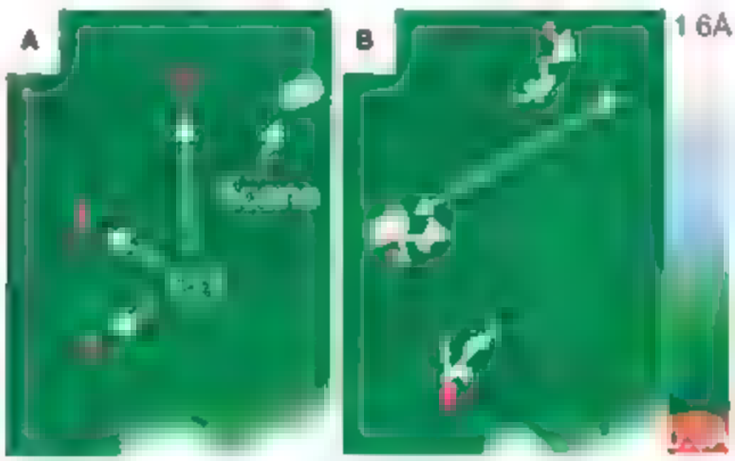

Fig. 1. (**A** and **B**) The diffusion of AQ (protrusions, white) and CO_2 (indentations, red) molecules between two STM images (voltage V = −1.5 V, current I = 180 pA, temperature T = 26 K, area A = 95 × 130 Å) taken 2 hours apart. The diffusion pathways (white lines) were obtained from intermediary images.

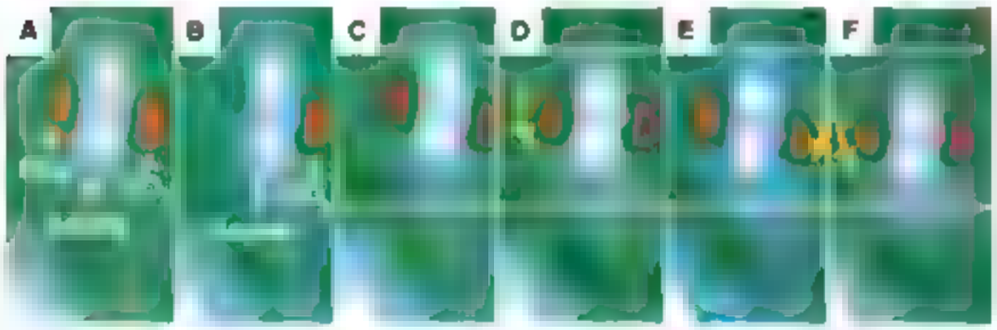

Fig. 2. (**A** to **C**) Detachment and reattachment of a CO_2 molecule (depression, red) on the left side of an AQ (protrusion, blue-white). (**C** to **F**) Diffusion of AQ with two CO_2 molecules by means of individual steps of its oxygen atoms (see Fig. 3). In all images, V = −35 mV, I = 60 pA, T = 50 K, and A = 20 × 40 Å. Note the edge of a cluster of AQ molecules in the bottom left, serving as a marker, and the Cu(111) surface state oscillations.

Density functional theory calculations show that the linear diffusion of AQ with and without attached CO_2 proceeds by alternating steps of its carbonyl groups along a substrate high-symmetry line (Fig. 3). In contrast to a previous report on the linear diffusion of dicarbonitrile in a similar fashion (*6*), the molecular orientation is associated with the individual step of the substrate lattice. Steps can be observed in STM as the AQ-CO_2 complex steps across the surface. Frequently the AQ moiety is found to be angled ~10° with respect to the substrate high-symmetry direction. A sequence of three steps of an AQ carrying two CO_2 molecules is shown in Fig. 2, C to F.

The calculations indicate a horizontal adsorption both for isolated CO_2 molecules and ones attached to AQ (Fig. 3), which is in agreement with spectroscopic measurements on isolated species (*21*). All calculations used the VASP code (*22*) with the generalized-gradient approximation (*23*) for the exchange-correlation functional and the plane-wave pseudopotential method (*24*) with ultrasoft pseudopotentials (*25*). Our calculations used a supercell of 5 × 6 substrate atoms, and results obtained with two and three substrate layers were similar. The attractive interaction between CO_2 and AQ (E_{inter}) was calculated by comparing the total energies of copper

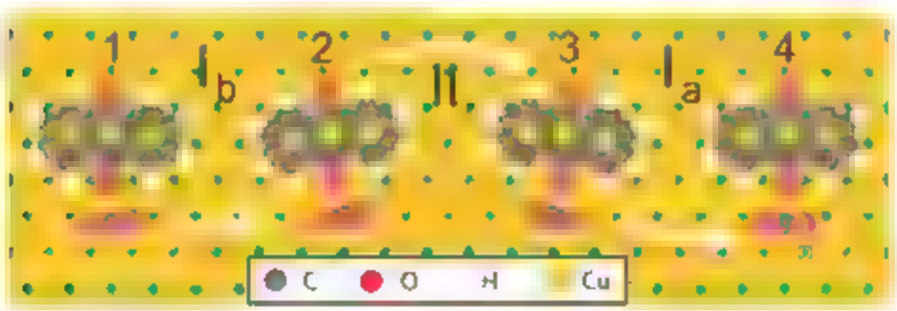

Fig. 3. Model of the diffusion of an AQ molecule with one CO_2 attached; results for zero and two CO_2 molecules are very similar. AQ diffuses along the substrate high-symmetry direction by sequentially moving either one (l_a, l_b) or the other (ll) of its oxygen substrate linkers (red). Steps la and lb are inversion-symmetric and often occur in direct succession so that the molecule appears to step between configurations 2 and 3 (Fig. 2).

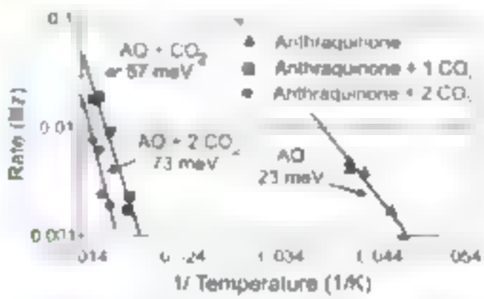

Fig. 4. Arrhenius plot of the diffusion of AQ molecules with zero, one, and two CO_2 molecules attached. The resultant diffusion barriers are indicated. The error bars are smaller than the symbols, and the statistical error of each of the barriers is below 10 meV. The prefactors are low (kHz regime), similar to (*31*).

slabs without any adsorbate (E_0), with only CO_2 (E_{CO_2}), with only AQ (E_{AQ}), and with AQ and CO_2 (E_{both}): $E_{inter} = E_{both} + E_0 - E_{CO_2} - E_{AQ}$ = 0.12 eV. This interaction is mediated by the substrate (*26*–*30*) rather than involving a direct intermolecular bond, its energy correlates well with the occasional observation of spontaneous separation at ≥50 K.

The velocity of AQ decreases when it carries a CO_2 load. From temperature-dependent measurements of hundreds of steps of AQ (with zero, one, or two CO_2 molecules attached), we obtained the Arrhenius plot shown in Fig. 4. It translates that the diffusion barrier for AQ of 0.02 eV increases by ~0.03 eV upon attachment of the first CO_2 molecule and by an additional 0.02 eV for the second molecule, thus roughly doubling and tripling, respectively. Although the diffusion barriers of Fig. 4 are very low in absolute terms, they correspond well with other species and complexes on Cu(111) (e.g., Cu atoms, 0.037 eV (*30*); CO chevrons, 0.010 eV (*31*)).

AQ's ability to reversibly attach CO_2 provides a means for transport of CO_2 molecules along a line from point A to point B on a surface, as long as A and B are connected by any of the three Cu(111) high-symmetry directions. This result is in stark contrast to CO_2's native isotropic diffusion. As such, our observations are proof of principle for the application of molecules at surfaces as molecular-scale analogs of macroscopic machinery ("molecular machines") that is, as entities that change the position or properties of separate, molecular-scale objects in a predetermined fashion.

References and Notes

1. J. S. Moore, *Acc. Chem. Res.* **30**, 402 (1997).
2. G. S. Kottas, L. I. Clarke, D. Horinek, J. Michl, *Chem. Rev.* **105**, 1281 (2005).
3. J. P. Collin, C. Dietrich-Buchecker, P. Gaviña, M. C. Jimenez-Molero, J. P. Sauvage, *Acc. Chem. Res.* **34**, 477 (2001).
4. J. K. Gimzewski *et al.*, *Science* **281**, 531 (1998).
5. Y. Shirai, A. J. Osgood, Y. M. Zhao, K. F. Kelly, J. M. Tour, *Nano Lett.* **5**, 2330 (2005).
6. K. Y. Kwon *et al.*, *Phys. Rev. Lett.* **95**, 166101 (2005).
7. R. Otero *et al.*, *Angew. Chem. Int. Ed.* **43**, 2092 (2004).
8. L. Gross *et al.*, *Phys. Rev. Lett.* **93**, 056103 (2004).
9. V. Balzani, A. Credi, F. M. Raymo, J. F. Stoddart, *Angew. Chem. Int. Ed.* **39**, 3348 (2000).
10. R. A. van Delden *et al.*, *Nature* **437**, 1337 (2005).
11. T. R. Kelly, H. De Silva, R. A. Silva, *Nature* **401**, 150 (1999).
12. J. V. Barth, G. Costantini, K. Kern, *Nature* **437**, 671 (2005).
13. F. Rosei *et al.*, *Prog. Surf. Sci.* **71**, 95 (2003).
14. S. J. Stranick, M. M. Kamna, P. S. Weiss, *Science* **266**, 99 (1994).
15. R. Otero *et al.*, *Nat. Mater.* **3**, 779 (2004).
16. J. A. Theobald, N. S. Oxtoby, M. A. Phillips, N. R. Champness, P. H. Beton, *Nature* **424**, 1029 (2003).
17. H. Brune, M. Giovannini, K. Bromann, K. Kern, *Nature* **394**, 451 (1998).
18. S. Horch *et al.*, *Nature* **398**, 134 (1999).
19. G. S. McCarty, P. S. Weiss, *J. Am. Chem. Soc.* **126**, 16772 (2004).
20. A corresponding movie appears on *Science* Online.
21. K. H. Ernst, D. Schlatterbeck, K. Christmann, *Phys. Chem. Chem. Phys.* **1**, 4105 (1999).
22. G. Kresse, J. Hafner, *Phys. Rev. B* **47**, 558 (1993).
23. J. Perdew, Y. Wang, *Phys. Rev. B* **45**, 13244 (1992).
24. M. Payne, M. Teter, D. Allan, T. Arias, J. Joannopoulos, *Rev. Mod. Phys.* **64**, 1045 (1992).
25. D. Vanderbilt, *Phys. Rev. B* **41**, 7892 (1990).
26. E. C. H. Sykes *et al.*, *Acc. Chem. Res.* **36**, 945 (2003).
27. T. Mitsui, M. K. Rose, E. Fomin, D. F. Ogletree, M. Salmeron, *Phys. Rev. Lett.* **94**, 036101 (2005).
28. S. Lukas, G. Witte, C. Wöll, *Phys. Rev. Lett.* **88**, 028301 (2002).
29. G. Pawin, K. L. Wong, K. Y. Kwon, L. Bartels, *Science* **313**, 961 (2006).
30. J. Repp *et al.*, *Phys. Rev. Lett.* **85**, 2981 (2000).
31. A. J. Heinrich, C. P. Lutz, J. A. Gupta, D. M. Eigler, *Science* **298**, 1381 (2002).

32. Supported by U.S. Department of Energy joint grants DE-FG02-03ER15464/S. We thank the Academic Associates Program of the San Diego Supercomputer Center for computational resources.

Supporting Online Material

www.sciencemag.org/cgi/content/full/1135302/DC1
Movie S1

19 September 2006; accepted 5 January 2007
Published online 18 January 2007
10.1126/science.1135302
Include this information when citing this paper.

Multifunctional Encoded Particles for High-Throughput Biomolecule Analysis

Daniel C. Pregibon,[1] Mehmet Toner,[2] Patrick S. Doyle[1]*

High-throughput screening for genetic analysis, combinatorial chemistry, and clinical diagnostics benefits from multiplexing, which allows for the simultaneous assay of several analytes but necessitates an encoding scheme for molecular identification. Current approaches for multiplexed analysis involve complicated or expensive processes for encoding, functionalizing, or decoding active substrates (particles or surfaces) and often yield a very limited number of analyte-specific codes. We present a method based on continuous flow lithography that combines particle synthesis and encoding and probe incorporation into a single process to generate multifunctional particles bearing over a million unique codes. By using such particles, we demonstrate a multiplexed single-fluorescence detection of DNA oligomers with encoded particle libraries that can be scanned rapidly in a flow-through microfluidic channel. Furthermore, we demonstrate with high specificity the same multiplexed detection using individual multiprobe particles.

The ability to quantify multiple proteins, cytokines, or nucleic-acid sequences in parallel using a single sample allows researchers and clinicians to obtain high-density information with minimal assay time, sample volume, and cost. Such multiplexed analysis is accompanied by several challenges, including molecular encoding and the need to retain assay sensitivity, specificity, and reproducibility with the use of complex mixtures. There are two broad classes of technologies used for multiplexing: planar arrays (*1*–*3*) and suspension (particle-based) arrays (*4*–*21*), both of which have application-specific advantages. Planar arrays, such as DNA and protein microarrays, are best suited for applications requiring ultra-high-density analysis. In comparison, suspension arrays benefit from solution kinetics, ease of assay modification, higher sample throughput, and better quality control by batch synthesis (*22*). Although particle-based arrays have been used for high-density genotyping applications (*23*), they are most favorable over microarrays when detecting a modest number of targets over large populations or when rapid probe-set modification is desired. Whereas planar arrays rely strictly on positional encoding, suspension arrays have used a great number of encoding schemes that can be classified as spectrometric (*4*–*11*), graphical (*12*–*16*), electronic (*17*–*19*), or physical (*20*, *21*).

Spectrometric encoding uses specific wavelengths of light or radiation [including fluorophores (*4*–*7*), chromophores (*8*), photonic structures (*9*), and Raman tags (*10*, *11*)] to identify a species. Fluorescence-encoded microbeads (*4*–*7*) can be rapidly processed by using conventional flow cytometry [or on fiber-optic arrays (*24*)] making them a popular platform for multiplexing. However, there are several disadvantages of using multiple fluorescent signals as means of barcoding, including (i) the limited barcodes achievable (typically ~100) because of spectral overlap, (ii) the lack of portability for bulky flow cytometers, (iii) added cost with each fluorescent exciter and detector needed, and (iv) potential interference of encoding fluorescence with analyte-detection fluorescence. For these reasons, single-fluorescence methods

[1]Department of Chemical Engineering, Massachusetts Institute of Technology, Cambridge, MA 02139, USA. [2]BioMEMS Resource Center and Center for Engineering in Medicine, Massachusetts General Hospital, and Harvard Medical School, Boston, MA 02114, USA.

*To whom correspondence should be addressed. E-mail: pdoyle@mit.edu

exist that use graphical techniques to spatially encode barcodes on microcarriers.

Graphical barcodes rely on the patterning of optical elements on a microcarrier; some examples include striped rods (*12*, *13*), ridged particles (*14*), and dot-patterned particles (*14*, *15*). The chemistries used to fabricate such particles (metallic or photoresist) require additional coupling chemistries to conjugate biomolecules to the surface, and, in the case of striped rods, each metallic pattern needs to be generated one batch at a time. Typically, the patterns on these particles can only be distinguished if the fluorescence of the target signal is sufficiently high. Another graphical method for microcarrier encoding is the selective photobleaching of codes into fluorescent beads (*16*). In this method, both particle synthesis and decoding are time-consuming, making it an unlikely candidate for high-throughput analysis. A method that eliminates fluorescence altogether uses radio frequency memory tags (*17*–*19*). This approach is very powerful because it allows for nearly unlimited barcodes ($>10^{12}$) and decouples the barcoding scheme from analyte quantification (fluorescence), but the synthesis of any appreciable number (thousands or millions) of these electronic microchip-based carriers may prove to be expensive and slow. These and several other methods developed for multiplexed analysis have been thoroughly reviewed elsewhere (*25*, *26*).

We introduce a technique that overcomes many of these multiplexing limitations. By exploiting laminar flows characteristic of microfluidics, we demonstrate the ability to generate multifunctional particles with distinct regions for analyte encoding and target capture (Fig. 1). In a typical experiment, we flowed two monomer streams (one loaded with a fluorescent dye and the other with an acrylate-modified probe) adjacently down a microfluidic channel and used a variation of continuous-flow lithography (*27*) to polymerize particles [with 30-ms bursts of ultraviolet (UV) light] across the streams (*28*) (movie S1). In this manner, particles with a fluorescent, graphically encoded region and a probe-loaded region can be synthesized in a single step. Each particle is an extruded two-dimensional (2D) shape (Fig. 1B) whose morphology is determined by a photomask that is inserted into the field-stop position of the microscope and whose chemistry is determined by the content of the coflowing monomer streams. The cross-linked polymer particles then flow down the channel [without sticking due to oxygen inhibition near the channel surfaces (*27*)], where they are collected in a reservoir. The particles can be rinsed of excess monomer and then used for biological assays.

We used polyethylene glycol) (PEG) (well known as a bio-inert polymer) as the particle foundation to eliminate the need to "block" surfaces after probe conjugation and as a transparent material to allow transmission of fluorescent signal from both particle faces. These properties should enhance both specificity and sensitivity of analyte detection. We used a simple dot-coding scheme to generate particles that can bear over a million (2^{20}) codes (Fig. 1C). Particles were designed to be "read" along five lanes down their length, with alignment indicators that were used to identify the code position and the read "direction" despite the particle orientation (Fig. 1C). The flat, long shape of the particles helps align them for scanning in a flow-through device. The spatial separation of various chemistries on the particles allows decoding and target detection to be achieved by using a single fluorophore.

To demonstrate the versatility of particle syntheses, we selectively labeled monomer streams with a fluorophore and used a variety of channel designs to generate particles bearing a single probe region, multiple probe regions, and probe-region gradients (Fig. 1, E to G). Multiprobe particles (Fig. 1F), made with the use of channels with several inlet streams, allow for a direct, single-particle comparison of several targets. Furthermore, probe gradients (Fig. 1G), made by simply allowing diffusion of the probe across streams in a long channel, are useful for broadening the detection range of an analyte when using a fixed detection sensitivity (when the signal can saturate). If magnetic nanoparticles are incorporated in a gradient, it may be possible to produce a temperature variation along particles when stimulated in an oscillating magnetic field (*29*).

A key feature of our method is the direct incorporation of probes into the encoded particles. This is accomplished by simply adding acrylate-modified biomolecules into the monomer solution. After polymerization, the probes are covalently coupled to the polymer network. This process is applicable for both oligonucleotide and protein probes (*30*–*32*). We demonstrate that the short bursts of UV used to synthesize probe-conjugated particles are not detrimental to the functionality of incorporated oligonucleotides. Previously, we showed similar results with bead-bound antibodies that were incorporated into polymer structures made from nearly identical monomer constituents (*28*, *33*).

To demonstrate multiplexing capabilities, we used acrylate-modified oligonucleotide probes (which are commercially available) for DNA sequence detection (Fig. 2, A to C). We synthesized three batches of particles, one of which was loaded with 20 base pair (bp) oligonucleotide probe 1 (5′-ATA GCA GAT CAG CAG CCA GA-3′), another with probe 2 (5′-CAC TAT GCG CAG GTT CTC AT-3′), and a third with no probe to serve as a control. Targets were fluorescently labeled oligonucleotides with complementary sequences to the two probes. We mixed the particles and incubated them for 20 min at room temperature in microwells containing either target 1 (at 1 μM), target 2 (at 1 μM), both targets (both at 0.5 μM), or no target (*28*). A positive target

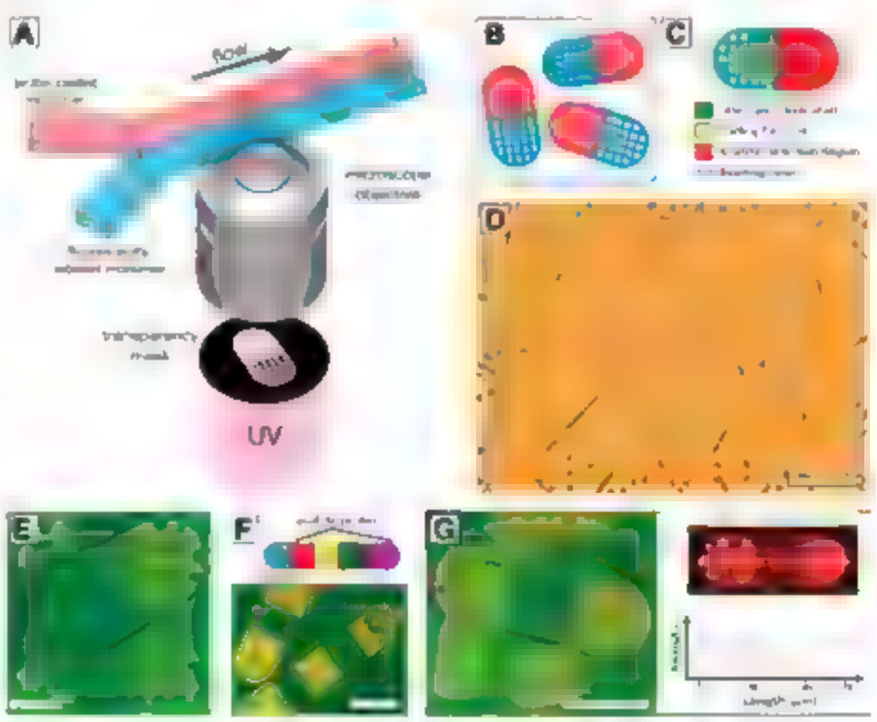

Fig. 1. (**A**) Schematic diagram of dot-coded particle synthesis showing polymerization across two adjacent laminar streams to make single-probe, half-fluorescent particles [shown in (**B**)]. (**C**) Diagrammatic representation of particle features for encoding and analyte detection. Encoding scheme shown allows the generation of 2^{20} (1 048 576) unique codes. (**D**) Differential interference contrast (DIC) image of particles generated by using the scheme shown in (A). (**E** to **G**) Overlap of fluorescence and DIC images of single-probe (E), multiprobe (F, bottom), and probe-gradient (G, left) encoded particles. Shown also is a schematic representation of multiprobe particles (F, top) and a plot of fluorescent intensity along the center line of a gradient particle (G, right). Scale bars indicate 100 μm in (D), (F), and (G) and 50 μm in (E).

detection was indicated by probe-region fluorescence, which was more pronounced near the particle edges. This result suggested that targets were able to diffuse and hybridize several μm into the particle body (28). In each instance, the particles showed uniformity (28) with high specificity to the oligomers, exhibiting fluorescence only when the target was present (Fig. 2C).

To further demonstrate the power of our multiplexing scheme, we performed the same sequence detection assay with the use of particles with multiple adjacent functionalities (Fig. 2, D to F). In this manner, we were able to simultaneously assay for the two target sequences (with a negative control) on a single particle. Again, the assay was highly specific (Fig. 2F) and very uniform from particle to particle (Fig. 2D) (28). The interfaces between probes on the particles are very sharp, and thinner stripes could be used for even greater multiplexing capabilities.

In order to prove that this method of multiplexed analysis is practical for high-throughput applications, we developed a simple scheme to scan particles in a flow-through device (Fig. 3). Multiprobe particles used in the hybridization experiment just described (Fig. 2, D to F) were flowed through a microfluidic channel and observed on an inverted fluorescence microscope (28). Particles were aligned by using flow focusing and traveled down a channel only slightly larger than the particle width (Fig. 3A). We used a biofriendly surfactant (28) to ensure that the particles flowed smoothly down the channels without sticking. Images were taken at a designated detection region in the channel with an exposure of 1/125 s as the particles passed the field of view (using a 20× objective). Image sequences were later analyzed to determine the particle code and quantify targets (movie S2).

A representative particle image is shown (Fig. 3B) with corresponding intensity plots along the five particle "reading lanes." The code along each lane can be determined by analyzing the sharp dips and plateaus in the intensity plots. By using the control-region fluorescence, we define a positive target detection as the control average intensity plus three standard deviations for each particle. We were able to accurately identify the presence of both oligonucleotide targets after only a short 10-min incubation.

The throughput of our system is primarily determined by the detection scheme and the particle size. The particles synthesized for this study are relatively large compared with those in other flow-through methods, measuring 90 μm in width, ~30 μm in thickness, and 180 to 270 μm in length. Large size not only limits the throughput of a system but also increases the sample volume. However, the great particle-to-particle reproducibility we have demonstrated (28) will afford a much lower redundancy than is typical in flow-through systems, improving efficiency. By using conservative estimates, we found that our system should be capable of providing rapid, high-density analysis with a manageable sample volume (28) despite the seemingly large particle size.

In addition to being very reproducible, we have also shown that our system is very sensitive. With 30-min incubations, we can detect DNA oligomers comfortably at 500 attomoles without biomolecule-aided signal amplification (28). This leads us to believe that our system will be at least as sensitive as current commercially available multiplexing techniques with the added advan-

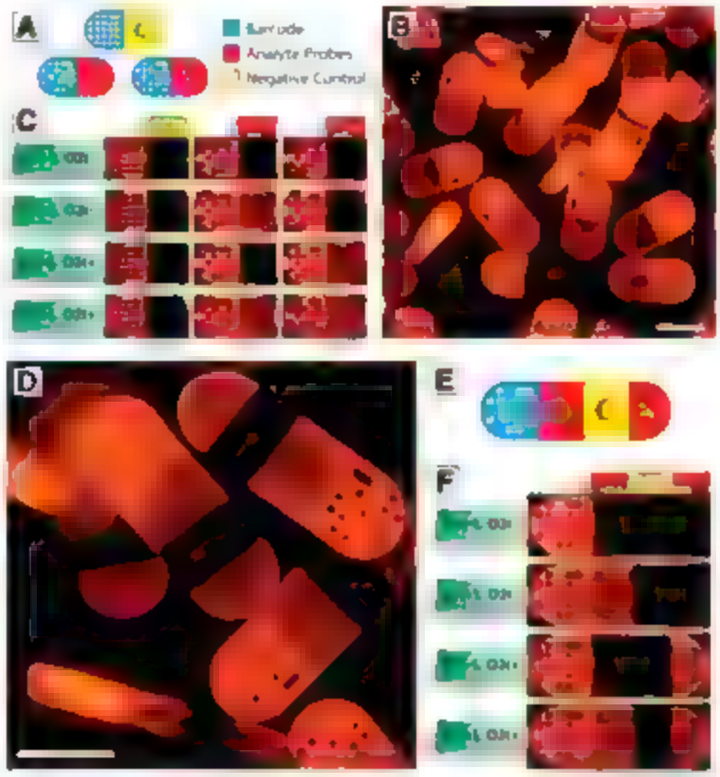

Fig. 2. Multiplexed analysis using single- (A to C) and multiprobe (D to F) encoded particles. The particles were loaded with DNA oligomer probes (O1, 5′-ATA GCA GAT CAG CAG CCA GA-3′, or O2, 5′-CAC TAT GCG CAG GTT CTC AT-3′) or no probe (negative control, Ctl) as shown schematically in (A) and (E). Shown are representative fluorescence images for single-probe (B) and multiprobe (D) particles after a 10-min incubation with both fluorescent-labeled targets. Fluorescence in the probe regions indicates target detection. Also shown are individual particles after incubation in solutions containing no targets, target 1 only, target 2 only, or both targets [(C) and (F)]. Scale bars, 100 μm.

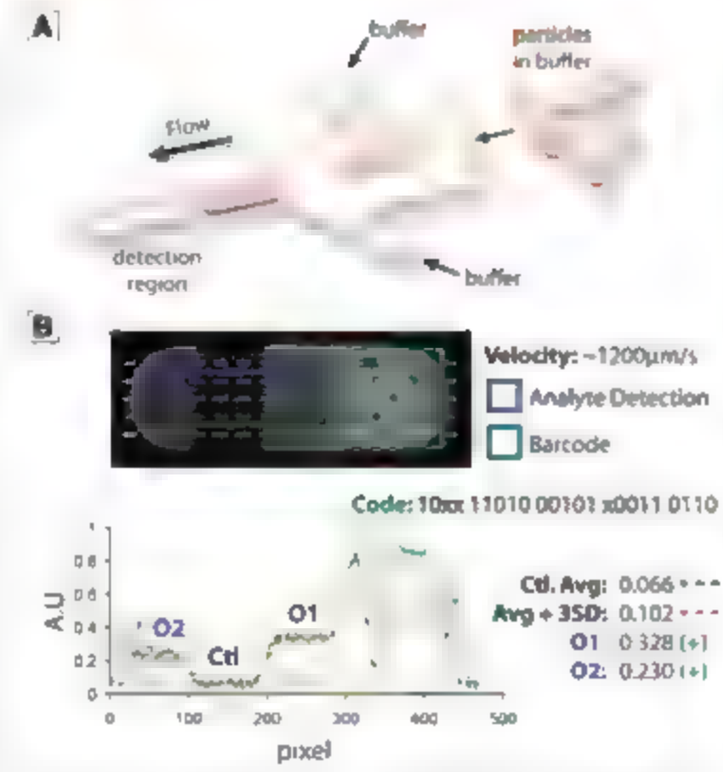

Fig. 3. Flow-through particle reading. (A) Schematic representation of a flow-focusing microfluidic device used to align and read particles after hybridization experiments. Particles are directed down a narrow channel and are imaged by using fluorescence microscopy. (B) A typical image of a particle taken in a flow-through device as shown in (A). The image was captured by using a microscope-mounted camera with an exposure of 1/125 s as the particle flowed at a velocity of ~1200 μm/s through the channel. Scans of fluorescent intensity were taken across the five lanes of the particle to reveal the code and detect oligomer targets (O1 and O2). With the particle in this orientation, the code is read from right to left and top to bottom, where 1, 0, and *x* represent a hole, no hole, and an alignment marker, respectively. Particle shown is 90 μm by 270 μm. A.U., arbitrary units.

tages of all-in-one particle synthesis, incorporation of multiple probes, low cost (~$8), virtually unlimited codes, and implementation using little more than a standard fluorescence microscope.

References and Notes

1. D. Gershon, *Nature* **416**, 685 (2002).
2. S. P. Fodor *et al.*, *Nature* **364**, 555 (1993).
3. G. MacBeath, S. L. Schreiber, *Science* **289**, 1760 (2000).
4. R. J. Fulton, R. L. McDade, P. L. Smith, L. J. Kienker, J. R. Kettman Jr., *Clin. Chem.* **43**, 1749 (1997).
5. B. J. Battersby *et al.*, *J. Am. Chem. Soc.* **122**, 2138 (2000).
6. H. Xu *et al.*, *Nucleic Acids Res.* **31**, e43 (2003).
7. M. Han, X. Gao, J. Z. Su, S. Nie, *Nat. Biotechnol.* **19**, 631 (2001).
8. X. W. Zhao *et al.*, *Chem. Mater.* **18**, 2443 (2006).
9. F. Cunin *et al.*, *Nat. Mater.* **1**, 39 (2002).
10. X. Su *et al.*, *Nano Lett.* **5**, 49 (2005).
11. H. Fenniri, S. Chun, L. Ding, Y. Zyrianov, K. Hallenga, *J. Am. Chem. Soc.* **125**, 10546 (2003).
12. S. R. Nicewarner-Peña *et al.*, *Science* **294**, 137 (2001).
13. M. Y. Sha *et al.*, *Anal. Bioanal. Chem.* **384**, 658 (2006).
14. M. Evans, C. Sewter, E. Hill, *Assay Drug Dev. Technol.* **1**, 199 (2003).
15. Z. L. Zhi, Y. Morita, O. Hasan, E. Tamiya, *Anal. Chem.* **75**, 4125 (2003).
16. K. Braeckmans *et al.*, *Nat. Mater.* **2**, 169 (2003).
17. E. J. Moran *et al.*, *J. Am. Chem. Soc.* **117**, 10787 (1995).
18. K. C. Nicolaou, X. Y. Xiao, Z. Parandoosh, A. Senyei, M. P. Nova, *Angew. Chem. Int. Ed.* **34**, 2289 (1995).
19. R. F. Service, *Science* **270**, 577 (1995).
20. T. M. McHugh, R. C. Miner, L. K. Logan, D. P. Stites, *J. Clin. Microbiol.* **26**, 1957 (1988).
21. A. R. Vaino, K. D. Janda, *Proc. Natl. Acad. Sci. U.S.A.* **97**, 7692 (2000).
22. J. P. Nolan, L. A. Sklar, *Trends Biotechnol.* **20**, 9 (2002).
23. J. B. Fan, M. S. Chee, K. L. Gunderson, *Nat. Rev. Genet.* **7**, 632 (2006).
24. J. A. Ferguson, F. J. Steemers, D. R. Walt, *Anal. Chem.* **72**, 5618 (2000).
25. N. H. Finkel, X. Lou, C. Wang, L. He, *Anal. Chem.* **76**, 352A (2004).
26. K. Braeckmans, S. C. D. Smedt, M. Leblans, R. Pauwels, J. Demeester, *Nat. Rev. Drug Discov.* **1**, 447 (2002).
27. D. Dendukuri, D. C. Pregibon, J. Collins, T. A. Hatton, P. S. Doyle, *Nat. Mater.* **5**, 365 (2006).
28. Materials and methods are available as supporting material on *Science* Online.
29. R. Hergt *et al.*, *IEEE Trans. Magn.* **34**, 3745 (1998).
30. A. Y. Rubina *et al.*, *Biotechniques* **34**, 1008 (2003).
31. A. V. Vasiliskov *et al.*, *Biotechniques* **27**, 592 (1999).
32. F. N. Rehman *et al.*, *Nucleic Acids Res.* **27**, 649 (1999).
33. D. C. Pregibon, M. Toner, P. S. Doyle, *Langmuir* **22**, 5122 (2006).

34. We gratefully acknowledge support from NSF grant CTS-0304128 and the Dumbros Fellowship.

Supporting Online Material

www.sciencemag.org/cgi/content/full/315/5817/1393/DC1
Materials and Methods
Figs. S1 to S3
Tables S1 to S3
References
Movies S1 and S2

11 September 2006; accepted 4 January 2007
10.1126/science.1134929

Inverse Relations Between Amounts of Air Pollution and Orographic Precipitation

Daniel Rosenfeld,[1]* Jin Dai,[2] Xing Yu,[2] Zhanyu Yao,[3] Xiaohong Xu,[2] Xing Yang,[2] Chuanli Du[2]

Particulate air pollution has been suggested as the cause of the recently observed decreasing trends of 10 to 25% in the ratio between hilly and upwind lowland precipitation downwind of urban and industrial areas. We quantified the dependence of this ratio of the orographic-precipitation enhancement factor on the amounts of aerosols composed mostly of pollution in the free troposphere, based on measurements at Mt. Hua near Xi'an, in central China. The hilly precipitation can be decreased by 30 to 50% during hazy conditions, with visibility of less than 8 kilometers at the mountaintop. This trend shows the role of air pollution in the loss of significant water resources in hilly areas, which is a major problem in China and many other areas of the world.

Large concentrations of submicron particulate air pollution have been documented to suppress precipitation-forming processes by serving as cloud-drop condensation nuclei that form clouds with small drops that are slower to coalesce into raindrops and to glaciate into ice hydrometeors (*1*–*4*). This is manifested as less precipitation on the ground when the lifetime of the cloud is shorter than the time for the conversion of cloud water into precipitation. Such short-lived cloud elements typically form as air rises over topographic barriers and evaporate when forced down across the ridge line. Therefore, decreasing trends in the orographic enhancement factor of the precipitation (Ro), which is the ratio between the hill and the upwind plains precipitation, were suggested to reflect the trend of increasing air pollution during that period (*5*). This hypothesis was supported by the documented reductions of 10 to 25% in the past half century in much of the mountain ranges of the western United States, downwind of major urban and industrial areas (*5*–*8*). However, because of a lack of historical records of ambient aerosols, it was not possible to quantitatively relate the amounts of air pollution to Ro. We used a set of measurements taken since 1954 on a mountaintop in central China to quantify the impact of aerosol loading on precipitation in that area.

A meteorological observatory at the top of Mt. Hua (34.27°N, 109.54°E, 2060 m), 120 km east of Xi'an, China (see location in Fig. 1), provides a complete record of four measurements per day of all meteorological elements, except for one measurement per day of precipitation depth. The visibility (VIS) before 1980 was recorded as 10 classes, and the values after 1980 were estimated directly in kilometers, with respect to landmarks of known distance in the mountainous landscape. In order to reduce the effect of relative humidity (RH) on visibility, RH values greater than 40 and less than 99% were converted to the equivalent visibility in dry conditions (i.e., RH = 40%). When RH < 40%, the visibility did not need to be corrected for RH. The correction formula is expressed as $VIS/VIS(dry) = 0.26 + 0.4285 \log(100 - RH)$, where RH is in percent and the log is on the basis of 10. If there was fog or precipitation at all visibility observation times in a day, the visibility of that day was excluded from the corrected visibility series. The daily average values are presented in Fig. 2. The visibility at the mountaintop, shown in Fig. 2, had a marked decreasing trend for the whole measurement period. This trend reflects the trend of increasing air pollution in China (*9*, *10*) during that time. Consistent with the hypothesis that air pollution suppresses orographic precipitation, Ro shows statistically significant decreasing trends of 14 and 17%, with respect to the low-level rain gauges of Huayin and Xi'an (see locations in Fig. 1), respectively (Fig. 3).

The cause for the association of visibility and Ro trends can be tested by ignoring the time factor and testing Ro directly, as a function of the visibility distance. This was done for the uncorrected visibility (Fig. 4), because many of the precipitation events are excluded with the corrected visibility. We hypothesize that reduced visibility indicates the presence of more aerosols and cloud

[1]Institute of Earth Sciences, The Hebrew University of Jerusalem, Jerusalem, Israel. [2]Meteorological Institute of Shaanxi Province, Xi'an 710015, China. [3]Key Laboratory for Cloud Physics and Weather Modification of Chinese Meteorological Association, Chinese Academy of Meteorological Sciences, Beijing 100081, China.

*To whom correspondence should be addressed. E-mail: daniel.rosenfeld@huji.ac.il

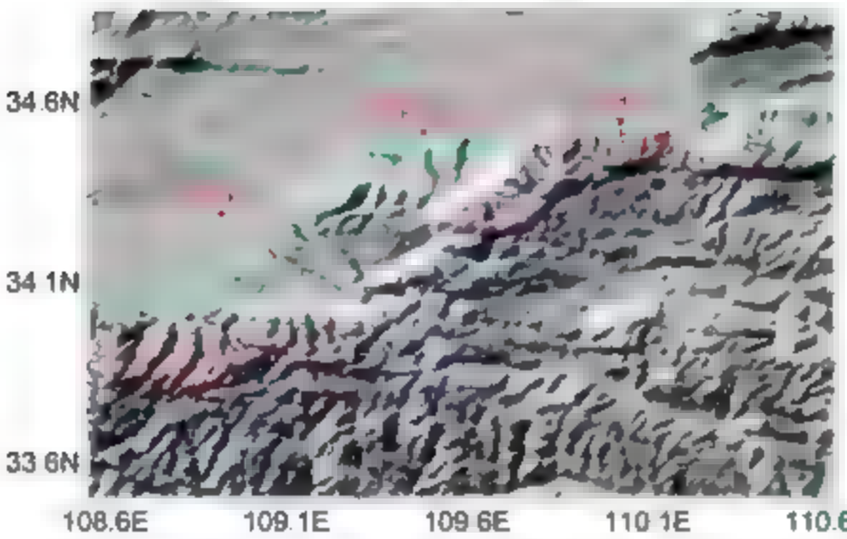

Fig. 1. Topographic map of the study area. The height contours represent elevations of 500 (green), 1500 (blue), and 2000 m above sea level (red), respectively.

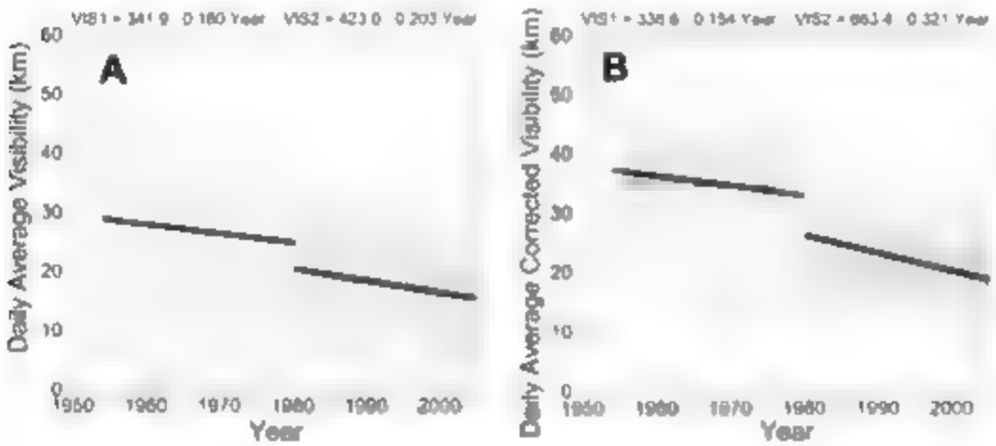

Fig. 2. Trends of (**A**) the observed visibility and (**B**) the corrected visibility at Mt. Hua during the whole observation period. Each point represents the averaged visibility for 1 day. The linear trends are calculated separately for the periods before (VIS1) and after (VIS2) 1980, when the observation methodology was changed. See table S1, A and B, for data.

condensation nuclei (CCN) that reduce the precipitation over Mt. Hua. If this hypothesis is incorrect and visibility does nothing to the precipitation amounts, a reduced visibility should be mainly a result of greater RH and more precipitation at the location of visibility observations (Mt. Hua). This phenomenon should cause an association of decreased visibility with increased precipitation over the mountain, with respect to the reference precipitation in Huayin, which is the closest and best-correlated rain gauge to Mt. Hua. However, the observed relations presented in Fig. 4 show exactly the opposite result. The average precipitation over Mt. Hua is almost double that of Huayin in relatively good visibility of ~20 km. That ratio decreases and the amount of precipitation at Mt. Hua approaches that of Huayin at visibilities of 8 km and below. The effect of decreasing Ro with reduced visibility due to enhanced aerosol loading overpowers the expected opposite bias because of the reduction of visibility over Mt. Hua at times of enhanced precipitation and RH. This observation supports the suggestion that the association between the trends of decreasing visibility and Ro is caused by the impact of increased aerosols, with time causing a trend of suppression in the precipitation over Mt. Hua that is greater than that shown by the plains rain gauge, which is characterized by a decreasing trend of Ro.

According to the curves in Fig. 4, Ro decreased from almost 2 in periods of good visibility to nearly 1 when visibility was less than 8 km. The calculated average Ro for visibility intervals was about 1.65 in periods of good visibility (~20 km) and decreased to nearly 1.2 for visibility of less than 8 km. This average

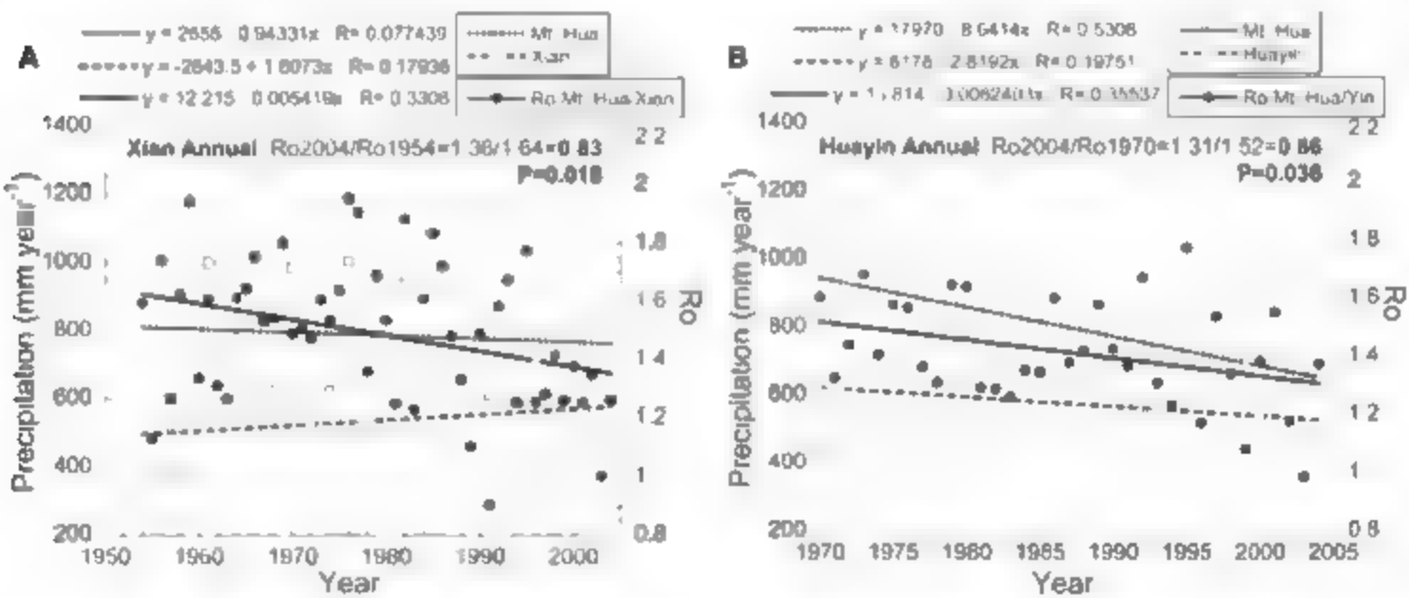

Fig. 3. Trends of annual precipitation amounts and Ro between Mt. Hua and the plain stations of (**A**) Xi'an and (**B**) Huayin. The overall decreasing trend in Ro is given as a solid line within each plot, as the ratio between Ro as estimated by the regression line at the end of the time series and Ro at the beginning of the series. The regression equations for the three lines are given above the top of each plot. See table S2, A and B, for data.

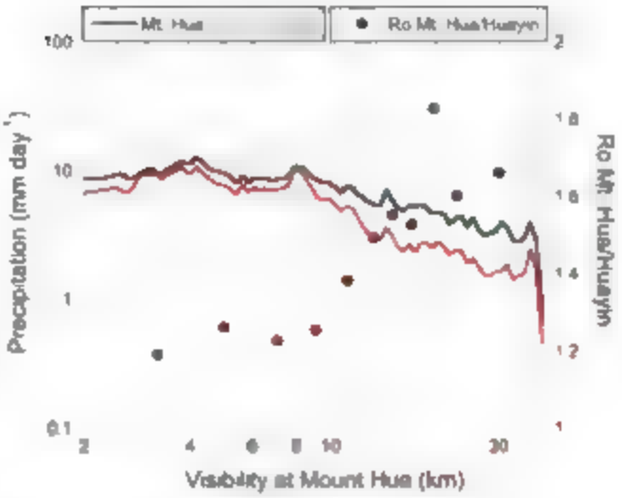

Fig. 4. The daily rainfall at Mt. Hua and Huayin as a function of the visibility at Mt. Hua for 1980 to 2004. The red and black lines are interpolated curve fits with a weight applied. The weight is applied to 20% of the data (−10% to +10% of the data around the current point). Ro, which is the distance between the lines along the logarithmic ordinate, is reduced for lower-visibility distances. Ro for discrete visibility intervals (between 2, 4, 6, 8, 10, 12, 14, 16, 18, 21, 25, and 42 km) is denoted by the large black circles with the values on the right ordinate. The suppression effect saturates at a visibility distance of ~8 km. See table S3, A and B, for data.

decrease in Ro of about 30% is consistent with the findings of the case study reported at the Rocky Mountain top observatory, where a 50% reduction in the snow rate was related to aerosols that caused smaller cloud drops and reduced the efficiency of their riming on snowflakes (*11*).

These observations show that a proxy to CCN concentrations in the free troposphere, the visibility at the top of Mt. Hua at 2060 m above sea level, is directly correlated with the decreasing trend of Ro on a climatologically meaningful scale. The observed suppression of precipitation at Mt. Hua is only one such observation in China, but given the extensive occurrence of this phenomenon elsewhere in the world, it is likely that this is a major cause for suppressing precipitation at the mountain ranges that provide much of the world's water resources.

The sensitivity of the precipitation from orographic clouds to the detrimental impact of pollution aerosols is not one-sided. This also means that seeding the same clouds with aerosols that are engineered to accelerate the conversion of cloud water into precipitation can enhance the precipitation, especially under conditions where the water losses resulting from air pollution are the greatest. This has already been shown to be the case in Israel (*12*).

Quantifying the response of precipitation to aerosol amounts addresses the recommendation of the U.S. National Research Council (*13*) that the concept of radiative forcing should be expanded to metrics of nonradiative forcing, such as those caused by the effects of aerosols on clouds and precipitation, which affect Earth's water and energy cycles.

References and Notes

1. R. Gunn, B. B. Phillips, *J. Meteorol.* **14**, 272 (1957).
2. D. Rosenfeld, *Geophys. Res. Lett.* **26**, 3105 (1999).
3. D. Rosenfeld, *Science* **287**, 1793 (2000).
4. M. O. Andreae *et al.*, *Science* **303**, 1337 (2004).
5. A. Givati, D. Rosenfeld, *J. Appl. Meteorol.* **43**, 1038 (2004).
6. D. Rosenfeld, A. Givati, *J. Appl. Meteorol.* **45**, 893 (2006).
7. I. L. Jirak, W. R. Cotton, *J. Appl. Meteorol.* **45**, 236 (2006).
8. D. A. Griffith, M. E. Solak, D. P. Yorty, *J. Weather Modif.* **37**, 14 (2005).
9. Q. Jinhuan, Y. Luquan, *Atmos. Environ.* **34**, 603 (2000).
10. X. M. Zong, J. Qiu, P. C. Wang, *Chin. Environ. Res.* **10**, 201 (2005) (in Chinese).
11. R. D. Borys, D. H. Lowenthal, S. A. Cohn, W. O. J. Brown, *Geophys. Res. Lett.* **30**, 1538 (2003).
12. A. Givati, D. Rosenfeld, *J. Appl. Meteorol.* **44**, 1298 (2005).
13. Committee on Radiative Forcing Effects on Climate, Climate Research Committee, National Research Council, *Radiative Forcing of Climate Change: Expanding the Concept and Addressing Uncertainties* (National Academies Press, Washington, DC, 2005).

14. This research was supported by the National Natural Science Foundation of China (grant 40575004), the Chinese Ministry of Science and Technology (grant 2005DIB3J099), the Foreign Expert Bureau of Shaanxi Province, and the Meteorological Bureau of Shaanxi Province. We are grateful to the Meteorological Information Center of Shaanxi Province for providing all data in this research.

Supporting Online Material

www.sciencemag.org/cgi/content/full/315/5817/1396/DC1
Tables S1 to S3
SOM Table Legends

27 November 2006; accepted 30 January 2007
10.1126/science.1137949

Autophagy-Dependent Viral Recognition by Plasmacytoid Dendritic Cells

Heung Kyu Lee,[1]* Jennifer M. Lund,[1]*† Balaji Ramanathan,[1]* Noboru Mizushima,[2,3] Akiko Iwasaki[1]‡

Plasmacytoid dendritic cells (pDCs) detect viruses in the acidified endosomes by means of Toll-like receptors (TLRs). Yet, pDC responses to certain single stranded RNA (ssRNA) viruses occur only after live viral infection. We present evidence here that the recognition of such viruses by TLR7 requires transport of cytosolic viral replication intermediates into the lysosome by the process of autophagy. In addition, autophagy was found to be required for the production of interferon-α by pDCs. These results support a key role for autophagy in mediating ssRNA virus detection and interferon-α secretion by pDCs and suggest that cytosolic replication intermediates of viruses serve as pathogen signatures recognized by TLR7.

Detection of viral infection by the innate arm of the mammalian immune system relies on several distinct pathways. The classical viral recognition pathway, used by most cell types, involves cytoplasmic pattern recognition molecules to detect viral signatures such as double-stranded RNA (dsRNA) structures (*1*) and 5′-triphosphate RNA (*2*, *3*). In contrast, the plasmacytoid dendritic cells (pDCs) are thought to detect viruses without being directly infected and achieve this through the use of Toll-like receptors (TLRs) in the endosomes (*4*). Viral particles containing dsDNA genomes, such as herpes simplex viruses (HSV) and murine cytomegalovirus, are recognized by TLR9 (*5*, *6*), whereas those containing single-stranded RNA (ssRNA) genomes, such as influenza virus and vesicular stomatitis virus (VSV), are detected by TLR7 (*7*–*9*). When experimentally targeted to the endosome by liposomal agents, purified dsDNA and ssRNA can trigger TLR-dependent expression of type I interferons (IFNs) (*7*, *9*, *10*). Moreover, ultraviolet (UV) irradiated HSV (*6*, *11*, *12*) and heat-inactivated (*7*) or formaldehyde-fixed (*13*) influenza virus can induce IFN-α responses comparable to their live counterparts in pDCs. pDC recognition of HIV-1 occurs independently of fusion or replication but requires attachment and endocytosis, showing that infection by live virus is not required (*14*). These observations have led to the idea that the TLR-mediated recognition of viruses in pDCs occurs without direct infec-

tion and that the presence of viral genomic nucleic acids within the endosomal lysosomal compartments is sufficient to activate antiviral pathways (*15*). However, this paradigm does not explain why UV irradiation renders particular ssRNA viruses, such as respiratory syncytial virus (*16*) and VSV (*17*), incapable of inducing IFN-α secretion from pDCs. In these cases, the mechanism of recognition of ssRNA viruses by pDCs remains unclear and suggests that a separate pathway may be operating to ensure recognition of such viruses in pDCs.

To explore the intracellular mechanisms of ssRNA viral recognition in pDCs, we examined the requirement of different stages in viral infection. In contrast to the situation with HSV recognition (*6*, *11*, *12*), robust IFN-α production by purified pDCs (*18*) in response to the ssRNA viruses, Sendai virus (SV), and VSV, required live virus infection (Fig. 1). Thus, UV-irradiated SV and VSV induced comparatively lower levels of IFN-α production in pDCs relative to live viruses (Fig. 1A). This difference in IFN-α levels could not be accounted for by increased virion production with live viruses, because pDCs failed to produce a significant number of virions during 18 hours of incubation (fig. S1). In contrast to SV and VSV, both UV-irradiated and live influenza virus particles induced comparable levels of IFN-α (Fig. 1A). In addition, recognition of all of these ssRNA viruses depended entirely on TLR7 in pDCs (Fig. 1B). Thus, robust IFN-α production in pDCs after stimulation with VSV and SV, but not influenza (*7*), requires a recognition event coupled to viral replication.

We reasoned that if viral replication intermediates were being detected in pDCs following VSV and SV infection, then fusion and entry of viruses must precede recognition. To examine this possibility, we used a VSV mutant with a single amino acid deletion (methionine 51) in the matrix (M) protein (VSVΔM51) (*19*). In wild-type (WT) VSV, the M protein blocks transport of mRNA from the nucleus to the cytosol (*20*), thus preventing translation of host genes, including IFN-α. We reasoned that if fusion and viral protein synthesis were a prerequisite for viral recognition, the VSV mutant lacking a functional M protein would be expected to result in higher levels of IFN-α synthesis. Indeed, VSVΔM51 induced significantly higher levels of IFN-α than did WT VSV, at the same multiplicity of infection (MOI) (Fig. 1C) in the absence of productive virion synthesis (fig. S1). These results supported the hypothesis that viral replication intermediates generated after viral fusion and delivery of the viral nucleoprotein particles to the cytosol provide a major stimulus for IFN-α production by pDCs upon VSV infection.

It was unclear how cytosolic viral replication intermediates were recognized by TLR7 in the lysosome of pDCs. A well-known pathway by which cytosolic materials are introduced to the lysosome involves autophagy (*21*). To determine whether autophagy is involved in the transport of cytosolic viral replication intermediates to the lysosome for TLR7-mediated detection of viruses in pDCs, we first examined the formation of autophagic vesicles in pDCs after virus stimulation. Historically, autophagosomes have been detected by electron microscopy (EM). However, it is difficult to distinguish and quantitate true autophagic vacuoles from other structures by morphology solely based on EM. Therefore, we used transgenic mice expressing the LC3 protein fused with the green fluorescent protein (GFP), which allowed us to visualize autophagosome formation in real time in live cells (*22*). During autophagosome formation, LC3 undergoes transition from the cytosolic form to a membrane-associated form, which is scored as cytoplasmic puncta by fluorescence microscopy (*23*). The LC3-GFP transgene expression had no effect on the biological functions of pDCs (fig. S2). To obtain statistically significant quantification of autophagosomes, we used multispectral imaging flow cytometry (MIFC), which allows characterization of single cells within a population by assessing a combination of morphology and immunofluorescence patterns. Autophagosomes in pDCs were quantitated by enumerating CD11c$^+$ PDCA-1$^+$ cells displaying cytosolic punctate GFP pattern (Fig. 2). These analyses revealed that autophagosome formation occurs constitutively in pDCs and that infection with VSV did not result in a significant increase in the percentage of pDCs containing autophagosomes (table S1).

We next examined the requirement for autophagy in innate viral recognition by pDCs. To this end, we stimulated bone marrow cells with VSV in the presence of different doses of pharmacological inhibitors of autophagy, 3-methyladenine (3-MA) (*24*) and Wortmannin (*25*). At doses of 3-MA (1 to 10 mM) and Wortmannin (10 to 100 nM) that are known to specifically inhibit autophagy (*24*, *25*), IFN-α production was completely abolished in response to VSV (Fig. 3). Further, in purified pDCs, lower doses of these inhibitors still resulted in selective partial inhibition of responses to VSV, but not influenza, without affecting cell survival (fig. S3 and supporting online material text). One potential complication in the use of Wortmannin is that it can also inhibit endocytosis (*26*). To rule out this possibility, we examined the extent of infection by VSV, which depends on endocytosis, at varying doses of 3-MA and Wortmannin. The inhib-

[1]Department of Immunobiology, Yale University School of Medicine, New Haven, CT, USA. [2]Department of Cell Physiology, Tokyo Medical and Dental University, Graduate School and Faculty of Medicine, Tokyo, Japan. [3]Solution-Oriented Research for Science and Technology, Japan Science and Technology Agency, Kawaguchi, Japan.

*These authors contributed equally to this work.
†Present address: Department of Immunology, University of Washington, Seattle, WA.
‡To whom correspondence should be addressed. E-mail: akiko.iwasaki@yale.edu

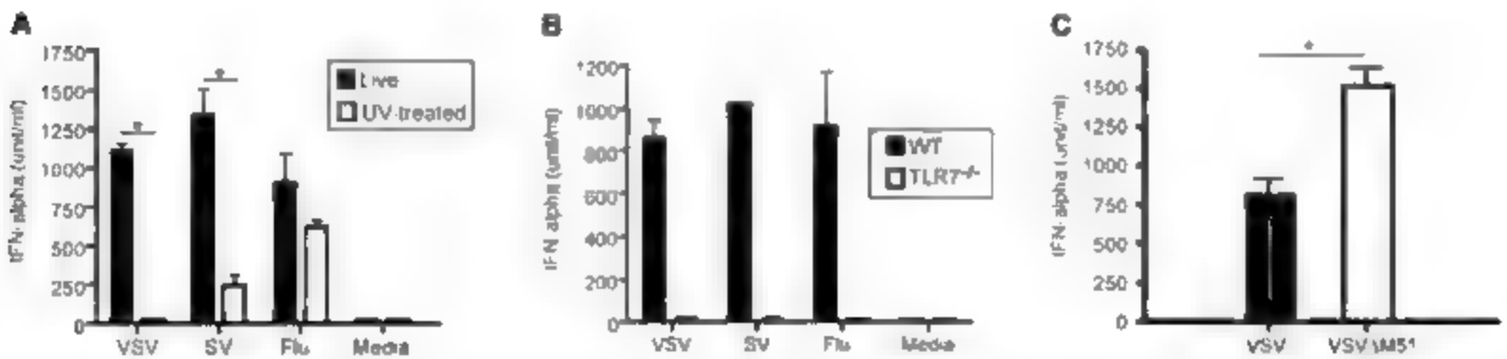

Fig. 1. Differential recognition of ssRNA viruses by pDCs. (**A** to **C**) WT or (**B**) TLR7$^{-/-}$ mouse bone marrow pDCs (2×10^5) were sorted by fluorescence-activated cell sorting (FACS) and stimulated for 18 hours with [(A) and (B)] live or UV inactivated VSV (MOI = 10), SV (2.8×10^5 chicken embryo ID_{50}/ml), or influenza A/PR8 (MOI = 5); or (C) VSV ΔM51 or VSV (both at MOI = 10). IFN-α levels were detected in culture supernatants by enzyme-linked immunosorbent assay. Asterisk, $P < 0.05$. The data are representative of three similar experiments.

itors at the ranges effective in suppressing IFN-α production did not affect endocytosis or subsequent steps involved in VSV infection in pDCs or in non-pDCs, as determined by the VSV G-GFP expression (Fig. 3). These results indicated that 3-MA and Wortmannin specifically inhibited autophagosome formation without affecting viral entry and infection, and inhibited VSV recognition in pDCs.

To definitively demonstrate the role of autophagy in viral recognition, we used a genetic approach by examining pDCs isolated from mice deficient in ATG5, a gene essential for autophagosome formation (27). Because ATG5$^{-/-}$ mice are incapable of survival beyond 1 day of life (27), mature ATG5$^{-/-}$ pDCs were obtained from lethally irradiated WT mice reconstituted with liver and spleen cells from the ATG5$^{-/-}$ neonates. Upon full reconstitution with ATG5$^{-/-}$ cells (fig. S4A),

Fig. 2. Formation of autophagosomes in pDCs. PDCA-1$^+$CD11c$^+$ cells obtained from LC3-GFP transgenic mice were analyzed for the presence of punctate GFP$^+$ autophagosomes by MIFC 5 hours after incubation with VSV at the indicated MOIs or media control. The upper four cells in the media control represent cytosolic GFP$^+$ cells, whereas the rest of the cells represent pDCs with GFP puncta. The columns represent bright-field (BF) imaging (gray) and PDCA-1 (orange), LC3-GFP (green), DRAQ5 nuclear (Nuc, red), and GFP/nuclear (overlay) stains. Scale bars, 10 μm. Each row is a composite of different micrographs of the same cells. These experiments have been repeated three times with similar results.

all hematopoietic cells lacked the ATG gene (fig. S4B). Such mice had no obvious defects in survival or growth, and reconstituted hematopoietic compartments, including pDCs in the spleen, lymph nodes, and bone marrow (Fig. 4A), indicating that ATG5 is not required for the development of pDCs in vivo. To examine the requirement for autophagy in innate viral recognition, pDCs purified from the ATG5$^{+/+}$ or ATG5$^{-/-}$ chimeras were infected with VSV. After VSV infection, secretion of both IFN-α and interleukin-12 (IL-12) was diminished in the absence of ATG5 (Fig. 4, B and C). The diminished

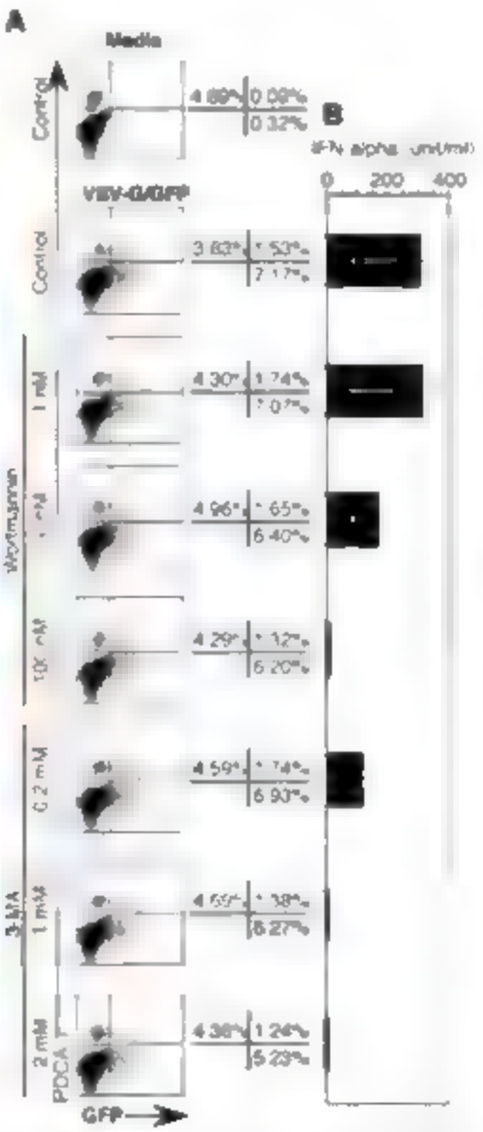

Fig. 3. Inhibitors of autophagy block VSV recognition. Bone marrow cells were stimulated with VSV-G/GFP (MOI = 10) in the presence of the indicated doses of inhibitors of autophagy, Wortmannin and 3-MA, and (**A**) infection (GFP) and (**B**) IFN-α secretion were assessed. Neither infection of pDCs (upper right quadrant) nor infection of non-pDCs (lower right quadrant) was affected by these inhibitors at any doses examined, whereas IFN-α production was inhibited in a dose-dependent manner. The data are representative of three similar experiments.

cytosine secretion could not be accounted for by the difference in the rate of infection (Fig. 4D) or survival of pDCs (fig. S6). In contrast, HSV-1 or CpG stimulation of ATG5$^{-/-}$ pDCs resulted in similar secretion of IL-12 and decreased levels of IFN-α (fig. S5). These data indicated that, although innate recognition of HSV-1 and CpG remains intact in ATG5$^{-/-}$ pDCs, the IFN-α production pathway is altered in the absence of ATG5. Although the mechanism is unknown, the selective defect in IFN-α, but not IL-12 production by the ATG5$^{-/-}$ pDCs might reflect defective sorting of the TLR downstream signaling components to the lysosomes. Further, to investigate the role of autophagy in antiviral responses by pDCs in vivo, ATG5$^{+/+}$ and ATG5$^{-/-}$ chimeric mice were infected with VSV. Systemic infection with VSV is known to target splenic pDCs and induce peak IFN-α production in the serum at around 12 hours (*17*). Since IL-12 and other inflammatory cytokines are secreted by non-pDCs in response to VSV infection, we measured serum IFN-α levels. Infection of ATG5$^{-/-}$ chimeric mice resulted in significantly reduced IFN-α responses compared with the ATG5$^{+/+}$ chimeras (Fig. 4E). Collectively, our data indicated that autophagy occurs constitutively in pDCs and is required for recognition of VSV, but not HSV-1, infection in pDCs. In addition, autophagy is required for pDC production of type I IFNs in vitro and in vivo.

Autophagy is an ancient pathway for homeostatic turnover of long-lived intracellular components and for nutrient acquisition during starvation. Recent studies indicated the importance of autophagosomes as an antimicrobial mechanism used to degrade and destroy cytosolic pathogens. Certain virus infections such as HSV-1 are known to trigger autophagy (*28*) for the purposes of viral degradation (*29*), whereas poliovirus and rhinovirus usurp autophagosomal machinery for viral synthesis (*30*). Our study reveals the importance of autophagy in innate recognition of viral pathogens and IFN-α production in pDCs. The findings of this report highlight the differential requirement for recognition of diverse classes of viruses in pDCs. A broad spectrum of viruses and their infection cycles, from the virion-associated genomic nucleic acids in the endosomes to the replication of viral genomes in the cytosol, are detected by pDCs. Finally, immunological interventions designed to combat certain chronic viral infections might benefit from incorporating agents to promote autophagy for both viral degradation and innate recognition.

References and Notes

1. H. Kato *et al.*, *Nature* **441**, 101 (2006).
2. A. Pichlmair *et al.*, *Science* **314**, 997 (2006).
3. V. Hornung *et al.*, *Science* **314**, 994 (2006).

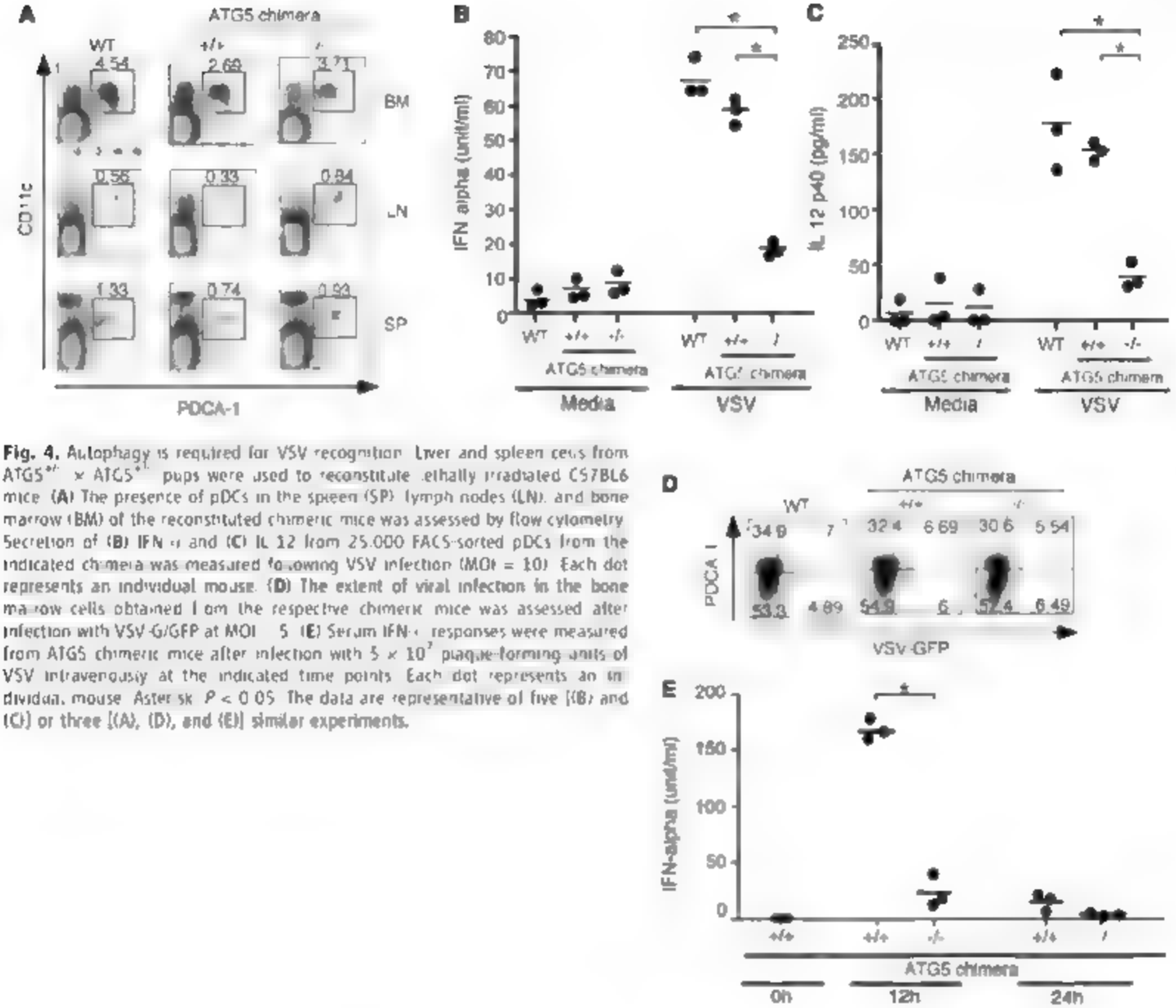

Fig. 4. Autophagy is required for VSV recognition. Liver and spleen cells from ATG5$^{+/+}$ × ATG5$^{+/+}$ pups were used to reconstitute lethally irradiated C57BL6 mice. (**A**) The presence of pDCs in the spleen (SP), lymph nodes (LN), and bone marrow (BM) of the reconstituted chimeric mice was assessed by flow cytometry. Secretion of (**B**) IFN-α and (**C**) IL-12 from 25,000 FACS-sorted pDCs from the indicated chimera was measured following VSV infection (MOI = 10). Each dot represents an individual mouse. (**D**) The extent of viral infection in the bone marrow cells obtained from the respective chimeric mice was assessed after infection with VSV-G/GFP at MOI = 5. (**E**) Serum IFN-α responses were measured from ATG5 chimeric mice after infection with 5×10^7 plaque-forming units of VSV intravenously at the indicated time points. Each dot represents an individual mouse. Asterisk, $P < 0.05$. The data are representative of five [(B) and (C)] or three [(A), (D), and (E)] similar experiments.

4. N. Kato *et al.*, *Immunity* **23**, 19 (2005).
5. A. Krug *et al.*, *Immunity* **21**, 107 (2004).
6. J. Lund, A. Sato, S. Akira, R. Medzhitov, A. Iwasaki, *J. Exp. Med.* **198**, 513 (2003).
7. S. S. Diebold, T. Kaisho, H. Hemmi, S. Akira, C. Reis e Sousa, *Science* **303**, 1529 (2004).
8. J. M. Lund *et al.*, *Proc. Natl. Acad. Sci. U.S.A.* **101**, 5598 (2004).
9. F. Heil *et al.*, *Science* **303**, 1526 (2004).
10. K. Yasuda *et al.*, *J. Immunol.* **174**, 6129 (2005).
11. A. Krug *et al.*, *Blood* **103**, 1433 (2004).
12. M. L. Gilfillan, G. V. Alm, *Scand. J. Immunol.* **49**, 391 (1999).
13. C. Asselin-Paturel *et al.*, *Nat. Immunol.* **2**, 1144 (2001).
14. A. S. Beignon *et al.*, *J. Clin. Invest.* **115**, 3265 (2005).
15. K. Crozat, B. Beutler, *Proc. Natl. Acad. Sci. U.S.A.* **101**, 6835 (2004).
16. V. Hornung *et al.*, *J. Immunol.* **173**, 5935 (2004).
17. W. Barchet *et al.*, *J. Exp. Med.* **195**, 507 (2002).
18. Materials and methods are available as supporting material on *Science* Online.
19. D. F. Stojdl *et al.*, *Cancer Cell* **4**, 263 (2003).
20. C. von Kobbe *et al.*, *Mol. Cell* **6**, 1243 (2000).
21. N. Mizushima, Y. Ohsumi, T. Yoshimori, *Cell Struct. Funct.* **27**, 421 (2002).
22. N. Mizushima, A. Yamamoto, M. Matsui, T. Yoshimori, Y. Ohsumi, *Mol. Biol. Cell* **15**, 1101 (2004).
23. Y. Kabeya *et al.*, *EMBO J.* **19**, 5720 (2000).
24. P. O. Seglen, P. B. Gordon, *Proc. Natl. Acad. Sci. U.S.A.* **79**, 1889 (1982).
25. E. F. Blommaart, U. Krause, J. P. Schellens, H. Vreeling-Sindelarova, A. J. Meijer, *Eur. J. Biochem.* **243**, 240 (1997).
26. N. Araki, M. T. Johnson, J. A. Swanson, *J. Cell Biol.* **135**, 1249 (1996).
27. A. Kuma *et al.*, *Nature* **432**, 1032 (2004).
28. Z. Jaliocz *et al.*, *Proc. Natl. Acad. Sci. U.S.A.* **99**, 190 (2002).
29. Z. Jaliocz, H. W. Virgin IV, B. Levine, *Autophagy* **2**, 24 (2006).
30. W. T. Jackson *et al.*, *PLoS Biol.* **3**, e156 (2005).

31. We are grateful to J. Publicover and J. Rose for reagents and expertise, R. Medzhitov for critical review of the manuscript, W. Mothes for helpful discussions, and M. Zamora and G. Lyon for technical assistance. We thank P. J. Morrissey, B. Hall, and T. C. George of Amnis Corporation for analysis of samples using ImageStream technology. This work was supported by Public Health Service grants AI054359 and AI064705 (to A.I.) from NIH. J.M.L. was supported by the training grant AI07019 from NIH. H.K.L. was supported by the Ministry of Science and Technology of Korea. A.I. holds an Investigators in Pathogenesis of Infectious Disease Award from the Burroughs Wellcome Fund.

Supporting Online Material

www.sciencemag.org/cgi/content/full/1136880/DC1
Materials and Methods
SOM Text
Figs. S1 to S6
Table S1
References

30 October 2006; accepted 12 January 2007
Published online 1 February 2007;
10.1126/science.1136880
Include this information when citing this paper.

Structural Insight into the Transglycosylation Step of Bacterial Cell-Wall Biosynthesis

Andrew L. Lovering, Liza H. de Castro, Daniel Lim, Natalie C. J. Strynadka*

Peptidoglycan glycosyltransferases (GTs) catalyze the polymerization step of cell-wall biosynthesis, are membrane-bound, and are highly conserved across all bacteria. Long considered the "holy grail" of antibiotic research, they represent an essential and easily accessible drug target for antibiotic-resistant bacteria, including methicillin-resistant *Staphylococcus aureus*. We have determined the 2.8 angstrom structure of a bifunctional cell wall cross-linking enzyme, including its transpeptidase and GT domains, both unliganded and complexed with the substrate analog moenomycin. The peptidoglycan GTs adopt a fold distinct from those of other GT classes. The structures give insight into critical features of the catalytic mechanism and key interactions required for enzyme inhibition.

The bacterial cell wall is built by glycosyltransferase (GT) and transpeptidase (TP) enzymes, which together produce a cross-linked peptidoglycan mesh that gives the bacterium its strength and shape. These enzymes are excellent drug targets because they are essential, are accessible from the periplasm, and have no equivalent in mammalian cells. TP enzymes [also known as penicillin-binding proteins (PBPs)] are the target of the β-lactam group of antibacterials, to which a disturbingly high degree of resistance has developed over the past two decades of clinical use. The peptidoglycan GT protein family, GT_{51} (www.cazy.org), has no structural representatives to date and is an attractive candidate for the structure-based drug design of new antibacterial compounds.

GT_{51} and TP enzymes may be present as monofunctional or bifunctional proteins (*1*), with the more prevalent bifunctional enzymes possessing an N-terminal GT_{51} domain and a C-terminal TP domain, separated by a small linker region. The GT_{51} domains are always membrane-bound, and they polymerize a lipid II pentapeptide substrate into β1,4-linked *N*-acetylmuramic acid, *N*-acetyl glucosamine polymers [(NAM-NAG)$_n$]. The TP domains are solvent-exposed and catalyze the cross-linking of the peptide substituents on the 3′ acetyl groups of NAM. Inhibitors of the GT_{51} reaction may be less subject to the development of resistance than TP inhibitors, which can be rendered ineffective by alteration of the peptide substituents—notably in vancomycin-resistant strains (*2*, *3*). There is only one well-characterized inhibitor of the GT_{51} reaction, the *Streptomyces* natural product moenomycin, which is not effective in humans because of poor absorption properties (*4*). Despite its extensive use as a growth promoter in animal feed, no plasmid-borne resistance to moenomycin has been detected so far (*5*). Understanding of the specific moenomycin-GT_{51} interactions would be useful in designing a similar compound to treat human bacterial infections. Here, we report two crystal structures of a soluble truncated version of PBP2 (the only bifunctional enzyme identified in the pathogen *Staphylococcus aureus*), an apoenzyme structure (2.9 Å resolution), and a complex of the enzyme with the antibiotic moenomycin (2.8 Å). The growth of both crystal forms required the detergent lauryldimethylamine-oxide (*6*). Both structures have favorable stereochemistry (table S1), with R_{work}/R_{free} values of 19.1/24.6% for the apoenzyme and 23.1/28.0% for the moenomycin-bound form.

The PBP2 structure reveals a bilobal fold (dimensions 55 by 60 by 110 Å), with the GT_{51} and TP domains separated by a short β-rich linker region (Fig. 1). The construct used (amino acids 59 to 716) omitted the N-terminal transmembrane sequence and some of the low-complexity C-terminal tail. Electron density is visible for residues 67 to 692, except for a few short loops in the GT_{51} domain (127 to 139 and 160 to 163 in the apoenzyme and 137 to 144 in the moenomycin complex). The TP domain structure has high structural homology to *Streptococcus pneumoniae* PBP1a (*7*) [29% sequence identity for the 293-to-679 region, with a root mean square deviation (RMSD) of 2.0 Å for Cα]. Either, but not both, of the GT_{51}-TP catalytic domains are superimposable when comparing the two crystal forms, indicating that there is some flexibility around the linker region.

The GT_{51} domain has two putative catalytic glutamic acid residues [E114 and E171 (*8*)], and their importance has been demonstrated in mutational studies on the *Escherichia coli* PBP1b enzyme (*9*). The overall fold of the lipid II–dependent GT_{51} domain shows no similarity to either of the GT-A or GT-B folds that have been observed in all preceding GT enzyme class structures. The structure is primarily α-helical and is composed of two segments: one globular "head" region situated next to the linker domain and a smaller "jaw" region beneath this, closer to the membrane (Fig. 1). The globular segment has seven α helices and a small β region, and it has low structural similarity to bacteriophage λ lysozyme (λL) [DALI gives a *Z* score of 3.5, 12% sequence identity for the 98-to-266 region, with an RMSD of 4.2 Å for Cα]. Given that the two enzymes act on similar substrates, it is possible that the GT_{51} module was acquired by the bacteriophage at a point long ago in its evolution. Despite low sequence identity, there is good overlap of the secondary structure between the two enzymes, and the first putative glutamate catalytic residue of the GT_{51} domain overlays that of λL (E114 with E19, respectively; Fig. 2A). The helical topology is preserved between the lysozyme and GT_{51} folds, with the soluble β-rich domain 1 of λL replaced by the membrane-associated GT_{51} jaw subdomain (residues 121 to 182). The jaw is composed of three α helices, with the outermost helix containing the second putative catalytic residue E171. A pocket formed

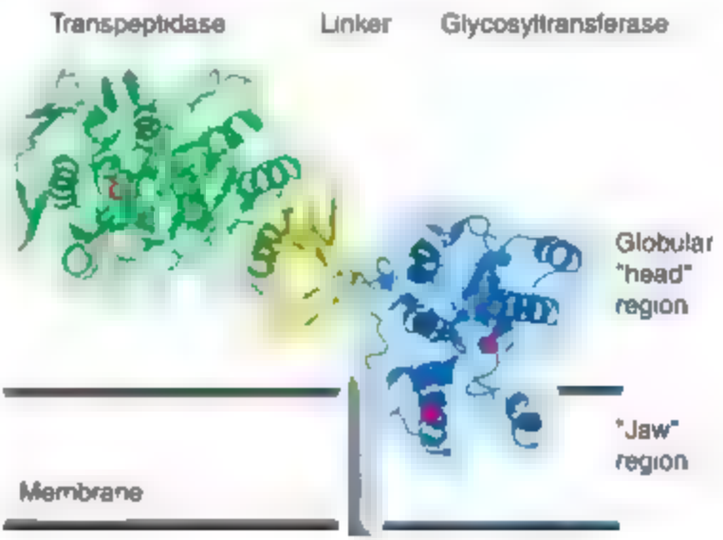

Fig. 1. Overall structure of PBP2. The modular nature of the GT_{51} and TP folds is shown, with the predicted position of the transmembrane region represented by a vertical blue rectangle. The active-site residues for the GT_{51} (lower, E171, upper, E114) and TP (S398) functionalities have their Cα atoms shown as red spheres. The GT_{51} domain is proposed to be at least partly submerged in the bilayer in order to access the lipid II substrate, which is consistent with observations that catalytic activity and crystallization were dependent on the presence of detergents.

Department of Biochemistry and Molecular Biology, and Center for Blood Research, University of British Columbia, 2350 Health Sciences Mall, Vancouver, Canada.

*To whom correspondence should be addressed. E-mail: natalie@byron.biochem.ubc.ca

by residues close to the linker region shows sequence conservation in other GT_{51} enzymes and may be important for contacting the end of the transmembrane segment. A cleft between the globular and jaw subdomains connects this pocket with a larger pocket on the opposite side of the molecule. The cleft superimposes with the substrate binding site in λL and related lysozyme folds (Fig. 2A).

The active site of the TP domain contains the characteristic SXXK, (S/Y)X(N/C), and (K/H)T S/G motifs (*1*). The TP catalytic S398 residue lies ~70 Å from the putative catalytic residue E114 of the GT_{51} domain. The GT_{51} fold possesses five signature motifs, conserved in both the monofunctional and bifunctional GT_{51} enzymes (*1*) (fig. S1). Motifs I and III contain the GT_{51} catalytic glutamic acids (E114 and E171, respectively), with their Cδ atoms ~14 Å apart in the apoenzyme. Of the five signature motifs, motifs IV and V appear to largely play a role in maintaining the structure of the GT_{51} fold, whereas motif II forms the innermost helix of the jaw subdomain that divides the two pockets and is probably involved in substrate recognition. Constraints imposed by the location of N-terminal residues 68 to 73, the hydrophobicity of the lower part of the jaw subdomain, and the hydrophilic nature of the TP domain lead to a model for membrane orientation (Fig. 3).

The moenomycin-bound structure (Fig. 3) was obtained by cocrystallization. The electron density of this complex inhibitor is well defined for all groups other than the C_{25} lipid unit (Fig. 3C). Moenomycin binds in the cleft between the head and jaw regions of the GT_{51} fold, in an extended conformation that probably mimics that of the growing sugar-chain substrate or product. Rings B to F (Fig. 3B), modeled in a chair conformation, form a twisted plane, with ring F nearest the putative E114 catalytic residue, ring B located toward the linker region, and ring D projecting out into the bulk solvent. Consistent with this model, moenomycin derivatives lacking ring D retain antibiotic activity (*11*). Ring A exits the channel on the side farthest from the membrane and may be positioned similarly to a peptide substituent from a NAM substrate. The phosphoric acid diester group of moenomycin is under the plane of rings B to F, in an orientation that potentially directs the lipid group toward the membrane. The interactions between the protein and inhibitor are extensive (Fig. 3A), consistent with moenomycin and related compounds possessing some of the lowest median inhibitory concentration values known for antibiotics (*12*). The head subdomain is largely identical between the apoenzyme and moenomycin-bound GT_{51} structures, whereas

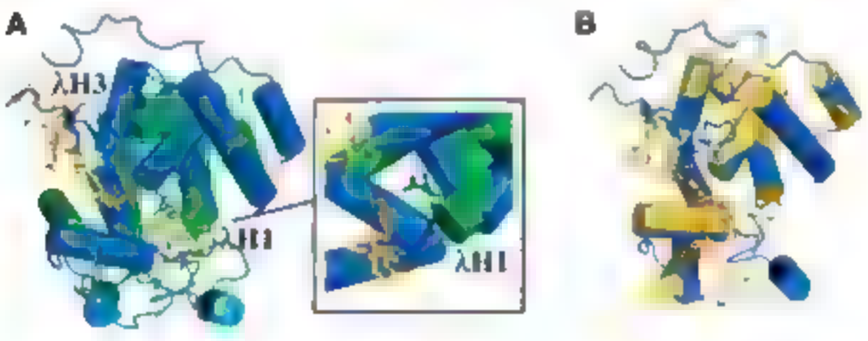

Fig. 2. GT_{51} domain comparison with lysozyme and conformational change between the apoenzyme and liganded forms. (**A**) Structure-based alignment of the GT_{51} domain (blue) with that of λL (green). Helices H1 and H3 of λL have counterparts in all related G- C- and V-type lysozyme folds (*20*). The putative E114 catalytic residue of the GT_{51} domain aligns well with that of λL (both in stick representation) at the end of λL helix H1. (Inset) Orthogonal view with loops omitted. The lysozyme structure from deposition 1D9U (*15*) is shown, with the poly-NAG ligand in stick form. The figure highlights both the striking similarity in secondary structure (localized only to the GT_{51} head subdomain) and the conservation of an active-site cleft between the two enzyme types. The regions below the cleft have no structural similarity and are presumably different because of the need for the GT_{51} domain to be localized at the membrane and to bind a lipidic substrate. (**B**) Conformational change in the jaw subdomain upon binding moenomycin (represented in stick form). The moenomycin-bound form is blue, and the apoenzyme is yellow.

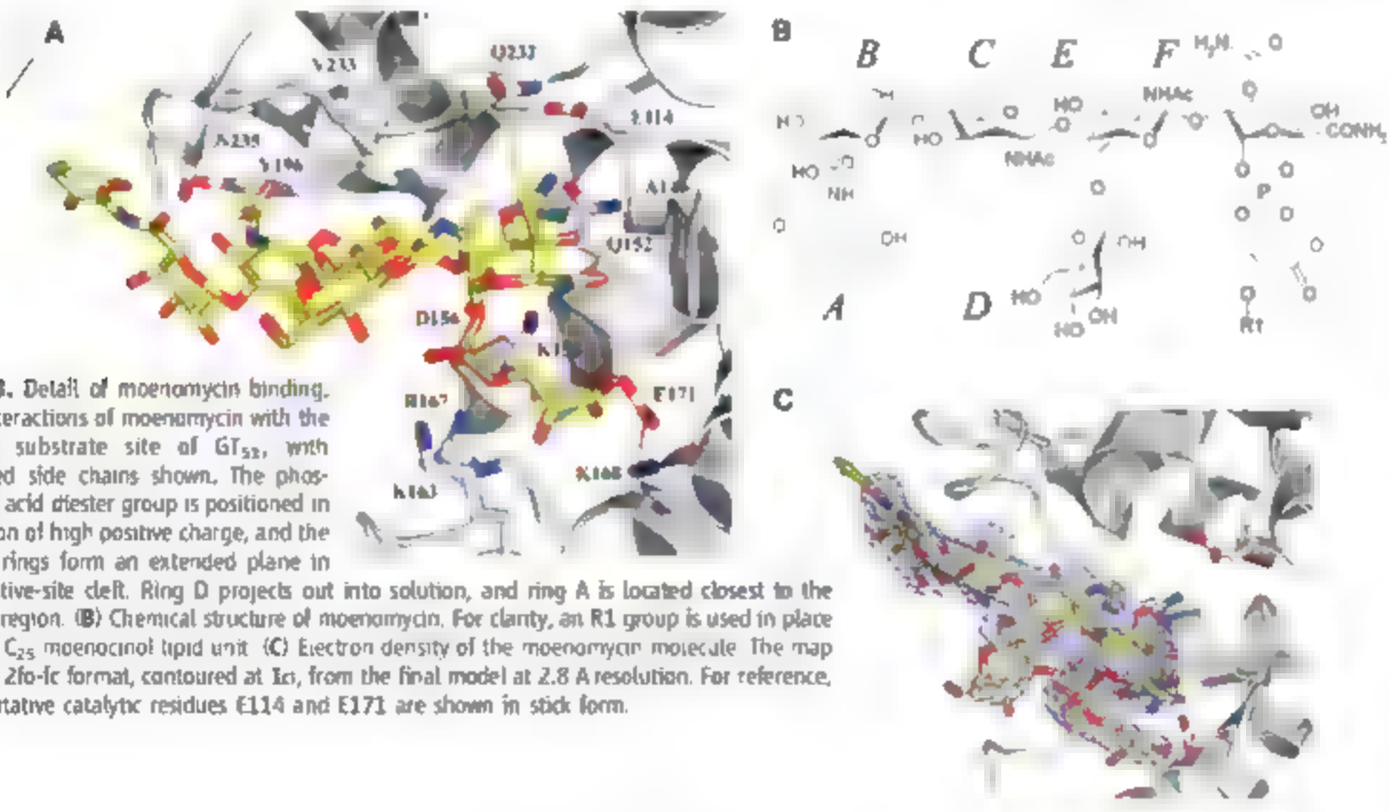

Fig. 3. Detail of moenomycin binding. (**A**) Interactions of moenomycin with the donor substrate site of GT_{51}, with selected side chains shown. The phosphoric acid diester group is positioned in a region of high positive charge, and the sugar rings form an extended plane in the active-site cleft. Ring D projects out into solution, and ring A is located closest to the linker region. (**B**) Chemical structure of moenomycin. For clarity, an R1 group is used in place of the C_{25} moenocinol lipid unit. (**C**) Electron density of the moenomycin molecule. The map is of a 2fo-fc format, contoured at 1σ, from the final model at 2.8 Å resolution. For reference, the putative catalytic residues E114 and E171 are shown in stick form.

large conformational changes occur in the gw subdomain (Fig. 2B). The strictly conserved D115, H121, K184, and H187 residues and the largely conserved A173, T150, and E179 residues are located in the hinge region between the two subdomains and may be important in the ability of the GT_{51} domain to undergo such a conformational change. Based on chemical similarity, it has been proposed that rings C and E of moenomycin would bind in the same way as a NAM-NAG disaccharide of the substrate. In the complex of GT_{51} with moenomycin, the ring oxygens and N-acetyl groups of rings C and E and all three β1,4 linkages are spaced in agreement with a linear glycan chain. Arranging the β-1,4 linkages of the growing chain substrate to mimic those of the inhibitor places the reducing 4-OH end of the chain furthest from the catalytic machinery, identical to that of the lysozyme family of enzymes.

The differences between the moenomycin ring F phosphoric acid diester C_{35} moieties and the substrate NAM pyrophosphate C_{55} moieties must be responsible for GT_{51} inhibition by moenomycin. To investigate this hypothesis, we modeled a productive complex of both the lipid II and growing chain substrates on the moenomycin-bound structure. Whether lipid II is the donor or acceptor in the polymerization reaction has been extensively debated (*13*). From constraints imposed by the structures of the apoenzyme- and moenomycin-bound forms, we can now almost definitely conclude that lipid II is the acceptor and the growing chain is the donor, with support from numerous experimental sources [summarized by Welzel (*13*)]. Modeling the growing chain (donor) substrate onto the moenomycin structure, a NAG group is placed over ring E, and the adjoining NAM sugar superimposes with ring F. The moenomycin-based model also situates the NAM peptide substituents so that no steric clashes occur with the active-site cleft. Replacing the β1,4 linkage between a NAM-NAG disaccharide with a β1,2 linkage between rings E and F in moenomycin results in each ring F substituent of moenomycin correlating with the C_{-2} substituent of NAM (e.g., the C3 OCONH$_2$ group of ring F with the C5 CH$_2$OH group of NAM). Because of this staggering, the C1 phosphoryl groups of both the inhibitor and the substrate point in similar (axial) orientations, and the C4 OH of moenomycin is roughly equivalent to the modeled ring oxygen of NAM [as suggested earlier in (*14*)]. This positions the axial methyl on C4 of the inhibitor above the plane of NAM, over the ring oxygen. The methyl group lies between the donor C1 site of nucleophilic attack and the region occupied by E114 and the incoming 4-OH end of the acceptor. In our structures, there is ample space to model the lipid

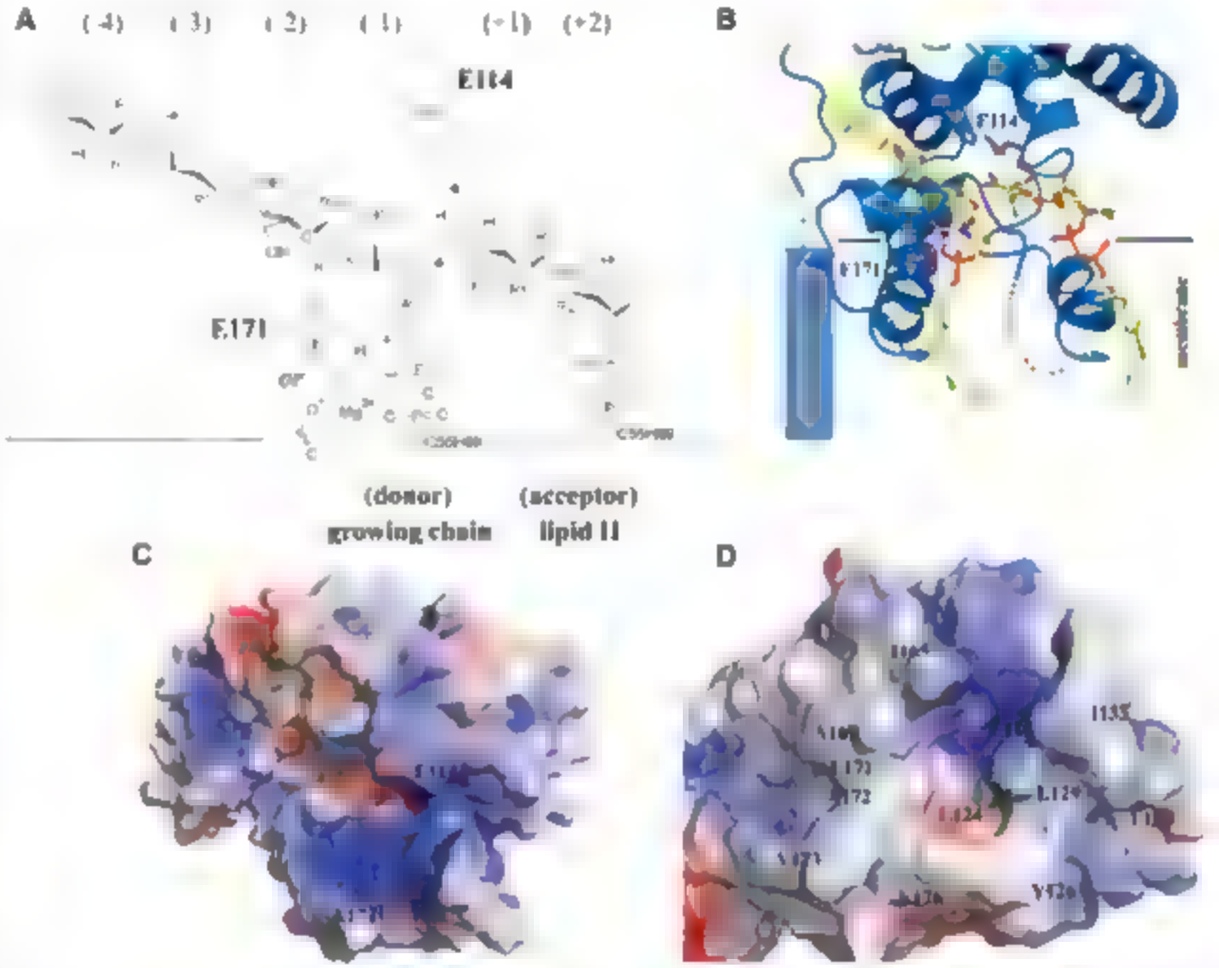

Fig. 4. Proposed mechanism for lipid II polymerization. To simplify these diagrams, the peptide substituents on lipid II have been omitted. (**A**) Schematic for lipid II polymerization. For clarity, R1 and R2 groups are used in place of the OAc and NHAc groups, respectively. For comparative purposes, the respective lysozyme sugar subsites are labeled in parentheses (the traditional nomenclature using subsites a to f has been avoided to prevent confusion with the moenomycin ring labeling). In this model, lipid II is the acceptor (right side), and the growing glycan chain is the donor (left side). Residue E114 acts to deprotonate the acceptor 4-OH group, which concomitantly attacks C1 of the donor, in an S_N2-like reaction that inverts the α-linked precursors into a β1,4-linked product. Residue E171 may assist this process by direct protonation of the phosphate-sugar bond or by stabilizing the pyrophosphate group through interaction with a divalent cation. (**B**) Spatial representation of the lipid II polymerization model. The membrane interface (horizontal black line), transmembrane region (vertical blue rectangle), and missing polypeptide (dotted blue line) are shown for effect. The protein structure is unmodified from the moenomycin-bound complex, with the growing glycan-chain donor (left side) modeled over moenomycin rings E and F and the lipid II acceptor (right side) fitted manually between the glycan-chain donor and the E114 catalytic residue (shown with E171 in stick form). After polymerization, the product would be translocated in the direction denoted by the yellow arrow. Any sugar chain larger than four sugar units (discounting the incoming two sugar units of the acceptor) would project out from the GT_{51} domain, and there are no steric barriers in our structure to prevent this from occurring. The stronger positive charge on the left side of the active site, relative to that on the right side [see (C)], may assist in movement of the retained acceptor lipid-pyrophosphate group into the donor position. (**C**) Detail of active-site pockets and cleft. Residues E114 and E171 are shown in space-filling form. The electrostatic potentials (red, negative; blue, positive) indicate a conserved region of positive charge across the middle of the pocket. This region binds the phosphoric acid diester group of moenomycin in our structure and is located in a position to bind both pyrophosphates in our substrate model. (**D**) Details of the hydrophobic platform of the GT_{51} fold. The view is approximately 90° from (C), with residues shown in stick form. Green, hydrophobic platform; gray, E114 and E171.

II acceptor adjacent to the proposed donor site with the 4-OH end available for interaction with both E114 and C1 of the donor sugar. This position of lipid II is comparable to that of subsites +1 and +2 of the substrate in λL (*15*), with the prereaction GT_{51} substrates similar to the postreaction lysozyme products.

We propose that E114 is a Brønsted base and acts to directly abstract a proton from the 4-OH group of the lipid II acceptor. The deprotonated form of E114 may be stabilized by the adjacent R249 residue, strictly conserved as part of motif V. The proton abstraction step probably occurs concomitantly with the electrophilic migration of the donor C1 toward the acceptor 4-OH group (Fig. 4, A and B). In the moenomycin complex, the conserved E171 residue lies closer to the glycerol moiety than the phosphate-sugar linkage (the β phosphate in our substrate model), which in combination with pH activity profiles of the *E. coli* PBP1b enzyme (*16*) casts some doubt on whether E171 protonates the sugar-phosphate linkage to assist catalysis. Furthermore, mutants of this residue in *E. coli* PBP1b retain some residual activity, whereas those of our predicted Brønsted base 1 + 4, do not (*9*). If E171 does not act to protonate the substrate, then we propose that it helps to coordinate the pyrophosphate group of the donor, either directly or via a divalent metal cation. The variable pH optima and divalent cation requirements of the GT_{51} family of enzymes (*17*–*19*) may result from varying local environments of the E171 residue. The S_N2-like reaction occurs between donor and acceptor, causing inversion at the donor C1 anomeric carbon and formation of the β1,4-linked product. The lipid-pyrophosphate leaving group of the donor is then free to diffuse away and be recycled in lipid II synthesis. We propose that translocation of the newly formed product to the donor site is assisted by a higher affinity for the pyrophosphate moiety in the donor site than in the acceptor site, with the conserved positively charged K155, K163, R167 and K168 residues located near the donor pyrophosphate region of the active site (Fig. 4C). This model is again reminiscent of the lysozyme active site, where the +1 and +2 subsites that match the modeled GT_{51} acceptor sugars possess the lowest substrate affinity of all the subsites. These two structures now provide a basis for addressing further questions about the mechanism of this important family of enzymes and for the design of new antibacterials. This work also opens the door for understanding structure and function relationships in other clinically important families of lipid-sugar GTs.

References and Notes

1. C. Goffin, J. M. Ghuysen, *Microbiol. Mol. Biol. Rev.* **62**, 1079 (1998).
2. T. D. Bugg *et al.*, *Biochemistry* **30**, 10408 (1991).
3. C. T. Walsh, *Science* **261**, 308 (1993).
4. R. C. Goldman, D. Gange, *Curr. Med. Chem.* **7**, 801 (2000).
5. P. Butaye, L. A. Devriese, F. Haesebrouck, *Antimicrob. Agents Chemother.* **45**, 1374 (2001).
6. Materials and methods are available as supporting material on *Science* Online.
7. C. Contreras-Martel *et al.*, *J. Mol. Biol.* **355**, 684 (2006).
8. Single-letter abbreviations for the amino acid residues are as follows: A, Ala; C, Cys; D, Asp; E, Glu; F, Phe; G, Gly; H, His; I, Ile; K, Lys; L, Leu; M, Met; N, Asn; P, Pro; Q, Gln; R, Arg; S, Ser; T, Thr; V, Val; W, Trp; and Y, Tyr.
9. M. Terrak *et al.*, *Mol. Microbiol.* **34**, 350 (1999).
10. L. Holm, C. Sander, *Nucleic Acids Res.* **27**, 244 (1999).
11. P. Welzel *et al.*, *Tetrahedron* **43**, 585 (1987).
12. J. Halliday, D. McKeveney, C. Muldoon, P. Rajaratnam, W. Meutermans, *Biochem. Pharmacol.* **71**, 957 (2006).
13. P. Welzel, *Chem. Rev.* **105**, 4610 (2005).
14. D. Ritzeler *et al.*, *Tetrahedron* **53**, 1675 (1997).
15. A. K. Leung, H. S. Duewel, J. F. Honek, A. M. Berghuis, *Biochemistry* **40**, 5665 (2001).
16. B. Schwartz *et al.*, *Biochemistry* **42**, 12552 (2002).
17. D. S. Barrett, A. Chen, M. K. Litterman, S. Walker, *Biochemistry* **43**, 12375 (2004).
18. D. Barrett *et al.*, *J. Bacteriol.* **187**, 2215 (2005).
19. M. Terrak, M. Nguyen-Disteche, *J. Bacteriol.* **188**, 2528 (2006).
20. C. Errard, J. Fastrez, J. P. Declercq, *J. Mol. Biol.* **276**, 151 (1998).

21. We thank S. Withers for helpful mechanistic discussion. We are grateful for beam time and assistance at the Advanced Light Source. The atomic coordinates and structure factors of the apoenzyme and moenomycin complex have been deposited at the Protein Data Bank, with accession numbers 2OLU and 2OLV, respectively. Figures were prepared using PyMol (www.pymol.org). N.C.J.S. is a Howard Hughes Medical Institute (HHMI) international scholar, a Canadian Institute of Health Research (CIHR) scientist, and a Michael Smith Foundation for Health Research (MSHR) senior scholar. A.C.S. is a MSHR and CIHR fellow. This work was funded by CIHR and HHMI operating funds and infrastructure funds from the Canada Foundation of Innovation and MSHR.

Supporting Online Material

www.sciencemag.org/cgi/content/full/315/5817/1402/DC1
Materials and Methods
SOM Text
Fig. S1
Table S1
References

23 October 2006; accepted 24 January 2007
10.1126/science.1136611

Dynamics of Replication-Independent Histone Turnover in Budding Yeast

Michael F. Dion,[1]*† Tommy Kaplan,[2,3]* Minkyu Kim,[4] Stephen Buratowski,[4] Nir Friedman,[2] Oliver J. Rando[1]†‡

Chromatin plays roles in processes governed by different time scales. To assay the dynamic behavior of chromatin in living cells, we used genomic tiling arrays to measure histone H3 turnover in G1-arrested *Saccharomyces cerevisiae* at single-nucleosome resolution over 4% of the genome, and at lower (~265 base pair) resolution over the entire genome. We find that nucleosomes at promoters are replaced more rapidly than at coding regions and that replacement rates over coding regions correlate with polymerase density. In addition, rapid histone turnover is found at known chromatin boundary elements. These results suggest that rapid histone turnover serves to functionally separate chromatin domains and prevent spread of histone states.

Characterizing the dynamic behavior of nucleosomes is key to understanding the diversity of biological roles of chromatin. Nucleosomes are evicted at many yeast promoters during gene activation (*1*–*4*) and are reassembled in trans upon repression (*5*). In *Drosophila*, active transcription leads to replacement of histone H3 by the variant isoform H3.3 (*6*, *7*), whereas in budding yeast (whose only H3 is an H3.3 homolog), passage of RNA polymerase II (Pol II) results in eviction of nucleosomes from some (*8*), but not all (*9*), coding regions. In contrast, studies in *Physarum polycephalum* suggest that H3 is not replaced during Pol II transcription (*10*). Furthermore, recent results in yeast suggest that H3 deposition is independent of transcription status (*11*). The disagreement between these studies leads us to map the locus-specific turnover rate of histone H3 at genomic scale so as to address two questions. First, is there evidence for general transcription-dependent H3 turnover? Second, are there additional mechanisms for histone turnover?

To measure turnover rates, we used yeast carrying constitutively expressed Myc-tagged histone H3, as well as an inducible Flag-tagged H3 (*5*) (fig. S1). Flag-H3 was induced in G1-arrested cells for varying amounts of time, chromatin was cross-linked and digested to mononucleosomes (*12*), and Myc- and Flag-tagged histones were immunoprecipitated sepa-

[1]Faculty of Arts and Sciences, Center for Systems Biology, Harvard University, Cambridge, MA 02138, USA. [2]School of Computer Science and Engineering, The Hebrew University, Jerusalem 91904, Israel. [3]Department of Molecular Genetics and Biotechnology, Faculty of Medicine, The Hebrew University, Jerusalem 91120, Israel. [4]Department of Biological Chemistry and Molecular Pharmacology, Harvard University, 240 Longwood Avenue, Boston, MA 02115, USA.

*These authors contributed equally to this work.
†Present address: Department of Biochemistry and Molecular Pharmacology, University of Massachusetts Medical School, Worcester, MA 01605, USA.
‡To whom correspondence should be addressed. E-mail: Oliver.Rando@umassmed.edu

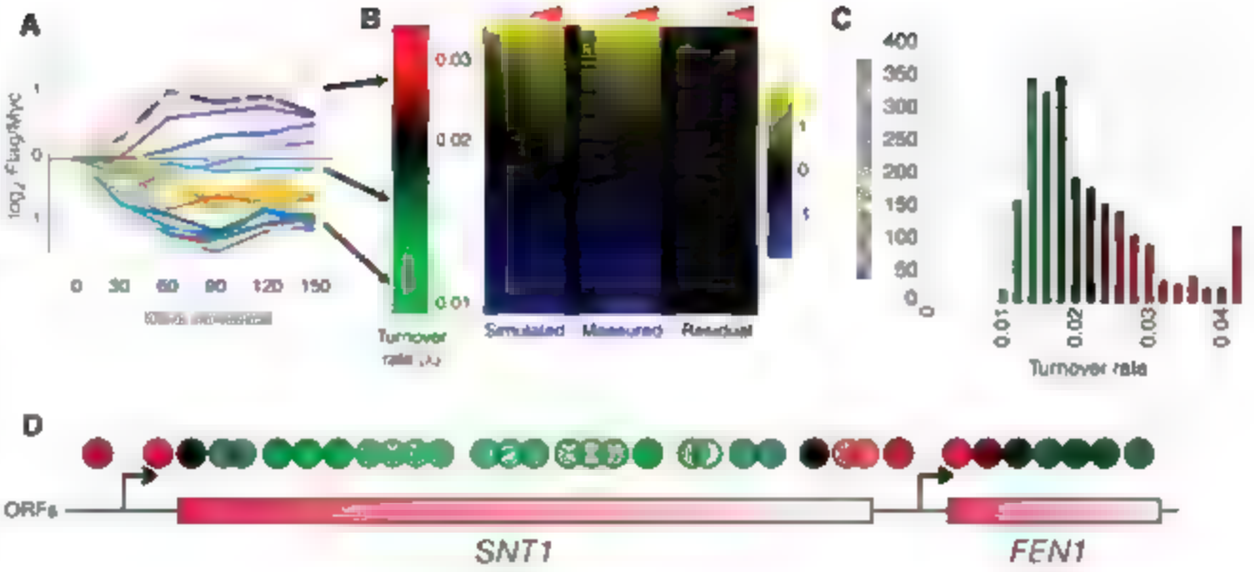

Fig. 1. Time courses of histone turnover in yeast. (**A**) H3 turnover for 23 adjacent nucleosomes in G1-arrested yeast cultures. Flag and Myc were immunoprecipitated at various time points after Flag-H3 induction (*x* axis), and Flag/Myc ratios (*y* axis) were measured by microarray. (**B**) A computational model reduces time course data to a single turnover parameter λ (frequency of histone turnover events, in units of min^{-1}), represented as the leftmost red-to-green color bar. Measured time-course data and data simulated using λ values are represented as blue-yellow heat maps (right). The minor differences (Residual) between measured and simulated data demonstrate that our model captures the majority of histone turnover dynamics during G1 arrest. (**C**) Distribution of turnover rates for nucleosomes in G1 arrested yeast. Binned turnover rates are color coded as in (B). (**D**) Sample genomic stretch, with nucleosomes (A) color coded by turnover rate.

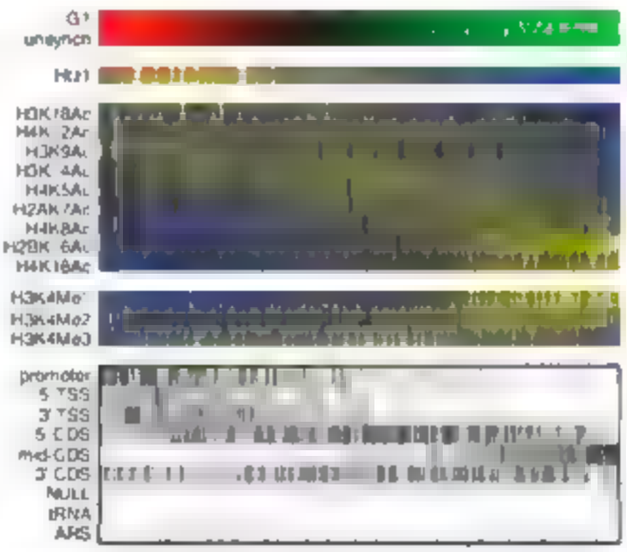

Fig. 2. Relation between histone modifications and H3 turnover. nucleosomes (columns) versus annotations (rows). Nucleosomes are ordered by turnover rate (red-to-green). Modification and Htz1 levels (*12*, *18*) are shown in yellow-to-blue heat maps, where yellow represents enrichment. The bottom panel shows genomic locations (*12*): 5′ and 3′ TSS refer to nucleosomes surrounding the transcriptional start site; promoter indicates other upstream probes. Protein-coding sequences are separated into 5′, middle, and 3′. Other annotations describe autonomously replicating sequences (ARSs), tRNA genes, and Null (any other intergenic region).

tively. Amplified DNAs were competitively hybridized to a 20 base pair (bp) resolution microarray covering 4% of the genome (*13*) yielding Flag/Myc ratios at each time point for each nucleosome on our array (Fig. 1A). We then estimated the turnover rate (number of H3 replacement events per unit time) of each nucleosome using a simple analytical model that best fit the experimental data with a small number of parameters (*14*, *15*) (Fig. 1B).

To test the validity of our results, we repeated the experiment in unsynchronized yeast (fig. S2), observing well-correlated but consistently faster turnover rates, as expected given global H3 deposition during genomic replication (Fig. 2 and fig. S3). We analyzed turnover rates in G1-arrested cells across the entire yeast genome using commercial microarrays with ~265-bp resolution (*16*, *17*) (fig. S4) and obtained a high correlation between rates from the two distinct measurement platforms (fig. S5). We also measured whole-genome histone occupancy (*7*, *8*), finding that H3 replacement rates were weakly anticorrelated with H3 occupancy (fig. S6).

These results are consistent with those expected of H3 replacement from a free pool of H3 and demonstrate that we can recover semiquantitative turnover rates from time-course experiments. The time required for production of Flag-H3 (30 to 45 min) limits our ability to measure the rates of the hottest nucleosomes, which accumulate Flag-H3 before this protein can be detected by Western blot. We therefore caution against literal interpretation of turnover rates, because parameter choices (e.g., Flag-H3 degradation rate) affect absolute turnover rates, however, over a wide range of parameters, the ratio between estimated rates is robust. The resulting rates estimates span one to two orders of magnitude, depending on measurement platform, between "cold" nucleosomes that rarely turn over and hot ones whose replacement rate is faster than the time granularity of our experiment (Fig. 1C and Fig. 3B).

We compared high-resolution turnover rates to previously measured features of these nucleosomes (*12*, *17*, *18*) (Fig. 2 and fig. S7). Nucleosomes over protein-coding regions were coldest, whereas promoter nucleosomes were generally hot. Correspondingly, hot nucleosomes were depleted of the histone modifications that are "stereotypically" depleted surrounding the transcription start site (TSS) (*12*) and were conversely enriched for the histone H2A variant Htz1 (*16*, *18*).

These results are notable for two reasons. First, they suggest that replacement of TSS-adjacent nucleosomes with an appropriately modified nucleoplasmic pool could be partially responsible for promoter patterns of histone modification. Second, erasure of histone modifications due to rapid turnover would result in a steady-state picture of stereotyped promoter chromatin that does not capture transient states, potentially hiding any number of informative histone modification events.

Analysis of median replacement rates for various genomic loci confirmed that the most rapid turnover occurs over promoters, tRNA, and small nucleolar RNA genes (Fig. 3, A and B, and fig. S8). Most unexpected, given the dynamic H3.3 replacement over *Drosophila* genes (*7*, *19*), was the slow H3 turnover over protein-coding genes. Indeed, the coldest probes, mid-coding region probes, cover 28% of the genome yet account for only 10% of turnover. Despite the slower H3 turnover in coding regions, relative variation of turnover rates among coding regions might correlate with polymerase activity. For example, histone turnover over the alpha factor inducible gene *FUS1* is more rapid in alpha factor–arrested cells than in unsynchronized cells (Fig. 3C and fig. S9). We therefore measured Pol II enrichment across the entire yeast genome, finding that polymerase enrichment over genes exhibited good correlation ($r^2 = 0.54$, $P < 6$ [illegible] $^{-17}$)

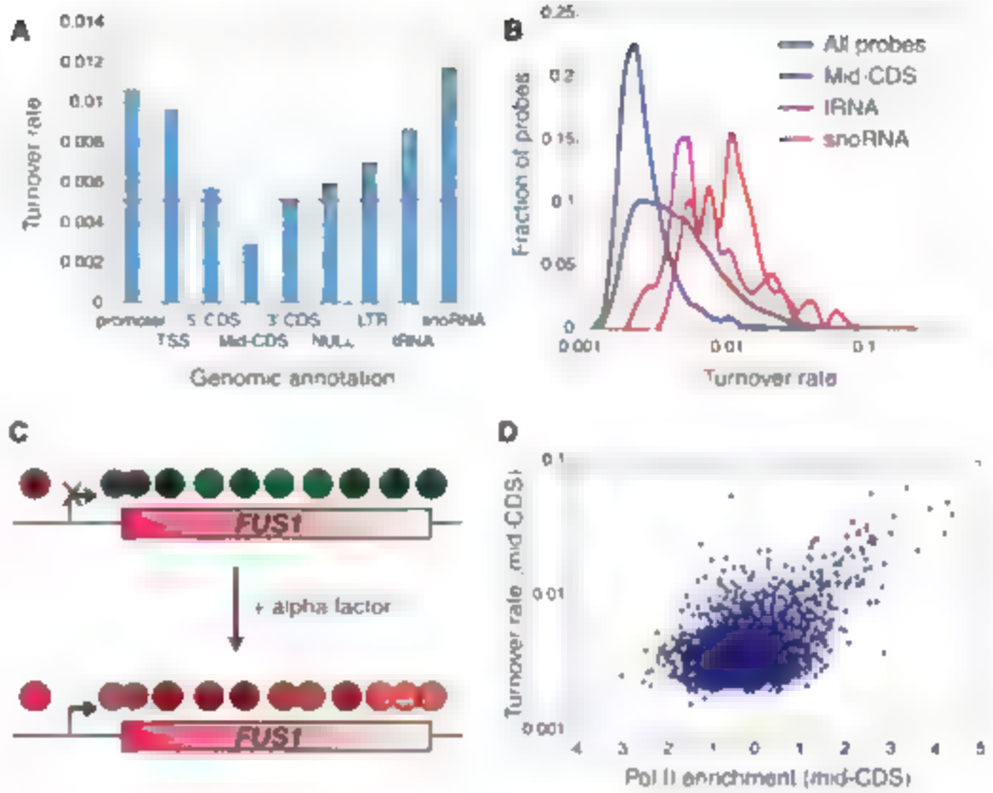

Fig. 3. Slow histone replacement over protein-coding genes. (**A**) Median turnover rates for genomic annotations (from whole-genome data). (**B**) Probe-level distributions of transcribed regions compared with the entire data set. *X* axis (logarithmic scale) shows turnover rate. *Y* axis shows fraction of probes within each rate bin. (**C**) *FUS1* coding region and associated nucleosomes, color coded according to turnover rates from high-resolution microarray experiments on unsynchronized yeast cultures (top), and G1-arrested cultures (bottom). (**D**) Scatter plot of coding region histone turnover (whole-genome data) versus $\log_2$ of Pol II enrichment.

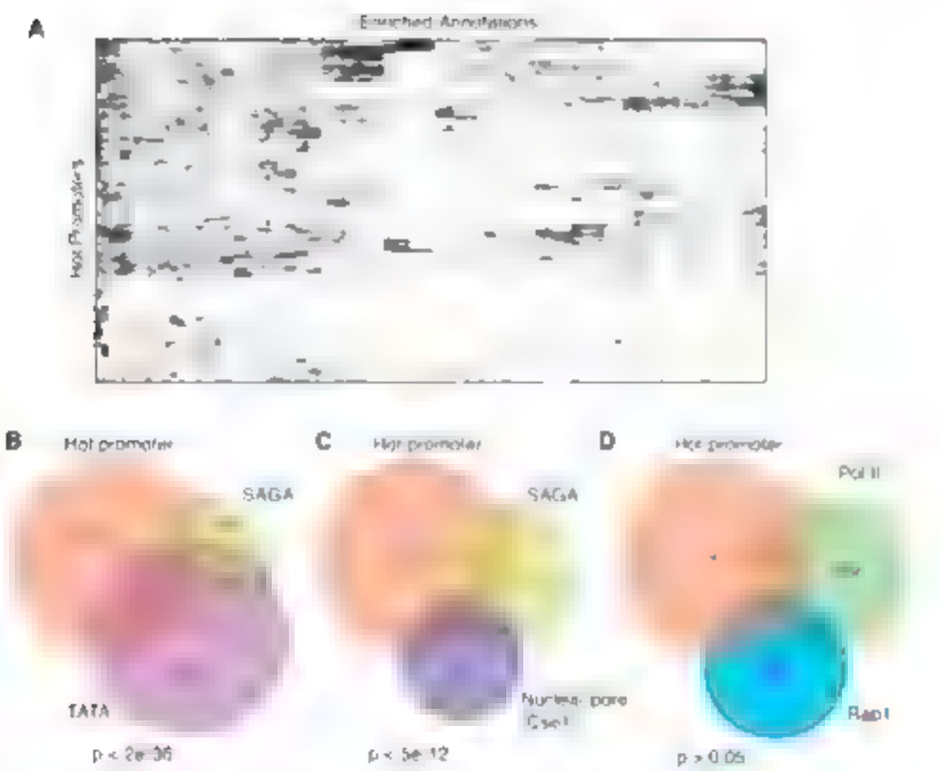

Fig. 4. Rapid turnover at promoters is associated with multiple partially overlapping features. (**A**) Hot promoters were tested for significantly enriched ($p < 10^{-7}$) annotations. Cluster diagram shows hot promoters as rows, annotations (table S6 and fig. S11) as columns. Black bars indicate positive annotations for a given promoter. (**B** to **D**) Overlap between hot promoters and pairs of enriched annotations. *P* value shows significance of overlap between pairs of annotations given the extent of their overlap with hot promoters (hypergeometric distribution). SAGA-dominated genes are enriched for TATA-containing promoters (B) and are moderately correlated with Cse1-bound genes (C), whereas promoters with Rap1 sites are not enriched upstream of genes exhibiting high Pol II levels in our experiment (D).

with histone replacement rates (Fig. 3D). This is consistent with RNA polymerase passage evicting nucleosomes in some cases, although many highly transcribed genes (*RPL37B*, for example) exhibit low turnover rates.

Although polymerase passage and the resulting histone eviction represent a plausible first step for coding region histone turnover, they are unlikely to account for the bulk of histone replacement (Fig. 3A). Promoters of hot coding regions tend to be hot, but the converse is not true. Most hot promoters were adjacent to cold coding regions (e.g., Fig. 1D). Moreover, replacement rates at promoters were, unlike those at coding regions, poorly correlated with polymerase abundance, either at the promoter or over the coding region (fig. S10), making it unlikely that promoter turnover is solely a result of polymerase activity.

To systematically characterize promoter histone turnover, we tested the hottest subset of promoters for enrichment of published experimental and computational annotations (table S6). The hottest promoters include those carrying binding sites for a subset of transcription factors (such as Rap1, Reb1, Gcn4, and Adr1), those upstream of genes regulated by chromatin-modulating complexes (e.g., Ssn6-Tup1, Mediator, SAGA, Swi-Snf, and Sir), and those upstream of genes associated with nuclear pore components (e.g., Cse1, Mlp1, Nup116, and Nup2). Clustering hot promoters based on enriched annotations yielded independent clusters (Fig. 4A and fig. S11), such as a group of hot promoters associated with nuclear pore components (*20*). These separate clusters suggest that the many enrichments identified potentially

reflect multiple, partially overlapping mechanisms for rapid promoter turnover (Fig. 4, B to D). Some enrichments suggest clear hypotheses about the mechanism for rapid turnover (e.g., rapid histone replacement at Swi/Snf-regulated promoters may well be a consequence of Swi/Snf action), whereas other enrichments are less illuminating (e.g., what causes rapid replacement at nuclear pores?).

Many features of hot nucleosomes (including Htz1, tRNA genes, nuclear pore association, and Rap1 and Reb1 sites) are associated with boundaries that block heterochromatin spreading in yeast (*27*, *28*). How do boundaries block lateral spreading (*25*) of chromatin states? Suggested mechanisms include long gaps between nucleosomes, or recruited acetylases that compete with spreading deacetylation (*26*, *27*). The rapid H3 replacement at boundary-associated regions suggests an alternative hypothesis, that constant replacement of nucleosomes serves to erase a laterally spreading chromatin domain before it spreads any further (fig. S12). To investigate the role of Htz1 (whose role in boundary function is poorly understood) in histone replacement, we measured Flag-H3 incorporation in *htz1*Δ mutants, finding globally slowed H3 incorporation but few locus-specific effects (*14*). Further experiments will be required to untangle this relationship and to evaluate the role of rapid turnover at chromatin boundaries.

We have measured H3 replacement rates throughout the yeast genome, finding that nucleosomes over coding regions are replaced at high transcription rates, although most turnover occurs over promoters and small RNA genes. What function is served by histone replacement at promoters? Rapid turnover could transiently expose occluded transcription factor binding sites or it could ensure, by erasure of promoter chromatin marks, that transcriptional reinitiation occurs only in the continuing presence of an activating stimulus. Whatever the function, one important implication is that steady-state localization studies of histone marks could be confounded by dilution with histones carrying the average modification levels of the free histone pool, making dynamic or genetic studies key to deciphering any instructive roles of histone marks in transcriptional control. Finally, rapid turnover occurs at chromatin boundaries [see also (*28*)]. We propose that erasure of histone marks (or associated proteins) by rapid turnover delimits the spread of chromatin states. We further speculate that the widespread histone turnover at promoters throughout the compact yeast genome could serve, in a sense, to "expand" the genome by preventing chromatin states of adjacent genes from affecting each other.

References and Notes

1. B. E. Bernstein, C. L. Liu, E. L. Humphrey, E. O. Perlstein, S. L. Schreiber, *Genome Biol.* **5**, R62 (2004).
2. H. Boeger, J. Griesenbeck, J. S. Strattan, R. D. Kornberg, *Mol. Cell* **11**, 1587 (2003).
3. C. K. Lee, Y. Shibata, B. Rao, B. D. Strahl, J. D. Lieb, *Nat. Genet.* **36**, 900 (2004).
4. H. Reinke, W. Horz, *Mol. Cell* **11**, 1599 (2003).
5. U. J. Schermer, P. Korber, W. Horz, *Mol. Cell* **19**, 279 (2005).
6. K. Ahmad, S. Henikoff, *Mol. Cell* **9**, 1191 (2002).
7. Y. Mito, J. G. Henikoff, S. Henikoff, *Nat. Genet.* **37**, 1090 (2005).
8. M. A. Schwabish, K. Struhl, *Mol. Cell. Biol.* **24**, 10111 (2004).
9. A. Kristjuhan, J. Q. Svejstrup, *EMBO J.* **23**, 4243 (2004).
10. C. Thiriet, J. J. Hayes, *Genes Dev.* **19**, 677 (2005).
11. J. Unger, J. K. Tyler, *Eukaryot. Cell* **5**, 1780 (2006).
12. C. L. Liu *et al.*, *PLoS Biol.* **3**, e328 (2005).
13. G. C. Yuan *et al.*, *Science* **309**, 626 (2005).
14. Materials and methods are available as supporting material on *Science* Online.
15. Genomic turnover rates can be viewed at the University of California, Santa Cruz, Genome Browser on *S. cerevisiae*: http://compbio.cs.huji.ac.il/Turnover
16. B. Guillemette *et al.*, *PLoS Biol.* **3**, e384 (2005).
17. D. K. Pokholok *et al.*, *Cell* **122**, 517 (2005).
18. R. M. Rasmer *et al.*, *Cell* **123**, 233 (2005).
19. K. Ahmad, S. Henikoff, *Proc. Natl. Acad. Sci. U.S.A.* **99**, (Suppl. 4), 16477 (2002).
20. J. M. Casolari *et al.*, *Cell* **117**, 427 (2004).
21. D. Donze, C. R. Adams, J. Rine, R. T. Kamakaka, *Genes Dev.* **13**, 698 (1999).
22. K. Ishii, G. Arib, C. Lin, G. Van Houwe, U. K. Laemmli, *Cell* **109**, 551 (2002).
23. M. D. Meneghini, M. Wu, H. D. Madhani, *Cell* **112**, 725 (2003).
24. Q. Yu *et al.*, *Nucleic Acids Res.* **31**, 1224 (2003).
25. L. N. Ruscbe, A. L. Kirchmaier, J. Rine, *Annu. Rev. Biochem.* **72**, 481 (2003).
26. X. Bi, J. R. Broach, *Curr. Opin. Genet. Dev.* **11**, 199 (2001).
27. Y. H. Chiu, Q. Yu, J. J. Sandmeier, X. Bi, *Genetics* **165**, 115 (2003).
28. Y. Mito *et al.*, *Science* **315**, 1408 (2007).

29. We thank K. Ahmad, N. Francis, A. Gasch, N. Habib, A. Jamovich, R. Kupferman, H. Margalit, and I. Wapinski for critical reading of the manuscript. We thank P. Korber for the generous gift of the USY6 strain. O.J.R. is supported in part by a Career Award in Biomedical Sciences from the Burroughs Wellcome Fund. This research was supported by grants to O. R., S.B., and N.F. from the National Institute of General Medical Sciences, NIH, to O.J.R. from the Human Frontiers Science Program, and to N.F. from the Israeli Science Foundation. O.J.R. designed the experiments, and M.F.D. carried them out. S.B. designed, and M.K. carried out, Pol II chromatin immunoprecipitation. T.K., N.F. and O.J.R. analyzed the data. O.J.R. and N.F. wrote the paper.

Supporting Online Material

www.sciencemag.org/cgi/content/full/315/5817/1405/DC1
Materials and Methods
Figs. S1 to S18
Tables S1 to S6

18 August 2006; accepted 6 February 2007
10.1126/science.1134053

Histone Replacement Marks the Boundaries of cis-Regulatory Domains

Yoshiko Mito,[1,2] Jorja G. Henikoff,[1] Steven Henikoff[1,3]*

Cellular memory is maintained at homeotic genes by cis-regulatory elements whose mechanism of action is unknown. We have examined chromatin at *Drosophila* homeotic gene clusters by measuring, at high resolution, levels of histone replacement and nucleosome occupancy. Homeotic gene clusters display conspicuous peaks of histone replacement at boundaries of cis-regulatory domains superimposed over broad regions of low replacement. Peaks of histone replacement closely correspond to nuclease-hypersensitive sites, binding sites for Polycomb and trithorax group proteins, and sites of nucleosome depletion. Our results suggest the existence of a continuous process that disrupts nucleosomes and maintains accessibility of cis-regulatory elements.

Chromatin can be differentiated by the replication-independent replacement of one histone variant with another (*1*). For example, histone H3.3 is deposited throughout the cell cycle, replacing H3 that is deposited during replication (*2*–*4*). Unlike replication-coupled assembly of H3, which occurs in gaps between old nucleosomes on daughter helices, the insertion of H3.3 is preceded by disruption of preexisting histones during transcription and other active processes (*3*, *5*). We have previously shown that H3.3 replacement profiles resemble those for RNA polymerase II (*2*), which suggests that gradual replacement of H3.3 occurs in the wake of transiting polymerase to repair disrupted chromatin (*1*). Here, we ask whether histone replacement and nucleosome occupancy are also distinctive at cis-regulatory elements.

Log-phase *Drosophila melanogaster* S2 cells were induced to produce biotin-tagged H3.3 for two or three cell cycles (*2*). DNA was extracted from streptavidin pull-down assay and input material, labeled with Cy3 and Cy5 dyes, and cohybridized to microarrays. To provide a standard, we profiled biotin-tagged H3-containing chromatin in parallel. Analysis of H3.3/H3 levels over the entire 3R chromosome arm revealed that the ~350-kb trithorax complex (BX-C) region displays the lowest H3.3/H3 ratio of any region of comparable size on 3R, and the Antennapedia

[1]Basic Sciences Division, Fred Hutchinson Cancer Research Center, 1100 Fairview Avenue North, Seattle, WA 98109, USA. [2]Molecular and Cellular Biology Program, University of Washington, Seattle, WA 98195, USA. [3]Howard Hughes Medical Institute, Fred Hutchinson Cancer Research Center, Seattle, WA 98109, USA.

*To whom correspondence should be addressed. E-mail: steveh@fhcrc.org

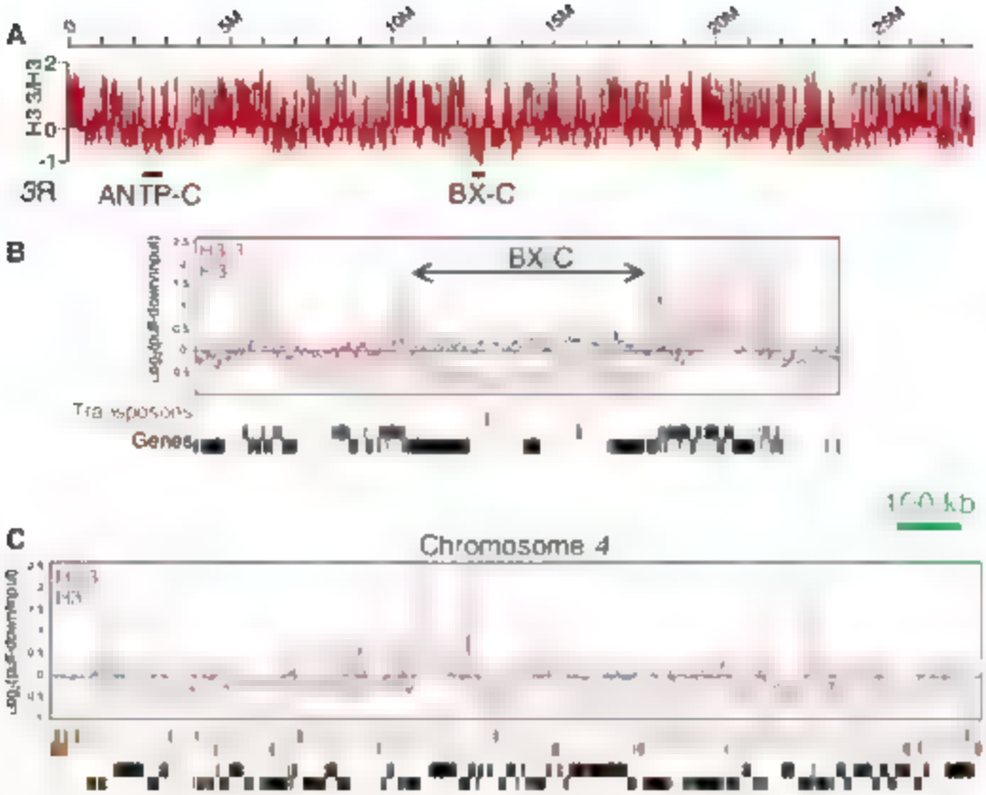

Fig. 1. The BX-C is extensively depleted in H3.3. (**A**) H3.3/H3 log-ratio profile of chromosome arm 3R. Orientation is proximal (0 on base-pair scale) to distal (~28 Mb). The location of the two homeotic gene clusters are indicated with horizontal bars. (**B**) H3.3 (red) and H3 (blue) profiles for the BX-C and flanking regions. (**C**) Same as (B) for chromosome 4. The locations of annotated transposons (brown boxes) and genes (black boxes) are shown beneath each panel, oriented 5′ to 3′ above the line and 3′ to 5′ below. Profiles are displayed as moving averages, with a 1-kb (A) or a 2.5-kb (B and C) window, in 100-bp intervals.

homeotic gene complex (ANTP-C) also displays an unusually low H3.3/H3 ratio (Fig. 1A). Low H3.3/H3 ratios at the homeotic gene clusters are attributable to infrequent histone replacement, and not to low nucleosome occupancy, because H3.3 levels at the BX-C are far below the median ($\log_2 = 0$) for all of 3R, whereas H3 levels are slightly above the median overall (Fig. 1B). Even the heterochromatic chromosome *4* (*6*) includes only shorter (~100-kb) stretches that are as depleted in H3.3 as the BX-C (Fig. 1C).

A close-up view of the BX-C *iab* region reveals the presence of several prominent H3.3 peaks (Fig. 2A). Notably, the seven highest peaks correspond to the functional boundaries of the seven proximal-to-distal cis-regulatory domains that regulate the *abd-A* (*iab2* to *iab4*) and *Abd-B* (*iab5* to *iab8*) homeotic genes successively from anterior to posterior in the abdomen (*7*). Conspicuous peaks of H3.3 also correspond to the *bxd* Polycomb response element (PRE) and to promoters within the *Abd-B* gene, which is known to be active in S2 cells (*8, 9*). Therefore, each of the most prominent H3.3 peaks in the region corresponds to a previously defined cis-regulatory element. Our findings are likely to be general, because in coding regions, promoters and boundaries are also sites of nucleosome replacement (*10*).

A characteristic feature of both boundaries and PREs in the BX-C is that they span clusters of DNaseI hypersensitive (DHS) hypersensitive sites in a variety of cell types, including S2 cells (*11*). To better delineate histone replacement patterns in the vicinity of hypersensitive sites, we tiled the entire BX-C at 20-bp resolution (fig. S1).

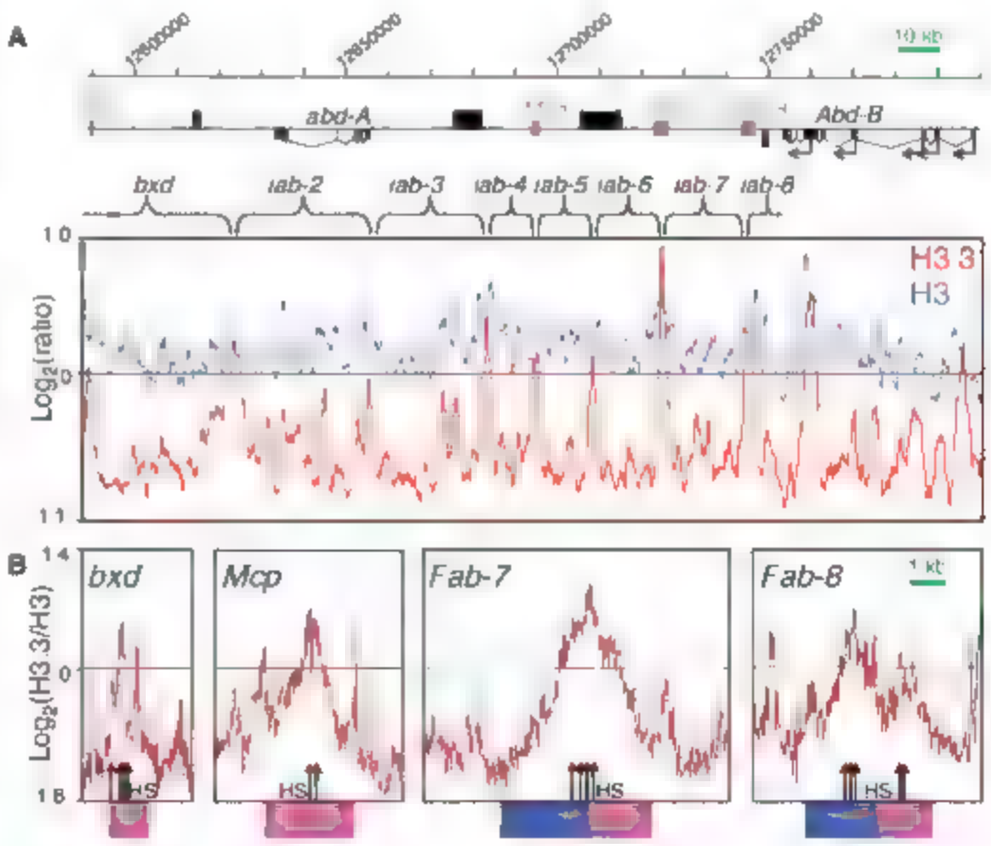

Fig. 2. Conspicuous histone replacement at cis-regulatory domain boundaries and DNaseI hypersensitive sites within the BX-C. (**A**) Map and histone profiles for the abdominal and flanking regions of the BX-C, including four well-mapped PRE-boundaries (magenta boxes (*11, 13, 25*)). The scale at top indicates genomic location on 3R, with genes and PRE-boundaries indicated on the line below. The five *Abd-B* promoters are marked with horizontal arrows. H3.3 (red) and H3 (blue) $\log_2$-ratio profiles are displayed as 1-kb moving averages. Boundaries between adjacent cis-regulatory domains are indicated with brackets above the log-ratio plots. (**B**) H3.3/H3 log ratios (brown) are shown for the PREs (magenta) and boundaries (blue) for which DNaseI-hypersensitive sites have been mapped (indicated with vertical arrows).

The *bxd*, *Mcp*, *Fab-7*, and *Fab-8* PRE-boundaries each encompass conspicuous peaks of H3.3 abundance (Fig. 2B) that closely correspond to all the known nuclease-hypersensitive sites within the region (*11*, *13*). Nuclease hypersensitivity identifies sites of relatively accessible DNA, so that their correspondences to peaks of histone replacement suggest that continuous disruption of nucleosomes exposes cis-regulatory DNA relative to surrounding regions.

PRE-boundary elements in the BX-C and other regions are binding sites for multiple Polycomb group (PcG) proteins, which have been mapped in an S2 cell line at high resolution (*8*). If the process that disrupts nucleosomes also facilitates PcG binding, then we would expect a correspondence between peaks of PcG binding and peaks of H3.3. Indeed, when we compared H3.3 profiles with those for Enhancer-of-zeste (E(Z)) and Posterior-sex-combs (PSC) PcG proteins, we found that all 10 peaks of PcG binding in the abdominal region are also local peaks of H3.3 (Fig. 3A and table S1). Likewise at the ANTP-C, all 13 peaks of PcG binding in the *Scr-Antp* region correspond to high levels of H3.3 (Fig. 3B and table S1). H3.3 enrichment at PcG-binding sites is not attributable to higher nucleosome occupancy, because essentially identical results were obtained for H3.3/H3 profiles (figs. S2 and S3).

Not all PREs in the BX-C are found to be sites of PcG binding; for example, neither *Fab-7* nor *Fab-8* is detectably bound by E(Z) or PSC (*8*). The fact that all PcG sites are peaks of histone replacement, but not vice versa, suggests that histone replacement at PREs and boundaries is constitutive and independent of the expression of the homeotic genes that they regulate. For example, *Abd-B* is expressed at high levels in S2 cells and displays the typical H3.3 5′ peak for an active gene (Fig. 2A), whereas *Ubx* and *abd-A* are nearly inactive (*8*, *9*), yet the PREs and boundaries regulating all three genes are sites of conspicuous histone replacement over a low background.

We also examined histone replacement averaged over the 175 genomewide E(Z)+PSC peaks outside of the BX-C and ANTP-C (table S1) and observed an H3.3 peak centered over the PcG maximum (Fig. 3C and fig. S4). Therefore, the strong association between PcG protein binding and histone replacement is not limited to homeotic gene clusters. The genomewide H3.3 peak is higher than that for the BX-C and ANTP-C, presumably because other PcG-binding sites are not superimposed over such deep H3.3 valleys (fig. S5).

The colocalization of PcG-binding sites and local peaks of H3.3 suggests that the process that disrupts nucleosomes locally maintains the accessibility of cis-regulatory DNA to PcG proteins. If so, then there should be a lower average occupancy of nucleosomes over sites of PcG protein binding than over their surrounding regions (*8*, *14*). To test this possibility, we hybridized nucleosomal DNA and fragmented genomic DNA on the same microarrays and measured nucleosomal/genomic DNA log ratios. Around peak regions of E(Z)+PSC binding, nucleosomal DNA was clearly depleted on average (Fig. 3D and table S1), similar to the depletion seen for active gene promoters (*2*) (fig. S1), and essentially the same results were obtained with different methods for genomic DNA fragmentation (fig. S6). We conclude that the correspondence between histone replacement and nucleosome depletion is a genomewide feature of PcG-binding sites.

In *Drosophila*, many cis-regulatory elements, including PREs and boundaries, are bound by the trxG proteins, Zeste and GAGA factor (GAF) (*15*). To test the possibility that histone replacement is enhanced and nucleosome occupancy is reduced where Zeste protein preferentially binds, we aligned 390 Zeste-binding sites identified by high-resolution chromatin immunoprecipitation (ChIP) combined with tiling microarrays (ChIP-chip profiling) (*16*) and averaged log ratios of H3.3/H3 and nucleosome occu-

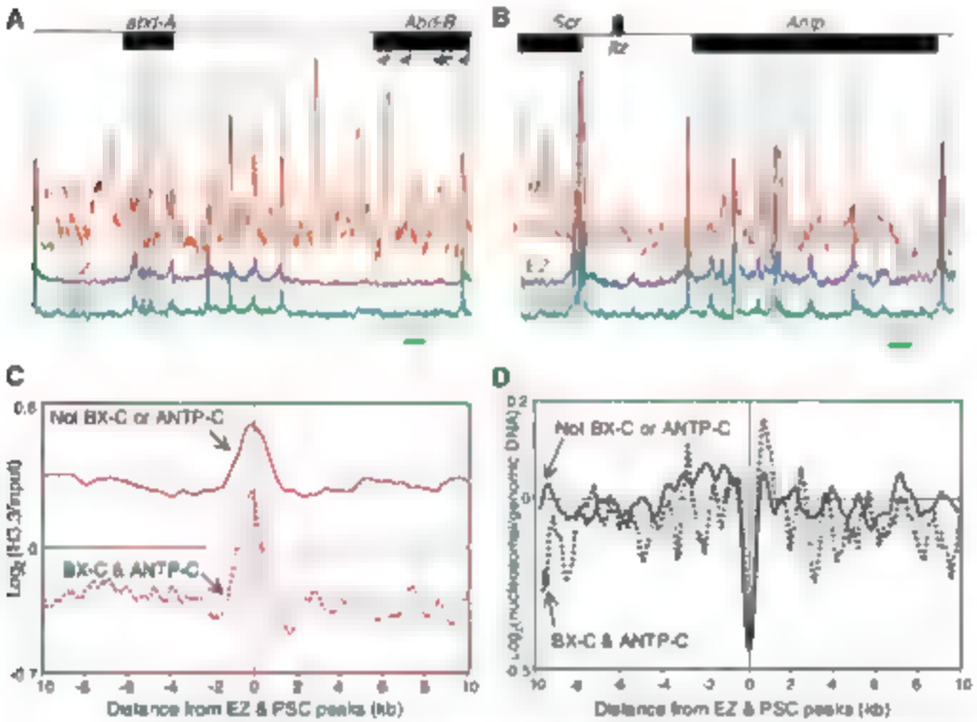

Fig. 3. Sites of PcG binding correspond to local peaks of histone replacement and reduced nucleosome occupancy. Comparison of the H3.3 log-ratio profile to E(Z) and PSC profiles (*8*) at (**A**) the BX-C (from Fig. 2A) and (**B**) the ANTP-C. Locations of prominent E(Z) and PSC peaks are marked with vertical dotted lines. Arbitrary scaling was used to facilitate visual comparison between H3.3/H3 log ratios and linear E(Z) and PSC profiles. Actual scales are shown in fig. S5. (**C**) H3.3 log-ratio profiles aligned around E(Z)+PSC peaks for the BX-C and ANTP-C regions (dotted line) and for the remainder of the genome (solid line), showing moving averages using a 500-bp window. (**D**) Same as (C), except showing the moving averages for nucleosomal/genomic DNA log-ratio profiles.

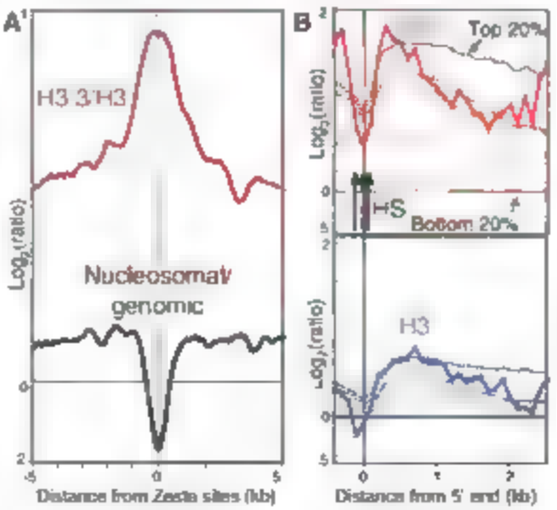

Fig. 4. Binding sites for trxG proteins and poised promoters are associated with conspicuous histone replacement and reduced nucleosome occupancy. (**A**) Average H3.3/H3 and nucleosome occupancy log-ratio profiles aligned at 390 Zeste-binding sites. (**B**) Average H3.3 (red) and H3 (blue) log ratios at uninduced heat shock genes. Dotted gray lines are histone profiles for all annotated genes on 3R, shown in decreasing intensity from the most active (top 20%) to the least active (bottom 20%) gene sets. Very similar H3.3 profiles were obtained in three different experiments (fig. S10).

pancy. We observed a prominent maximum of histone replacement and a sharp minimum of nucleosome occupancy centered over the point of alignment (Fig. 4A and table S2). Similar results were obtained for predicted GAF sites (figs. S7 and S8), which suggests that nucleosome disruption is a general feature of trxG protein DNA-binding sites. H3.3 enrichment at PcG- and trxG protein binding sites results from a replication-independent replacement process, because essentially identical profiles were obtained for H3.3^{core}, which lacks the N-terminal tail and does not assemble during replication (fig. S9).

Like *Fab-7* and *Fab-8*, heat shock gene promoters are prominent sites of GAF binding, nuclease hypersensitivity, and reduced nucleosome occupancy (*17*). Heat shock protein Hsp70 genes are constitutively "poised" for rapid induction but do not produce detectable mRNAs in the uninduced state. We aligned Hsp70 genes at their 5′ ends and averaged H3.3 and H3 profiles. For comparison, we averaged similarly aligned H3.3 and H3 profiles for all 2165 genes on 3R with known 5′ and 3′ ends, divided into quintiles based on expression levels. H3.3 patterns were similar to those of highly active genes (Fig. 4B and fig. S10), with histone replacement levels peaking on either side of heat shock promoters. As do transcriptionally active gene promoters (*2*), heat shock genes display prominent H3.3 and H3 dips in abundance that are attributable to partial nucleosome depletion (*17*). Constitutive histone replacement also appears to be a feature of poised promoters in vertebrates, because H3.3 is strongly enriched in the upstream region of the chicken folate receptor gene, regardless of whether the gene is active or inactive (*19*).

What process maintains the chromatin of cis-regulatory elements in a state of flux? Many DNA-binding and chromatin-binding proteins involved in gene regulation display short residence times on DNA (*19*), and some mouse transcription factors show dynamic behavior at their functional binding sites (*20, 21*). A model for this process has been proposed, involving alternating cycles of nucleosome disruption by a Brahma-related SWI/SNF chromatin-remodeler and transcription factor binding (*21*). The binding of PcG and trxG proteins is also dynamic (*22, 23*), and we propose that a similar cycle of nucleosome disruption and factor binding takes place at boundaries and PREs. Nucleosome disruption by SWI/SNF remodeling complexes would occasionally evict nucleosomes (*24*) and transiently expose DNA, which would become available to other diffusible factors, including PcG proteins. The continued local presence of nucleosome remodelers would result in another cycle of remodeling, nucleosome depletion, nuclease hypersensitivity, and histone replacement at the site. This model could account for the diversity of trxG proteins (*19*), which include DNA-binding proteins (Zeste and GAF), nucleosome remodelers (Brahma and Kismet), and histone methyltransferases (Trithorax and Ash1) that are specific for H3K4, a modification that is highly enriched on H3.3. The resulting dynamic process would allow for proteins that promote opposite epigenetic outcomes to act at common cis-regulatory sites.

References and Notes

1. S. Henikoff, K. Ahmad, *Annu. Rev. Cell Dev. Biol.* **21**, 133 (2005).
2. Y. Mito, J. Henikoff, S. Henikoff, *Nat. Genet.* **37**, 1090 (2005).
3. B. E. Schwartz, K. Ahmad, *Genes Dev.* **19**, 804 (2005).
4. C. Wirbelauer, O. Bell, D. Schübeler, *Genes Dev.* **19**, 1761 (2005).
5. S. M. Janicki *et al.*, *Cell* **116**, 683 (2004).
6. F. L. Sun *et al.*, *Mol. Cell. Biol.* **24**, 8210 (2004).
7. R. K. Maeda, F. Karch, *Development* **133**, 1413 (2006).
8. Y. B. Schwartz *et al.*, *Nat. Genet.* **38**, 700 (2006).
9. A. Breiling, B. M. Turner, M. E. Bianchi, V. Orlando, *Nature* **412**, 651 (2001).
10. M. F. Dion, T. Kaplan, M. Kim, S. Buratowski, O. J. Rando, N. Friedman, *Science* **315**, 1405 (2007).
11. F. Karch *et al.*, *Nucleic Acids Res.* **22**, 3138 (1994).
12. A. Mohd-Sarip *et al.*, *Mol. Cell* **24**, 91 (2006).
13. S. Barges *et al.*, *Development* **127**, 779 (2000).
14. B. Papp, J. Muller, *Genes Dev.* **20**, 2041 (2006).
15. H. W. Brock, C. L. Fisher, *Dev. Dyn.* **232**, 633 (2005).
16. A. M. Moses *et al.*, *PLoS Comput. Biol.* **2**, e130 (2006).
17. B. A. Leibovitch *et al.*, *Mol. Cell. Biol.* **22**, 6148 [illegible].
18. C. Jin, G. Felsenfeld, *Proc. Natl. Acad. Sci. U.S.A.* **103**, 574 (2006).
19. R. D. Phair *et al.*, *Mol. Cell. Biol.* **24**, 6393 (2004).
20. D. Brasse *et al.*, *EMBO J.* **25**, 798 (2006).
21. A. K. Hagarch, D. A. Walker, R. Wolford, G. L. Hager, *Mol. Cell* **14**, 163 (2004).
22. I. S. Platero, A. K. Csink, A. Quintanilla, S. Henikoff, *J. Cell Biol.* **140**, 1297 (1998).
23. G. Fitz, R. Hennemann, D. J. Arndt-Jovin, *Development* **132**, 3963 (2005).
24. J. L. Workman, *Genes Dev.* **20**, 2009 (2006).
25. Y. B. Schwartz, T. G. Kahn, V. Pirrotta, *Mol. Cell. Biol.* **25**, 432 (2005).

26. We thank members of our laboratory and F. Karch for helpful discussions, and T. Bryson and A. Morgan for assistance. Microarray data have been deposited in Gene Expression Omnibus accession GSE6234.

Supporting Online Material

www.sciencemag.org/cgi/content/full/315/5817/1408/DC1
Materials and Methods
Figs. S1 to S10
Tables S1 to S3
References

17 August 2006; accepted 9 February 2007
10.1126/science.1134004

Anaphase Onset Before Complete DNA Replication with Intact Checkpoint Responses

Jordi Torres-Rosell,[1]*† Giacomo De Piccoli,[1]* Violeta Cordon-Preciado,[1] Sarah Farmer,[1] Adam Jarmuz,[1] Felix Machin,[1]‡ Philippe Pasero,[2] Michael Lisby,[3] James E. Haber,[4] Luis Aragón[1]§

Cellular checkpoints prevent mitosis in the presence of stalled replication forks. Whether checkpoints also ensure the completion of DNA replication before mitosis is unknown. Here, we show that in yeast *smc5-smc6* mutants, which are related to cohesin and condensin, replication is delayed, most significantly at natural replication-impeding loci like the ribosomal DNA gene cluster. In the absence of Smc5-Smc6, chromosome nondisjunction occurs as a consequence of mitotic entry with unfinished replication despite intact checkpoint responses. Eliminating processes that obstruct replication fork progression restores the temporal uncoupling between replication and segregation in *smc5-smc6* mutants. We propose that the completion of replication is not under the surveillance of known checkpoints.

Eukaryotes have acquired cellular mechanisms that prevent or delay progression through the cell cycle when DNA is damaged (*1*). These mechanisms are referred to as checkpoints. Completion of DNA replication before mitotic entry is thought to be subjected to regulation by a checkpoint (*1*), because premature entry into mitosis would be detrimental to the integrity of the genome. Such a replication-completion checkpoint should prevent mitosis by sensing the persistence of unreplicated DNA or ongoing fork progression in an otherwise normal S phase.

The arguments supporting the existence of a replication-completion checkpoint derive from observations demonstrating that budding yeast cells activate a reversible checkpoint when cells are treated with the drug hydroxyurea (HU) (*2*). However, the checkpoint response to HU is caused by the accumulation of single-stranded DNA on replication forks rather than unreplicated DNA (*3–5*). Indeed, indirect evidence from several studies suggests that yeast cells might lack a replication-completion checkpoint (*6–8*).

The Smc5-Smc6 complex is related to cohesin and condensin and functions in DNA repair (*9*). Cells expressing the *smc5-smc6* mutant alleles showed S phase– and anaphase-entry times similar to those of wild-type (WT) cells (Fig. 1A and fig. S1A), and the central checkpoint kinase Rad53 was activated only after the first mitosis under nonpermissive conditions (*10*). The ribosomal DNA (rDNA) array in the

middle of chromosome XII is a major binding site for the Smc5-Smc6 complex (*10*). Segregation analysis of chromosome XII with the use of fluorescence detection of DNA-based tags, which were inserted at different positions along the chromosome, revealed that tags located between the centromere and the rDNA segregated equally to daughter nuclei in WT and mutant cells, whereas tags between the rDNA and the telomere missegregated to one pole in *smc5-smc6* mutants (fig. S1B) (*10*). Thus, unresolved linkages between sister chromatids seem to cause chromosome nondisjunction in these mutants. Deletion of the recombination gene *RAD52* partially suppresses the *smc6-9* growth defect (*10*). We observed a modest reduction in nondisjunction of chromosome XII when we deleted different recombination genes (fig. S2, A and B). Therefore, the majority of nondisjunction events in *smc6-9* cells are not recombination structures.

Segregation analysis with the use of different growth regimes (fig. S3) showed that Smc5-Smc6 function is required during S phase (Fig. 1, B and C). To explore possible defects in replication forks, we compared actively replicating rDNA from WT and *smc6-9* mutant cells by two-dimensional (2D) gel electrophoresis (see supporting online material). We detected an increase in replication fork barrier (RFB) arrest, recombination, and termination structures in *smc6-9* mutants during S phase (Fig. 2, A and B). The accumulation of structures in *smc6-9* was not caused by an increase in origin firing because WT levels of bubble intermediates were observed in the mutant (fig. S4). Unexpectedly, we found that unlike WT cells, *smc6-9* mutants exhibited an increase in Y-arc replication structures when cells were arrested in metaphase (Fig. 2C) (*10*). Thus, *smc6-9* cells are still replicating rDNA during metaphase, demonstrating that there is a delay in the replication of this region. To further confirm this possibility, we monitored the replication of individual rDNA containing chromosomes by their extension on silanized glass surfaces (*11*). Cells were induced to incorporate bromodeoxyuridine (BrdU) in their DNA during the previous replication. In addition, we blocked cells in metaphase to ensure that they did not enter another cell cycle. We digested chromosomes with restriction enzymes that cut throughout the genome but not within the 2-megabase rDNA region; thus, long DNA fibers that were extended on the silanized glass surfaces represent ribosomal gene arrays (*12*). Replicated regions incorporated BrdU and were identified after immunodetection, whereas BrdU gaps in the fibers revealed unreplicated regions. We detected a twofold increase in unreplicated gaps in *smc6-9* cells relative to WT cells (Fig. 2D). Moreover, the average length of the rDNA fibers in *smc6-9* cells was significantly shorter than that in WT cells (Fig. 2D), suggesting that *smc6-9* fibers break during the protocol. Thus, this procedure underestimates the amount of unreplicated rDNA gaps in these mutant cells. In addition, gaps smaller than a few kilobases are not detectable by this technique (*12*). We conclude that replication of the rDNA region is delayed, and not completed by metaphase, in *smc6-9* cells.

The fact that *smc6-9* mutants are not delayed in mitotic entry (fig. S1A) suggests that they might execute anaphase before they finish replication, at least for chromosome XII. We evaluated whether replication is completed in *smc6-9* mutants before segregation using pulsed-field gel electrophoresis (PFGE). Incompletely replicated chromosomes do not resolve by PFGE and remain in the wells. In WT cells, unreplicated (Fig. 3A, time: 0 min) and fully replicated (Fig. 3A, time: >80 min) chromosomes entered the gel, however, at

[a]Cell Cycle Group, Medical Research Council (MRC) Clinical Sciences Centre, Faculty of Medicine, Imperial College London, Hammersmith Hospital Campus, Du Cane Road, London W12 0NN, UK. [b]Institute of Human Genetics, CNRS Unité Propre de Recherche 1142, 141 Rue de la Cardonille, 34396 Montpellier, France. [c]Department of Genetics, Institute of Molecular Biology and Physiology, University of Copenhagen, Øster Farimagsgade 2A, DK-1353 Copenhagen, Denmark. [d]Rosenstiel Center, Brandeis University, 415 South Street, Mail Stop 029, Waltham, MA 02454–9110, USA.

[*]These authors contributed equally to this work.
[†]Present address: Departament Ciències Mèdiques Basiques, Facultat de Medicina, Universitat de Lleida, Montserrat Roig 2, 25008 Lleida, Spain.
[‡]Present address: Unidad de Investigación, Hospital Universitario Nuestra Señora de Candelaria, Carretera del Rosario sin número, 38010, Santa Cruz de Tenerife, Spain.
[§]To whom correspondence should be addressed. E-mail: uhs.aragon@csc.mrc.ac.uk

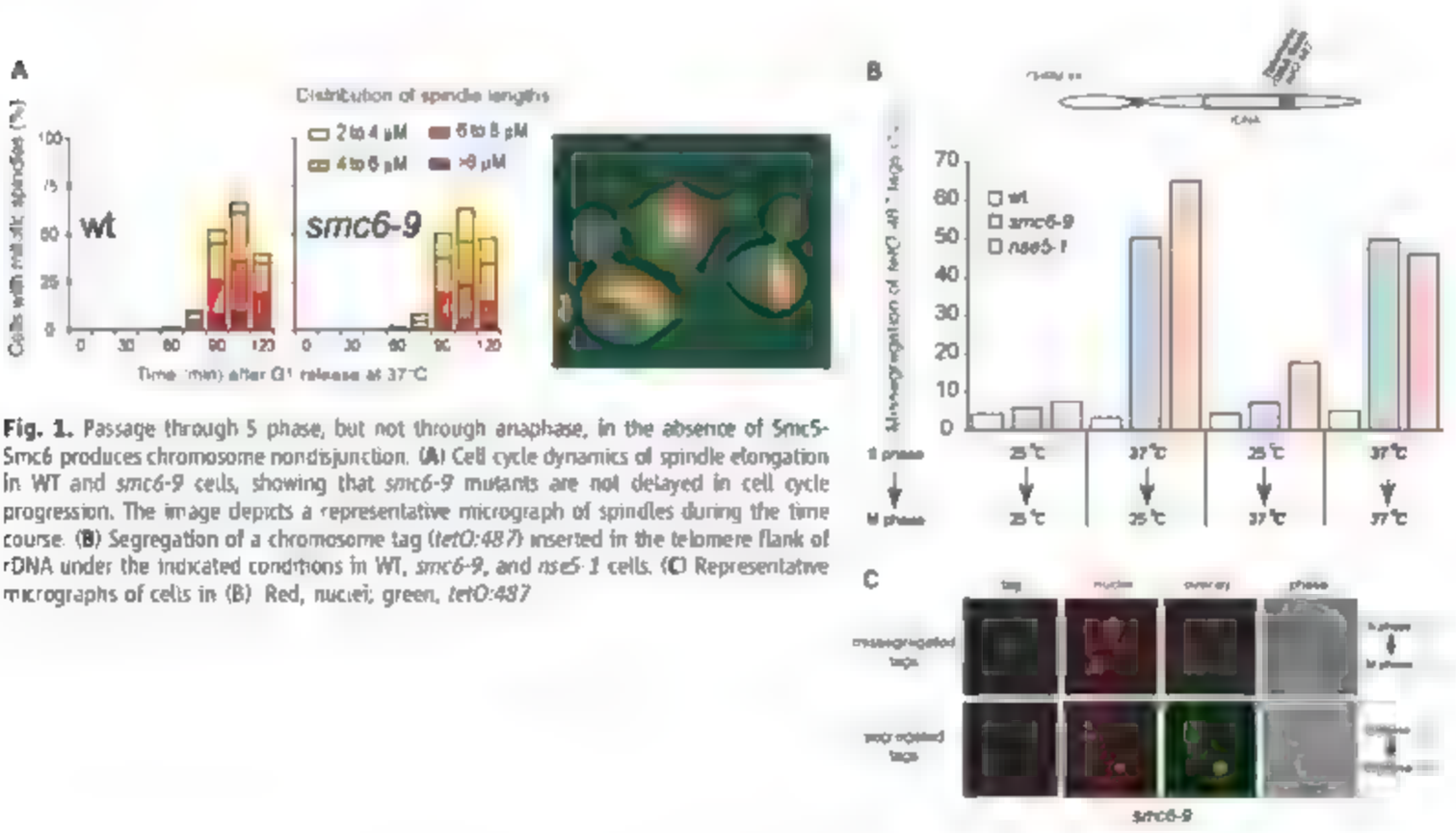

Fig. 1. Passage through S phase, but not through anaphase, in the absence of Smc5-Smc6 produces chromosome nondisjunction. (**A**) Cell cycle dynamics of spindle elongation in WT and *smc6-9* cells, showing that *smc6-9* mutants are not delayed in cell cycle progression. The image depicts a representative micrograph of spindles during the time course. (**B**) Segregation of a chromosome tag (*tetO:487*) inserted in the telomere flank of rDNA under the indicated conditions in WT, *smc6-9*, and *nse5-1* cells. (**C**) Representative micrographs of cells in (B). Red, nuclei; green, *tetO:487*.

chromosomes failed to enter the gel with replicating (Fig. 3A, from 20 to 60 min). In *smc6-9* cells, the amount of chromosome XII that failed to enter the gel after replication (and even segregation) was much greater than that in WT cells (Fig. 3A), and the deletion of *RAD53* had little effect (Fig. 3A).

To analyze whether *smc6-9* cells are deficient in the activation of known checkpoint pathways, we tested whether *smc6-9* mutants activate Rad53 in response to replication stress. Similar levels of Rad53 phosphorylation were detected in WT and *smc6-9* cells exposed to the ribonucleotide reductase inhibitor HU (Fig. 3B) (*17*). Both WT and *smc6-9* cultures arrested as budded cells with one nucleus in response to HU, indicating that both strains halt the cell cycle when the S phase checkpoint is activated. We obtained similar results when cells were exposed to methyl methanesulfonate. In addition, *smc6-9* mutants are also competent in the activation of the DNA damage checkpoint in response to a single double-strand break (DSB) at the *MAT* locus induced by expression of the HO endonuclease (HO) (Fig. 3C). After 4 hours of HO induction, both asynchronous WT and *smc6-9* cells arrested in G_2-M with a single focus of the checkpoint protein Ddc2 (fig. S5A), and Rad53 activated (Fig. 3C). Checkpoint activation also occurs when DSBs occur inside the nucleolus. In a strain carrying the I-SceI recognition site in the middle of

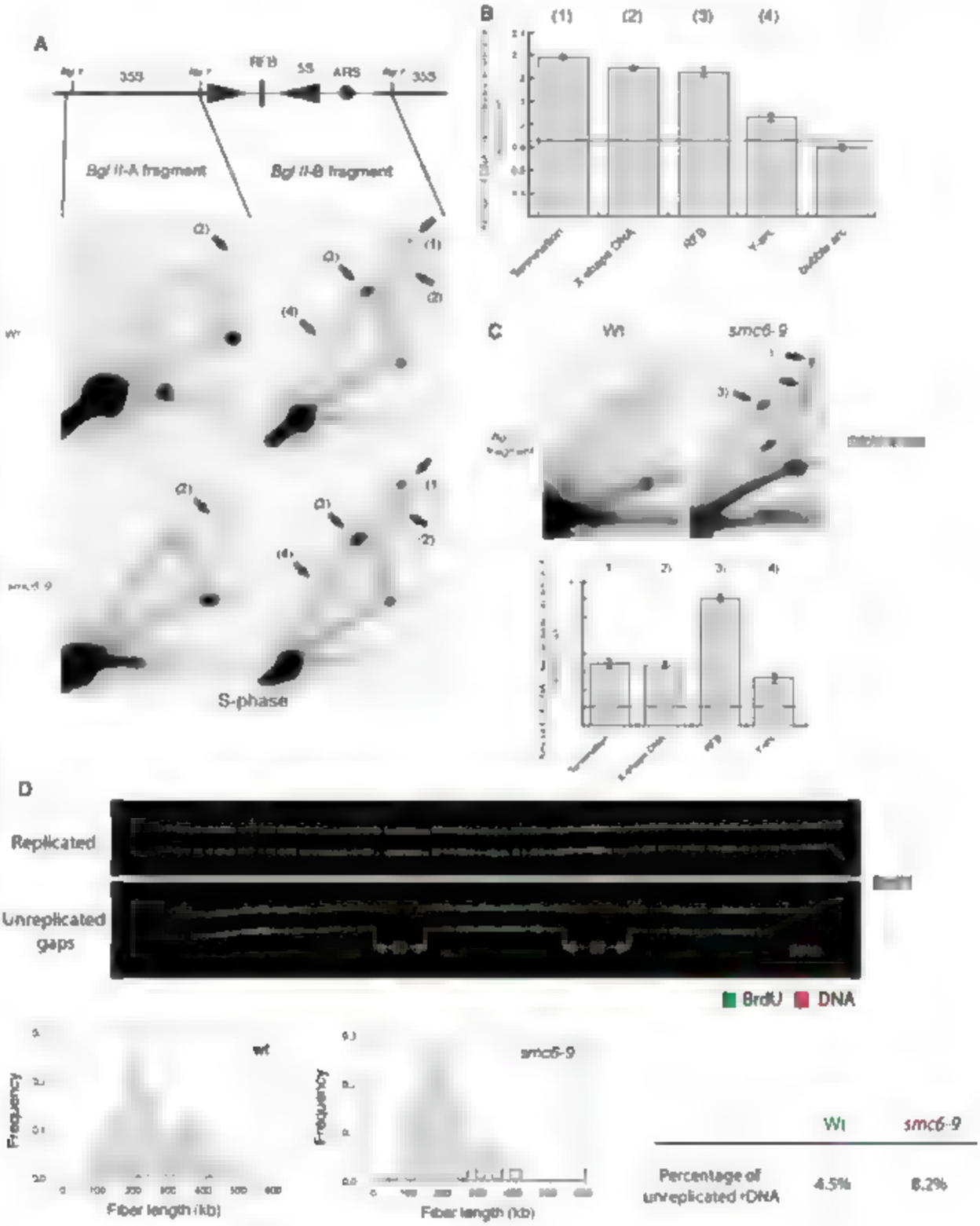

Fig. 2. Replication of rDNA regions is not finished in metaphase in *smc6-9* mutants. (**A**) Replication intermediates of a rDNA region in WT and *smc6-9* cells digested with BglII and separated by 2D gel electrophoresis. Schematic representations of yeast rDNA and restriction enzyme sites are shown. ARS, autonomously replicating sequences. Numbers in parentheses represent different structures on the 2D gels quantified. (**B**) Quantification of rDNA replication structures in (A). (**C**) WT and *smc6-9* cultures arrested in metaphase and analyzed by 2D gel electrophoresis as in (A). Quantification of corresponding rDNA structures is shown. (**D**) DNA combing analysis of completion of DNA replication at the ribosomal genes array. Two representative rDNA fibers, either completely replicated or presenting unreplicated gaps, are shown. Gap lengths are indicated in kb. Red, propidium iodide stain of total DNA; green, antibodies to BrdU. Error bars in B) and (C) indicate SD from three independent experiments.

the ribosomal gene array and expressing the I-SceI endonuclease under the galactose promoter, we detected Rad53 activation in WT and *smc6-9* cells (Fig. 3D). We conclude that breaks in the rDNA are also under normal checkpoint surveillance. Finally, *smc6-9* mutants are competent in the spindle checkpoint, because their sensitivity to the spindle-depolymerizing drug benomyl was comparable to that of WT cells (fig. S5B). We conclude that mitotic entry before the completion of rDNA replication in *smc6-9* mutants is not caused by failures in the cellular checkpoint machineries.

Our data indicate that replication of the rDNA region is severely delayed in the absence of Smc5-Smc6 function (Figs. 2 and 3A). We tested whether eliminating processes that obstruct replication forks in the rDNA would reduce the delay and suppress the chromosome XII nondisjunction phenotype. The rDNA is composed of tandem repeats that are unidirectionally replicated because of the presence of a polar RFB, mediated by the Fob1 protein, which is next to the 35S transcription termination site (*14*, *15*). In WT cells, replication of rDNA has to deal with the presence of RFBs and the clustering of active origins (*12*), which generates a situation where large fragments are replicated by a single rightward-moving fork. In the absence of Fob1, leftward-moving forks are not blocked at the RFB site; thus, replication is accelerated by the presence of two active forks (instead of one). Deletion of *FOB1* in *smc6-9* cells reduced chromosome XII nondisjunction from 63 to 34% (Fig. 4A and fig. S6A). In addition to RFBs, the high transcription rates in rDNA genes are also likely to pose a challenge for active replication across the locus. Inactivation of ribosomal RNA (rRNA) gene transcription can be achieved by the simultaneous deletion of the yeast RNA polymerase (Pol) I subunit A135 and the introduction of a multicopy plasmid containing the 35S rRNA coding region fused to an RNA Pol II promoter (*16*). The inactivation of chromosomal rRNA gene transcription reduced chromosome XII nondisjunction from 63 to 19% in *smc6-9* (Fig. 4B). The simultaneous inactivation of transcription and replication barriers allows segregation of chromosome XII in *smc6-9* mutants with virtually WT efficiency (Fig. 4B and fig. S6B). Thus, the delay in rDNA replication observed in *smc6-9* mutants is a direct consequence of the inability to promote and ensure stable fork progression through the rDNA.

A cellular checkpoint can be defined as a mechanism that halts the cell cycle in WT cells in response to a certain condition (e.g., a cellular insult such as DNA damage). If a gene is classified as part of a checkpoint if mutants of this gene do not arrest the cell cycle as WT cells do. We have shown that *smc6-9* mutant cells behave exactly like WT cells with respect to activation and maintenance of all known cellular checkpoints, namely the S phase checkpoint, DNA-damage checkpoint, and spindle checkpoint. Therefore, the Smc5-Smc6 complex is not part of any of these mechanisms. We find that, despite the fact that all known checkpoints are intact in *smc6-9* mutants, the replication delay in these cells does not hold up mitotic entry before completing replication (Fig. 4C). The function of the Smc5-Smc6 complex is important for coping with the replication program, particularly on challenging templates such as rDNA. We do not know the exact reason why *smc5-smc6* mutants are retarded in replication. One possibility is that Smc5-Smc6 function might be required for

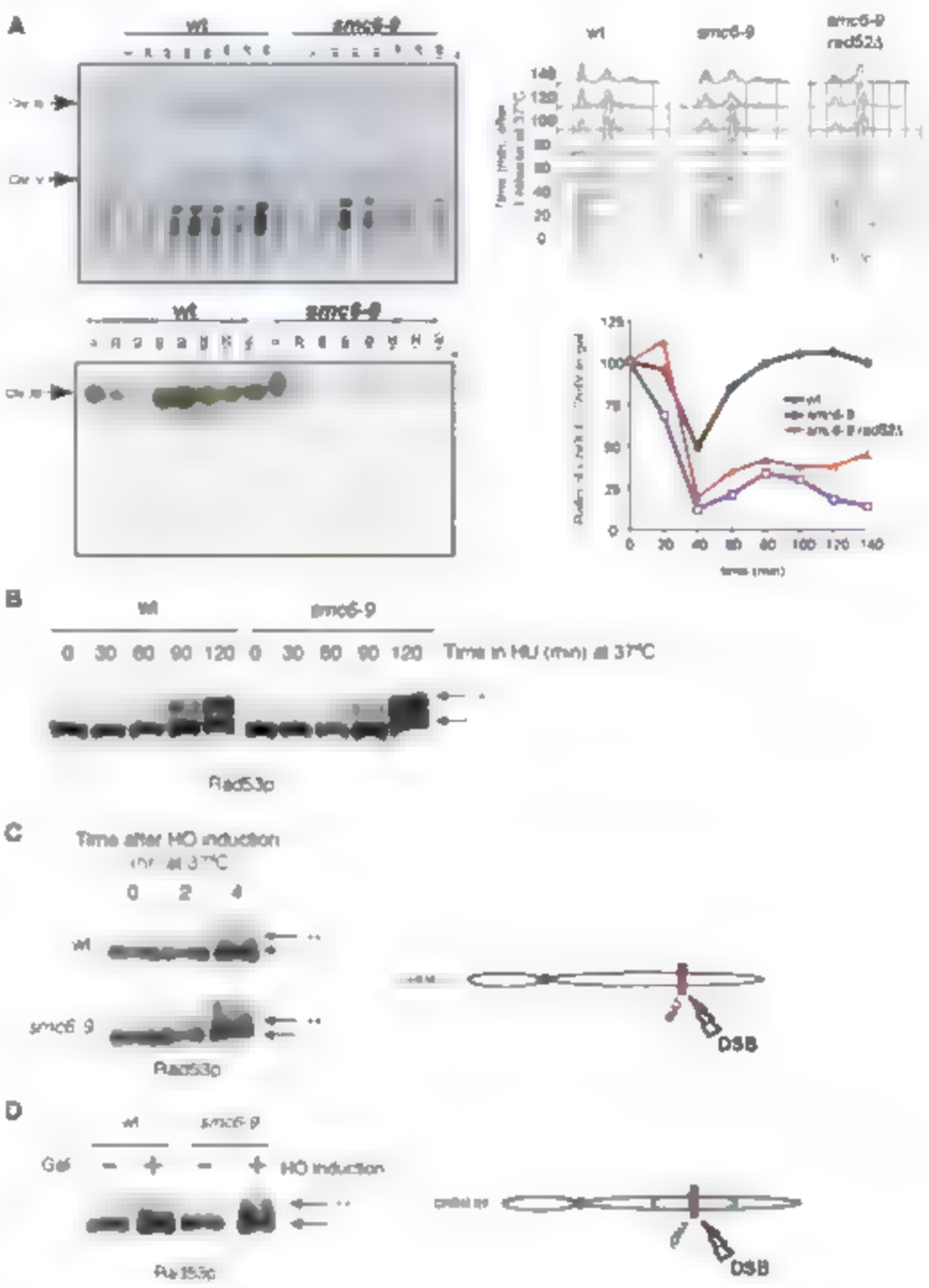

Fig. 3. *smc6-9* cells enter anaphase before completing replication of chromosome XII despite the presence of intact checkpoint responses. (**A**) Synchronized WT and *smc6-9* cultures analyzed by PFGE to visualize yeast chromosomes and their replication. PFGs were transferred and hybridized with a probe to various chromosomes to quantify entry of individual chromosomes. Quantification of chromosome XII entry into the gel is shown for WT, *smc6-9*, and *smc6-9 rad52Δ* cells. The single asterisk indicates the axis label (time in min) after G_1 release at 37°C. In (**B**) Rad53p is similarly phosphorylated in WT and *smc6-9* cells after HU treatment. A DSB at *MAT* (**C**) or rDNA (**D**) induces Rad53 phosphorylation in WT and *smc6-9* cells. Arrows in (B) to (D) indicate Rad53p species. Phosphorylated Rad53p is indicated (**).

accurate fork restart after pausing. We propose that neither ongoing forks nor unreplicated segments of rDNA triggers a classical checkpoint response (Fig. 4D). Here, we have used the rDNA as a model for replication completion. The rDNA region might be considered as a "special genomic locus." However, we have shown that it is under normal checkpoint surveillance. Because rDNA represents 8 to 12% of the yeast genome, mitotic entry before completion of rDNA replication is detrimental to the integrity of the whole genome. We also note that failure to replicate certain genomic regions, such as centromeres, could potentially induce a cell cycle arrest through activation of the spindle checkpoint or the Rad9-dependent mid-anaphase checkpoint. In mammalian cells, fragile sites have been shown to replicate late and to be sensitive to replication delays (*17*, *19*), which suggests that forks progressing through these regions in late G_2 do not signal a mitotic delay and that the chromosomal breaks and gaps observed in metaphase cells are due to unreplicated DNA. The *smc6-9* mutant cells show an increase in chromosomal rearrangements at a non-rDNA locus (*20*), which, as in mammalian fragile sites, could be attributed to the segregation of partially replicated chromosomes. Studies with the origin recognition complex have shown that, during S phase, there is a fork threshold for checkpoint activation (*21*). Similarly, in unperturbed cell cycles, ongoing forks below a threshold level might fail to activate a checkpoint during G_2-M. Therefore, we propose that both the timely separation between replication and segregation and the reservoir of unused origins are the crucial factors ensuring replication before mitosis.

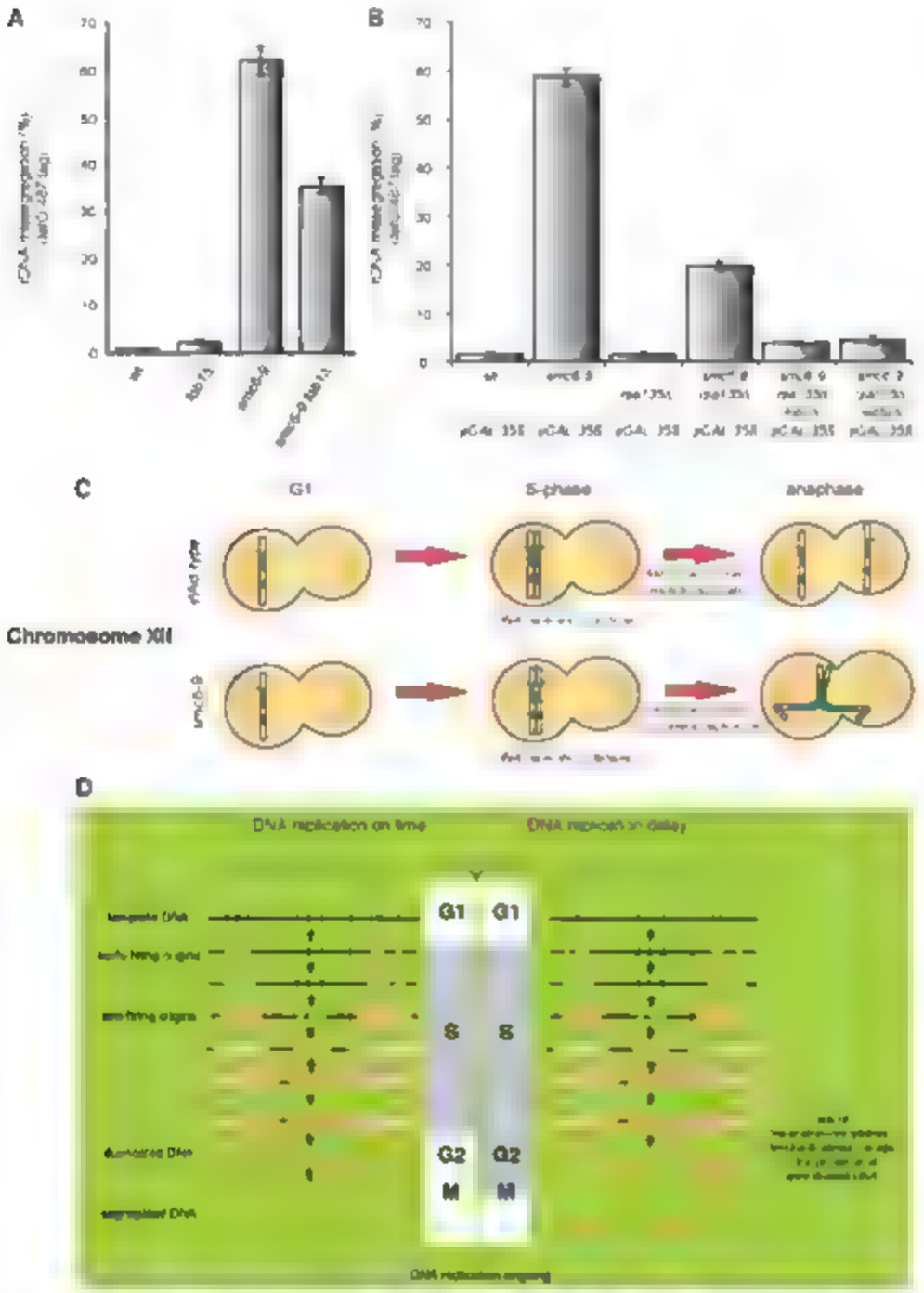

Fig. 4. Eliminating replication impediments restores segregation in *smc6-9* cells. (**A**) Segregation of *tetO:487* tag in *smc6-9* and *smc6-9 fob1*Δ strains. (**B**) Segregation of *tetO:487* tag in *smc6-9*, *smc6-9 rpa135*Δ, and *smc6-9 fob1*Δ *rpa135*Δ strains. (**C**) Diagrammatic representation of the segregation of yeast chromosome XII in WT and *smc6-9* mutants. (**D**) Delayed replication forks in yeast cells do not trigger a replication-completion checkpoint. Error bars in (A) and (B) indicate SD from three independent experiments.

References and Notes

1. F. Weinert, *Curr. Opin. Genet. Dev.* **8**, 185 (1998).
2. F. A. Weinert, G. A. Kiser, L. H. Hartwell, *Genes Dev.* **8**, 652 (1994).
3. J. A. Tercero, M. P. Longhese, J. F. Diffley, *Mol. Cell* **11**, 1323 (2003).
4. J. M. Sogo, M. Lopes, M. Foiani, *Science* **297**, 599 (2002).
5. L. Zou, S. J. Elledge, *Science* **300**, 1542 (2003).
6. A. Lengronne, E. Schwob, *Mol. Cell* **9**, 1067 (2002).
7. S. Piatti, C. Lengauer, K. Nasmyth, *EMBO J.* **14**, 3788 (1995).
8. P. Pasero, S. P. Duncker, E. Schwob, S. M. Gasser, *Genes Dev.* **13**, 2159 (1999).
9. A. R. Lehmann *et al.*, *Mol. Cell. Biol.* **15**, 7067 (1995).
10. J. Torres-Rosell *et al.*, *Nat. Cell Biol.* **7**, 412 (2005).
11. K. Michalet *et al.*, *Science* **277**, 1518 (1997).
12. P. Pasero, A. Bensimon, E. Schwob, *Genes Dev.* **16**, 2479 (2002).
13. Y. Sanchez *et al.*, *Science* **271**, 357 (1996).
14. B. J. Brewer, W. L. Fangman, *Cell* **55**, 637 (1988).
15. M. H. Linskens, J. A. Huberman, *Mol. Cell. Biol.* **8**, 4927 (1988).
16. Y. Hoga, R. Yano, M. Nomura, *Proc. Natl. Acad. Sci. U.S.A.* **88**, 3962 (1991).
17. M. M. Le Beau *et al.*, *Hum. Mol. Genet.* **7**, 755 (1998).
18. A. Hellman *et al.*, *Mol. Cell. Biol.* **20**, 4420 (2000).
19. A. Paulsdottir, Y. Han, Y. Jiang, M. M. Le Beau, *Genes Chromosomes Cancer* **39**, 71 (2004).
20. G. De Piccoli *et al.*, *Nat. Cell Biol.* **8**, 1032 (2006).
21. K. Shimada, P. Pasero, S. M. Gasser, *Genes Dev.* **16**, 3236 (2002).

22. We thank J. Dalgaard and N. Rhind for helpful advice and discussion. Funding for the Haber laboratory was from NIH grant GM 20056. J.T.-R. was supported by a Marie Curie European Reintegration Grant and a "Ramon y Cajal" contract from the Spanish government. Work in the Pasero laboratory was supported by FRM (Equipe FRM, soutenue par la Fondation Recherche Medicale). Work in the Lisby laboratory was supported by the Danish Natural Science Research Council. The Aragon laboratory was supported by the MRC of the UK.

Supporting Online Material

www.sciencemag.org/cgi/content/full/315/5817/[page]/DC1
Materials and Methods
SOM Text
Figs. S1 to S6
References

17 August 2006; accepted 25 January 2007
10.1126/science.1134025

From Swimming to Walking with a Salamander Robot Driven by a Spinal Cord Model

Auke Jan Ijspeert,[1]* Alessandro Crespi,[1] Dimitri Ryczko,[2,3] Jean-Marie Cabelguen[2,3]

The transition from aquatic to terrestrial locomotion was a key development in vertebrate evolution. We present a spinal cord model and its implementation in an amphibious salamander robot that demonstrates how a primitive neural circuit for swimming can be extended by phylogenetically more recent limb oscillatory centers to explain the ability of salamanders to switch between swimming and walking. The model suggests neural mechanisms for modulation of velocity, direction, and type of gait that are relevant for all tetrapods. It predicts that limb oscillatory centers have lower intrinsic frequencies than body oscillatory centers, and we present biological data supporting this.

The salamander, an amphibian, is regarded as the tetrapod most closely resembling the first terrestrial vertebrates and represents, therefore, a key animal from which the evolutionary changes from aquatic to terrestrial locomotion can be inferred (*1*, *2*). It is capable of rapidly switching between two locomotion modes: swimming and walking (*3*–*5*). The swimming mode is similar to that of the lamprey, a primitive fish, with fast axial undulations being propagated as traveling waves from head to tail, while the limbs are folded backward. On firm ground, the salamander switches to a slower stepping gait, in which diagonally opposed limbs are moved together while the body makes S-shaped standing waves with nodes at the girdles (*3*, *6*).

Using the salamander as an animal model, we address three fundamental issues related to vertebrate locomotion: (i) the modifications undergone by the spinal locomotor circuits during the evolutionary transition from aquatic to terrestrial locomotion, (ii) the mechanisms necessary for coordination of limb and axial movements, and (iii) the mechanisms that underlie gait transitions induced by simple electrical stimulation of the brain stem. We address these questions with the help of a numerical model of the salamander's spinal cord that we implement and test on a salamander-like robot capable of swimming and walking. Consequently, this study is also a demonstration of how robots can be used to test biological models, and in return, how biology can help in designing robot locomotion controllers.

As in other vertebrate animals, salamander gaits are generated by a central pattern generator (CPG) (*7*, *8*). As in the lamprey (*9*, *10*) and in the *Xenopus* embryo (*11*, *12*), the CPG for axial motion—the body CPG—is distributed along the entire length of the spinal cord. It forms a double chain of oscillatory centers (groups of neurons that exhibit rhythmic activity) located on both sides of the spinal cord and generates traveling waves corresponding to fictive swimming when activated by *N*-methyl-D-aspartate bath application in isolated spinal cord preparations (*7*). The neural centers for the movements of the limbs—forming the limb CPG—are located in the cervical segments for the forelimbs and in the thoracolumbar segments for the hindlimbs (*13*, *14*). Locomotion can be induced by simple electrical stimulation of the mesencephalic locomotor region (MLR) located in the midbrain (*15*). Low levels of stimulation induce the slow walking gait and, at some threshold, higher stimulation induces a rapid switch to the faster swimming mode. In both modes, the frequency of motion is proportional to the stimulation strength. Gait transitions by MLR stimulation have been observed in all classes of vertebrates and appear to be a common property of vertebrate locomotor control (*16*).

Although these data show the general organization of the locomotor CPG, they do not explain how the different oscillatory centers are coupled together and how they are driven by command signals for gait generation and modulation. We have developed a numerical model of the salamander CPG to explore these questions, which are relevant to all tetrapods. Previous numerical models (*17*–*20*) have provided insights into possible mechanisms for gait transition, but failed to explain the MLR stimulation experiment described above (*15*) and the observation that swimming frequencies are systematically higher than walking frequencies.

Our model is based on four main hypotheses. Hypothesis 1: The body CPG is like that of the lamprey and spontaneously produces traveling waves when activated with a tonic drive (e.g., simple continuous stimulation). The limb CPG, when activated, forces the whole CPG into the walking mode, as previously proposed in (*1*). Hypothesis 2: The strengths of the couplings from limb to body oscillators are stronger than those from body to body oscillators and from body to limb oscillators. This allows the limb CPG to "overrule" the natural tendency of the body CPG to produce traveling waves and force it to produce standing waves. Hypothesis 3: Limb oscillators cannot oscillate at high frequencies, that is, they saturate and stop oscillating at high levels of drive. This provides a mechanism for automatically switching between walking and swimming when the drive is varied (*15*) and explains why swimming frequencies are systematically higher than walking frequencies (*3*, *5*). Hypothesis 4: For the same drive, limb oscillators have lower intrinsic frequencies than the body oscillators. This explains the rapid increase of frequency during the switch from walking to swimming and the gap between walking and swimming frequency ranges (*3*, *5*).

The CPG model is composed of a body CPG and a limb CPG, implemented as a system of coupled nonlinear oscillators (Fig. 1A). Similar to lamprey models (*21*), the bursting properties of an oscillatory center—the oscillations between bursts of motoneuron activity and periods of rest—are modeled by means of a phase oscillator with controlled amplitude:

$$\dot{\theta}_i = 2\pi\nu_i + \sum_j r_j\, w_{ij} \sin(\theta_j - \theta_i - \phi_{ij})$$

$$\dot{r}_i = a_i\left(\frac{a_i}{4}(R_i - r_i)\right)$$

$$x_i = r_i(1 + \cos\theta_i)$$

Where θ_i and r_i are the state variables representing the phase and the amplitude of oscillator i, ν_i and R_i determine its intrinsic frequency and amplitude, and a_i is a positive constant. Couplings between oscillators are defined by the weights w_{ij} and phase biases ϕ_{ij}. A positive oscillatory signal, x_i, represents the burst produced by the center.

In the lamprey and the salamander, the amplitude and frequency of bursts depend on the amount of stimulation (*15*, *22*). Typically, when an increasing drive is applied, three phases can be distinguished: (i) a subthreshold phase without bursts; (ii) an oscillating phase where the frequency and amplitude of bursts increase with the drive; and (iii) a saturation phase where centers stop oscillating. We replicate this effect by introducing a piecewise linear saturation function, which similarly modulates the intrinsic frequency and amplitude ν_i and R_i according to a drive signal d_i between a lower oscillation threshold, $d_{i_{low}}$, and an upper one, $d_{i_{high}}$. Limb and body oscillators are provided with different saturation functions, with the limb oscillators systematically oscillating at lower frequencies than body oscillators for the same drive (hypothesis 4) and saturating at a lower threshold $d_{i_{high}}$ (hypothesis 3). Except for turning, all oscillators receive the same drive d.

The coupling parameters w_{ij} and ϕ_{ij} are set such that the body CPG produces traveling waves (hypothesis 1) and the limb CPG produces the salamander stepping. There are unidirectional couplings from limb oscillators to body oscillators (Fig. 1A) whose strengths are larger than those within the body CPG (hypothesis 2). More details and parameters are provided in the Supporting Online Material (*23*).

Robots are increasingly used as tools to test hypotheses concerning biological systems (*24*). Here, we test the spinal cord model on a salamander robot whose purpose is threefold: (i) to

[1]School of Computer and Communication Sciences, Ecole Polytechnique Fédérale de Lausanne (EPFL), Station 14, CH-1015 Lausanne, Switzerland. [2]INSERM, U 862, Bordeaux, F-33077, France. [3]University Bordeaux 2, Bordeaux, F-33077, France.

*To whom correspondence should be addressed. E-mail: auke.ijspeert@epfl.ch

show that our CPG model can generate forward motion with variable speed and heading (i.e., aspects that need a "body" for validation and cannot be studied at a neuronal level alone); (ii) to quantitatively compare the gaits generated to those of the real salamander; and (iii) to show that the concept of CPGs can lead to robust locomotion control for robots with multiple articulated joints.

The 85-cm-long robot is designed to approximately match the kinematic structure of salamanders (Fig. 1B). The robot can move its four limbs as well as produce lateral undulations of the spine with six actuated hinge joints. Unlike the real animal, limbs perform continuous rotation. The rotation replicates the rotational thrust that salamander legs apply to the ground while in stance phase and allows the alternation between swing and stance. Setpoints for the motor controllers are based on the difference

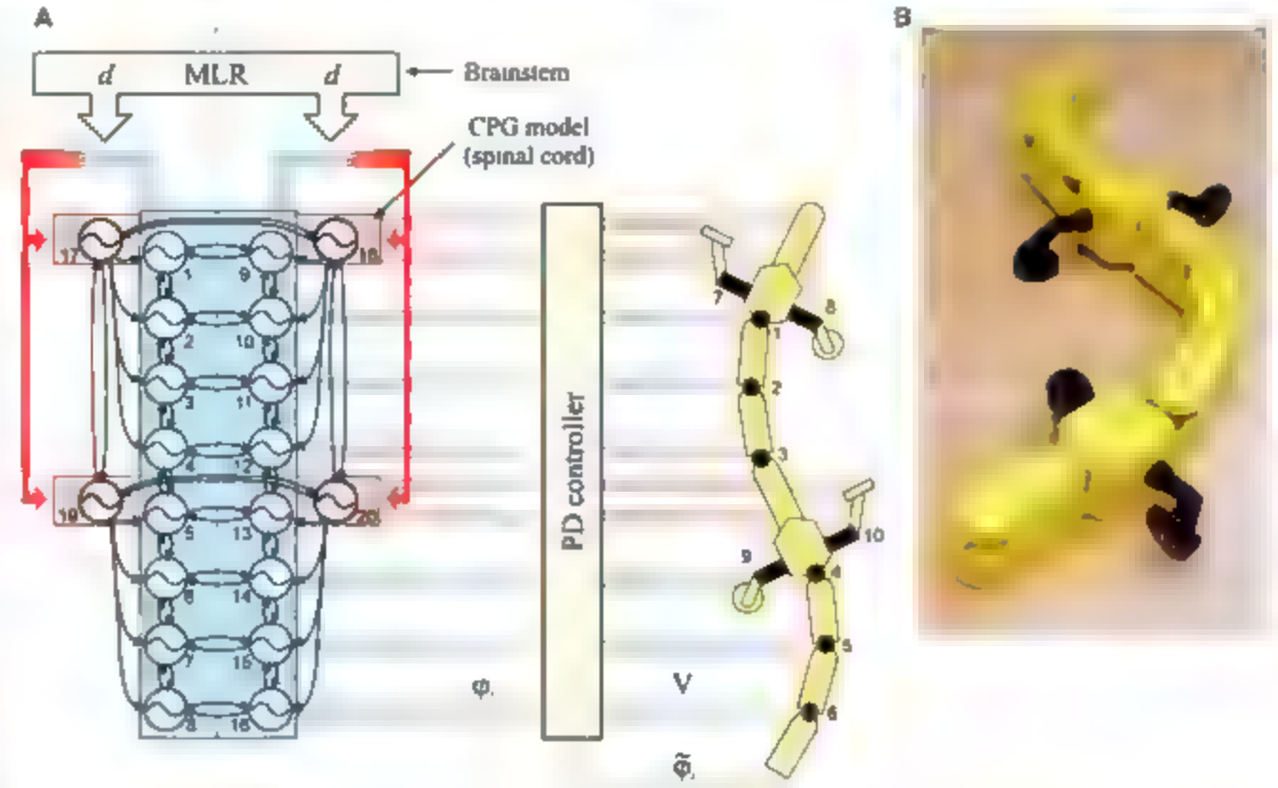

Fig. 1. Configuration of the CPG model (**A**) and salamander robot (**B**). The robot is driven by 10 dc motors, which actuate six hinge joints for the spine (black disks in the schematic view of the robot) and four rotational joints for the limbs (black cylinders). The CPG is composed of a body CPG—a double chain of 16 oscillators with nearest-neighbor coupling for driving the spine motors—and a limb CPG—4 oscillators for driving the limb motors. The outputs of the oscillators are used to determine the setpoints φ_i (desired angles) provided to proportional-derivative (PD) feedback controllers that control the motor torques (through their voltage V_i) given the actual angles $\tilde{\varphi}_i$. The CPG model receives left and right drives d representing descending signals from the MLR region in the brain stem. The velocity, direction, and type of gait exhibited by the robot can be adjusted by modifying these two signals.

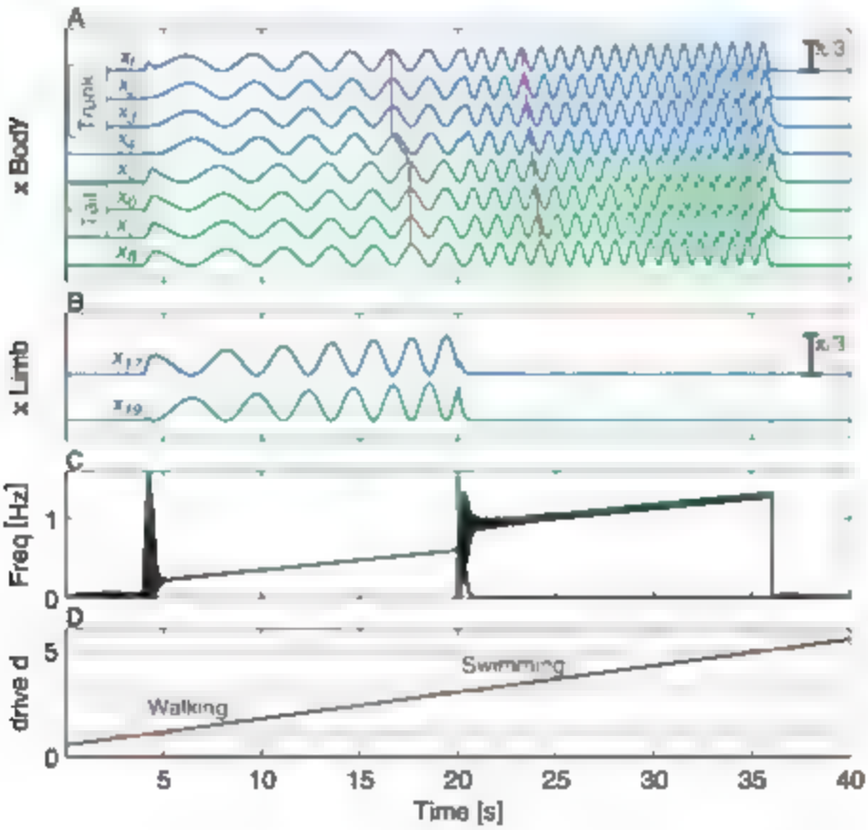

Fig. 2. Switching from walking to swimming; activity of the CPG model when the drive signal is progressively increased. (**A**) x_i signals from the left body CPG oscillators (oscillators on the right side are exactly in antiphase). The numbering corresponds to that of Fig. 1A. Units are in radians (scale bar on the top right). The red lines illustrate the transition from standing waves (with synchrony in the trunk, synchrony in the tail, and an antiphase relation between the two, 4 s < t <20 s) to traveling waves (20 s < t <36 s). (**B**) x_i signals from the left-limb CPG oscillators. Ipsilateral fore- and hindlimbs are in antiphase. (**C**) Instantaneous frequencies measured as $\frac{\dot{\theta}_i}{2\pi}$ in cycles/s. The variations in the instantaneous frequencies among individual oscillators at times t = 4 s and t = 20 s correspond to brief accelerations and decelerations before resynchronization. (**D**) Linear increase of the drive d applied to all oscillators. The horizontal red lines correspond to the lower ($d^{limb}_{low} = d^{body}_{low} = 1$) and upper ($d^{limb}_{high} = 3$, $d^{body}_{high} = 5$) oscillation thresholds for limb and body oscillators in arbitrary drive units. Movie S2 shows a similar switch from walking to swimming in the robot.

between the r_i signals from the left and right body oscillators for the spine motors, and on the phases θ_i of the limb oscillators for the limb motors. See (*23*) for additional design information.

The CPG model produces swimming and walking patterns that are consistent with those of the real salamander. As observed in MLR stimulation experiments (*15*), the model produces an abrupt transition between gaits simply by varying the drive (Fig. 2). During walking (i.e., at low drive), the strong couplings from limb to body oscillators force the body CPG to oscillate at a low frequency with an S-shaped standing wave, as in the electromyogram (EMG) recordings (*5*). The frequency and amplitude of oscillations increase proportionally with the drive. At t = 20 s, the limb oscillators saturate, and this induces a rapid gait transition to the higher-frequency swimming mode. Traveling waves for swimming are released, also as in the EMG recordings (*5*). These traveling waves increase in amplitude and frequency as the drive is further increased, until the body oscillators reach their upper oscillation threshold and stop oscillating.

These numerical results agree with detailed kinematic analyses of the gait transitions, which found that traveling waves in the body axis are not observed simultaneously with limb movements (*4*). Another important similarity with the MLR stimulation experiments and with recordings in tadpoles (*12*) is the step increase of frequencies during the transition from walking to swimming. In the model, the limb oscillators slow down the rhythms during walking, and once silent, rapidly release faster swimming rhythms due to the higher intrinsic frequencies of the body oscillators. This can also explain why salamander walking and swimming frequencies do not overlap (*3*, *5*), but have distinct ranges with a gap between them (e.g., walking from 0.6 to 1.2 Hz, swimming from 1.6 to 2.9 Hz in the salamander *Pleurodeles waltlii*). In our model, walking and swimming frequencies range, respectively, from 0.2 to 0.6 Hz and, from 0.9 to 1.3 Hz. The intrinsic frequencies of the model have been reduced compared to those of the real salamander to fit within the torque limits of the robot motors. Although Fig. 2 shows an example with a simple linear increase of the drive, the model can readily deal with abruptly and continuously varied drives (as likely occurs in a freely behaving animal) and modulate the velocity and type of gait accordingly (*24*).

In addition to similarities in neural patterns, the gaits produced by the robot are similar to those of a real salamander. In the walking gait (Fig. 3), the body makes an S-shaped standing wave with nodes at the girdles. The envelopes of lateral displacements compared to the direction of motion (Fig. 3C) are quantitatively similar for the robot and the salamander, with minimal displacements close to the girdles (note that the hindlimb girdle is located closer to the tail for the robot). The axial undulations resemble that of the salamander with two exceptions. The tail of the robot is bent over its whole length, whereas the tip of the salamander's tail tends to remain straight, and the head of the robot makes more lateral displacements because it lacks joints in the neck. The body-limb coordination in both the robot and the real salamander optimizes stride length (*23*). Increasing the drive leads to an augmentation of the speed of walking, due to the higher frequency and amplitude of oscillations. The walking velocities obtained range from 0.03 to 0.09 m/s (0.04 to 0.11 body lengths/s). In relative terms, the robot is slower than a *P. waltlii* which walks at velocities in the range of 0.1 to 0.4 body lengths/s. The difference can be explained by the lower frequencies used in the robot.

The swimming mode of the robot is also consistent with that of a real salamander (Fig. 4). The traveling wave of body undulation allows the salamander robot to propel itself forward in water. The lateral displacements are similar to those of the salamander, with points of minimal displacement traveling from head to tail (Fig. 4, A and B, arrows). The envelope of maximal lateral displacement has a more complex profile than that of the real salamander, in which the maximal lateral displacement increases more or less monotonically from head to tail (Fig. 4C). In the robot, there is a bump in the envelope just above the hindlimb girdle. This is probably because the lack of a hinge joint at the girdle and the increased mass of the hindlimb module affect lateral displacements. Consistent with salamander kinematics and EMG recordings, an undulation wavelength of one body length is maintained even when the frequency of oscillations is modified with the drive. The swimming velocities range from 0.07 to 0.12 m/s (0.08 to 0.14 body lengths/s). In relative terms, the robot swims more slowly than *P. waltlii* (from 0.4 to 1.2 body lengths/s). The difference likely results from a combination of three factors. The robot has lower frequencies, fewer actuated joints, and a less profiled body than *P. waltlii*. Nonetheless, considering the rela-

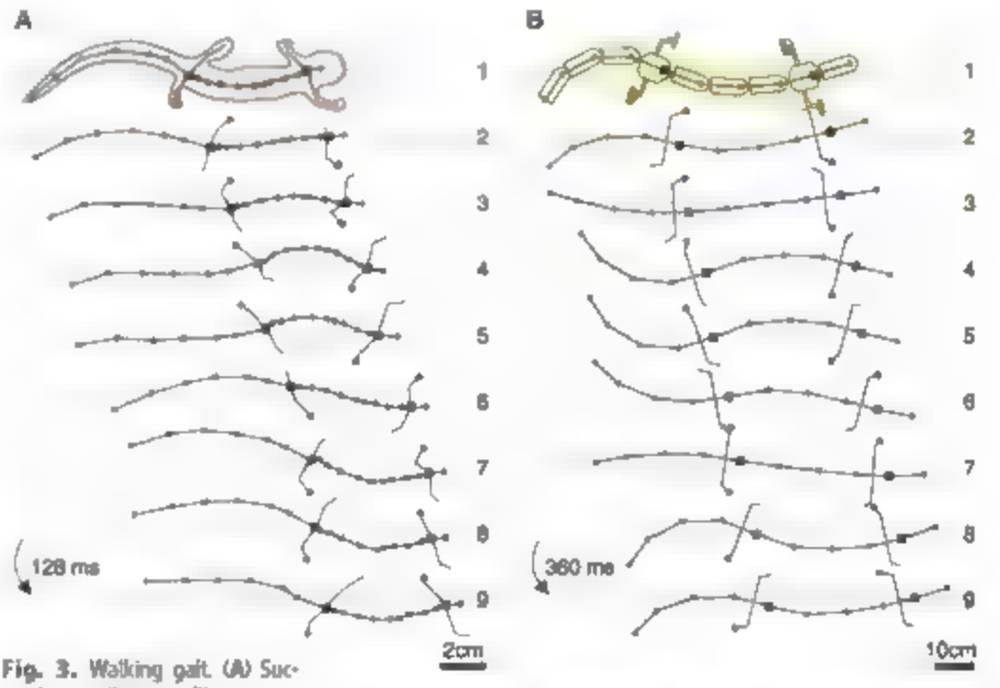

Fig. 3. Walking gait. (**A**) Successive midline profiles reconstructed from digitized video fields by means of 18 marker points (black dots) during a complete stepping cycle of one individual salamander (velocity = 0.06 m/s = 0.34 body lengths/s). Squares indicate girdles. A dot at the extremity of a limb indicates the estimated foot contact with the ground. The horizontal lines show the overall direction of forward travel. (**B**) Same measurement with 10 markers on the robot (drive = 2.0, velocity = 0.06 m/s = 0.07 body lengths/s). (**C**) Envelopes corresponding to the maximal lateral displacements in the salamander and the robot. The data points and error bars correspond to the averages and standard deviations of 5 sequences at various velocities for the salamander and 25 sequences for the robot (*23*). See also movies S1 and S2. BL denotes body length.

tively simple design of the robot, its overall performance captures many elements of the salamander's locomotor behavior.

Lateral turning can be induced during both walking and swimming by applying asymmetrical drives between left and right sides of the body CPG. Such a mechanism is in agreement with the activity patterns of reticulospinal neurons observed during lateral turns in the swimming lamprey. [See (23) and movie S2.]

The model leads to the following four predictions. (i) It predicts that limb oscillators saturate at lower frequencies than body oscillators (hypothesis 3). The saturation could be due either to a spinal mechanism (i.e., limb oscillators are intrinsically limited to lower frequencies) and or to a mechanism in the reticulospinal neurons (i.e., these neurons could stop transmitting the locomotor command to the limb oscillators if the signal exceeds a threshold). (ii) Hypothesis 4 predicts that motoneuron signals to limb and axial muscles should exhibit different oscillation frequencies for the same drive when body oscillators are isolated from limb oscillators. Experiments show this prediction to be true (see Section 4 of the Materials and Methods). (iii) We predict that, similar to the lamprey, asymmetrical stimulation of the brain stem will lead to turning in salamanders. (iv) We predict that lesioning the neural pathways from limb centers to body centers will modify the walking gait—the body will tend to make traveling waves, and there will be a loss of coordination between limb movements and body undulations—but not the swimming mode.

The main implication of this study for vertebrate locomotion is to show how a tetrapod locomotion controller can be built on top of a primitive swimming circuit and explain the mechanisms of gait transition, the switch between traveling and standing waves of body undulations, and the coordination between body and limbs. This work extends models of gait transitions as bifurcation phenomena (25–27) by taking evolutionary modifications into account and proposing that the addition of oscillatory centers together with the modification of intrinsic and saturation frequencies in spinal oscillators could provide a general mechanism for the generation of multiple gaits in vertebrates.

Finally, this work also contributes to robotics. There is currently no well-established methodology for controlling the locomotion of robots with multiple degrees of freedom, in particular for non steady-state locomotion in complex environments. CPGs offer an interesting approach to solving the problem of online trajectory generation by using the limit cycle behavior of coupled oscillators to produce the motor commands in real time. CPG-based control allows one to reduce the dimensionality of the locomotion control problem while remaining highly flexible to continuously adjust velocity, direction, and type of gait according to the environmental context.

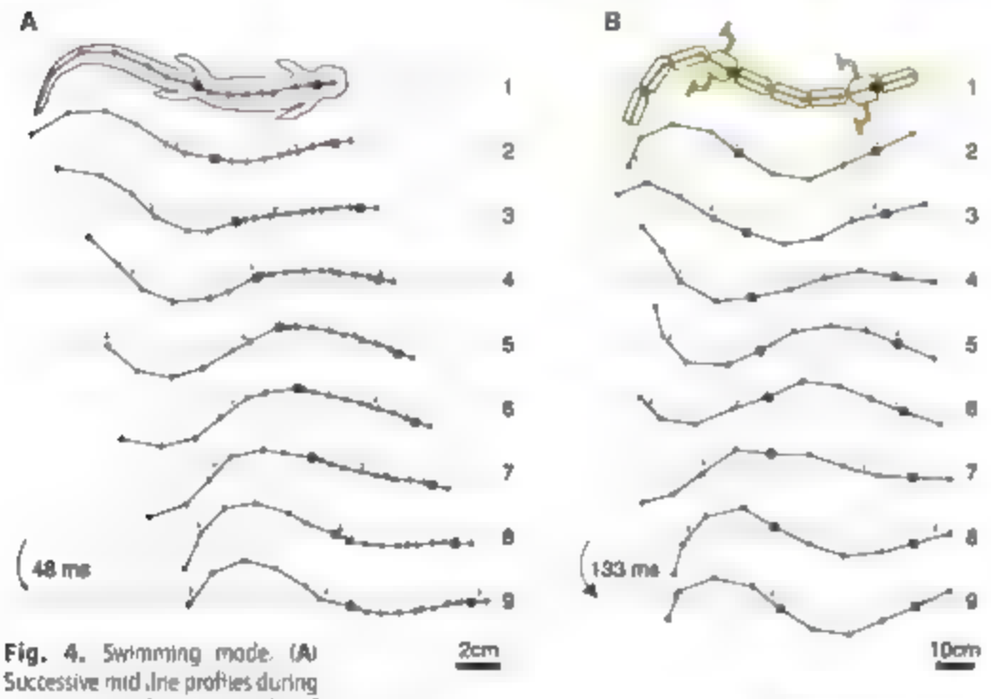

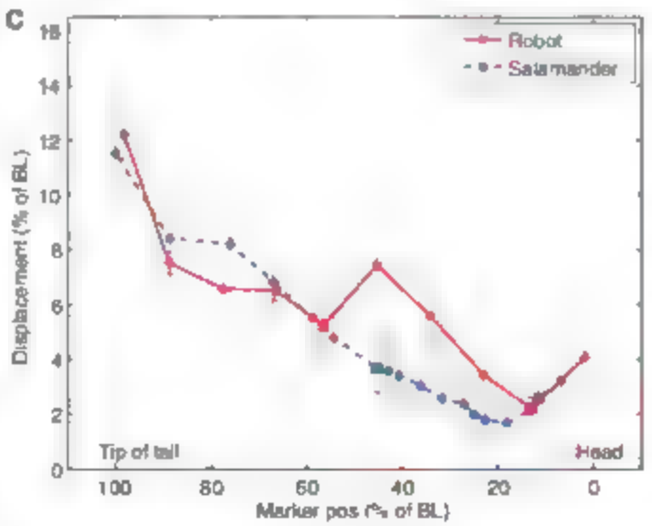

Fig. 4. Swimming mode. (**A**) Successive mid-line profiles during a complete swimming cycle of one individual salamander (velocity = 0.17 m/s = 0.89 body lengths/s). Same representation as in Fig. 3A. Arrows indicate the points of minimal lateral displacement from the overall direction of forward travel (horizontal lines). Note the traveling wave in the body undulation. (**B**) Undulations in the robot (drive = 4.0, velocity = 0.11 m/s = 0.13 body lengths/s). (**C**) Envelopes corresponding to the maximal lateral displacements. The data points and error bars correspond to the averages and standard deviations of 6 sequences at various velocities for the salamander and 25 sequences for the robot (*23*). See also movies S1 and S2.

References and Notes

1. A. H. Cohen, in *Neural Control of Rhythmic Movements in Vertebrates*, A. H. Cohen, S. Rossignol, S. Grillner, Eds. (Wiley, New York, 1988), pp. 129–166.
2. K.-Q. Gao, N. H. Shubin, *Nature* **410**, 574 (2001).
3. L. M. Frolich, A. A. Biewener, *J. Exp. Biol.* **62**, 107 (1992).
4. M. A. Ashley-Ross, B. F. Bechtel, *J. Exp. Biol.* **207**, 461 (2004).
5. L. Delvolvé, I. Bem, J.-M. Cabelguen, *J. Neurophysiol.* **78**, 638 (1997).
6. P. Roos, *Proc. Ned. Akad. Wetten. C.* **67**, 223 (1964).
7. L. Delvolvé, P. Branchereau, R. Dubuc, J.-M. Cabelguen, *J. Neurophysiol.* **82**, 1074 (1999).
8. M. Wheatley, K. Jovanovic, R. B. Stein, V. Lawson, *J. Neurophysiol.* **71**, 2025 (1994).
9. A. H. Cohen, P. Wallen, *Exp. Brain Res.* **41**, 11 (1980).
10. S. Grillner *et al.*, *Trends Neurosci.* **18**, 270 (1995).
11. M. J. Tunstall, A. Roberts, *J. Physiol. (London)* **474**, 393 (1994).
12. D. Combes, S. D. Mertyweit, J. Simmers, K. T. Sillar, *J. Physiol. (London)* **559**, 17 (2004).
13. J. Cheng *et al.*, *J. Neurosci.* **18**, 4295 (1998).
14. G. Székely, G. Czéh, in *Frog Neurobiology, a Handbook*, R. Llinas, W. Precht, Eds. (Springer, Berlin, 1976), pp. 765–797.
15. J. M. Cabelguen, C. Bourcier-Lucas, J. Dubuc, *J. Neurosci.* **23**, 2434 (2003).
16. S. Grillner, A. P. Georgopoulos, L. M. Jordan, in *Neurons, Networks and Motor Behavior*, P. S. G. Stein, S. Grillner, A. Selverston, D. G. Stuart, Eds. (MIT Press, Cambridge, MA, 1997), pp. 3–19.
17. B. Ermentrout, N. Kopell, *SIAM J. Appl. Math.* **54**, 478 (1994).
18. A. J. Ijspeert, *Biol. Cybern.* **84**, 331 (2001).
19. T. Bem, J.-M. Cabelguen, O. Ekeberg, S. Grillner, *Biol. Cybern.* **88**, 79 (2003).
20. A. J. Ijspeert, A. Crespi, J. M. Cabelguen, *Neuroinformatics* **3**, 171 (2005).
21. T. L. Williams, K. A. Sigvardt, N. Kopell, G. B. Ermentrout, M. P. Remler, *J. Neurophysiol.* **64**, 862 (1990).
22. S. Grillner *et al.*, *Brain Res. Brain Res. Rev.* **26**, 184 (1998).
23. Supporting online movies and text are available on *Science* Online.
24. B. Webb, *Nature* **417**, 359 (2002).
25. J. J. Collins, S. A. Richmond, *Biol. Cybern.* **71**, 375 (1994).
26. G. Schöner, J. A. S. Kelso, *Science* **239**, 1513 (1988).
27. M. Golubitsky, I. Stewart, P.-L. Buono, J. J. Collins, *Nature* **401**, 693 (1999).

28. We acknowledge support from the Swiss National Science Foundation and the French "Ministère de la Recherche et de la Technologie" (ACI NIC 032362). We are grateful to

B. Webb, M. Daley, B. Ermentrout, A. Roberts, G. Le Masson, and S. Schaal for useful comments; A. Guignard and A. Badertscher for help in the construction of the robot, L. Delvolvé for kinematic recordings, and F. Mondada for providing the PD motor controller

Supporting Online Material
www.sciencemag.org/cgi/content/full/315/5817/1416/DC1
Materials and Methods
Figs. S1 to S7
Table S1

References and Notes
Movies S1 and S2

4 December 2006; accepted 25 January 2007
10.1126/science.1138353

Ecological Speciation in South Atlantic Island Finches

Peter G. Ryan,[1]* Paulette Bloomer,[1,2] Coleen L. Moloney,[1] Tyron J. Grant,[2] Wayne Delport[1,2]

Examples of sympatric speciation in nature are rare and hotly debated. We describe the parallel speciation of finches on two small islands in the Tristan da Cunha archipelago in the South Atlantic Ocean. *Nesospiza* buntings are a classic example of a simple adaptive radiation, with two species on each island: an abundant small-billed dietary generalist and a scarce large-billed specialist. Their morphological diversity closely matches the available spectrum of seed sizes, and genetic evidence suggests that they evolved independently on each island. Speciation is complete on the smaller island, where there is a single habitat with strongly bimodal seed size abundance, but is incomplete on the larger island, where a greater diversity of habitats has resulted in three lineages. Our study suggests that the buntings have undergone parallel ecological speciation.

During much of the 20th century, speciation among sexually reproducing organisms was assumed to require an allopatric phase, when the incipient species were isolated (*1*–*3*). Over the past decade, models have been developed suggesting that speciation can occur through natural or sexual selection in parapatry or sympatry, with partial or complete overlap between populations (*4*–*6*). Initial segregation is driven by frequency-dependent disruptive selection, in which individual fitness is determined by the composition of the population through competition. This is termed adaptive speciation to stress the importance of biological interactions (*4*), although adaptive processes also may reinforce segregation in allopatrically derived lineages (*7*, *8*). Ecological speciation is a similar process, whereby reproductive isolation results from divergent selection for different environments or niches, but it makes no assumptions about the initial spatial structure of populations (*7*). It also predicts the independent evolution of convergent ecomorphs in similar environments (*7*).

There is much debate about adaptive sympatric speciation (*2*, *5*, *6*, *9*), with recent theoretical studies suggesting that speciation through competitive interactions is either unlikely (*9*) or plausible only under far more restrictive conditions than originally proposed (*5*, *6*). In sexually reproducing organisms, assortative mating is necessary to reduce gene flow between lineages, although the number of loci affecting a trait under selection may also play a role (*6*). In empirical studies it is difficult to exclude the possibility of initial allopatric segregation and subsequent dispersal (*1*). The most plausible examples are found in host-specific insects and freshwater fish (*4*, *10*, *11*). Among birds, the specialization of brood parasitic species on different hosts may lead to sympatric speciation (*12*), but resource specialization is not known to drive speciation, with intraspecific competition being reduced through sexual dimorphism or, more rarely, through trophic polymorphism (*13*, *14*).

Island finches have been especially influential in the development of evolutionary theory (*15*, *16*). Lack's classic study of Darwin's finches (*16*) provided strong support for the allopatric model of speciation. Although recent studies have shown that hybridization and introgression are important in the evolution of Darwin's finches (*17*–*19*) and that competitive interactions reinforce species differences in sympatry (*8*), the initial development of morphological diversity is still considered to have occurred in isolation (*15*). However, the large number of islands and finch species makes it difficult to infer evolutionary

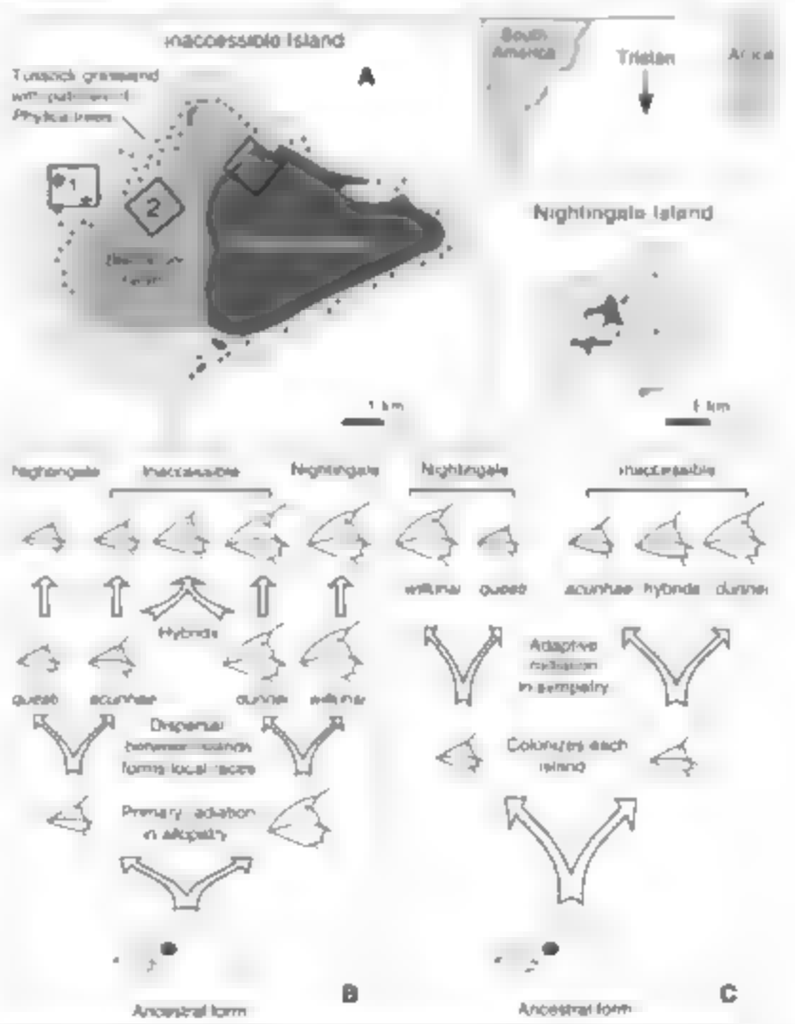

Fig. 1. The Tristan da Cunha archipelago (**A**) showing the distributions of habitat types on Inaccessible Island (14 km^2) and Nightingale Island (4 km^2). Squares 1 to 3 show the main study areas on Inaccessible Island. The diversity of *Nesospiza* buntings could result from either allopatric speciation (**B**) or parallel sympatric radiations (**C**).

*Percy FitzPatrick Institute, Department of Science and Technology/National Research Foundation Centre of Excellence, University of Cape Town, Rondebosch 7701, South Africa. [2]Molecular Ecology and Evolution Programme, Department of Genetics, University of Pretoria, Pretoria 0002, South Africa.

*To whom correspondence should be addressed. E-mail: Peter.Ryan@uct.ac.za

histories (*20*). We provide evidence for parallel ecological speciation in the simpler radiation of *Nesospiza* buntings at Tristan da Cunha (*16*, *21*).

The Tristan da Cunha archipelago comprises three volcanic islands 20 to 35 km apart in the central South Atlantic Ocean (Fig. 1A). The islands differ in size and age, with the largest island (Tristan, 96 km^2) being approximately 300,000 years old, whereas Nightingale Island (4 km^2) is at least 18 million years old (*22*). Inaccessible Island is intermediate in size (14 km^2) and age (3 million years) (*23*). Palynological studies indicate that the vegetation has remained relatively unchanged for at least the past 20,000 years (*23*). Like Darwin's finches (*24*), *Nesospiza* buntings evolved from finch-tanagers (Thraupini). Their South American ancestors were carried on the prevailing westerly winds across 3000 km of ocean (*25*). Vagrant finches also colonized Gough Island, 350 km south of Tristan, giving rise to the endemic Gough bunting *Rowettia goughensis* (*25*). Two *Nesospiza* species are recognized. Tristan bunting *N. acunhae* is an abundant small-billed dietary generalist, whereas Wilkins' bunting *N. wilkinsi* is a scarce large-billed specialist on the woody fruit of *Phylica arborea*. Both species occur on Inaccessible and Nightingale Islands, with separate subspecies on each island (Fig. 1, B and C). *N. acunhae* became extinct on the main island of Tristan about a century ago, after the introduction of mice and rats. A large-billed form was not known to occur on Tristan, despite the presence of *Phylica* trees. The other two islands have been little influenced by humans. We used morphological, ecological and genetic data to analyze speciation within *Nesospiza* (*25*).

The two species differ greatly in size on Nightingale Island (Fig. 2A), a relatively low-lying island (mostly <300 m) dominated by the tall tussock grass *Spartina arundinacea* and scattered *Phylica* trees (*26*) (Fig. 1A). Inaccessible Island is larger, with an extensive plateau 300 to 600 m above sea level. The coastal lowlands and cliffs support tussock grass and *Phylica* copses, but the plateau has two additional habitats (Fig. 1A). The lower, more sheltered eastern plateau supports *Phylica* woodland, whereas the higher, western plateau lacks *Phylica* trees and is dominated by *Blechnum palmiforme* heath (*26*). This greater diversity of habitat is accompanied by a greater variety of bunting phenotypes (*27*), but their size differences are smaller, with considerable overlap because of hybridization on the eastern plateau (Fig. 2A). Wilkins' (*dunnei*) and Tristan (*acunhae*) buntings co-occur in coastal tussock grass, but *N. w. dunnei* is largely absent from the western plateau whereas the eastern plateau supports a hybrid swarm of birds with bills ranging between large and small (*27*). In addition, "upland" Tristan buntings on the plateau have distinctly brighter plumage than drably colored "lowland" birds along the coast (*27*).

Bill depth in finches is directly correlated with the crushing force they can exert and thus the size of seeds they can exploit (*15*). Bill size in *Nesospiza* is highly heritable (*28*), with close correspondence between bill depth and seed availability in each habitat (Fig. 2B). Tussock grassland with scattered *Phylica* trees provides a bimodal distribution of seed sizes, favoring the evolution of two finch taxa. Segregation is complete on Nightingale Island. Each species has a distinctive song and defends territories only against conspecifics, and there is no evidence of hybridization (*27*). A similar situation occurs in the same coastal habitat on Inaccessible Island, although one mixed-species pair (<0.1% of all pairs) and occasional hybrids have been observed. On the western plateau, there are no *Phylica* fruit and hence few large-billed birds (Fig. 2B). Sedges predominate with smaller seeds than *Spartina* tussock grass, favoring the evolution of a smaller-billed bird (upland *acunhae*) than Tristan buntings found at the coast (lowland *acunhae*). The eastern plateau offers relatively low densities of sedge seeds and *Phylica* fruits (Fig. 2B); birds in this area consume more invertebrates than other populations (*29*). Large-billed birds predominate where *Phylica* fruit are abundant, with small-billed birds predominating where there are few fruit, even among adjacent territories (fig. S1). Hybrids have a different song from buntings elsewhere on the island (*29*), but mating is random with respect to phenotype at the ecotone (*25*).

The traditional allopatric model of speciation posits that the two species evolved in isolation, presumably on separate islands, with subsequent dispersal between islands to form local races (Fig. 1B). Alternatively, small- and large-billed forms could have evolved independently on each island (Fig. 1C). This model is supported by sequence data for the mitochondrial gene for cytochrome b (*25*) (fig. S2). There is near-complete lineage sorting by island, with monophyly relative to Gough buntings. Only one Tristan bunting from Nightingale had an allele shared with Inaccessible buntings (*25*), indicating migration or incomplete lineage sorting. This individual was larger than all other Tristan buntings caught on Nightingale, which suggests that it may have arrived from Inaccessible. On the basis of morphology, it was the only case of movement between the islands among 925 birds sampled.

Low levels of cytochrome b allelic diversity (0.536) relative to Darwin's finches (0.933), with comparable levels of nucleotide diversity (*Nesospiza*, 0.023; *Geospiza*, 0.011), are consistent with a small founder population (*25*) and thus provide low resolution. However, microsatellite data also support independent radiations on each island (Table 1 and Fig. 3) (*25*). Bayesian

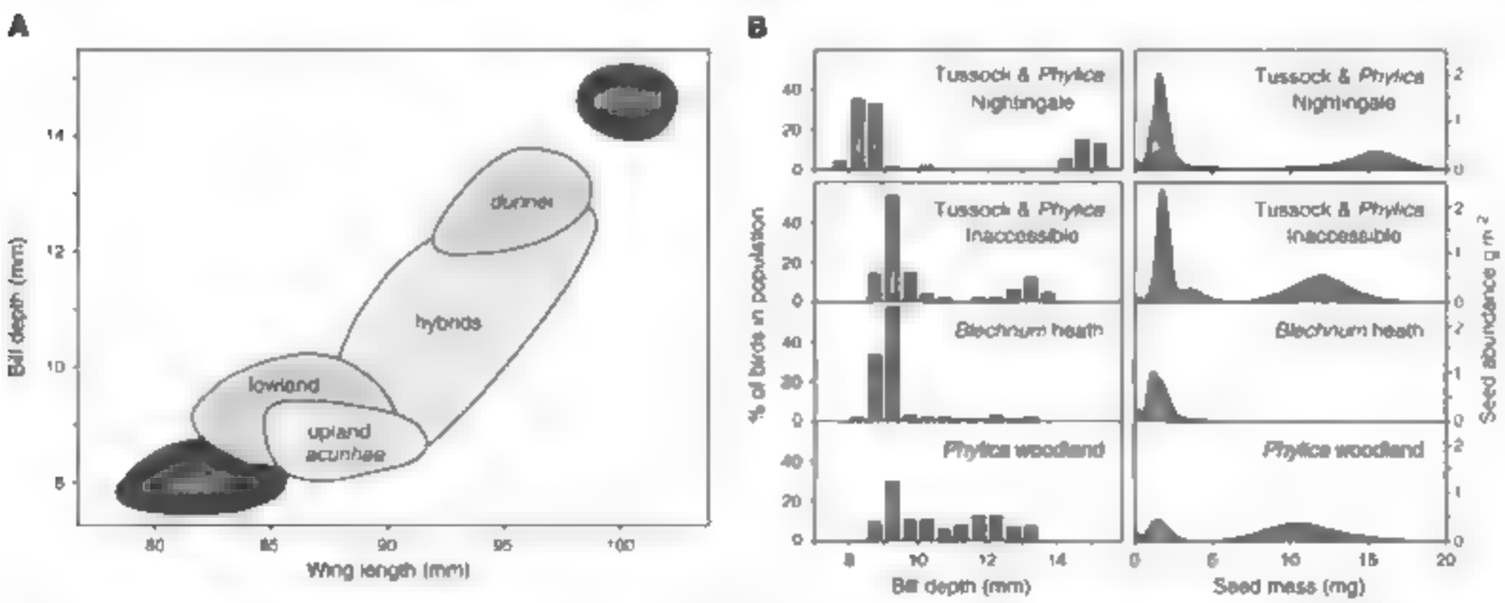

Fig. 2. Variation in male *Nesospiza* bill and body size (**A**) shows greater morphological segregation on Nightingale Island (*N. w. wilkinsi* and *N. a. questi*) than on Inaccessible Island (all other taxa), where hybridization occurs. Bill sizes closely match peaks in the abundance of seeds of different sizes on Nightingale Island and in each of the three main habitats on Inaccessible Island (**B**).

assignment tests without prior definition of populations identified five lineages when buntings from Tristan and Gough were analyzed together ($n = 4$ loci), discriminating Gough buntings from Tristan (*N. a. questi*) and Wilkins (*N. w. wilkinsi*) buntings on Nightingale Island (Fig. 3B). Buntings from Inaccessible were distinct from their counterparts on Nightingale Island but mutually showed little intraisland structure (Fig. 3B). However, three lineages emerged when they were analyzed separately for seven loci (Fig. 3C). These lineages are not completely sorted, but correspond to *N. w. dunnei* and the two color morphs of *N. a. acunhae*, with hybrids showing an even contribution from the three lineages (Fig. 3C and table S1). The lack of lineage sorting may result either from ongoing speciation or from an equilibrium between selection and recurrent hybridization.

Table 1. Pairwise *F* statistics between morphologically described taxa. All microsatellite (upper matrix, $P < 0.001$) and mtDNA (lower matrix, $P < 0.05$) pairwise *F* statistics indicated significant differentiation. Only nonzero mtDNA *F* statistics are shown. Dashes indicate no difference, blank spaces indicate self-comparisons.

Species	Inaccessible Island				Nightingale Island	
	1	2	3	4	5	6
1. Lowland *N. a. acunhae*		0.053	0.033	0.099	0.262	0.394
2. Upland *N. a. acunhae*	–		0.022	0.087	0.204	0.284
3. Hybrids	–	–		0.033	0.196	0.330
4. *N. w. dunnei*	–	–	–		0.202	0.413
5. *N. a. questi*	0.75	0.52	0.75	0.75		0.425
6. *N. w. wilkinsi*	1.00	0.80	1.00	1.00	–	

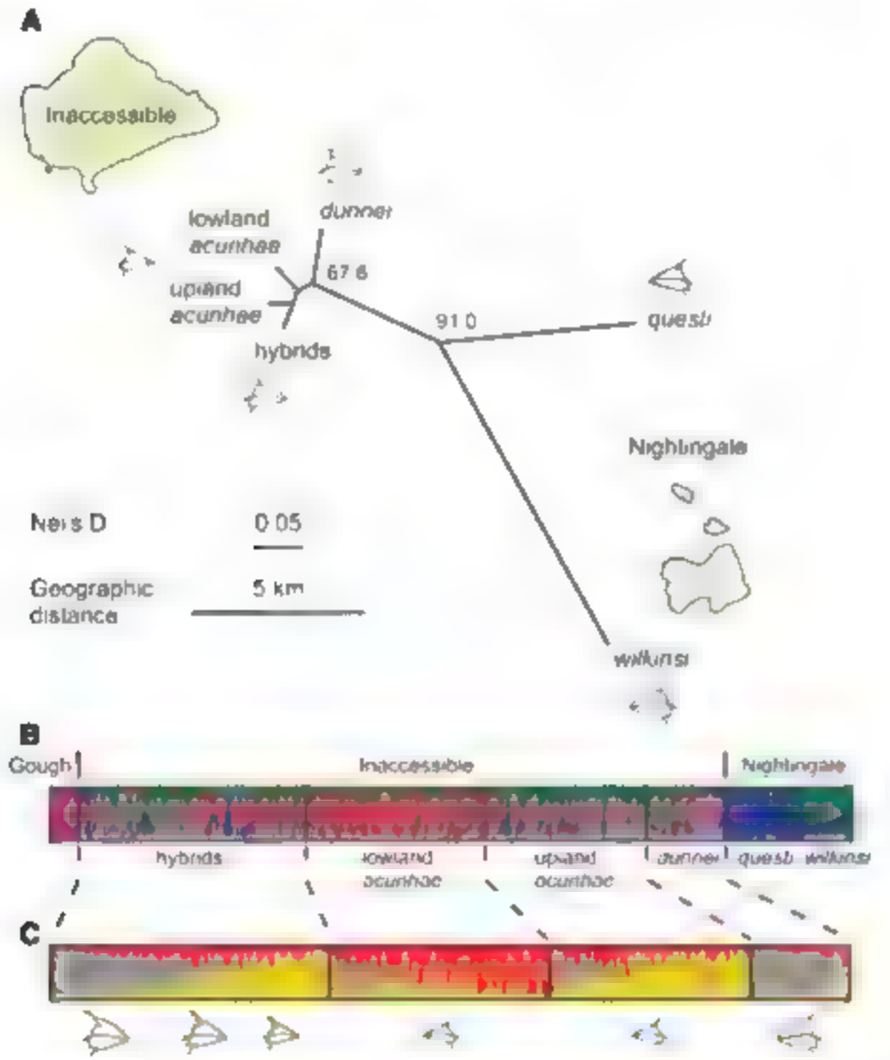

Fig. 3. Phylogeography of *Nesospiza* based on microsatellites. An unrooted dendrogram (**A**) shows clear genetic segregation between island populations (unweighted pair-group method with arithmetic mean based on Nei's unbiased genetic distance *D*). Bayesian assignment probabilities of individuals to lineages, where each vertical line represents an individual and colors indicate the proportion of an individual's genotype assigned to a particular lineage, show clear segregation between islands (**B**) but little structure on Inaccessible when all data are analyzed together (four loci). However, when birds from Inaccessible are analyzed separately (seven loci), there are frequency differences in the assignment of individuals to lineages between morphological taxa (**C**).

Independent radiations on Inaccessible and Nightingale Islands provide a parsimonious explanation for our data (Fig. 1C), especially the origin of three lineages linked to different habitats on Inaccessible Island. We cannot exclude the possibility that initial segregation occurred in allopatry, with genetic similarity between island populations resulting from subsequent hybridization. This would explain why taxa on each island have identical mitochondrial sequences but differ in microsatellites. However, this could result from a founder effect, with the diversity of biparentally inherited microsatellites recovering faster than maternally inherited mitochondrial DNA (mtDNA) because of elevated mutation rates and the reduced impact of a bottleneck on microsatellite allelic diversity. Adaptive sympatric speciation requires frequency-dependent disruptive selection and assortative mating (*4*, *5*). The former is promoted by the high density of buntings (up to 18 pairs ha^{-1} in tussock grassland) (*29*), which favors individuals that exploit novel niches. The latter is promoted by three factors. Juveniles recruit to areas close to their natal territories (*29*); plumage color is determined by diet, which varies with habitat (*27*); and vocal differences are linked to phenotype, with small birds having fast, high-pitched songs (*29*). Plumage color and song structure are both important cues in mate selection (*29*). Irrespective of whether segregation occurred initially in sympatry or allopatry, *Nesospiza* provides a compelling example of ecological speciation, because ecological processes appear to be responsible for the evolution and maintenance of morphological diversity, despite localized hybridization on Inaccessible Island.

References and Notes

1. J. A. Coyne, H. A. Orr, *Speciation* (Sinauer, Sunderland, MA, 2004).
2. S. Gavrilets, *Evol. Int. J. Org. Evol.* **57**, 2197 (2003).
3. E. Mayr, *The Growth of Biological Thought: Diversity, Evolution, and Inheritance* (Belknap, Cambridge, MA, 1982).
4. U. Dieckmann, M. Doebeli, J. A. J. Metz, D. Tautz, Eds., *Adaptive Speciation* (Cambridge Univ. Press, Cambridge, 2004).
5. R. Bürger, K. A. Schneider, *Am. Nat.* **167**, 190 (2006).
6. M. Kopp, J. Hermisson, *Evol. Int. J. Org. Evol.* **60**, 1537 (2006).
7. D. Schluter, *Trends Ecol. Evol.* **16**, 372 (2001).
8. K. Petren, P. R. Grant, B. R. Grant, L. F. Keller, *Mol. Ecol.* **14**, 2943 (2005).
9. J. Polechová, N. H. Barton, *Evol. Int. J. Org. Evol.* **59**, 1194 (2005).
10. M. Barluenga, K. N. Stölting, W. Salzburger, M. Muschick, A. Meyer, *Nature* **439**, 719 (2006).
11. S. Via, *Trends Ecol. Evol.* **16**, 381 (2001).
12. M. D. Sorenson, K. M. Sefc, R. B. Payne, *Nature* **424**, 928 (2003).
13. T. B. Smith, *Nature* **363**, 618 (1993).
14. T. B. Smith, S. Skúlason, *Annu. Rev. Ecol. Syst.* **27**, 111 (1996).
15. P. R. Grant, *Ecology and Evolution of Darwin's Finches* (Princeton Univ. Press, Princeton, NJ, 1999).

16. D. Lack, *Darwin's Finches* (Cambridge Univ. Press, Cambridge, 1947).
17. P. R. Grant, B. R. Grant, J. A. Markert, L. F. Keller, K. Petren, *Evol. Int. J. Org. Evol.* **58**, 1588 (2004).
18. P. R. Grant, B. R. Grant, K. Petren, *Am. Nat.* **166**, 56 (2005).
19. P. R. Grant, B. R. Grant, *Science* **313**, 224 (2006).
20. R. M. Zink, *Auk* **119**, 864 (2002).
21. I. Abbott, *J. Zool.* **184**, 119 (1978).
22. C. D. Ollier, *Z. Geomorphol.* **28**, 367 (1984).
23. R. C. Preece, K. D. Bennett, J. R. Carter, *J. Biogeogr.* **13**, 1 (1986).
24. K. J. Burns, S. J. Hackett, N. K. Klein, *Evol. Int. J. Org. Evol.* **56**, 1240 (2002).
25. See supporting material available on *Science* Online.
26. J. P. Rous, P. G. Ryan, S. J. Milton, C. L. Moloney, *Bothalia* **22**, 93 (1992).
27. P. G. Ryan, C. L. Moloney, J. Hudon, *Auk* **111**, 314 (1994).
28. P. G. Ryan, *Condor* **103**, 429 (2001).
29. P. G. Ryan, thesis, University of Cape Town, Cape Town, South Africa (1992).
30. The Administrator and Island Council of Tristan da Cunha gave permission to work at Inaccessible, C. Dorse, B. Watkins, Ovenstone Fishing, Tristan Natural Resources Department, and the South African Department of Environmental Affairs and Tourism gave field support. F. Joubert facilitated the use of a high-performance computing cluster (http://deepthought.bup.ac.za). The National Geographic Society, South African Department of Science and Technology, South African National Research Foundation, and University of Cape Town provided funding.

Supporting Online Material

www.sciencemag.org/cgi/content/full/315/5817/1420/DC1
Materials and Methods
SOM Text
Figs. S1 and S2
Tables S1 to S6
References

14 December 2006; accepted 25 January 2007
10.1126/science.1138829

Coupling Diurnal Cytosolic Ca^{2+} Oscillations to the CAS–IP_3 Pathway in *Arabidopsis*

Ru-Hang Tang,[1]* Shengcheng Han,[2]* Hailei Zheng,[2,3,4]* Charles W. Cook,[1] Christopher S. Choi,[1] Todd E. Woerner,[4] Robert B. Jackson,[1] Zhen-Ming Pei[1]†

Various signaling pathways rely on changes in cytosolic calcium ion concentration ($[Ca^{2+}]_i$). In plants, resting $[Ca^{2+}]_i$ oscillates diurnally. We show that in *Arabidopsis thaliana*, $[Ca^{2+}]_i$ oscillations are synchronized to extracellular Ca^{2+} concentration ($[Ca^{2+}]_o$) oscillations largely through the Ca^{2+}-sensing receptor CAS. CAS regulates concentrations of inositol 1,4,5-trisphosphate (IP_3), which in turn directs release of Ca^{2+} from internal stores. The oscillating amplitudes of $[Ca^{2+}]_o$ and $[Ca^{2+}]_i$ are controlled by soil Ca^{2+} concentrations and transpiration rates. The phase and period of oscillations are likely determined by stomatal conductance. Thus, the internal concentration of Ca^{2+} in plant cells is constantly being actively revised.

Organisms, from single-celled to multicellular, exploit the unique physical and chemical properties of the calcium ion to carry out essential biological functions. $[Ca^{2+}]_i$ increases transiently and/or repetitively in response to many abiotic and biotic stimuli (*1*–*3*) and also displays diurnal oscillations in animals and plants (*4*, *5*). In plants, the resting circadian $[Ca^{2+}]_i$ oscillations occur at the whole-tissue level (*6*), in contrast to those seen in specific neurons in animals (*4*, *7*), and are regulated by photoperiod and light intensity (*8*). This oscillating feature implies a robust regulatory machinery that synchronizes $[Ca^{2+}]_i$ throughout the plant. However, due to the lack of the knowledge of sensory receptors and Ca^{2+} channels (*2*, *5*, *9*), the underlying mechanisms for the resting $[Ca^{2+}]_i$ and its oscillations remain largely unknown.

We have cloned a receptor for external Ca^{2+} (Ca^{2+}_o), CAS, from *Arabidopsis* (*10*). CAS is expressed in the shoot, localizes to the plasma membrane, binds to Ca^{2+}, and mediates Ca^{2+}_o-induced $[Ca^{2+}]_i$ increases (CICI) in stomatal guard cells. We have generated *CAS* antisense lines (*CASas*) and shown that its mRNA and protein levels are reduced and that CICI is abolished (*10*). Identification of CAS and genetic manipulation of its activity may provide a powerful tool to dissect the mechanisms controlling $[Ca^{2+}]_i$ oscillations. We hypothesized not only that Ca^{2+}_o serves as a signal triggering $[Ca^{2+}]_i$ increases, but also that Ca^{2+}_o and CAS control the resting $[Ca^{2+}]_i$. To test this hypothesis, we measured the resting $[Ca^{2+}]_i$ using aequorin bioluminescence–based Ca^{2+} imaging (*6*, *8*, *11*) and found that the resting $[Ca^{2+}]_i$ was lower in *CASas* than in wild-type plants (Fig. 1A).

Next, we asked whether $[Ca^{2+}]_i$ oscillations were affected in *CASas*. Biological oscillations can be described by three parameters: amplitude, phase, and period (*12*). Quantitative analyses of leaf aequorin luminescence showed that the amplitudes of $[Ca^{2+}]_i$ oscillations were reduced in *CASas* throughout a long day (Fig. 1B; $P < 0.001$). The average resting $[Ca^{2+}]_i$ and absolute amplitude (peak − trough) were reduced by 46.0 ± 2.3% and 50.2 ± 3.5% ($P < 0.001$), respectively. However, the phase and period were not altered in *CASas* ($P > 0.1$), indicating that CAS is required for maintaining appropriate oscillating amplitudes. Similar results were seen in three *CASas* lines, *CASas1* to *CASas3* (*10*).

The reduced luminescence in *CASas* was not due to low abundance of cytosolic aequorin. Aequorin-expressing *CASas* lines were generated from a cross between *CASas* and a wild-type line carrying the *35S.aequorin* construct. The stability of aequorin expression in wild-type plants was confirmed for eight generations. The *CASas* and wild-type lines had similar aequorin protein levels (fig. S1A), which remained stable throughout a long day (fig. S1B). Finally, the maximum luminescence was identical in both genotypes, as estimated by discharging excess Ca^{2+}.

Our data prompted us to investigate how $[Ca^{2+}]_i$ is regulated. Ca^{2+} is dissolved in water in the apoplast (extracellular spaces) and transported primarily from the root to the shoot through the transpiration stream (*13*, *14*). The transpiration rate is governed by stomatal conductance, which displays diurnal oscillations (*15*). We reasoned that $[Ca^{2+}]_i$ is synchronized to stomatal-conductance oscillations, and $[Ca^{2+}]_i$ oscillations are perceived by CAS and converted into $[Ca^{2+}]_i$ oscillations. Thus, the soil Ca^{2+}–signaling cascade would be as follows: soil Ca^{2+} → Ca^{2+} uptake and transport → Ca^{2+}_o oscillations → CAS → $[Ca^{2+}]_i$ oscillations.

To test this hypothesis, we analyzed whether media Ca^{2+} affects $[Ca^{2+}]_i$. In wild-type plants, $[Ca^{2+}]_i$ was elevated with increases in media Ca^{2+}, whereas in *CASas* this response was reduced (Fig. 1C; $P < 0.001$). We monitored $[Ca^{2+}]_i$ oscillations in plants grown under physiological (1 mM) and elevated (30 mM) Ca^{2+} concentrations. The overall amplitudes of $[Ca^{2+}]_i$ were elevated in both wild-type and *CASas* plants with increases in media Ca^{2+}, but much more so in the wild type, although the phases were not altered (Fig. 1D).

We assessed how media Ca^{2+} regulates $[Ca^{2+}]_o$ and whether $[Ca^{2+}]_o$ oscillates. We monitored $[Ca^{2+}]_o$ directly by expressing aequorin in the apoplast as described previously (*16*). We found that $[Ca^{2+}]_o$ also displayed diurnal oscillations, which were similar in wild-type and *CASas* plants (Fig. 2A). Ca^{2+}_o increased with increases in media Ca^{2+}, and both genotypes showed virtually identical responses (Fig. 2B). To ensure equivalent activity of apoplastic aequorin in both genotypes, we measured extracellular aequorin under conditions similar to those for cytosolic aequorin (*17*). The aequorin protein abundance was similar in wild-type and *CASas* plants (fig. S2).

[1]Department of Biology, Duke University, Durham, NC 27708, USA. [2]Department of Biology, Xiamen University, Xiamen, Fujian 361005, China. [3]State Key Laboratory of Marine Environmental Science, Xiamen University, Xiamen, Fujian 361005, China. [4]Department of Chemistry, Duke University, Durham, NC 27708, USA.

*These authors contributed equally to this work.
†To whom correspondence should be addressed. E-mail: zpei@duke.edu

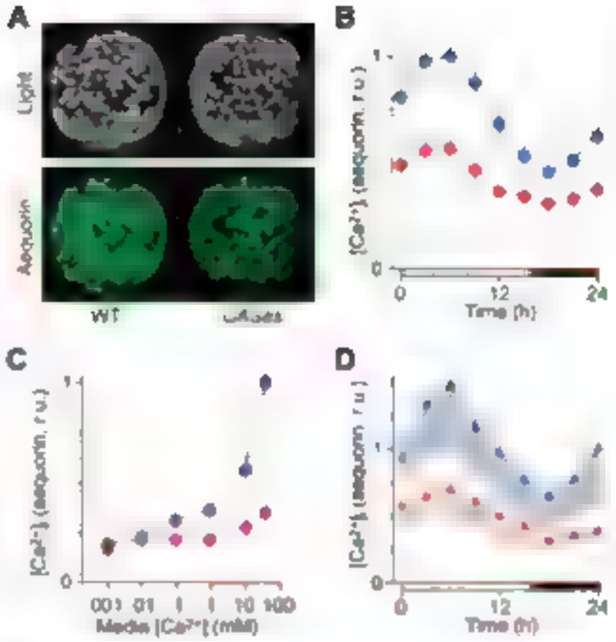

Fig. 1. Media Ca^{2+} and CAS control diurnal $[Ca^{2+}]_i$ oscillations. Blue, WT; red, *CASos*. (**A**) Imaging the resting $[Ca^{2+}]_i$ in *Arabidopsis* wild-type (WT) and *CAS* antisense (*CASos*). The bright light-field and aequorin luminescence images were taken at 8 hours after dawn from plants grown on ½ MS media under long-day conditions. (**B**) $[Ca^{2+}]_i$ oscillations in leaves. The aequorin luminescence images were taken from plants as in (A) every 3 hours starting from dawn. The luminescence was normalized to that discharged with excessive Ca^{2+}, and the maximum value was arbitrarily set to 1. The white and black bars represent objective light on and off, respectively. r.u., relative unit. Data from five separate experiments are shown [mean ± SD; $n = 150$ plants; two-way analysis of variance (ANOVA), $P < 0.001$]. (**C**) The effect of media Ca^{2+} on $[Ca^{2+}]_i$. Plants were grown on agar media containing varied $[Ca^{2+}]$ under long-day conditions for 2 to 3 weeks. Aequorin luminescence images were taken as in (B). Data from three experiments are shown (mean ± SD; $n = 120$ plants; two-way ANOVA, $P < 0.001$). (**D**) $[Ca^{2+}]_i$ oscillations in plants grown in 1 mM (solid lines) or 30 mM Ca^{2+} (triangles) (mean ± SD; $n = 120$ plants, two-way ANOVA, $P < 0.001$)

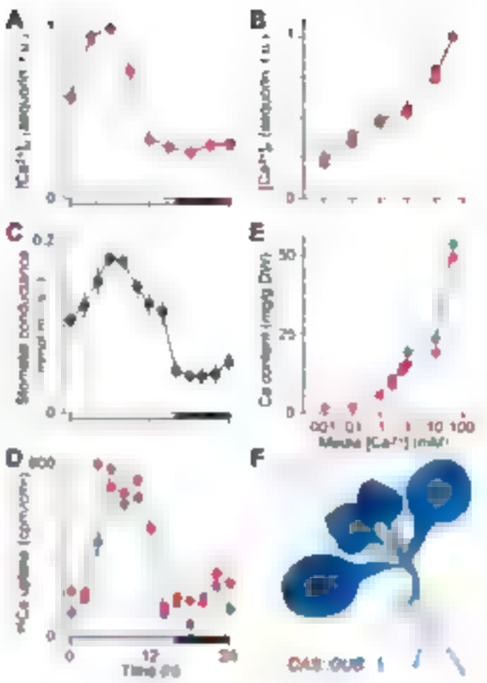

Fig. 2. Media Ca^{2+} and stomatal conductance control diurnal $[Ca^{2+}]_i$ oscillations. Blue, WT; red, *CASos*. (**A**) $[Ca^{2+}]_i$ oscillations in leaves. The luminescence images were taken every 3 hours, starting at dawn from plants expressing apoplastic aequorin grown on ½ MS. The luminescence was normalized to that discharged with excessive Ca^{2+}, and the maximum value was set to 1. Data from three separate experiments are shown (mean ± SD; $n = 75$ plants; two-way ANOVA, $P > 0.5$). (**B**) The effect of media Ca^{2+} on the resting $[Ca^{2+}]_i$. Luminescence images were taken as in Fig. 1C. The other conditions were the same as in (A). Data are shown as the mean ± SD ($n = 75$ plants; two-way ANOVA, $P > 0.5$). (**C**) WT plants were grown in soil for 3 weeks under long-day conditions, and stomatal conductance was monitored (mean ± SEM; $n = 3$). (**D**) ^{45}Ca uptake measured over a long day. ^{45}Ca was added to the growth solution at dawn. Shoots were collected every 2 hours for 2 days, and ^{45}Ca radioactivity was measured (*17*). The data for the second day are shown. cpm/cm^2 counts per minute/leaf area (cm^2). (**E**) The effect of media Ca^{2+} on the shoot Ca content in plants grown under conditions as in Fig. 1C. mg/g DW, milligrams Ca per gram dry weight (mean ± SD; $n = 15$ to 25 plants; two-way ANOVA, $P > 0.5$). (**F**) The analysis of *CAS promoter:GUS* reporter (*17*).

Finally, we determined whether stomatal-conductance oscillations are correlated with Ca^{2+} uptake and transport, $[Ca^{2+}]_o$ oscillations, and Ca^{2+} oscillations. As expected, the stomatal conductance of wild-type plants was high in the day and low at night (Fig. 2C). We also found that wild-type and *CASos* plants displayed similar diurnal oscillations in ^{45}Ca uptake and transport (Fig. 2D). These experiments confirmed previous reports that Ca^{2+} uptake and transport to leaves are controlled mainly by transpiration that is regulated by stomatal conductance (*13*, *14*). The shoot Ca content of seedlings grown at various concentrations of media Ca^{2+} was similar between wild-type and *CASos* plants (Fig. 2E). Thus, the reduced $[Ca^{2+}]_i$ oscillations in *CASos* were due not to reduced Ca content, but rather to a defect in Ca^{2+}_o sensing.

It appears that the phases and periods of oscillations in stomatal conductance, ^{45}Ca uptake, $[Ca^{2+}]_o$, and $[Ca^{2+}]_i$ were well correlated. CAS seems to control the amplitude of $[Ca^{2+}]_i$ oscillations, but not Ca uptake or $[Ca^{2+}]_o$ oscillations. Media Ca^{2+} concentration regulates the oscillating amplitudes of both $[Ca^{2+}]_o$ and $[Ca^{2+}]_i$. In addition, the expression patterns of CAS, noticeably in mesophyll cells and vascular tissues in the shoot (Fig. 2F), fit well with the route of Ca^{2+} transport and distribution in the shoot (*17*), supporting the function proposed for CAS.

Next, we asked how CAS couples $[Ca^{2+}]_i$ with $[Ca^{2+}]_o$, i.e., whether CAS mediates Ca^{2+} influx or release from internal stores. In animals, although diurnal $[Ca^{2+}]_i$ oscillations at the whole-tissue level have not been observed (*4*–*7*), fast $[Ca^{2+}]_i$ spiking at the cellular level has been well studied (*1*). External signals are perceived by cell-surface receptors, which activate phospholipase C (PLC), increasing inositol 1,4,5-trisphosphate (IP_3) concentration. IP_3 activates IP_3 receptors (IP_3Rs) in the endoplasmic reticulum (ER), resulting in Ca^{2+} release. Then Ca^{2+} ions are reabsorbed by the ER, leading to $[Ca^{2+}]_i$ oscillations. In plants, although cell-surface receptors and IP_3Rs are unknown (*18*), it is possible that CAS might serve as a receptor triggering Ca^{2+} release. To explore this possibility, we investigated the function of CAS as CICI in a heterologous system as well as in planta.

CAS confers CICI in human embryonic kidney 293 (HEK293) cells (*10*). We observed that the CAS green fluorescent protein (GFP) was localized in the vicinity of the plasma membrane in HEK293 cells (Fig. 3A), consistent with the subcellular localization in plants (*10*). We found that Ca^{2+}_o triggered IP_3 production in CAS-expressing HEK293 cells (Fig. 3B). The PLC blockers, neomycin and U-73122, inhibited CICI (Fig. 3C). These results indicate that CAS can function as a receptor in the IP_3 pathway in HEK293 cells.

Next, we assessed whether CAS also serves as a receptor in the putative IP_3 pathway in *Arabidopsis*. In plants, some of the components seen in the animal IP_3 pathways have been identified (*17*, *18*). For instance, increases in IP_3 have been detected in response to several stimuli, which enhance the activities of PLCs. High-affinity IP_3 binding sites in internal membranes have been detected, although it is not clear whether plants have IP_3Rs. IP_3 can also trigger Ca^{2+} release from internal stores. Nonetheless, the molecular nature of corresponding cell-surface receptors remains obscure.

We found that neomycin abolished CICI in *Arabidopsis* guard cells (Fig. 3D). Similarly, we observed CICI in mesophyll cells and also detected CICI in intact leaves using aequorin imaging, which suggests that CICI occurs in cells other than guard cells and at the whole-leaf level. To analyze further whether IP_3 participates in CICI, we measured the IP_3 content of leaves. Ca^{2+}_o induced IP_3 generation (Fig. 3E, $P < 0.01$), and neomycin eliminated the IP_3 production (Fig. 3F, $P > 0.5$). Together, these results suggest that Ca^{2+}_o may evoke the IP_3 pathway in *Arabidopsis*.

To verify Ca^{2+}_o-induced IP_3 production, we carried out single-cell imaging of IP_3. The com-

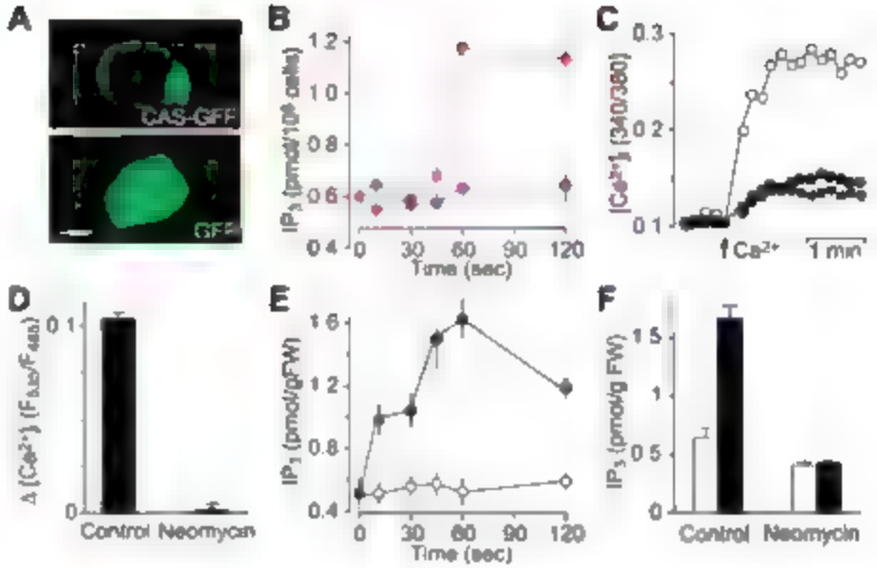

Fig. 3. CAS is a cell-surface receptor in the IP_3 pathway. (**A**) Plasma membrane localization of CAS in HEK293 cells expressing a *CAS-GFP* construct (upper) with GFP as a control (lower). Scale bar, 5 μm. (**B**) The effect of $Ca^{2+}{}_o$ on IP_3 generation in HEK293 cells expressing *CAS* (red). The control (blue) was cells transfected with empty vector. Cells were bathed in 0.1 mM Ca^{2+} before addition of 2.5 mM Ca^{2+} and harvested at the times indicated. The IP_3 content was determined by [^{3}H]IP_3 radioreceptor assay (*17*) (mean ± SEM; $n = 6$). (**C**) Inhibition of ClCl by PLC blockers in HEK293 cells expressing *CAS*. Cells were incubated with 0.1 mM Ca^{2+} without (white circles) or with 100 μM neomycin (black circles) or U-73122 (black squares) before Ca^{2+} stimulation. Ca^{2+} at 2.5 mM was added at the time indicated (arrow), and $[Ca^{2+}]_i$ was monitored by Fura-2 imaging (*17*). (**D**) Inhibition of ClCl by neomycin in guard cells. Epidermal peels carrying the Ca^{2+}-indicator cameleon were incubated in solution containing 50 μM Ca^{2+} for 2 hours, and then treated with 2.5 mM Ca^{2+} (*10*). Neomycin (100 μM) was added 15 min before addition of Ca^{2+}. $[Ca^{2+}]_i$ is shown as changes in emission fluorescence ratios ($\Delta[Ca^{2+}]_i$; $n = 15$ cells; $P < 0.001$). (**E**) $Ca^{2+}{}_o$ induces IP_3 generation in *Arabidopsis* leaves. Leaves were incubated in the solution containing 50 μM Ca^{2+} for 2 hours, then transferred to the same solution (white circles) or the solution containing 10 mM Ca^{2+} (black circles), and harvested at the times indicated. IP_3 was determined by [^{3}H]IP_3 assay (mean ± SEM, $n = 6$). (**F**) Neomycin inhibits $Ca^{2+}{}_o$-induced IP_3 generation in leaves. The samples were collected before addition of Ca^{2+} (white bars) or 60 s after addition of 10 mM Ca^{2+} (black bars). Neomycin (100 μM) was added 15 min before Ca^{2+} stimulation (mean ± SEM, $n = 6$). pmol/gFW, picomole per gram fresh weight.

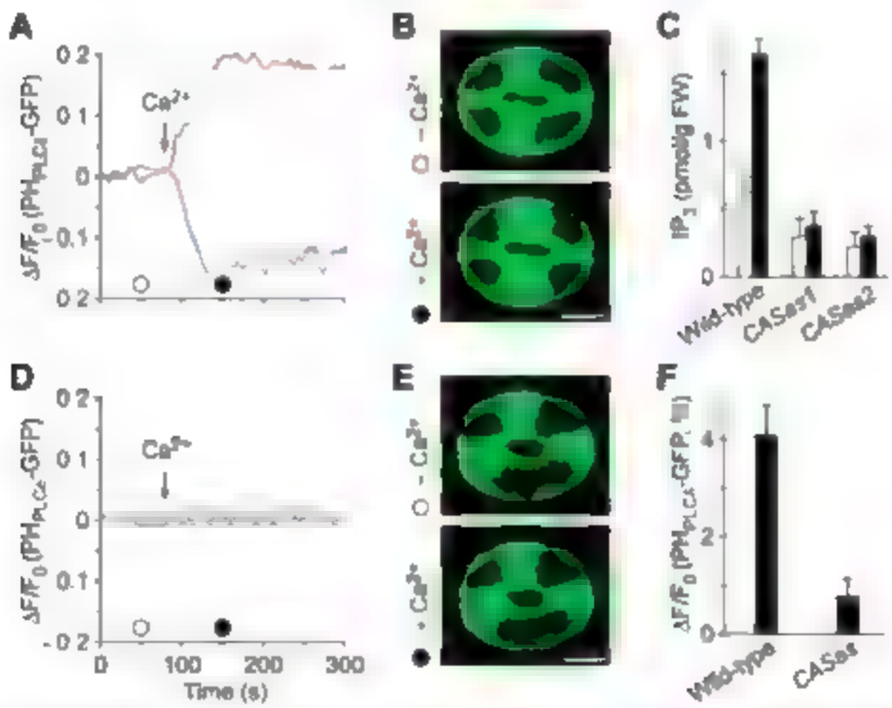

Fig. 4. CAS is required for the $Ca^{2+}{}_o$-evoked IP_3 pathway. (**A** and **B**) $Ca^{2+}{}_o$-induced IP_3 production in single WT guard cells. The leaf epidermis was incubated with 50 μM Ca^{2+} and treated with 10 mM Ca^{2+}. $Ca^{2+}{}_o$-triggered $PH_{PLC\delta}$-*GFP* translocation from the plasma membrane (blue) to the cytosol (red). The images in (B) correspond to before (○) and after (●) Ca^{2+} stimulation in (A). (**C**) IP_3 content in WT and *CASas* leaves with (black bars) and without (white bars) addition of 10 mM Ca^{2+} (mean ± SEM; $n = 6$. $P < 0.02$ for WT; $P > 0.5$ for *CASas1* and *CASas2*). (**D** and **E**) Defect in $Ca^{2+}{}_o$-induced IP_3 generation in *CASas* guard cells. The *CASas* line expressing $PH_{PLC\delta}$-*GFP* was generated from a cross between *CASas* and the wild-type $PH_{PLC\delta}$-*GFP* line as in (A). (**F**) Increases in $PH_{PLC\delta}$-GFP fluorescence in the cytosol with addition of Ca^{2+} were analyzed from experiments as in (A) and (D). Thirty-eight out of 133 guard cells (28.6%) for the wild type (A) and 4 out of 76 (5.3%) for *CASas* (E) showed increases. Data are shown as the mean ± SEM ($P < 0.001$). Scale bars, 5 μm.

monly used biosensor for IP_3 is the PLC-δ1 pleckstrin homology domain fused to GFP ($PH_{PLC\delta}$-GFP), which binds phosphatidylinositol-4,5-bisphosphate (PIP_2) and IP_3 (*19*, *20*). Without stimulation, $PH_{PLC\delta}$-GFP is located mainly at the plasma membrane, whereas upon PIP_2 hydrolysis and formation of IP_3, $PH_{PLC\delta}$-GFP binds to IP_3, dissociates from the membrane and translocates to the cytosol. This translocation can be used as an indicator of IP_3 (*21*, *23*). We generated *Arabidopsis* lines expressing 35S *$PH_{PLC\delta}$-GFP* and observed that $PH_{PLC\delta}$-GFP was localized primarily to the plasma membrane (fig. S3). Ca^{2+} triggered a reduction of $PH_{PLC\delta}$-GFP fluorescence in the plasma membrane but an elevation in the cytosol (Fig. 4, A and B), indicating an increase in IP_3 concentration.

To substantiate whether CAS is involved in the IP_3 pathway, we analyzed $Ca^{2+}{}_o$-induced IP_3 production in *CASas*. Both biochemical and single-cell imaging analyses showed that *CASas* was impaired in $Ca^{2+}{}_o$-induced IP_3 production (Fig. 4, C to F). These results suggest that CAS may act as a receptor in the IP_3 pathway, although CAS differs from its animal counterparts, the G protein–coupled receptors and receptor tyrosine kinases (*1*, *17*). Note that, because plant PLCs contain Ca^{2+} binding motifs and are activated by Ca^{2+} (*24*), it is also possible that PLCs are activated by stimulus-triggered $[Ca^{2+}]_i$ increases rather than by cell-surface receptors. Characterization of the relation between CAS and PLCs will allow us to address this possibility.

We have revealed that $[Ca^{2+}]_i$ oscillations are coupled to the $[Ca^{2+}]_o$ oscillations. CAS IP_3 pathway. Our data, together with previous studies, may explain how $[Ca^{2+}]_i$ oscillations are determined: the amplitude by the soil Ca^{2+} level and stomatal conductance, and the phase and period largely by stomatal-conductance oscillations. We can simulate $[Ca^{2+}]_i$ oscillations using a schematic model (fig. S4). First, CAS and a Ca^{2+}-influx channel, such as guard cell ICa (*25*), perceive $[Ca^{2+}]_o$ and convert it into $[Ca^{2+}]_i$. Second, $[Ca^{2+}]_o$ oscillates. The $[Ca^{2+}]_o$ is determined by two opposite processes: supplying fresh Ca^{2+} to the apoplast and sequestrating it into stores. For the sequestration, fresh Ca^{2+} ions bind

to newly synthesized cell-wall components, form Ca^{2+} oxalate, or move into internal stores (*13, 14*). Most sequestrated Ca^{2+} ions become immobile, and thus continuous Ca^{2+} supplies are needed and likely to be the regulated step. Third, the stomatal-conductance oscillations are regulated by photoperiod and the clock (*15*). Finally, soil Ca^{2+} is the primary source controlling the amplitudes of $[Ca^{2+}]_i$ oscillations. Our findings may also revise further the concept of resting $[Ca^{2+}]_i$ in plants. The constant remodeling includes oscillations at the basal concentration of ~0.1 μM (*6*), similar to those in specific neurons (*4, 7*), and shifts of this level according to soil Ca^{2+} status and CAS activity. Clearly, transpiration-mediated soil Ca^{2+} uptake and transport synchronize the resting $[Ca^{2+}]_i$ throughout the plant. Because the transpiration rate is regulated by numerous factors (*26*) and because soil Ca^{2+} levels can fluctuate throughout the year in nature (*27*), this soil Ca^{2+}-CAS-IP_3 pathway may be physiologically relevant (*7*).

References and Notes

1. M. J. Berridge, M. D. Bootman, H. L. Roderick, *Nat. Rev. Mol. Cell Biol.* **4**, 517 (2003).
2. A. M. Hetherington, C. Brownlee, *Annu. Rev. Plant Biol.* **55**, 401 (2004).
3. H. Knight, M. R. Knight, *Trends Plant Sci.* **6**, 262 (2001).
4. C. S. Colwell, *Eur. J. Neurosci.* **12**, 571 (2000).
5. A. N. Dodd, J. Love, A. A. Webb, *Trends Plant Sci.* **10**, 15 (2005).
6. C. H. Johnson *et al.*, *Science* **269**, 1863 (1995).
7. M. Ikeda *et al.*, *Neuron* **38**, 253 (2003).
8. J. Love, A. N. Dodd, A. A. Webb, *Plant Cell* **16**, 956 (2004).
9. D. Sanders, J. Pelloux, C. Brownlee, J. F. Harper, *Plant Cell* **14**, S401 (2002).
10. S. Han, R. Tang, L. K. Anderson, T. E. Woerner, Z.-M. Pei, *Nature* **425**, 196 (2003).
11. M. R. Knight, A. K. Campbell, S. M. Smith, A. J. Trewavas, *Nature* **352**, 524 (1991).
12. C. R. McClung, *Plant Cell* **18**, 792 (2006).
13. P. K. Hepler, *Plant Cell* **17**, 2142 (2005).
14. P. J. White, M. R. Broadley, *Ann. Bot. (London)* **92**, 487 (2003).
15. A. A. R. Webb, *New Phytol.* **160**, 281 (2003).
16. D. Gao, M. R. Knight, A. J. Trewavas, B. Sattelmacher, C. Plieth, *Plant Physiol.* **134**, 898 (2004).
17. Materials and methods are available as supporting material on *Science* Online.
18. H. J. G. Meijer, T. Munnik, *Annu. Rev. Plant Biol.* **54**, 265 (2003).
19. T. P. Stauffer, S. Ahn, T. Meyer, *Curr. Biol.* **8**, 343 (1998).
20. P. Varnai, T. Balla, *J. Cell Biol.* **143**, 501 (1998).
21. K. Hirose, S. Kadowaki, M. Tanabe, H. Takeshima, M. Iino, *Science* **284**, 1527 (1999).
22. M. S. Nash, K. W. Young, R. A. Challiss, S. R. Nahorski, *Nature* **413**, 381 (2001).
23. P. J. Bartlett, K. W. Young, S. R. Nahorski, R. A. Challiss, *J. Biol. Chem.* **280**, 21837 (2005).
24. B. Mueller-Roeber, C. Pical, *Plant Physiol.* **130**, 22 (2002).
25. Z.-M. Pei *et al.*, *Nature* **406**, 731 (2000).
26. J. I. Schroeder, J. M. Kwak, G. J. Allen, *Nature* **410**, 327 (2001).
27. S. B. McLaughlin, R. Wimmer, *New Phytol.* **142**, 373 (1999).

28. We thank E. Johannes and N. Allen for $PH_{PLC\delta}$-GFP analysis, M. Knight and C. Plieth for aequorin-expressing seeds and vectors, M. Iino for the *$PH_{PLC\delta}$-GFP* clone, A. Webb, M. Knight, C. Plieth, and C. Johnson for advice concerning aequorin imaging; D. Hu for ANOVA analyses; C. Lin and X. Yu for discussions; and J. Siedow, T.-p. Sun, P. Benfey, and X. Dong for supporting ChemiPro system and reading the manuscript. R.-H.T. was supported by a Hargitt fellowship, H.Z. by Xiamen University (NCET-XMU) and the Chinese Scholar Council, and C.W.C. by the Andrew Mellon Foundation. This work was supported by grants from the NSF (MCB 0451072) and U.S. Department of Agriculture (CSREES 2005-35304-16196) and by a Zhu Chongshi Presidential Award from Xiamen University (to Z.-M.P.).

Supporting Online Material
www.sciencemag.org/cgi/content/full/315/5817/1423/DC1
Materials and Methods
SOM Text
Figs. S1 to S4
References

29 August 2006; accepted 5 February 2007
10.1126/science.1134457

Odor Cues During Slow-Wave Sleep Prompt Declarative Memory Consolidation

Björn Rasch,[1*] Christian Büchel,[2] Steffen Gais,[1] Jan Born[1*]

Sleep facilitates memory consolidation. A widely held model assumes that this is because newly encoded memories undergo covert reactivation during sleep. We cued new memories in humans during sleep by presenting an odor that had been presented as context during prior learning, and so showed that reactivation indeed causes memory consolidation during sleep. Re-exposure to the odor during slow-wave sleep (SWS) improved the retention of hippocampus-dependent declarative memories but not of hippocampus-independent procedural memories. Odor re-exposure was ineffective during rapid eye movement sleep or wakefulness or when the odor had been omitted during prior learning. Concurring with these findings, functional magnetic resonance imaging revealed significant hippocampal activation in response to odor re-exposure during SWS.

Sleep facilitates the consolidation of newly acquired memories for long-term storage (*1–3*). The prevailing model assumes that this consolidation relies on a covert reactivation of the novel neuronal memory representations during sleep after learning (*3–6*). In rats, hippocampal neuronal assemblies implicated in the encoding of spatial information during maze learning are reactivated in the same temporal order during slow-wave sleep (SWS) as during previous learning (*7, 8*). The consolidation of hippocampus-dependent memories benefits particularly from SWS (*9–11*), and reactivation of the hippocampus in SWS after spatial learning has also been seen in humans observed with positron emission tomography (*12*). However, none of these studies experimentally manipulated memory reactivation during sleep. Therefore, its causal role in memory consolidation is still unproven.

We used an odor to reactivate memories in humans during sleep, because odors are well known for their high potency as contextual retrieval cues not only for autobiographic memories, as delicately described in Marcel Proust's *Remembrance of Things Past*, but also for various other types of memory, including visuospatial memories (*13, 14*). Notably, in the brain, primary olfactory processing areas bypassing the thalamus project directly to higher-order regions, including the hippocampus (*15*), which enables them to modulate hippocampus-dependent declarative memories (*16*). The use of olfactory stimuli for cueing memories during sleep is particularly advantageous because odors, in contrast to other stimuli, can be presented without disturbing ongoing sleep (*17*).

To establish a robust association between learning stimuli and a smell, we applied a purely olfactory stimulus (the smell of a rose) (*18*) repetitively while volunteers (n = 18) learned object locations in a two-dimensional (2D) object-location memory task in the evening before sleep. During the first two periods of subsequent SWS, the odor was presented again (in an alternating 30 s on/30 s off mode). In a control condition, odorless vehicle was delivered. The object-location task required visually learning the locations of 15 card pairs on a computer screen to a criterion of 60% correct responses (Fig. 1A). The task is sensitive to the memory-improving effect of sleep (*18*) and involves hippocampal function (*19*).

At retrieval testing after sleep, memory of the card locations was distinctly enhanced when the odor had been presented during SWS as compared to presentation of the vehicle alone. After the odor night, participants remembered 97.2 ± 4.1% of the card pairs they had learned before sleep, but they remembered only 85.8 ± 3.8% after the vehicle night (P = 0.001, Fig. 2A,

[1]Department of Neuroendocrinology, University of Lübeck, Ratzeburger Allee 160/23a, 23538 Lübeck, Germany. [2]NeuroImage Nord, Department of Systems Neuroscience, University Medical Center Hamburg-Eppendorf, Martinistrasse 52, 20246 Hamburg, Germany.

*To whom correspondence should be addressed. E-mail: born@kfg.uni-luebeck.de (J.B.); rasch@kfg.uni-luebeck.de (B.R.)

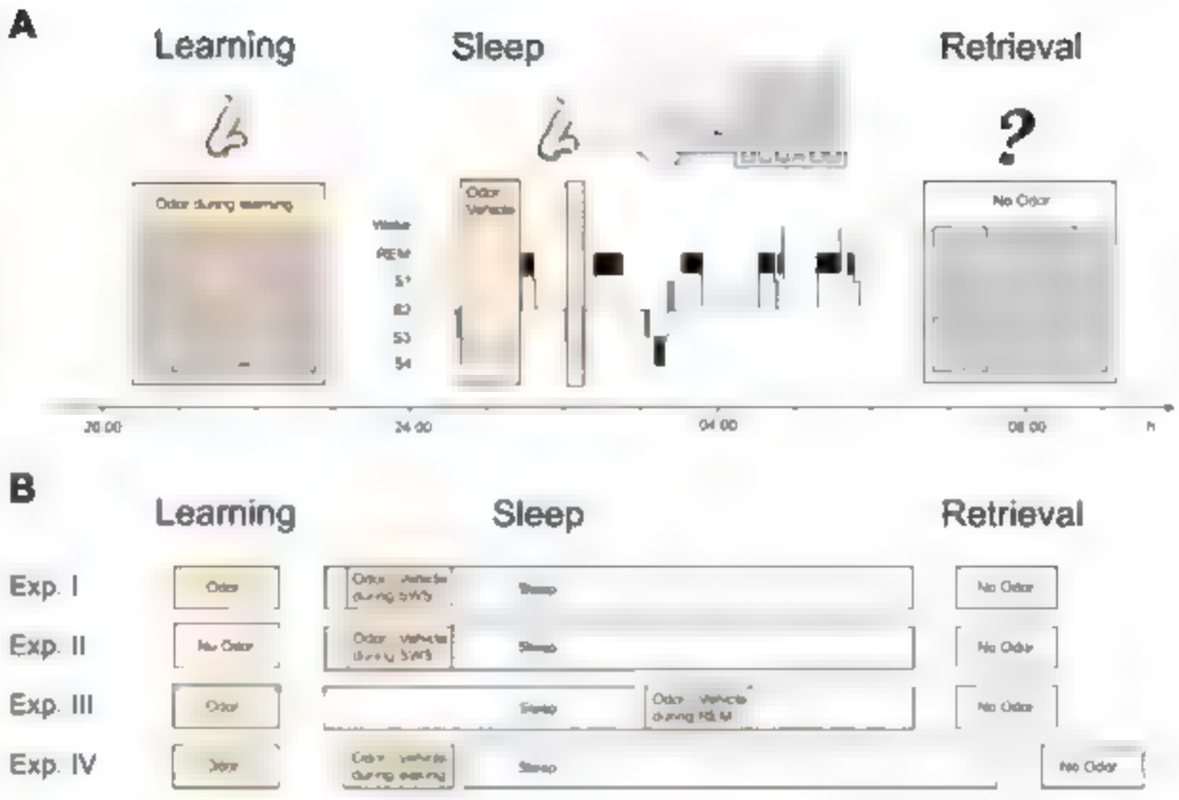

Fig. 1. (**A**) Volunteers learned a visuospatial 2D object-location task (and a procedural finger-tapping task, not illustrated) between 21:30 and 22:30 hours (Learning). The odor was administered time-locked to the learning stimuli. During subsequent sleep (lights off at 23:00 hours, awakening at 6:30 hours), the same odor (versus vehicle) was delivered during the first two periods of SWS in an alternating 30 s on/30 s off mode (to prevent habituation). Stimulation started with the first occurrence of SWS and was interrupted whenever the sleep stage changed. Retrieval was tested between 7:00 and 7:30 hours in the absence of odor (*18*). (**B**) Experiments I and II were identical except that in experiment I, the odor was presented at learning and again contingent upon SWS, whereas in experiment II, the odor was not presented at learning. In experiment III, the odor was presented at learning and again during post-learning REM sleep. In experiment IV, the odor was presented at learning, but post-learning re-exposure took place while participants were awake. Experiments were conducted according to a double-blind crossover design.

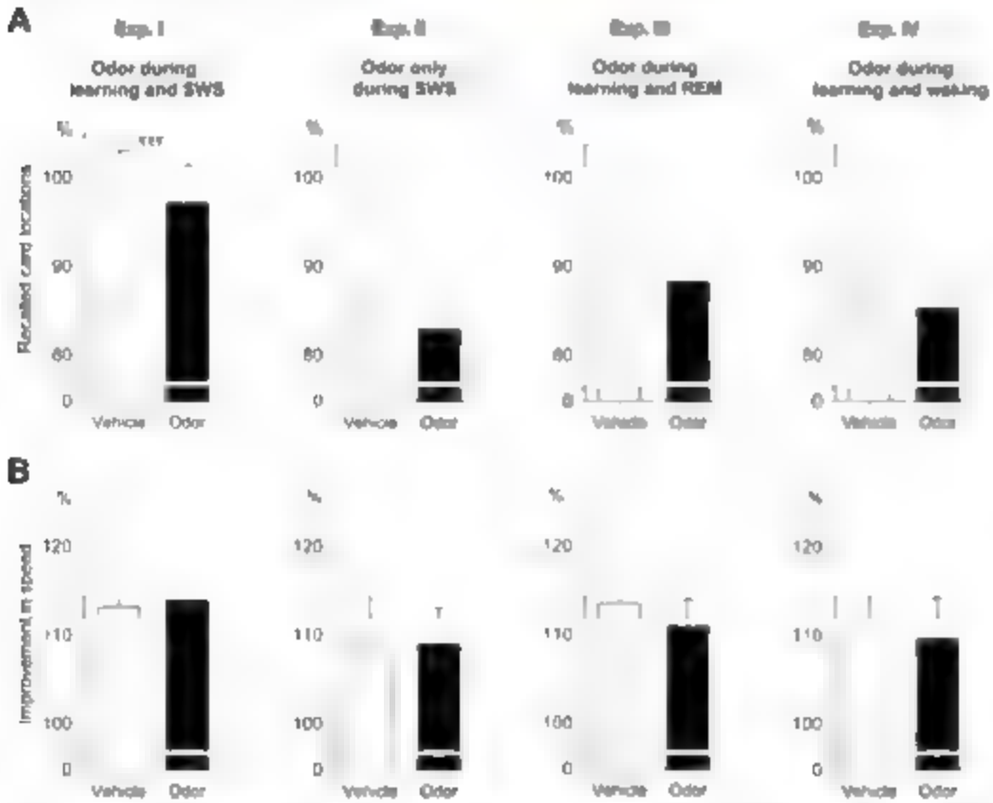

Fig. 2. Retention performance on the visuospatial 2D object-location task (upper panels) and the procedural finger sequence tapping task (lower panels) is shown for four different experiments, each comparing the effects of stimulation with odor and vehicle. (**A**) Only when memory was cued by the context odor during SWS (experiment I) was declarative memory of card locations enhanced. The interaction contrast between experiment I and all other experiments was significant ($P = 0.01$). (**B**) Overnight gains in procedural finger-tapping speed were not affected by odor cueing. Memory performance on both tasks is calculated as percentage of retrieval performance, with performance at learning before sleep set to 100%. Means ± SEM are shown. ***$P = 0.001$.

experiment I). No difference in initial learning performance between conditions was observed ($P > 0.4$; table S1). There was a new increase of the nocturnal odor treatment in the morning after sleep ($P > 0.6$). Odor cueing affected neither sleep architecture (table S2) nor electroencephalographic (EEG) spectral power (comparisons of odor-stimulated periods, $P > 0.4$; fig. S1).

We also tested participants on a procedural memory task (finger sequence tapping) that does not require hippocampal function but is likewise sensitive to the enhancing effects of sleep (*20*). During learning, participants repeatedly tapped a five-element finger sequence on a keyboard as fast and accurately as possible for 12 30-s periods with the odor was applied. At retrieval testing after sleep, tapping speed was improved after the presentation of both odor and vehicle during SWS ($P = 0.02$) (fig. 2B). However, in contrast to performance on the object-location task, sleep-associated gains in motor skill were not changed by re-exposing the participants to the odor during sleep after training ($P > 0.7$; Fig. 2B and table S3).

Our results support the hypothesis that once an odor has become associated as the context of learned object locations, reapplication of the odor during subsequent SWS activates a widely distributed memory trace and thereby boosts its consolidation. However, it can be argued that odor presentation during SWS exerted a non-specific effect on the ongoing consolidation of memories and was independent of any previously formed association between odor and learning

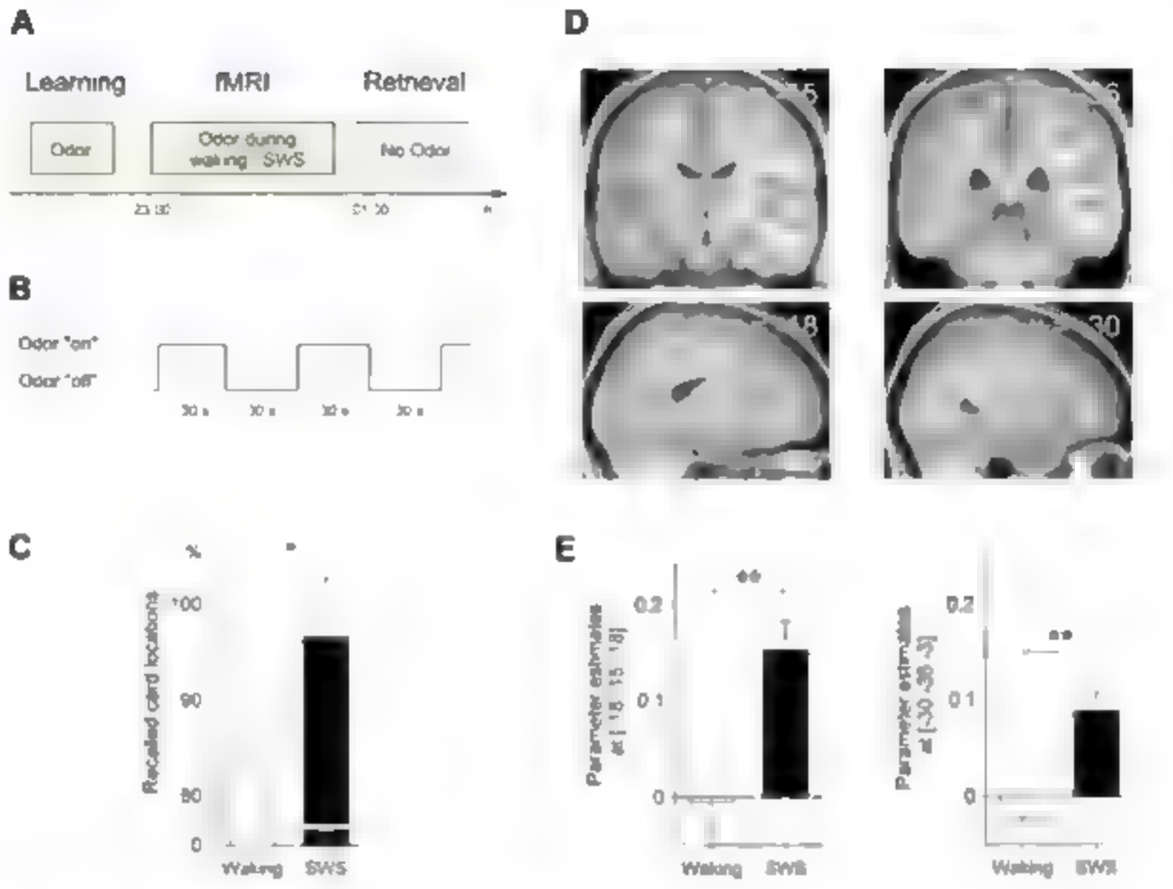

Fig. 3. (**A**) Procedure. The odor was presented during learning and again during post-learning SWS, or at a corresponding time after learning (~45 min) while participants were awake. (**B**) fMRI scans were obtained every 5.61 s during re-exposure to the odor presented, as in the behavioral studies, in an alternating 30 s on/30 s off pattern. (**C**) Retrieval tested after fMRI scanning revealed better retention on the 2D object-location task when participants had slept (for 55.0 ± 4.9 min) than after the corresponding wake interval (*$P < 0.05$, one-tailed test). Note that the shorter retention interval (2 hours) renders the comparison of performance with experiments I to IV difficult. (**D**) Brain activation in response to odor presentation during SWS (threshold set at $P < 0.005$ uncorrected; superimposed on the average structural MRI of all volunteers). BOLD responses to odor-on periods indicate activation in the left anterior hippocampus (left panels) and in the left posterior hippocampus (right panels). (**E**) Parameter estimates (regression coefficients with arbitrary units) for waking and SWS conditions, at the coordinates of local maxima observed during SWS in the left anterior (left panel) and left posterior (right panel) hippocampus. Means ± SEM are indicated. **$P < 0.01$.

Table 1. Brain regions showing significant activity during odor-on periods. Based on a priori hypotheses, significances are corrected for small volumes of interest (SVCs) covering the left (L.) and right hippocampus. Results of an exploratory whole brain analysis with a threshold set at $P < 0.001$ (minimal voxel size $k = 3$) are also indicated where applicable. Post-hoc comparisons between SWS and waking were restricted to the left hippocampus. No significant activations were observed for waking > SWS or on > off. MNI, Montreal Neurological Institute.

	MNI coordinates (mm)				
	x	*y*	*z*	*Z* score	*P*
SWS, on > off					
L. anterior hippocampus	−18	−15	−18	3.59	$<0.05_{SVC}$
L. posterior hippocampus	−30	−36	3	3.39	$<0.05_{SVC}$
L. inferior frontal gyrus	−24	33	−9	3.24	<0.001
Waking, on > off					
L. anterior hippocampus	−33	−12	−18	3.39	$<0.1_{SVC}$
SWS > waking > on > off					
L. posterior hippocampus	−33	−38	−3	3.32	$<0.05_{SVC}$
L. anterior hippocampus	−18	−9	−15	3.03	$<0.05_{SVC}$

stimuli. This possibility was examined in a control experiment (experiment II, $n = 17$ participants) using a design and procedures identical to those of the main experiment, with the only exception being that no odor was presented during learning before sleep. In contrast to odor that had been linked to the learning stimuli (experiment I), odor presentation during SWS alone proved ineffective in enhancing memory. The percentage of recalled locations was 82.9 ± 5.7% in the odor condition and 85.9 ± 3.9% after vehicle presentation ($P > 0.6$, Fig. 2A and table S1). Restricting odor presentation to post-learning sleep also did not affect finger-tapping skill ($P > 0.4$, Fig. 2B and table S3).

Is the effect of odor cueing on object-location memory specific to SWS? In a third experiment (experiment III, $n = 17$ participants), we tested the effect of odor-stimulated memory reactivation during rapid eye movement (REM) sleep, which predominates during late nocturnal sleep (9). Experimental procedures (including the duration of odor stimulation; table S4) were again the same as in the main experiment, except that the timing of odor re-exposure was shifted to the first two periods of REM sleep occurring after 3 hours of sleep. Despite prior coupling of the odor to the learned stimuli, odor re-exposure during post-learning REM sleep failed to affect the memory of card locations (88.3 ± 4.4% versus 89.5 ± 5.2% after vehicle presentation, $P > 0.8$; Fig. 2A and table S1). Overnight gains in finger tapping skill did not differ between conditions either ($P > 0.4$, Fig. 2B and table S3). The lack of odor-related memory effects during REM sleep is unlikely to be ascribed to the longer time between acquisition and re-exposure, because experimental odors remain effective retrieval cues for days (*13*, *14*). Also, it cannot result from reduced olfactory processing, because sensitivity to olfactory stimuli is enhanced during REM sleep as compared with SWS (*17*). Whether the memory-enhancing effect of odor cueing extends to lighter forms of non-REM sleep (stage 2 sleep) remains to be tested.

The failure of REM sleep contingent odor stimulation to enhance procedural memory for finger-tapping skill might be unexpected, because previous findings indicated a reactivation of skill memories during post-learning REM sleep (*2*, *22*) as well as REM sleep related benefits for this type of memory (*2*, *9*, *23*). However, there is little evidence that procedural skills can be effectively conditioned to context cues such as odors (*14*), and olfactory processing areas may not have the same immediate access to the structures subserving skills (the motor cortex, striatum,

cerebellum, etc.) as they have to hippocampal structures (*24*). Therefore, the sleep-associated administration of odor stimuli seems to be an approach suitable only for reactivating hippocampus-dependent memories.

We also tested whether odor re-exposure depends on application during sleep or whether the same memory consolidation effect could be also observed during wakefulness (experiment IV, $n = 18$ participants), as suggested by previous studies (*25*, *26*). Re-exposure to odor (versus vehicle) took place during a 1-hour interval starting 45 min after learning, while participants performed a vigilance task (Fig. 1B). Thereafter, participants slept normally and retrieval was tested the next morning. Unlike SWS-contingent odor presentation, odor re-exposure during wakefulness did not affect the retention of visuospatial memories (85.3 ± 4.7% versus 87.4 ± 5.9% recalled locations after vehicle presentation; $P > 0.7$; Fig. 2A and table S1) or tapping skill ($P > 0.5$; Fig. 2B and table S3).

Central to our hypothesis is the notion that the odor-induced reactivations boosting the consolidation of hippocampus-dependent declarative memories are indeed related to hippocampal activity during SWS (*5*, *6*). Consequently, we used functional magnetic resonance imaging (fMRI) to examine whether odor cues that were previously associated with learning stimuli are capable of activating the hippocampus during post-learning SWS (experiment V, $n = 12$ participants). Odor stimulation was applied, as in the main experiment, during learning and again during subsequent SWS or during wakefulness (Fig. 3). In the sleep condition, all of these participants reached SWS averaging 15.5 ± 4.1 min (*18*). As hypothesized, re-exposure to the odor cue during SWS activated the hippocampus (Table 1). Significant blood oxygenation level dependent (BOLD) responses to odor-on periods were revealed in the left anterior and posterior hippocampus [P small volume corrected (P_{SVC}) < 0.05; Fig. 3D]. A trend for activation in the left anterior hippocampus was also observed in response to odor stimulation presented during wakefulness ($P_{SVC} < 0.08$). Direct comparisons between the waking and sleep conditions revealed an even stronger activation in response to odor presentation during SWS than during wakefulness in both the anterior and posterior part of the left hippocampus ($P_{SVC} < 0.05$; Fig. 3E). The data fit well with previous findings on brain imaging during wakefulness, indicating no or only short-lived hippocampal activation in response to passive smelling of experimental odors (*15*, *27*), whereas substantial activation in the left anterior and posterior hippocampus was reported by Herz *et al.* (*28*) in response to odors (personal perfume) that were strongly associated with autobiographic episodes. However, it is noteworthy that odor cues activate the hippocampus during SWS to a much greater extent than during wakefulness. Beyond showing that memory-associated odors have access to the hippocampus during SWS, this observation points to a particular sensitivity of hippocampal networks in this sleep stage to stimuli that are capable of reactivation.

Currently, two diverging concepts are discussed regarding how sleep might enhance the consolidation of hippocampus-dependent memories. One assumes that enhanced memory is an indirect consequence of a global downscaling of synaptic connectivity that is induced by slow oscillatory activity during SWS, which basically increases the signal-to-noise ratio for newly encoded information (*29*, *30*). The other concept, examined here, assumes that memory consolidation evolves from repeated covert reactivation of newly encoded hippocampal representations during SWS, which takes place in a synchronized dialogue between thalamocortical and hippocampal circuitry and which eventually leads to the transfer of the representations to neocortical regions for long-term storage (*3*, *5*). Although our results do not exclude processes of synaptic downscaling during SWS, they support the latter concept, indicating that covert reactivations are a causative factor for the consolidation of hippocampal memories during sleep.

References and Notes

1. P. Maquet, *Science* **294**, 1048 (2001).
2. R. Stickgold, *Nature* **437**, 1272 (2005).
3. J. Born, B. Rasch, S. Gais, *Neuroscientist* **12**, 410 (2006).
4. J. L. McClelland, B. L. McNaughton, R. C. O'Reilly, *Psychol. Rev.* **102**, 419 (1995).
5. G. Buzsáki, *J. Sleep Res.* **7**, 17 (1998).
6. G. R. Sutherland, B. McNaughton, *Curr. Opin. Neurobiol.* **10**, 180 (2000).
7. M. A. Wilson, B. L. McNaughton, *Science* **265**, 676 (1994).
8. D. Ji, M. A. Wilson, *Nat. Neurosci.* **10**, 100 (2007).
9. W. Pihal, J. Born, *J. Cogn. Neurosci.* **9**, 534 (1997).
10. M. Mölle, L. Marshall, S. Gais, J. Born, *Proc. Natl. Acad. Sci. U.S.A.* **101**, 13963 (2004).
11. L. Marshall, H. Helgadóttir, M. Mölle, J. Born, *Nature* **444**, 610 (2006).
12. P. Peigneux *et al.*, *Neuron* **44**, 535 (2004).
13. S. Chu, J. J. Downes, *Nature* **403**, 304 (2000).
14. A. Parker, H. Ngu, H. J. Cassaday, *Appl. Cogn. Psychol.* **15**, 159 (2001).
15. C. Zelano, N. Sobel, *Neuron* **48**, 431 (2005).
16. L. R. Squire, C. E. Stark, R. E. Clark, *Annu. Rev. Neurosci.* **27**, 279 (2004).
17. M. A. Carskadon, R. S. Herz, *Sleep* **27**, 402 (2004).
18. Supplementary methods and results are available as supporting material on *Science* Online.
19. T. Sommer, M. Rose, J. Gläscher, T. Wolbers, C. Büchel, *Learn. Mem.* **12**, 343 (2005).
20. M. P. Walker, T. Brakefield, J. A. Hobson, R. Stickgold, *Nature* **425**, 616 (2003).
21. P. Maquet *et al.*, *Nat. Neurosci.* **3**, 831 (2000).
22. P. Peigneux *et al.*, *Neuroimage* **20**, 125 (2003).
23. A. Karni, D. Tanne, B. S. Rubenstein, J. J. Askenasy, D. Sagi, *Science* **265**, 679 (1994).
24. J. Doyon, H. Benali, *Curr. Opin. Neurobiol.* **15**, 161 (2005).
25. W. C. Gordon, in *Information Processing in Animals. Memory Mechanisms*, N. E. Spear, J. A. Kleim, Eds. (Erlbaum, Hillsdale, NJ, 1981), pp. 319–339.
26. Y. Dudai, *Curr. Opin. Neurobiol.* **16**, 174 (2006).
27. A. Poellinger *et al.*, *Neuroimage* **13**, 547 (2001).
28. R. S. Herz, J. Eliassen, S. Beland, T. Souza, *Neuropsychologia* **42**, 371 (2004).
29. G. Tononi, C. Cirelli, *Brain Res. Bull.* **62**, 143 (2003).
30. G. Tononi, C. Cirelli, *Sleep Med. Rev.* **10**, 49 (2006).

31. We thank L. Marshall, M. Mölle, I. Wilhelm, S. Diekelmann, and U. Wagner for discussion of our results and P. Pause, J. Keunecke, N. Langschwager, M. Palm, A. Otterbein, and K. Müller for technical assistance. Supported by the Deutsche Forschungsgemeinschaft (grant SFB 654).

Supporting Online Material

www.sciencemag.org/cgi/content/full/315/5817/1426/DC1
Methods and Results
Tables S1 to S4
References

8 December 2006; accepted 1 February 2007
10.1126/science.1138581

GPC System

The Viscotek Model 302 050 Tetra Array Detector is an integrated multi detector device designed for the character zation of natural and synthetic polymers and copolymers, proteins, protein conjugates, excipients and other macromolecules in a single gel permeation chromatography (GPC) experiment. The detector provides absolute molecular weight without the assumptions, extrapolations, or correc tions required by alternative techniques, molecular size expressed as hydrodynamic radius to less than 1 nm, and radius of gyration, intrinsic viscosity or molecular density and information on structure con formation, aggregation, branching, and copolymer or conjugate composition. The array consists of a differential refractive index detector, an ultraviolet detector, a four capillary differential viscometer detector, and a low angle light scattering detector. All the detectors reside within a temperature con trolled compartment that also has space for up to five GPC columns. This arrangement minimizes inter detector volumes to reduce band broadening effects and ensures that detectors, inter detector tubing, columns, and sample reside at the same temperature throughout the course of the analysis.

Viscotek For information 800-375-5966 www.viscotek.com

Surface Plasmon Resonance Instrument

Sens Q is a dual channel, semi automated surface plasmon resonance (SPR) system with innovative hardware and software tools designed to bring biomolecular interaction analysis to labs of all sizes. The instrument features advanced microfluidics, proven surface attachment methodologies, and state of the art data analysis tools to provide kinetic, affinity, and concentration data. Control and data handling wizards are designed to ensure easy operation through the entire experimental process. SPR has proved to be an invaluable tool for scientists involved in characterizing biomolecular interactions for a wide range of research activities such as antibody selection and screening, drug discovery, ligand fishing, binding specificity, and gene regulation. Researchers who have been dependent on core facilities and centralized labs for access to SPR technology can now perform binding interactions in real time and obtain high quality affinity and kinetic data in their labs.

Nomadics, ICx Technologies For information 405 372-9535 www.nomadics.com

Integration and Retrieval System

Version 5.6 of the BioRS Integration and Retrieval System for retrieving and using results from biological and biomedical databases expands the system's already robust functionality with enhanced performance, including options for taking advantage of relational structure that allow working groups to keep up with innovations in data management. The user friendly graphical interface provides optimized tools for convenient selection and administration of databases as well as specification of queries. Improvements have been made for query result display and subsequent use of results. The Biomax Database Update Tool is available for specifying and performing automatic database upload and processing to ensure that users work with the most up to date information. The system provides a sophisticated and easy to use system for searching and integrating heterogeneous public and proprietary databases in flat file and relational formats. Researchers can quickly search multiple databases simultaneously using convenient web interfaces. The system ensures security within a distributed environment, allowing safe data sharing between members of a large working group using data banks integrated at multiple locations.

Biomax Informatics For information +49 89 895574-0 www.biomax.com

Protein Fractionation Using Ultrafiltration

A new protocol offers efficient compartmentalizing of protein solutions using ultrafiltration in a centrifugal mode. Traditional fractionation techniques make use of size exclusion chromatography, which is laborious and time intensive. The new method offers greater speed and efficiency because Amicon Ultra centrifugal devices enable researchers to fractionate protein mixtures quickly and easily. The bi vertical housing limits membrane polarization, while the hydrophilic microstructure of the low binding Ultracel ultrafiltration membrane enables efficient protein separation. This method expedites the fractionation process by minimizing steps such as setting up columns, optimizing column flow rates, and collecting and concentrating various fractions. Fractionation is a process for separating a mixture into its component parts to eliminate the complexity of the proteome. Common applications include biomarker analysis from serum, protein purification, two dimensional polyacrylamide gel electrophoresis, and sample preparation for mass spectrometry analysis.

Millipore For information 978 762 5294 www.millipore.com

Programmable Peristaltic Pump

The Dose It programmable peristaltic pump is designed to make the dispensing of culture media, buffers, and other solutions easy and efficient. Simple programming and straightforward operation make the pump suitable for laboratories where several different dispensing protocols are frequently used. The pump head accommodates different tubing sizes (1 mm to 8 mm), so the dispensed volume can range from 0.1 ml to several liters. Typical applications include filling tubes with liquid broth, pouring to agar plates, filling bottles with buffers, and aliquoting stock solutions. The flow rate can be doubled by using a second pump head, a modification that also reduces flow pulsation. The compact design allows it to be moved and used virtually anywhere, and its versatility reduces the need to have several single purpose pumps. An intuitive multilingual user interface, a large display, and an ergonomically designed keypad make the pump simple to program and operate. Twenty different dosing protocols can be saved and recalled at the press of a button.

Integra Biosciences For information 41 81 286 9530 www.integra-biosciences.com

Newly offered instrumentation, apparatus, and laboratory materials of interest to researchers in all disciplines in academic, industrial, and government organizations are featured in this space. Emphasis is given to purpose, chief characteristics, and availability of products and materials. Endorsement by *Science* or AAAS of any products or materials mentioned is not implied. Additional information may be obtained from the manufacturer or supplier.

POSITIONS OPEN

ASSISTANT/ASSOCIATE PROFESSOR
Division of Pharmacology and Toxicology
University of Missouri, Kansas City
School of Pharmacy

The Division of Pharmacology and Toxicology in the School of Pharmacy invites applications for a 12 month, tenured or tenure-track position at the Assistant/Associate Professor level. Applicants should possess a Ph.D., Pharm.D. or M.D. in pharmacology, neuroscience, toxicology, or a related discipline. Preference will be accorded to applicants with interdisciplinary research experience involving [illegible] agents or substance abuse or translational research, outstanding candidates from other relevant areas are also strongly encouraged to apply. The successful applicant at the Associate Professor level is expected to have a vigorous, well-established, and externally funded research program; and to provide instruction in the Doctor of pharmacy professional program and dental pharmacology program. The position includes excellent compensation, startup package, and comprehensive benefits. Application review will begin immediately, and will continue until the position is filled.

University of Missouri, Kansas City, UMKC is a comprehensive research university exemplifying the values of education first, innovation, accountability, diversity and collaboration. More about UMKC is at website: http://www.umkc.edu or website: http://pharmacy.umkc.edu/

Applicants should electronically submit a cover letter and curriculum vitae with research plan, and arrange to have letters from three professional references e-mailed to:

Anil Kumar, Ph.D., Chair, Search Committee
Division of Pharmacology and Toxicology
University of Missouri-Kansas City
2411 Holmes Street
Kansas City, MO 64110-2741
Telephone: 816 235 2415
E-mail: currylc@umkc.edu

ASSISTANT PROFESSOR (PART TIME)
University of Saskatchewan
Department of Physiology
College of Medicine

We invite applications for a five-year part time (75 percent) term position at the level of Assistant Professor.

Candidates must have a Ph.D. or M.D. and post-doctoral experience. He or she must have demonstrated excellence in research in regulatory and integrative physiology with particular emphasis on neural systems and plasticity or cardiovascular regulation. This is primarily a teaching position for the interdepartmental course Form and Function of the Human Body for first year medical and dental students, for an introductory course to the allied health sciences, and for a laboration course, a joint course with biology as part of the core curriculum in the basic health sciences and specialized courses in the B.Sc. physiology program. The successful applicant will have an opportunity to apply for research grants and if successful will have laboration space. Opportunities exist to join the Neural Systems and Plasticity Research Group, the Cardiovascular Research Group, or any other group of choice.

Please send curriculum vitae and the names of three references by April 15, 2007 to:

Dr. Wolfgang Walz
Head of Physiology, College of Medicine
University of Saskatchewan
107 Wiggins Road
Saskatoon SK S7N 5E5 Canada
E-mail: wolfgang.walz@usask.ca
Fax: 306-966-6532

The University of Saskatchewan is committed to Employment Equity. Members of designated groups (women, Aboriginal people, people with disabilities, and visible minorities) are encouraged to self-identify on their applications. All qualified candidates are encouraged to apply; however, Canadians and permanent residents will be given priority.

POSITIONS OPEN

Chicago Medical University
LOYOLA UNIVERSITY CHICAGO
Stritch School of Medicine

TENURE-TRACK FACULTY POSITIONS

The Department of Pharmacology at Loyola University Chicago, Stritch School of Medicine is recruiting Tenure-Track Faculty at all ranks to establish their own independent research programs that interdigitate with existing programs within the Department and the Cardiovascular, Neuroscience, and Oncology Institutes. Candidates whose research focuses on the dissection of fundamental mechanisms for clinical/therapeutic applications and already have productive, established research programs are especially encouraged to apply. Generous startup funds and laboratory space are available. For more information about the Department visit website: **http://www.luhs.org/depts/pharmacology/index.html**. Applicants should have a Ph.D. and/or M.D. degree, and be committed to excellence in research and teaching of pharmacology. Applications should include curriculum vitae and a research interest statement. Three letters of reference to support the candidacy should be sent separately. Address all correspondence to: **Dr. Tarun B. Patel, Chair, Department of Pharmacology, Loyola University Chicago, Stritch School of Medicine, 2160 S. First Avenue, Maywood, IL 60153.** (No electronic applications accepted.) *Equal Employment Opportunity Affirmative Action Employer*

MICROBIOLOGIST, OPPORTUNISTIC PATHOGENS, University of Maine. The Department of Biochemistry, Microbiology, and Molecular Biology (**website: http://www.umaine.edu/bmmb**) will fill a research-teaching, tenure-track, academic year, **ASSISTANT PROFESSOR** level position with a microbiologist conducting research on microbial pathogens such as those involved in [illegible] associated with diseases such as cystic fibrosis, AIDS, et cetera. The academic year position will be available September 1, 2007. The successful candidate will teach and provide research opportunities for graduate students and undergraduates in capstone research, independent study, or thesis, and will engage in student advising. The successful applicant [illegible] be able to teach undergraduate pathogenic microbiology or [illegible] and a graduate offering in her/his specialty area. The successful candidate will use model systems for understanding the distribution, incidence, dynamics, and control of emerging infectious diseases using approaches from molecular to ecological that preferably include genomics/proteomics. The Department houses a state-of-the-art zebrafish facility. A Ph.D. in microbiology, or a relevant field, and postdoctoral research experience are required. Please send cover letter, curriculum vitae, research plans, and names and addresses of three references to **Dr. Carol Kim (e-mail: carolkim@maine.edu), Microbiologist Search Committee, Department of Biochemistry, Microbiology and Molecular Biology, 5735 Hitchner Hall, University of Maine, Orono, ME 04469-5735.** Review of applications will begin immediately and continue until the position is filled. *Women and minorities are encouraged to apply. The University of Maine is an Equal Opportunity/Affirmative Action Employer.*

CAREER OPPORTUNITY

This unique program offers the candidate with an earned Doctorate in the life sciences the opportunity to obtain the Doctor of Optometry (O.D.) degree in 27 months (beginning in March of each year). Employment opportunities exist in research, education, industry, and private practice. Contact the **Admissions Office, telephone: 800-824-5526** at the **New England College of Optometry, 424 Beacon Street, Boston, MA 02115.** Additional information at website: **http://www.neco.edu**, e-mail **admissions@neco.edu.**

Genzyme Corporation is a global biotechnology company dedicated to making a major positive impact on the lives of people with serious diseases. Around the world, Genzyme's more than 9,000 employees are united by our common and constant commitment to patients. As one of the five top biotech companies in the world, we offer an incredible environment in which individuals can excel, building upon their diverse skills, strengths and delivering their personal best.

Principal Scientist - #8908

We are seeking a highly motivated scientist to support all R&D and Process Development Sciences activities, build excellence into our Analytical R&D at Genzyme Orug and Biomaterial R&D, and enhance our capability in small molecule and synthetic polymer analysis. In this position, the scientist will work with an exciting multidisciplinary team to design and implement traditional and innovative R&D programs. The work encompasses all aspects of preclinical development and validation, including study design, data analysis, report and summary presentation.

The candidate should have a Ph.D. in analytical chemistry or related field and 10+ years of working experience in the pharmaceutical/biotechnology industry related to drug development. In depth knowledge of method development and validation in a GLP/GMP regulated environment is expected. Must have "hands on" experience with mass spectrometry, HPLC, CE, affinity separation, electro analytical methods, and UV and FTIR spectroscopy. In-depth knowledge of physico-chemical analysis in solution and at interfaces is desired. Extensive experience in sample preparation techniques, including dialysis, solid phase extraction and semi-preparative chromatography is required. Experience in HT method development and the analysis of complex biological samples using hyphenated or multidimensional techniques is essential. Prior supervisory experience and good organizational and interpersonal skills are a plus.

Please apply online at: www.Genzyme.com/careers - Job #8908.

Ranked #6 Employer among the World's Top 20 Biotechnology & Pharmaceutical Companies

FORTUNE 100 BEST COMPANIES TO WORK FOR

An equal opportunity employer committed to a culturally diverse workplace

www.genzyme.com/careers

NSU NOVA SOUTHEASTERN UNIVERSITY
Beyond the Classroom

FACULTY POSITION IN COASTAL ENVIRONMENTAL SCIENCE

NSU Oceanographic Center (www.nova.edu/ocean) invites applications for a 12-month position at the ASSISTANT or ASSOCIATE Professor level in Coastal Environmental Science. Applicants must have doctoral degree and experience. Fields of interest include coastal policy and resource management, applied environmental sciences, ecosystem modeling, remote sensing/GIS, ecotoxicology, and wetland, estuarine or coastal ecology. Responsibilities will be graduate teaching and extramurally funded research at the OC and undergraduate teaching at the Farquhar College of Arts and Sciences (www.undergrad.nova.edu).

Please apply online by March 31, 2007 to position **#995000**: **www.nsujobs.com**. Please include with the application: a CV, one-page research and teaching statements, and three letters of recommendation. Inquiries and recommendation letters should be mailed to **Coastal Search Committee, NSU Oceanographic Center, 8000 N. Ocean Drive, Dania Beach, FL 33004.**

Visit our website: **www.nova.edu**

Nova Southeastern University is an Equal Opportunity/ Affirmative Action Employer

---

DIRECTOR

International Computer Science Institute
Berkeley, CA

The International Computer Science Institute (ICSI), an independent non-profit laboratory closely affiliated with the Electrical Engineering and Computer Science Department at the University of California, Berkeley (UCB), invites applications for the position of Director, to begin in the Fall Semester of 2008.

The ICSI Director's primary responsibilities are to: oversee and expand ICSI's research agenda; act as a high-level external evangelist for ICSI research; identify and pursue strategic funding opportunities; and strengthen ICSI's relationship with UCB. The Director reports directly to ICSI's Board of Trustees.

ICSI is recognized for its world-class research activities in speech and language processing, networking, and computational biology, and is building a new competency in computer architecture. Several of ICSI's research staff have joint appointments at UCB, and many UCB graduate students perform their research at ICSI. In addition, ICSI places significant emphasis on international partnerships and visiting scholar programs with countries in Europe and Asia.

ICSI is seeking a Director with sufficient breadth, interest and professional connections to promote and augment ICSI's ongoing research efforts. Applicants should have recognized research leadership, as well as a strong record in research management and demonstrated success at government and industrial fundraising. Experience with international collaboration and fundraising is a plus.

Applications should include a resume, selected publications, and the names of three references who will send recommendations. Review begins May 1, 2007; candidates are urged to apply by that date.

To learn more about ICSI, go to **http://www.icsi.berkeley.edu**. To apply for the Director position, send the above material to **apply@icsi.berkeley.edu**. Recommenders providing letters should send them directly to **apply@icsi.berkeley.edu** by **July 1, 2007**.

ICSI is an Affirmative Action/Equal Opportunity Employer. Applications from women and minorities are especially encouraged.

THE CHINESE UNIVERSITY OF HONG KONG

Applications are invited for:-

Institute of Plant Molecular Biology and Agricultural Biotechnology

Research Associate Professor(s) Research Assistant Professor(s)

(Ref. 07/037/6054/2)

Applicants should have (a) a PhD degree in plant sciences, (b) postdoctoral experience in related fields, and (c) an excellent publication record in prestigious academic journals. Apart from teaching, the appointees will: (a) conduct rigorous research related to longer-term crop genetics and agronomy, crop transformation and genetic engineering, crop nutritional improvement, plant genomics, plant proteomics and metabolomics, or plant stress studies; and (b) apply for competitive grants. Appointments will normally be made on contract basis for one or two years initially commencing April 2007 or as soon as practicable thereafter, leading to longer-term appointment or substantiation later subject to performance, budget and mutual agreement. Applications will be accepted until the posts are filled.

Salary and Fringe Benefits

Salary will be highly competitive, commensurate with qualifications and experience. The University offers a comprehensive fringe benefit package, including medical care, plus a contract-end gratuity for appointments of two years, and housing benefits for eligible appointees.

Further information about the University and the general terms of service for appointments is available at *http://www.cuhk.edu.hk/personnel*. The terms mentioned herein are for reference only and are subject to revision by the University.

Application Procedure

Please send full resume, copies of academic credentials, a publication list and/or abstracts of selected published papers, together with names, addresses and fax numbers/e-mail addresses of three referees to whom the applicant's consent has been given for their providing references (unless otherwise specified), to the Personnel Office, The Chinese University of Hong Kong, Shatin, N.T., Hong Kong (Fax: (852) 2603 6852). The Personal Information Collection Statement will be provided upon request. Please quote the reference number and mark "Application - Confidential" on cover.

WWW.NIH.GOV
Positions NIH
THE NATIONAL INSTITUTES OF HEALTH

NIDDK

POSTDOCTORAL FELLOWSHIPS IN MOLECULAR AND CELL BIOLOGY AT THE NIH

We are a group of molecular and cell biologists on the main intramural campus of the National Institutes of Health (NIH) in Bethesda, Maryland, a 20-minute ride from Washington, D.C. The intramural program of the NIH offers an outstanding research environment and many opportunities for collaborations. Applications are invited from individuals of the highest caliber with Ph.D., M.D., or M.D., Ph.D. degrees. The current research interests of the group include:

Mechanisms of protein secretion in pathogenic and non-pathogenic bacteria. Our group uses a combination of biochemical, biophysical, and genetic methods to study protein secretion via both the classical Sec and autotransporter (type V) pathways. For recent work see Proc. Natl. Acad. Sci. (2005) **102**, 22, 226; Mol. Microbiol. (2005) **58**, 945-958; J. Biol. Chem. (2006) **281**, 9049-9056; Mol. Cell (2006) **22**, 587-598. **(Harris Bernstein; harris_bernstein@nih.gov)**

Biochemistry and molecular biology of double-strand break repair and homologous recombination. Current interests include mouse and human meiosis (Dev. Cell (2004) **4**, 497; Nat. Struct. Mol. Biol. (2005) **12**, 449; J. Cell Science (2005) **118**, 2351; J. Biol. Chem. (2006) **281**, 8426) and evolutionary genomics (Nature Genet. (2004) **36**, 642; Nature Genet. (2005) **37**, 3; Trends in Genet. (2005) **21**, 3). **(Dan Camerini-Otero)**

Molecular Mechanisms of DNA Mismatch Repair. Our focus is on the role of repair proteins in the cellular response to DNA damage involving checkpoint activation and apoptosis and the molecular mechanisms of post-replicative repair and mutation avoidance. (J. Mol. Biol. (2003) **334**, 949; Proc. Natl. Acad. Sci. (2004) **100**, 14822; Mol. Cell (2006) **22**, 501). **(Peggy Hsieh, ph52x@nih.gov)**

Interested candidates should submit a cover letter, a curriculum vitae, bibliography, and arrange to have three letters of recommendation sent to one of the investigators above, or to be considered for more than one lab to **Dan Camerini-Otero (camerini@helix.nih.gov)**.

Bldg. 5, Rm 201
5 Memorial Dr MSC 0538
National Institutes of Health
Bethesda, MD 20892-0538

Staff Scientist in Bone and Mineral Metabolism

The Craniofacial and Skeletal Diseases Branch of the NIDCR is recruiting a Staff Scientist in support of the Skeletal Clinical Studies Unit in its study of mechanisms of human bone and mineral biology. The incumbent will participate in the translational basic science efforts of a clinically-oriented research group that utilizes human specimens and relevant in vivo and vitro models of bone and mineral biology. This is a technical support position which does not involve independent resources for investigator initiated research. The incumbent is expected to be technically independent in the areas of cell and molecular biology. In addition to personally conducting experiments and publishing the results, supervision of junior personnel will also be required. As such, an addition to a high level of innovative and scientific technical expertise strong communication and interpersonal skills are necessary.

Minimum qualifications include a doctoral degree, completion of post-doctoral training, and a strong publication record demonstrating a high degree of intellectual ability. The ideal applicant will have significant experience in the field of bone and mineral biology. For additional information, contact **Dr. Michael Collins at mc247k@nih.gov**. To apply submit curriculum vitae, bibliography, brief statement of relevant background, and three letters of recommendation to **Mis Pulles, 30 Center Drive, MSC 4320, Building 30, Room 228, Bethesda, MD 20892-4320, USA or email: mpulles@mail.nih.gov.**

Postdoctoral, Research and Clinical Fellowships at the National Institutes of Health

www.training.nih.gov/pdopenings

www.training.nih.gov/clinopenings

Train at the bench, the bedside or both

Office of Intramural Training and Education
Bethesda, Maryland 20892-0210
800 445 8283

Group Leaders

CANCER RESEARCH UK

DIRECTOR OF LABORATORY OPERATIONS

FBR
Foundation for Blood Research

The Foundation for Blood Research (FBR), an independent, research laboratory established in 1973, is seeking applications for a Director of Laboratory Operations.

Dartmouth Medical School

The candidate must be either a Ph.D. or M.D. who fulfills all federal requirements for laboratory director as defined by CLIA. Five or more years of experience directing a high complexity laboratory is desirable. Responsibilities include overseeing the day-to-day operation and administration of the molecular genetics, prenatal screening and rheumatic disease testing laboratories including the management and employment of approximately 25 laboratory personnel. Additional requirements include the proven ability to plan and implement innovative new services within budget and time parameters, a history of effective leadership accomplishments demonstrated internally and externally, and a willingness to work with FBR's affiliate, Dartmouth Medical School. Must be a problem-solver with good people and communication skills.

To apply, please submit a letter of interest, curriculum vitae and three professional references to: Jane Sheehan, Esq., Vice President and Chief Operating Officer, Foundation for Blood Research, P.O. Box 190, Scarborough, ME 04070-0190. Alternatively, email the above information to jsheehan@fbr.org.

FBR is a 501 (c) (3), non-profit organization located minutes from sandy beaches, great skiing, and Maine's largest city (Portland). Boston is just 1½ hours by car. For more information please visit our web site at www.fbr.org.

www.fbr.org

EEOE

COLUMBIA UNIVERSITY

Faculty Position in Biomedical Engineering

The Department of Biomedical Engineering in the Fu Foundation School of Engineering and Applied Science at Columbia University invites applications for a tenure track faculty position at the Assistant, Associate or Full Professor level. Of particular interest are candidates with expertise and research interests in one or more of relevant interdisciplinary areas: neural engineering, neuroimaging, computational systems biology or functional tissue engineering. Successful candidates must demonstrate an ability to develop a world-class research program, be capable of obtaining competitive external research funding, and participate in and be committed to outstanding teaching at both the undergraduate and graduate levels. The candidate should have a doctorate in Biomedical Engineering or a related discipline. Applicants should send a complete curriculum vitae, three publication reprints, a statement of research interests, a statement of teaching experience and philosophy, and names and contact information for four references by May 1, 2007 to:

Professor Paul Sajda
Chair of the Faculty Search Committee
Department of Biomedical Engineering
Columbia University
351 Engineering Terrace, Mail Code 8904
1210 Amsterdam Avenue
New York, NY 10027

The search will remain open until the position has been filled.

Columbia University is an affirmative action/equal opportunity employer. Women and minorities are encouraged to apply.

Tenure Track Research Positions
Wadsworth Center

The Wadsworth Center is seeking outstanding research scientists at the level of assistant, associate or full professor to establish competitive research programs in:

MACROMOLECULAR MACHINES. Researchers with background and interests in the study of the structure and dynamics of large macromolecular complexes employing experimental techniques such as single-molecule FRET, atomic force techniques, cryo-electron microscopy, or x-ray crystallography are sought to join Wadsworth's new Center for Macromolecular Machines. Wadsworth is also home to the Resource for Visualization of Biological Complexes, an NIH-funded center for electron microscopy (**www.wadsworth.org/rvbc**) and is a charter member of the New York Structural Biology Center. Chair of search committee: **Dr. Joachim Frank (singlemolecule@wadsworth.org).**

BIOINFORMATICS AND COMPUTATIONAL BIOLOGY. Researchers focusing on computational approaches to functional studies of non-coding RNAs, genomics, proteomics or systems biology are sought to interact with research groups within the Center for Bioinformatics and the Genomics Institute. A strong biological background is desirable, and research having an experimental as well as computational component is welcome. The Center's home-base is a specialized, NIH-funded 12,000-square-foot facility with state-of-the-art computing and collaboratory resources. Chair of search committee: **Dr. Jean Curcio (bioinformatics@wadsworth.org)**

The Wadsworth Center is the country's most comprehensive state public health laboratory with a long history of research excellence. It has been recognized several times as a Top 10 place to work by *The Scientist*, most recently in 2005. It is located in Albany, the capital of New York state, which offers a vibrant academic community, diverse cultural and outdoor activities, and an attractive cost-of-living. Applicants must have a Ph.D., M.D., or equivalent. Successful candidates may join the faculty of the Department of Biomedical Sciences, University at Albany School of Public Health (**www.wadsworth.org/bms**). Review of applications will begin **April 9, 2007** with appointments to be initiated in Fall, 2007. Applicants should send curriculum vitae, summary of research interests and future plans, and arrange for three letters of reference to be sent to the chair of the relevant search committee at: **Wadsworth Center, New York State Department of Health, PO Box 509, Albany, NY 12201-0509**

The Wadsworth Center is an Affirmative Action/Equal Opportunity Employer.

USDA ars Agricultural Research Service
www.ars.usda.gov

The U.S. Department of Agriculture, Agricultural Research Service San Joaquin Valley Agricultural Sciences Center Parlier, California, invites applications for a **Research Plant Molecular Biologist Plant Physiologist** GS-12/13 14 ($63,417-$1,5,848 per annum) Incumbent conducts research independently and as part of a team on the biology of *Xylella fastidiosa* (Xf) strains that cause Pierce's disease (PD) of grapevines, almond leaf scorch, oleander leaf scorch, alfalfa dwarf and other xylellae and exotic and invasive diseases of agronomic, horticultural and ornamental crops **(announcement ARS-X7W-0018)** The candidate must have the ability to formulate new concepts and hypotheses, and develop new techniques and approaches to investigate *X. fastidiosa*-host interactions. This is a competitive, permanent appointment and U.S. citizenship is required

Vacancy announcements and where to apply can be found at **www.usajobs.com** or contact, **Drake Stenger (559) 596-2922** Closing date for applications is **April 13, 2007**

The USDA is an Equal Opportunity Provider and Employer

Informatics Director
(Assistant/Associate/Full Professor)
Clinical and Translational Science Program
The University of Vermont

The University of Vermont is recruiting for an Informatics Director for the Clinical and Translational Science Program. The qualified candidate will have an advanced degree and/or significant experience in the use of sophisticated informatics systems in translational and/or clinical research Preferred candidates will have experience working at the interfaces of different IT systems in different institutions with an emphasis on interconnectivity, experience with an electronic medical record would be an advantage The candidate will also be expected to have a track record and continue to publish in academic journals in aspects conjoining IT and clinical and/or translational research. The appointment will be made at the appropriate Professional level with or without tenure in the Clinical and Translational Science Program and in the appropriate primary department, depending on discipline. Applications will be accepted until the position is filled; however, we strongly encourage the submission of materials by **April 1, 2007** Applicants should send a copy of their CV, a letter outlining their interests and three letters of recommendation to **Richard Galbraith, M.D., Ph.D., Chair of the Search Committee, Associate Dean for Patient Oriented Research, MCHV/Ward 795, 111 Colchester Avenue, Burlington, VT 05401** or by applying at **www.uvmjobs.com**. *Applications are encouraged from women and individuals of diverse racial, ethnic and cultural backgrounds AN EQUAL OPPORTUNITY AFFIRMATIVE ACTION EMPLOYER*

University of Colorado Health Sciences Center

University of Colorado at Denver and Health Sciences Center
Assistant, Associate, Full Professor (Tenure-Track)
Department of Pharmaceutical Sciences, School of Pharmacy

The University of Colorado at Denver and Health Sciences Center School of Pharmacy is entering a new and exciting phase in its growth and development. The Health Sciences Center is moving to the newly developed Anschutz Medical Campus, located several miles away from its current location, a move that will greatly enhance the research, education and clinical practice environments As part of this move, the School of Pharmacy is designing and constructing a new building that will provide the school with expansion space for its growing research enterprise The School of Pharmacy will be situated adjacent to the new Bioscience Park providing the faculty with unparalleled opportunities to collaborate with both Health Sciences Center faculty and emerging bioscience companies in research and entrepreneurial endeavors. The School of Pharmacy will recruit for numerous faculty positions over the next three years to enhance its nationally renowned programs in basic, translational and clinical research, education and clinical practice

The Department of Pharmaceutical Sciences is a research-intensive group of faculty focusing their basic, translational and clinical research efforts in the areas of pharmaceutical biotechnology, molecular toxicology cancer pharmacology pharmacokinetics and pharmacogenomics. Current areas of research emphasis in the department can be found at

http://www.uchsc.edu/sop/pharmscience/2.Research_Programs/

In this initial phase of recruitment, the department is seeking applicants with a PhD or PharmD degree and an established record of excellence for tenure-track positions at the level of assistant, associate or full professor in the following areas

Pharmacokinetics/Cancer Pharmacology (Job Posting #800455)

Leadership position available to direct the Cancer Pharmacology Core of the University of Colorado Cancer Center and assist in the design and implementation of early clinical trials of novel anticancer agents. The Department of Pharmaceutical Sciences in collaboration with the Developmental Therapeutics Phase I Program has extensive expertise in phase I clinical trials of agents that target molecular pathways. The successful candidate will have experience in applying pharmacokinetics and pharmacodynamics to problems in cancer pharmacology and anticancer drug development Preferred areas of emphasis include PK-PD modeling biomarkers or drug design/delivery but all areas of cancer pharmacology will be considered

Drug Delivery (Job Posting #800456)

The successful candidate will have experience in novel drug delivery technologies applied to either small molecules or macromolecular therapeutics. Areas of emphasis might include transdermal, pulmonary parenteral, or oral delivery using needleless, patch, ultrasound, inhalation, or nanoparticle technology but preference will be given to individuals who interface with current research programs in pharmaceutical biotechnology and cancer pharmacology

Medicinal Chemistry/Drug Development – Two Positions (Job Posting #800457)

Preference will be given to individuals applying novel synthetic computational and analytical approaches to drug development. Areas of emphasis in the department include anticancer drug development and the development and stability of macromolecular therapeutics Successful applicants will be expected to contribute to an emerging campus focus in chemical biology

Medicinal Chemistry/Drug Metabolism (Job Posting #800458)

The successful candidate will have experience in metabolic chemistry and will be expected to incorporate synthetic, modeling and proteomic approaches in studies of drug metabolism. This position will complement current areas of emphasis which include the role of metabolism in toxicological response pharmacogenetics and pharmacogenomics. Successful applicants will be expected to contribute to an emerging campus focus in chemical biology

Clinical/Translational Research (Job Posting #800459)

The successful candidate will have experience in pharmacokinetic, pharmacodynamic, or pharmacogenetic approaches to clinical research and in their application to clinical trials. Diverse therapeutic areas will be considered but integration with existing departmental initiatives in pharmacokinetics or pharmacogenetics pharmacogenomics will be required. The successful individual will be expected to take leadership positions in the development of a center for pharmacokinetics and pharmacogenetics and in the training of clinical scientists

Successful candidates will be expected to develop or maintain an internationally competitive, extramurally funded research program and contribute to teaching at both the Pharm.D and Ph.D levels in the School of Pharmacy. Faculty rank and salary will be dependent upon qualifications and experience. Applicant screening will begin **April 2, 2007** and continue until the positions are filled Applicants **please apply electronically at www.jobsatcu.com to the job posting number of the position(s) of interest**. Applicants must submit electronically a letter of interest, brief research plan, curriculum vitae and the names of three references with regular and e-mail addresses, phone and Fax numbers. Any questions regarding the application process can be directed to **Jay Rodenburg**, Director of Personnel at **jay.rodenburg@uchsc.edu** or at **303/315-1053**

The University of Colorado is committed to diversity and equality in education and employment

Does your next career step need direction?

There's only one place to go for career advice if you value the expertise of *Science* and the long experience of AAAS in supporting career advancement - ScienceCareers.org. The pages of *Science* and our website ScienceCareers.org offer:

- Thousands of job postings
- Funding information
- Career advice articles and tools
- Networking opportunities

www.sciencecareers.org

Get the experts behind you.

www.ScienceCareers.org

- Search Jobs
- Next Wave
- Job Alerts
- Resume/CV Database
- Career Forum
- Career Advice
- Meetings and Announcements
- Graduate Programs

All features on ScienceCareers.org *are FREE to job seekers.*

ScienceCareers.org

We know science

AAAS

POSITIONS OPEN

The Zoological Society of San Diego is seeking a scientific innovator to lead a new research division devoted to plant conservation that focuses on sustainability and restoration of ecosystems. We seek a **CONSERVATION BIOLOGIST** who uses an applied, multidisciplinary approach to include several of the following areas: restoration biology, community ecology, genetics, invasive species management, spatial ecology, soil science, or rare plant populations. Also desirable is an interest in working in San Diego County, a biodiversity hotspot, as well as a history of building conservation partnerships. Extensive opportunities exist for collaboration with a dynamic research team (**website: http://www.zooconservation.org**). Candidates must have a Ph.D., a minimum of three years of postdoctoral experience and a proven track record in obtaining extramural funding; supervisorial management experience desired. Interested applicants should submit curriculum vitae, statement of research interest, up to five sample publications, and contact information for three references to: **San Diego Zoo's Wild Animal Park, Attn: Human Resources Number 172408, 15500 San Pasqual Valley Road, Escondido, CA 92027. Website: http://www.sandiegozoo.org/employment, Fax: 760 796 5614.** *Equal Opportunity Employer (position)? Contact* ***Human Resources at e-mail: humanresources@sandiegozoo.org***

Denison University, a selective liberal arts college, invites applications for a two-year position for an **ORGANISMAL BIOLOGIST** and a one-year position for a **MOLECULAR BIOLOGIST**, both to begin in August 2007. The teaching load for each position is two courses with companion laboratories each semester; all courses have enrollments of 24 or less. Teaching responsibilities are a sophomore level course (ecology and evolution or cell and molecular biology, respectively), an advanced course in the candidate's area of specialty, and a nonmajors biology course. Demonstrated ability in undergraduate teaching is expected and a Ph.D. is preferred (all but dissertation acceptable). For a detailed description of the Biology Department and our curriculum see website: **http://www.denison.edu/biology/.** Candidates should send letter of application clearly indicating the position and advanced course preferences, curriculum vitae, statement of teaching philosophy, transcripts (graduate and undergraduate), and three letters of reference to: **Chair, Search Committee, Biology Department, Denison University, Granville, OH 43023.** Review of applications will begin March 26, 2007, and continue until the positions are filled. *Denison is an Affirmative Action Equal Opportunity Employer. Women and minorities are encouraged to apply.*

ASSISTANT or ASSOCIATE PROFESSOR of NEUROBIOLOGY
Developmental Neurobiology Program
Institute of Molecular Medicine and Genetics
Medical College of Georgia

The Medical College of Georgia (MCG) invites applications for tenure track Assistant or Associate Professor positions in the Program in Developmental Neurobiology, Institute of Molecular Medicine and Genetics. Candidates should have Ph.D. or M.D., postdoctoral experience, and potential to develop or maintain a strong extramurally funded research program in developmental or regenerative neurobiology. The MCG is a growing state supported academic medical center located in a historic city with outstanding recreational and lifestyle opportunities. Interested applicants should submit curriculum vitae, a statement of research interests, and future plans, and should arrange for three letters of reference to **Dr. Lin Mei, c/o Deenie Cerasuolo (e-mail, dcerasuo@mcg.edu).** Applications will be received until the position is filled. Please reference ACH numbers 49384 and/or 49385 when applying. *Equal Employment Opportunity/Affirmative Action/Equal Access Employer*

CARDIOLOGY RESEARCH INSTRUCTOR
ASSISTANT PROFESSOR
Virginia Commonwealth University Medical Center
Division of Cardiology
Medical College of Virginia Physicians
Richmond, Virginia

ASSISTANT PROFESSOR. Research faculty member is sought for continued expansion of the Virginia Commonwealth University (VCU) Pauley Heart Center of Virginia Commonwealth University. The VCU Pauley Heart Center is a regional referral center with a reputation for excellence in routine, as well as complex, patient management. The Heart Center's faculty are leaders in diagnostics, interventional cardiology, cardiovascular research, and cardiac surgery. Expanding cardiac services is a key strategic initiative of the VCU Health System.

RESEARCH INSTRUCTOR. VCU Health System is seeking to expand science and research in molecular cardiology. The position will devote 100 percent to research endeavors. We are seeking candidates with experience working in the laboratory as a postdoctoral fellow. A Ph.D. in science is required. Successful candidate will have demonstrated success in peer-review grant and publication arena.

Interested candidates should forward their curriculum vitae to:

George W. Vetrovec, M.D.
Chairman, Division of Cardiology
Department of Internal Medicine
Virginia Commonwealth University
P.O. Box 980036
Richmond, VA 23298
Telephone: 804-628-1215, fax: 804-828-8321
E-mail: gwetrove@hsc.vcu.edu

Virginia Commonwealth University is an Affirmative Action/Equal Opportunity Employer. Women, minorities and persons with disabilities are encouraged to apply.

The Department of Anatomy and Neurobiology at the Virginia Commonwealth University School of Medicine invites applications for a tenure-track position at the **ASSISTANT PROFESSOR** level (#206810). Applicants should have a Ph.D., with significant postdoctoral research experience and productivity. The ideal candidate should have research interests that focus on the development and plasticity of the mammalian visual system. Successful candidates are expected to obtain or maintain an externally funded research program and to participate in graduate or professional teaching commensurate with their area of expertise. Interested candidates should submit their curriculum vitae, a letter of intent including career goals and the names, addresses, telephone numbers, fax numbers, and e-mail addresses of three references. Electronic submissions to e-mail: **anatrecruit@vcu.edu** are preferred. For mailing contact **Dr. John Bigbee, Chair, Faculty Search Committee, Virginia Commonwealth University Department of Anatomy and Neurobiology, P.O. Box 980709, Richmond, VA 23298-709.** Deadline for receipt of applications will be April 15, 2007.

Virginia Commonwealth University is an Equal Opportunity/Affirmative Action Employer. Women, minorities, and persons with disabilities are encouraged to apply.

The Department of Land Resources and Environmental Sciences at Montana State University seeks a talented and enthusiastic individual for a **TENURE TRACK FACULTY** position who will provide leadership in the Department's research and teaching programs related to geospatial analysis. The candidate should have research training in the integration of geographic information systems and other spatial analysis approaches within the natural resources/environmental sciences fields. The full position announcement and application instructions are at website: **http://www.montana.edu/level2/jobs.html.** Screening will begin April 23, 2007, and continue until a suitable applicant is found. *Montana State University is an Equal Opportunity Employer. ADA/Affirmative Action/Veteran's Preference*

Fourth International Conference
Ubiquitin, Ubiquitin-Like Proteins, and Cancer

February 7-9, 2008

Department of Cardiology
The University of Texas
M. D. Anderson Cancer Center
Houston, Texas

Organized by Edward T.H. Yeh
Introduction by John Mendelsohn

Meeting Enrollment Begins **July 1, 2007**

For more information visit:
www.sentrin.org

THE UNIVERSITY OF TEXAS
MD ANDERSON
CANCER CENTER
Making Cancer History®

Confirmed Speakers

James Chen
Zhu Chen
Jinke Cheng
Aaron Ciechanover
Mary Dasso
Hugues de Thé
Anne Dejean
George N. DeMartino
Ivan Dikic
Grace Gill
Ronald T. Hay
Avram Hershko
Mien-Chie Hung
Tony Hunter
Stefan Jentsch
Hsing-Jien Kung
Beth Levine
Christopher D. Lima
Leroy F. Liu
Bruno Martoglio
Michael Matunis
R John Mayer
Frauke Melchior
Shigeki Miyamoto
Michael Ohh
Bert O'Malley
Kim Orth
Michele Pagano
Cam Patterson
Frank J. Rauscher, III
Ze'ev Ronai
Hisato Saitoh
Brenda A. Schulman
Hsiu-Ming Shih
Ali Shilatifard
William P. Tansey
Keith D. Wilkinson
Yue Xiong
Yangping Zhang

Ubiquitin • Ubiquitin-like Proteins • Cancer

Celsense

A **Senior Scientist** position is available for a biologist at Celsense, Inc., in Pittsburgh, Pennsylvania. The successful candidate will participate in the development and commercialization of in vivo cellular imaging agents for magnetic resonance imaging (MRI) applications.

Requirements include: a Ph.D. in biological sciences or a related field with at least 3-5 years of bench R&D experience; a background in mammalian tissue culture; in vitro toxicity assays; animal models; molecular biology techniques. A background in immunology would be helpful. Candidates should have strong scientific problem solving skills; ability to communicate results in a clear and concise manner verbally and in writing; record of scientific achievement as documented by peer-reviewed journal publications. Scientific project management experience is preferred. Some travel is required. Celsense offers a competitive compensation and benefits package.

Interested candidates should send a resume/CV to:

Charles F. O'Hanlon
President and CEO, Celsense, Inc.
100 Technology Drive, Suite 400
Pittsburgh, PA 15219 USA
or email: charlie@celsense.com

The Baltic Summer School 2007

'INFLAMMATION: A Key to Common Complex diseases'

Organized by the Faculty Members of the Baltic Summer School coordinators Prof. Rikard Holmdahl and Dr. Bo Nilson, University Lund

Theoretical Course

2–13 September, 2007
University of Lund, Sweden

Worldwide experts will present the current knowledge:

- Evolution and Ontogeny of Inflammatory Response
- The Inflammatory Syndrome in Man and Animal Models for Human Inflammatory Diseases
- Genetic Approaches on Human Inflammatory Diseases
- Mimicking Human Diseases Using Genetic Approaches on Animals
- Innate and Adaptive Immunity and Inflammatory Effector Mechanisms
- Prediction, Monitoring and New Preventive and Therapeutic Treatment Strategies and Targets for Inflammatory Diseases

The Honorary Lecture will be given by Prof. Shimon Sakaguchi on Regulatory T cells. Invited speakers will participate in panel discussions. Course participants are expected to present posters on their work.

Laboratory Course

17–21 September, 2007
Universities of Lund, Kiel and Copenhagen

Open to 20 of the young scientists participating in the theoretical course, which have been selected for a BSS 2007-stipend. The participants will join on-going research projects covering the modern methodological aspects on inflammatory research.

Baltic Summer School Stipends

The Baltic Summer School is supported by the EU under the Marie Curie Program which has a special focus on young scientists with research experience at the late phase of their PhD studies as well as at the medical specialist or post-doc levels (or an equivalent academic training). Stipends are available for many participants. For further information see BSS homepage.

The meeting will also be open for a number of participants that do not receive a BSS-stipend.

Participation fee: Theoretical Course 250 Euro

Application deadline: Sunday, April 22, 2007
Programme and application details at: www.balticsummerschool
Email: bss@balticsummerschool.net

POSITIONS OPEN

POSTDOCTORAL POSITION
Germline Stem Cells

Studies involve culture, differentiation, and gene activity of male germline stem cells. See *Proc. Natl. Acad. Sci.* **101**:16489, 2004 and *Proc. Natl. Acad. Sci.* **103**:9524, 2006. Send curriculum vitae, names of three references, and a letter describing research experience to: **R. L. Brinster, School of Veterinary Medicine, University of Pennsylvania. E-mail: cpope@vet.upenn.edu.**

COMPUTATIONAL CELL BIOLOGY
at Virginia Tech

A **POSTDOCTORAL POSITION** is available immediately to conduct research in the area of eukaryotic cell cycle regulation in collaboration with **Professor John Tyson (website: http://mpf.biol.vt.edu).** The work involves modeling molecular regulatory pathways using nonlinear ordinary differential equations. Candidates must have a Ph.D. in a relevant discipline, peer-reviewed publications, and a strong background in mathematical modeling. For further information or to view a complete job description, go to **website: http://www.jobs.vt.edu, posting number 070074.** Interested candidates should submit an online application and attach curriculum vitae, bibliography, statement of career goals, and the names and contact information of three references. Individuals with disabilities desiring accommodation in the application process should notify the **Office for Equal Opportunity, telephone: 540-231-7500.** Review of applicants will begin on 26 March 2007. Questions about this search can be directed to **John Tyson, telephone: 540-231-4662.** *Virginia Tech is an Equal Opportunity/Affirmative Action Institution.*

The Midwest Regional Center for Excellence in Biodefense and Emerging Infectious Diseases Research (MRCE) invites applications for an NIH/NIAID-funded **POSTDOCTORAL FELLOWSHIP in BIOSAFETY.** The Fellowship will provide one to two years of training in how to safely work with and manage select agents, supervised by **Dr. Joseph Kanabrocki** at Washington University in Saint Louis. Upon completion of the program, the Fellow will be able to establish and supervise biosafety programs in a variety of academic, industrial, and government settings. Fellowships require an M.D., Ph.D., D.V.M., or other medically oriented professional degree, preferably in life sciences. Preference will be given to candidates currently affiliated with a Region VII (Iowa, Kansas, Missouri, Ohio, and Nebraska) institution.

Fellow must be a U.S. citizen. For more information contact **Scott Handley** at **telephone: 314-286-0192** or at **e-mail: shandle@id.wustl.edu.** For more information about the MRCE and the Biosafety Fellowship program, please visit **website: http://mrce.wustl.edu.**

RESEARCH ASSOCIATES/ POSTDOCTORAL FELLOWSHIPS

Two Postdoctoral positions are available in the laboratory of **Dr. Shunbin Xu** at the Department of Ophthalmology, Rush University Medical Center in Chicago to study the function of microRNAs in retinal stem cells, retinal development and diseases. Highly motivated candidates are encouraged to apply. A M.D. and/or Ph.D. in neurobiology or molecular biology and genetics are required. Strong background on molecular genetics and bioinformatics is preferred. Qualified candidates should send a statement of research interest, curriculum vitae, and three references to **e-mail: shunbin_xu@rush.edu** or write to: **Dr. Shunbin Xu, Department of Ophthalmology/Neurological Sciences, Rush University Medical Center, 1735 West Harrison Street, Suite 318, Chicago, IL 60612.**

STAFF ASSOCIATE

Candidate will lead and conduct molecular and bioinformatics analysis experiments designed to resolve the roles of aldose reductase and receptor for advanced glycation endproducts (RAGE) in heart failure and apoptosis models in the cardiomyocyte. Candidate will be responsible for a range of techniques with which he/she will be highly familiar and able to work on an independent basis. Duties will involve cell culture, molecular and cellular biology assays (it is required that successful candidate be fully proficient in RNA/DNA manipulation, subcloning, PCR, electrophoresis, and molecular cloning), and analysis of the biochemical pathways and key molecules linked to apoptosis. In addition, applicant must have extensive experience and training in bioinformatics in order to be able to carry out statistical analysis of a wide array of genes and gene patterns. Since this work involves in vivo experimentation, applicant must have some experience in mouse microsurgery, for example, background in vascular procedures in mouse models. Additionally, he/she will perform other related duties necessary to functioning of the laboratory, research project, or work unit as assigned. It is expected that the successful candidate will be able to perform each of the above duties independently and report findings to the principal investigator on a daily basis. Candidate must have a doctoral degree and have at least five years of experience in research including expertise in each of these areas. In addition, a degree in bioinformatics and computer science is highly desired. Please submit all resumes to: **Karen M. Evans, Division of Surgical Science, Department of Surgery, College of Physicians and Surgeons, Columbia University, 630 West 168th Street, New York, NY 10032.**

Columbia University takes Affirmative Action to assure Equal Employment Opportunity.

POSTDOCTORAL FELLOW
Immunology

A Postdoctoral Fellow position is available for work on NIH-funded projects studying human immune responses. These projects will include clinical studies on patient samples, as well as basic studies on the mechanisms of differentiation of human T cell subsets, and their contributions to immune responses. The University of Rochester Medical Center is a highly interactive environment with excellent collaborations between basic and clinical scientists. Excellent facilities include strong flow cytometry and cell sorting capabilities, computer modeling of immune responses, sophisticated image analysis of fluorescent images including Fluorospot assays, and the support of the Human Immunology Center with standard operating procedures and innovative methods. Curriculum vitae to: **Dr. Tim Mosmann, Director, David H. Smith Center for Vaccine Biology and Immunology, University of Rochester, 601 Elmwood Avenue, P.O. Box 609, Rochester, NY 14642.**

The University of Rochester is an Equal Opportunity Employer.

POSTDOCTORAL POSITION to study mitochondrial dysfunction in neurodegeneration using time-lapse microscopy. Successful applicants have a recent Ph.D./M.D. with a strong publication record. Experience in cell biology, neuroscience, biochemistry, image analyses (Metamorph), or electrophysiology is required. Send curriculum to: **Dr. Ella Bossy-Wetzel, Biomedical Science Center, University of Central Florida, 4000 Central Florida, FL 32816. E-mail: ebossywe@mail.ucf.edu.**

POSTDOCTORAL POSITION to study molecular mechanisms of myeloid differentiation. Prior experience in production/analysis of transgenic mice or evaluation of myelopoiesis preferred. Expertise in molecular biology will be helpful. Send curriculum vitae and names of three references to: **Dr. Daniel Johnson, Hillman Cancer Center, Room 2.18c, University of Pittsburgh, 5117 Centre Avenue, Pittsburgh, PA 15213. E-mail: johnsond@pitt.edu.**

Six **POSTDOCTORAL POSITIONS** available at the Hormel Institute, University of Minnesota, Austin, Minnesota, to study signal transduction in tumor promotion, chemoprevention and early development (see review articles: *Science's STKE*, **re4**, 2005; *Progress in Nucleic Acid Research and Molecular Biology*, **79**: 237-97, 2005; *Nature Review Cancer* **4**: 793-805, 2004; *Science's STKE*, **re2**, 2003). We are seeking self-motivated Ph.D.s with experience in biochemistry, molecular, and cellular biology specializing in one of three categories as follows: (1) Signal transduction, functional genomics, models such as mouse transgenic/knockout, *Xenopus*, zebrafish; (2) Proteomics, protein crystallization, x-ray crystallography and structure refinement; (3) Stem cell. If interested, please apply online at the University of Minnesota employment homepage **website: http://www.umn.edu/ohr/employment** and refer to requisition number 146599 when entering curriculum vitae and names of references. These positions will be open until qualified candidates are found. *The University of Minnesota is committed to the policy that all persons shall have equal access to its programs, facilities, and employment without regard to race, color, creed, religion, national origin, sex, age, marital status, disability, public assistance status, veteran status, or sexual orientation.*

POSTDOCTORAL POSITIONS
Prostate Cancer

An excellent opportunity for career development to Instructor and Junior Faculty Appointment. The position will study the development and growth of prostate cancer using mouse and tissue culture models. Focus will be on the role of the Pim protein kinase and regulation of TOR. Individuals should have a strong background in molecular biology, protein chemistry, and/or transgenic mouse models. Forward curriculum vitae and the name of three references to: **Andrew S. Kraft M.D., Director Hollings Cancer Center, 86 Johnathan Lucas Street, P.O. Box 250955, Charleston, SC 29425. E-mail: hccjobs@musc.edu.** Please reference ad number 395.

Columbia University Department of Surgery seeks **STAFF ASSOCIATE or SENIOR STAFF ASSOCIATE** to support activities related to quality assurance, performance improvement, and research in the Cardiothoracic Surgery Division's adult, pediatric, and heart source network. Minimum requirements include strong clinical knowledge in cardiothoracic surgery and technologies that can improve the data collection process, and basic programming skills. Send curriculum vitae and cover letter to **Larry Beils, e-mail: lv724@columbia.edu.** *We are an Affirmative Action/Equal Opportunity Employer.*

MARKETPLACE

Pierce® now sold as Thermo Scientific

Reuse. Recycle. Restore.

Restore™ Western Blot Stripping Buffers efficiently strip your antibody and let you recycle your Western blots

Highlights:

- No need to rerun gels; reprobe the membrane using the same target sample
- Provides more efficient removal than "home-brew" buffers
- Does not damage target protein after stripping and reprobing
- Odor-free
- Less expensive than competing stripping buffers

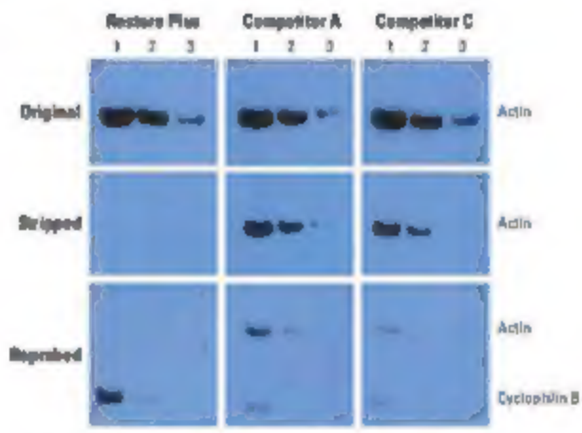

Reprobing with different antibodies.
HeLa cell lysate was probed for actin and detected with Pierce ECL Substrate (Original panel). Blots were then stripped with either Restore Plus Stripping Buffer or competitive stripping buffers (Stripped panel). The blots were then re-blocked and reprobed for cyclophilin B and detected with Pierce ECL Substrate (Reprobed panel).

Learn more today.

Visit www.piercenet.com/restore3, email Pierce.CS@thermofisher.com or call 800-874-3723 or 815-968-0747.

Part of Thermo Fisher Scientific

Thermo SCIENTIFIC

Tools for Cell Biology Research

R&D Systems Proteome Profiler™ Arrays

Simultaneously detect multiple proteins in a single sample.

R&D Systems offers these Array Kits:

- Human Cytokine Array Kit, Panel A
- Human Phospho-Immunoreceptor Array Kit
- Human Phospho-Mitogen-Activated Protein Kinase (MAPK) Array Kit
- Human Phospho-Receptor Tyrosine Kinase (RTK) Array Kit

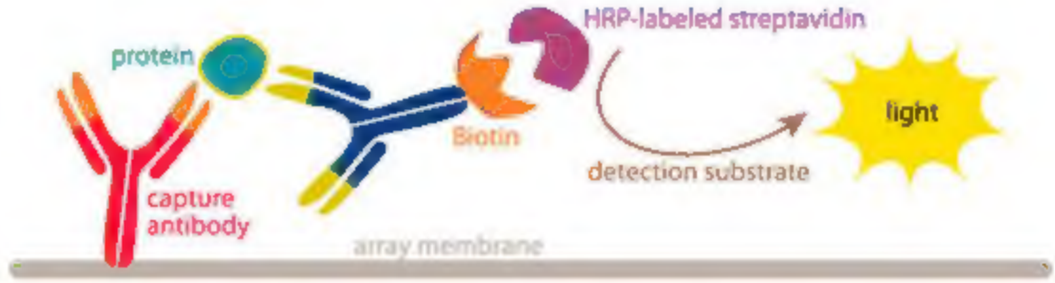

Proteome Profiler Arrays enable the measurement of the relative levels of phosphorylation or abundance of multiple proteins in a single serum, plasma, or cell culture supernatant sample. Proteome Profiler kits contain buffers, detection antibodies, and membranes spotted in duplicate with capture antibodies carefully selected for their specificity. And with chemiluminescent detection, no specialized equipment is necessary.

Rapid | **Highly specific** | **Sensitive** | **Efficient**

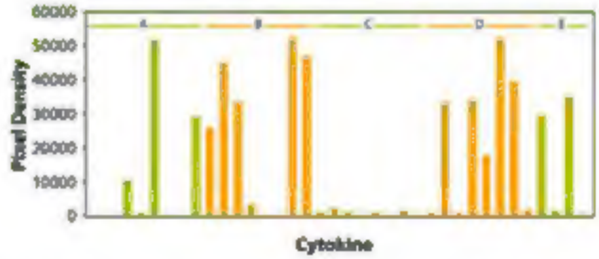

Sample data for **R&D Systems Human Cytokine Array, Panel A** demonstrating high-throughput multi-analyte profiling of 36 cytokines, chemokines, and acute phase proteins in a single sample of PBMC supernatant.

For more information visit our website at www.RnDSystems.com/go/ProteomeProfiler

For research use only. Not for use in diagnostic procedures.

U.S. & Canada
R&D Systems, Inc.
Tel: (800) 343-7475
info@RnDSystems.com

Europe
R&D Systems Europe Ltd.
Tel: +44 (0)1235 529449
info@RnDSystems.co.uk

Selection expanding weekly—visit www.RnDSystems.com to sign up for weekly new product updates.

R&D SYSTEMS®